



UCGE Reports
Number 20292

Department of Geomatics Engineering

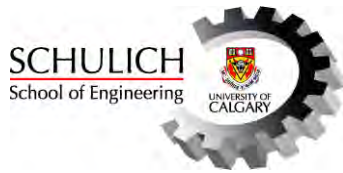
**Enhanced Narrowband Signal Detection and
Estimation with a Synthetic Antenna Array for
Location Applications**

(URL: <http://www.geomatics.ucalgary.ca/research/publications>)

by

Ali Broumandan

September 2009



UNIVERSITY OF CALGARY

Enhanced Narrowband Signal Detection and Estimation with a Synthetic Antenna Array
for Location Applications

by

Ali Broumandan

A THESIS

SUBMITTED TO THE FACULTY OF GRADUATE STUDIES
IN PARTIAL FULFILMENT OF THE REQUIREMENTS FOR THE
DEGREE OF DOCTOR OF PHILOSOPHY

DEPARTMENT OF GEOMATICS ENGINEERING

CALGARY, ALBERTA

September, 2009

© Ali Broumandan 2009

ABSTRACT

The main focus of this thesis is to develop a practical signal processing method based on the synthetic array concept applied to handheld location systems to enhance signal detection and parameter estimation in multipath environments. The antenna array is synthesized by moving one or two antennas along an arbitrary spatial trajectory while snapshot data is being collected. The synthetic array concept is introduced to reduce cost and complexity, and to improve receiver portability. The synthetic array is implemented for two applications of the antenna array, namely as a diversity system to enhance signal detection performance in dense multipath environments, and in the form of an Angle Of Arrival (AOA) estimation application.

Signal reception in indoor environments is susceptible to deep fading and signal attenuation. An antenna array utilizing spatial diversity can be implemented to reduce fading margins and to improve the signal detection performance. The indoor detection performance of narrowband signals based on a single moving antenna operating as a synthetic array, as compared to that of a static antenna, is investigated. The synthetic array provides a diversity gain through a combination of received signals at each synthetic antenna element. The processing gain achievable through spatial combining of a synthetic antenna is considered from a general theoretical perspective. The performance of the proposed method is theoretically analyzed in terms of the probability of false alarm and the probability of detection. Extensive sets of measurements based on CDMA-IS 95 pilot signals and GPS L1 C/A signals using a static antenna and a synthetic array are used to experimentally verify these theoretical findings.

In specular multipath environments, in which case the multipath channel is correlated, an approach for AOA estimation based on the use of a synthetic array utilizing the Estimation of Signal Parameters via Rotational Invariance Techniques (ESPRIT) algorithm is proposed. Taking advantage of the rotational invariance property of the ESPRIT algorithm, the antenna array is synthesized by moving a two-channel receiver. With this scheme, the synthetic array trajectory estimation, which is normally performed by using controllable moving motors or external aiding sensors, is removed. Simulation and experimental results verify the applicability of the proposed method.

ACKNOWLEDGMENTS

I would like to express sincere gratitude to my supervisor, Dr. Gérard Lachapelle, for his guidance, continuous encouragement and financial support during my Ph.D. program. I will always remember his positive attitude and understanding which helped me to shape my professional career and to know my strength and weakness better.

Thanks to my co-supervisor, Dr. John Nielsen, for his friendship, sharing his insights and assisting me in the theoretical work of this thesis. The research presented herein could not be completed without helpful suggestions of him.

Special thanks to Saloomeh Abbasian Nik for her support and for her constant love during my education. She was the reason of my happiness and peace. Also, thanks to my insightful friend, Ahmad Reza Abdolhosseini Moghaddam, for the supportive technical discussions during the initial period of my PhD program. I express my great appreciation to my trustworthy friend, Dr. Saeed Khalesehosseini, for his valuable pieces of advice before starting the program and his helps during the settlement period in Calgary.

I owe special thanks to my colleagues in the TOPS project. In particular, I would like to acknowledge the help of Dingchen Lu, Tao Lin, Alfredo Lopez, Surendran K. Shanmugam, Vahid Dehghanian and other TOPS members. This research could be much more challenging without their endeavors and support.

My acknowledgments and thanks go to my colleagues in the PLAN group, in particular Dr. Mark Petovello, Dr. Cillian O'Driscoll, Dr. Daniele Borio, Pejman L.

Kazemi and Ashkan Izadpanah for their kindness and helpful suggestions in technical issues.

Finally, I am greatly thankful to my parents, without whose support I would never have gotten this far. This thesis is a dedication to them and their unconditional love. Moreover, I would like to thank my sister and brother for their encouragement and love during my education when I was thousands of kilometers away from them.

DEDICATION

To my beloved parents, Farzin and Sima, my sister Tannaz and my brother Farbod.

TABLE OF CONTENTS

Abstract.....	iii
Acknowledgments.....	v
Dedication.....	vii
Table of Contents	viii
List of Tables	xii
List of Figures.....	xiii
List of Abbreviations	xix
List of Symbols	xxii
Chapter 1: Introduction.....	1
1.1 Background and Motivation	1
1.2 Applications of the antenna array in dense multipath fading environments.....	4
1.3 Application of antenna arrays for multipath and interference mitigation in specular multipath environments	7
1.4 Objectives and novel contributions.....	9
1.4.1 Signal detection enhancement in fading environments utilizing the synthetic array	10
1.4.2 AOA estimation utilizing the synthetic array	14
1.5 Thesis Outline	16
Chapter 2: Array Processing Background.....	20
2.1 Signal model received by an antenna array	21
2.2 Beamforming concept.....	25
2.2.1 Array performance metrics	27
2.3 Multiple signal model in the presence of additive noise.....	30
2.3.1 Narrowband snapshot model.....	31
2.4 Uniform linear array	33
2.5 Signal propagation models in wireless channels	35
2.5.1 Small-scale fading.....	36

2.5.2 Rayleigh fading	42
2.5.3 Signal model in fading environments	44
2.6 Performance of beamforming techniques in multipath fading channels	45
2.7 Diversity techniques.....	50
2.8 Detection of a signal in noise.....	52
2.8.1 Matched filter.....	52
2.8.2 Estimator-correlator	54
2.9 Summary	56
Chapter 3: Synthetic Array Model and Characterization of the Propagation Channel.....	57
3.1 Synthetic array system model	58
3.2 Characterization of the channel gain vector.....	64
3.2.1 Plane wave, known AOA and known channel gain.....	65
3.2.2 Plane wave, known AOA and unknown channel gain.....	67
3.2.3 Single plane wave, unknown AOA and channel gain is circularly Gaussian..	70
3.2.4 Multiple plane wave, unknown AOA and channel gain is circularly Gaussian ..	72
3.3 Performance of EC in different multipath scenarios.....	78
Chapter 4: Signal Detection Performance in Rayleigh Fading Environments with a Synthetic Antenna Array.....	89
4.1 System model and detection performance of the static antenna	91
4.1.1 Static antenna detection performance	95
4.2 Synthetic array system model in discrete mode.....	97
4.3 Synthetic array system model in continuous mode.....	100
4.3.1 Coherent integration loss due to antenna motion in Rayleigh fading.....	106
4.3.2 Selecting M for a given aperture in the Rayleigh fading model	109
4.4 Detection process of a narrowband signal in Rayleigh fading	110
4.4.1 Optimum detection performance of a narrowband signal in Rayleigh fading based on the Synthetic Array	111
4.4.2 Detection performance of the EG combiner in the Rayleigh fading channel based on the synthetic array	114
4.5 Discrete mode synthetic array detection performance and processing gain in uncorrelated Rayleigh fading.....	120
4.6 Discrete mode synthetic array detection performance and processing gain in correlated Rayleigh fading.....	128
4.7 Processing gain of the synthetic array in the continuous mode	133
4.8 Synthetic array implementation considerations	143
4.9 Conclusions.....	148

Chapter 5: Experimental results of signal detection enhancements in indoor fading environments	150
5.1 Field measurements of the discrete mode synthetic array detection performance in indoor environments utilizing CDMA IS-95 signals	151
5.1.1 CDMA IS-95 signal structure and receiver architecture.....	151
5.1.2 Data collection and experimental results based on the CDMA IS-95 pilot signals	156
5.1.3 Experimental results of data set 1	160
5.1.4 Experimental results of data set 2, synthetic array experimental results in a correlated Rayleigh fading.....	177
5.2 Experimental results on the detection performance of GPS signals in indoor environments based on the discrete synthetic array process.....	183
5.2.1 Signal model	183
5.2.2 Data collection Setup	185
5.2.3 Measurement results	189
5.3 Experimental results of detection performance of GPS indoor signals based on the continuous synthetic array	196
5.3.1 Data collection setup.....	197
5.3.2 Measurement results of data collection in medium size laboratory	198
5.3.3 Measurement results of data collection in large size laboratory.....	203
5.4 Conclusions.....	208
Chapter 6: AOA Estimation based on the Synthetic Antenna Array	210
6.1 AOA estimation problem.....	211
6.1.1 Array manifold and signal subspace	213
6.1.2 AOA estimation based on the MUSIC algorithm.....	215
6.1.3 ESPRIT angle of arrival estimation algorithm.....	216
6.1.4 AOA estimation based on the synthetic array utilizing the ESPRIT algorithm	220
6.2 Simulation results of AOA estimation based on the synthetic array	221
6.2.1 Baseline simulation.....	221
6.2.2 Sensitivity of the ESPRIT algorithm to the model order estimation	223
6.2.3 AOA estimation in correlated signal environments.....	225
6.3 Practical considerations and experimental results	227
6.3.1 Estimation of signal subspace dimension	228
6.3.2 Calibration process.....	229
6.3.3 Experimental results.....	230
6.4 Conclusions.....	243
Chapter 7: Conclusions and Recommendations	244
7.1 Conclusions.....	244

7.2 Recommendations	246
7.2.1 Signal detection performance in dense multipath environments	246
7.2.2 AOA estimation and signal detection performance in specular multipath environments	248
References	250
Appendix A: Limit of NIG for different values of v when $T \rightarrow \infty$	260
Appendix B: for larger values of M $\frac{d\rho_m}{dM} > 0$	261
Appendix C: Synthetic array detection performance utilizing signals of Market Mall BS	263

LIST OF TABLES

Table 5-1: CDMA IS-95 pilot characteristics	152
Table 5-2: Characteristics of IS-95 data collection scenarios.....	159
Table 5-3: Processing Gain of the moving antenna over static antenna for different spatial samples for data set 1	168
Table 5-4: Processing Gain of the moving antenna over the static antenna for different spatial samples, UofC BS, $T= 40 \mu\text{s}$	172
Table 5-5: Processing Gain of moving antenna over static antenna for different spatial samples, UofC BS, $T=80 \mu\text{s}$	173
Table 5-6: Processing Gain of moving antenna over static antenna for different spatial samples, UofC BS, $T= 160 \mu\text{s}$	174
Table 5-7: GPS L1 C/A characteristics.....	184
Table 5-8: Characteristics of indoor GPS data collection scenarios.....	189
Table 5-9: Processing Gain and MAT ratio of the synthetic array over the static antenna for different PRNs.....	196
Table 5-10: Characteristics of indoor GPS data collection scenarios in continuous mode	197
Table 5-11: Moving antenna detection statistics for PRN 7, 8 and 19	202
Table 5-12: Detection statistics of the moving antenna for PRN 31 ($T=100 \text{ ms}$)	205
Table 5-13: Detection statistics of the moving antenna for PRN 31 ($T=200 \text{ ms}$)	206
Table 5-14: Summery of field measurement experiments	209
Table 6-1: Means and variances of AOA estimation for different values of signal correlations.....	227
Table 6-2: Characteristics of indoor GPS data collection scenarios.....	231
Table 6-3: Summary of experimental results of AOA estimation	243

LIST OF FIGURES

Figure 1-1: Correlation process and TOA (range) estimation utilizing a 7-chip sequence (from http://www.amsat.org/amsat/articles/g3ruh/123.html , last accessed 29June 2009)	2
Figure 1-2: (a) AOA estimation, (b) beamforming concepts.....	3
Figure 1-3: (a) Multipath phenomenon, (b) received signal power in multipath environments.....	5
Figure 1-4: Thesis flow graph.....	17
Figure 2-1: Spherical coordinate system.....	21
Figure 2-2: Spatial sampling by sensors (Van Trees 2002).....	22
Figure 2-3: Narrowband beamformer block diagram	25
Figure 2-4: Quadrature demodulation.....	32
Figure 2-5: Uniform linear array configuration.....	33
Figure 2-6: Beampattern of a ULA, $M=10$ and $d = \kappa / 2$	34
Figure 2-7: Small-scale fading in a multipath environment	36
Figure 2-8: Multipath power delay profile.....	38
Figure 2-9: Rayleigh distribution.....	43
Figure 2-10: Spatial correlation coefficient for different values of φ_s and φ	47
Figure 2-11: Array gain for different values of M versus multipath angular spread φ_s for $\varphi = 0$	48
Figure 2-12: Array gain for different values of M versus multipath angular spread φ_s for $\varphi = 45$	48
Figure 2-13: Eigenvalues of spatial covariance matrix for different values of φ_s	49
Figure 2-14: Block diagram of antenna diversity systems.....	51
Figure 2-15: Detection process of a matched filter.....	53
Figure 2-16: EC detection process	55
Figure 2-17: Canonical for of the EC process	56
Figure 3-1: Diagram of moving antenna and positional vector definitions for snapshot collection for the m -th subinterval	60

Figure 3-2: Eigenvalues for $d = 0.5$, $M = 10$, $\varphi_s = 2$ degree, $\varphi = 45$ degree and $\sigma_n^2 = 1$ 81

Figure 3-3 Compass plot of principal eigenvector for $d = 0.5$, $M = 10$, $\varphi_s = 2$ degree, $\varphi = 45$ degree and $\sigma_n^2 = 1$ 82

Figure 3-4: Radiation pattern for $\varphi_s = 2$ degree, $\varphi = 45$ degree and $\sigma_n^2 = 1$ 83

Figure 3-5: Radiation pattern for $\varphi_s = 2$ degree, $\varphi = 45$ degree and $\sigma_n^2 = 0.1$ 83

Figure 3-6: Eigenvalues of signal covariance matrix $\varphi_s = 10$ degree, $\varphi = 45$ degree and

$\sigma_n^2 = 1$ 85

Figure 3-7: Principal eigenvector for $\varphi_s = 10$ degree, $\varphi = 45$ degree and $\sigma_n^2 = 1$ 85

Figure 3-8: Radiation pattern for $\varphi_s = 10$ degree, $\varphi = 45$ degree and $\sigma_n^2 = 1$ 86

Figure 3-9: Radiation pattern for $\varphi_s = 10$ degree, $\varphi = 45$ degree and $\sigma_n^2 = 0.1$ 86

Figure 3-10: Radiation pattern $\varphi_s = 50$ degree, $\varphi = 45$ degree and $\sigma_n^2 = 0.01$ 87

Figure 3-11: Radiation pattern $\varphi_s = 50$ degree, $\varphi = 45$ degree and $\sigma_n^2 = 10$ 88

Figure 4-1 Static antenna channel model and subsequent NP processing 94

Figure 4-2: Moving antenna and positional vector definitions for snapshot collection for the m -th and $(m+1)$ -th sub-intervals each of duration ΔT in discrete mode 97

Figure 4-3: Moving antenna and positional vector definitions for snapshot collection for continuous mode synthetic array 102

Figure 4-4: a) Correlation coefficient of a moving receiver versus receiver velocity for $T=1$ s and $M=1$, b) normalized correlation power versus T for constant $v=1$ and $M=1$ 108

Figure 4-5: Correlation coefficient for different values of M 110

Figure 4-6: Synthetic antenna channel model and subsequent EC processing 112

Figure 4-7: Channel model and equal-gain combining receiver processing for the moving antenna 115

Figure 4-8: Required average SNR for a static and moving antenna versus P_D 121

Figure 4-9: (a) Required average SNR for a static and moving antenna versus M (b) Achievable gain by moving antenna ($P_D=0.95$ and $P_{FA}=0.01$) 122

Figure 4-10: Synthetic array required average SNR versus P_D and M for $P_{FA}=0.01$	124
Figure 4-11: Synthetic array gain with respect to static antenna versus P_D and M for $P_{FA}=0.01$. The black line represents the optimum M as a function of P_D	124
Figure 4-12: (a) Optimum gain versus P_D , (b) M_{opt} versus P_D ($P_{FA}=0.01$).....	125
Figure 4-13: MAT ratio of static antenna to synthetic array	127
Figure 4-14: ROC curves for different values of M , SNR=16 dB	128
Figure 4-15:(a), (c) and (e) show the required SNR for the stationary and synthetic antenna with EC and EG for target values of P_{FA} and P_D ; (b), (d), and (f) show the processing gain of a synthetic array for the EC and EG combiner	130
Figure 4-16: ROC curves for given SNR and r	132
Figure 4-17: Synthetic array gain for $M=2$ versus different values of r and P_D	133
Figure 4-18: a) Required average SNR, b) Gain, and c) number of M versus different values of v	136
Figure 4-19: P_D of a moving receiver for given $T=1$, $P_{FA} = 0.05$, and $\rho = 15$ dB versus velocity of the receiver and different values of M	137
Figure 4-20: P_D versus receiver velocity and SNR for a given $P_{FA} = 0.01$ and $T=1$ s....	138
Figure 4-21: Required T versus v and SNR per second for detection targets of $P_{FA} = 0.01$ and $P_D = 0.95$	139
Figure 4-22: ROC curves of EC, SNR=10 dB and $d = \kappa$	139
Figure 4-23: PDF of EC for different values of M	141
Figure 4-24: ROC curves of the EG combiner, SNR=10 dB and $d = \kappa$	142
Figure 4-25: PDF of EG for different values of M	142
Figure 4-26: (a) Processing gain, and (b) normalized gain degradation for different values of r versus P_D	145
Figure 4-27: NGD for different values of correlation coefficients and P_D for $P_{FA}=0.05146$	
Figure 4-28: Values of the correlation coefficient where the performance of EG combiner becomes worse than static antenna	147
Figure 5-1: Down conversion and PRN code despreading	154
Figure 5-2: FFT based correlation method	154
Figure 5-3: IS-95 correlation function over two-dimensional hypothesis search.....	155

Figure 5-4: Normalized correlation outputs for a period of a CDMA IS-95 signal	156
Figure 5-5: Data collection setup.....	157
Figure 5-6: Vertical plane pattern of the antenna	158
Figure 5-7: Layout of office floor with the hashed area indicating the locations used for collecting experimental data	158
Figure 5-8: Data collection environment and measurement equipment (a) data set 1 (b) data set 2	159
Figure 5-9: Typical code delay correlation function of the CDMA pilot signal processing	161
Figure 5-10: Indoor channel normalized correlation coefficient	162
Figure 5-11: Measured and fitted PDF of the test statistics under H_1 state	163
Figure 5-12: Estimated PDF under H_0 and H_1 states for moving antenna $M=2$	164
Figure 5-13: Theoretical and numerically evaluated ROC curves based on measurements	166
Figure 5-14: Measured ROC curves for the static and moving antenna.....	167
Figure 5-15: Calculated PDFs under H_1 state based on measurements a) static, coherent integration b) static non-coherent integration c) synthetic array $M=2$	170
Figure 5-16: Calculated PDFs under H_0 state based on measurements a) static, coherent integration b) static, non-coherent integration c) synthetic array $M=2$	171
Figure 5-17: ROC curves for static coherent integration, static non-coherent process and the synthetic array, $T=40 \mu\text{s}$	172
Figure 5-18: ROC curves of static coherent integration, static non-coherent process and the synthetic array, $T=80 \mu\text{s}$	173
Figure 5-19: ROC curves of static coherent integration, static non-coherent process and the synthetic array, $T= 160 \mu\text{s}$	174
Figure 5-20: Instantaneous SNR for the static antenna and the synthetic array	176
Figure 5-21: Numerically calculated PDFs under H_0 and H_1 states for a static antenna	179
Figure 5-22: Numerically calculated PDFs under H_0 and H_1 states for a moving antenna	179
Figure 5-23: Numerically calculated ROC curves in an uncorrelated case	180
Figure 5-24: PDFs of the synthetic array under H_1 state for different antenna spacings.	181

Figure 5-25: Measured ROC curves for static antenna and synthetic array	182
Figure 5-26: Reference and indoor data collection setup	186
Figure 5-27: a) Measurements setup, b) geometry of visible satellites and data collection location, c) Layout of office floor with the hashed area indicating the area used for collecting experimental data	187
Figure 5-28: Demodulating process utilizing the reference signal	188
Figure 5-29: Correlation outputs and test statistics under H_0 and H_1 for GPS PRN 21..	190
Figure 5-30: Measured amplitude PDF and theoretical Rayleigh PDF for GNSS measurements.....	191
Figure 5-31: Estimated PDFs under H_1 (a, c and e) and H_0 (b, d and f) states for GNSS static antenna (a and b) and synthetic array with $M=2$ (c and d) and synthetic array with $M=4$ (e and f)	192
Figure 5-32: Estimated ROC curves based on GNSS measurements for the static antenna and the synthetic array with 2 and 4 elements for uncorrelated and coherent cases	193
Figure 5-33: Instantaneous SNR for static antenna and synthetic array with $M=2$ and $M=4$	194
Figure 5-34: Instantaneous SNR cumulative density functions.....	195
Figure 5-35: Measurements setup a) in the medium size laboratory b) in the large size laboratory	197
Figure 5-36: Measured PDF under H_0 (a, c and e) and H_1 (b, d and f) states for $M=1$ (a and b), $M=2$ (c and d) and $M=4$ (e and f).....	199
Figure 5-37: Estimated ROC curves based on measurements for the moving antenna for different values of M	200
Figure 5-38: a) ISNR for the moving antenna for different values of M , b) CDF of ISNR for different values of M	201
Figure 5-39: ROC curves of the static set1 and moving set2 antenna for $T=200$ ms	204
Figure 5-40: ISNR CDFs for (set1) and moving (set2) antennas for $T=200$ ms	204
Figure 5-41: ROC curves of the static and moving antennas for different values of T ..	207
Figure 6-1: ESPRIT array geometry	216
Figure 6-2: Array configuration utilized in the simulation	222

Figure 6-3: AOA estimation by the ESPRIT algorithm for 5000 runs	222
Figure 6-4: Estimated and fitted PDFs of AOA estimation.....	223
Figure 6-5: Histogram of AOA estimation by the ESPRIT algorithm, model order is underestimated (true angles are 50 and 60 degrees)	224
Figure 6-6: AOA estimation by the ESPRIT algorithm, model order is over estimated	225
Figure 6-7: PDFs of the estimated AOA in correlated signal environment.....	226
Figure 6-8: Measurement setup on the roof of the CCIT building	232
Figure 6-9: Topology of the receiver and BSs.....	232
Figure 6-10 Estimated phase values of two antennas at the calibration point.....	233
Figure 6-11: Phase differences of estimated phase values between two antennas at the output of the correlation function	234
Figure 6-12: PDF of phase differences between two channels and normal fit	235
Figure 6-13: Root MSE for AOA estimation degradation due to phase mismatches in the calibration process	236
Figure 6-14: AIC criterion as a function of the number of sources	237
Figure 6-15: Estimated AOA from Market Mall BS, $M=30, K=20$	238
Figure 6-16: AOA estimation PDF and normal fit for 18000 snapshots	238
Figure 6-17: AOA estimation PDF and normal fit for 18000 snapshots, UofC BS, $M=10,$ $K=1$	239
Figure 6-18: AOA estimation PDF and normal fit for 18000 snapshots	240
Figure 6-19: PDF of estimated AOA from UofC BS, $M=30, K=1$	240
Figure 6-20: PDF of Estimated AOA from UofC BS, $M=30, K=1$	241
Figure 6-21: PDF of estimated AOA from UofC BS, $M=30, K=20$	242

LIST OF ABBREVIATIONS

AG	Array Gain
AIC	Akaike's Information Criterion
AOA	Angle Of Arrival
BER	Bit Error Rate
BS	Base Station
C/A	Coarse/Acquisition
CDF	Cumulative Distribution Function
CDMA	Code Division Multiple Access
CIR	Channel Impulse Response
CN	Circular Normal
CRLB	Cramer-Rao Lower Bound
CWGN	Circular White Gaussian Noise
DOF	Degree Of Freedom
DS-CDMA	Direct-Sequence Code Division Multiple Access
DS-SS	Direct Sequence Spread-Spectrum
EC	Estimator Correlator
EG	Equal Gain
ESPRIT	Estimation of Signal Parameters via Rotational Invariance Techniques
FFT	Fast Fourier Transform
GD	Gain Degradation
GLRT	Generalized Likelihood Ratio Test
GNSS	Global Navigation Satellite Systems
GPS	Global Positioning System
IF	Intermediate Frequency
ISI	Inter Symbol Interference
ISNR	Instantaneous SNR
LOS	Line Of Sight

LPF	Low Pass Filter
LRT	Likelihood Ratio Test
MAT	Mean Acquisition Time
MEMS	Micro Electro Mechanical Systems
ML	Maximum Likelihood
MMSE	Minimum Mean Square Error
MS	Mobile Station
MUSIC	MULTiple SIgnal Classification
NGD	Normalized Gain Degradation
NI	National Instrument
NIG	Normalized Integration Gain
NP	Neyman-Pearson
PCS	Personal Communications Service
P_D	Probability of Detection
PDF	Probability Density Function
P_{FA}	Probability of False Alarm
PPS	Pulse Per Second
PRN	Pseudo Random Noise
PSD	Power Spectral nsity
RHCP	Right-Hand Circular Polarization
rms	root mean square
ROC	Receiver Operating Characteristics
SA	Synthetic Array
SAEC	Synthetic Aperture based on the Estimator-Correlator
SAEG	Synthetic Aperture based on the Equal-Gain
SNR	Signal-to-Noise Ratio
TCXO	Temperature Controlled Crystal Oscillator
TLS	Total Least Squares
TOA	Time Of Arrival
UCA	Uniform Circular Array

ULA

Uniform Linear Array

UofC

University of Calgary

LIST OF SYMBOLS

ϕ	Azimuth angle
θ	Polar angle
M	Number of synthetic array elements
N	Number of impinging signals
\mathbf{p}_m	Position of the m th antenna element
\mathbf{a}	Propagation direction vector
$s(t)$	Signal received at the origin of the array
c	Propagation speed
τ_m	Propagation delay of the m th sensor respect to the origin of the coordinate
ω_c	Carrier frequency
$\tilde{f}(t, \mathbf{p}_m)$	Complex envelop of signal
B_s	Signal bandwidth
ΔT_{\max}	Maximum possible delay between two antennas in the array
\mathbf{k}	Wavenumber vector
$\mathbf{v}_k(\mathbf{k})$	Array manifold vector
\mathbf{w}	Weigh vector for beamforming
$B(\omega; \theta, \phi)$	Array beam pattern
$P(\theta, \phi)$	Array power pattern
ζ	Lagrange multiplier
\mathbf{n}	Noise vector
d	Antenna spacing
κ	Carrier wavelength
B_c	Coherence bandwidth
σ_τ	rms delay spread
B_D	Doppler spread

f_d	Doppler frequency
T_c	Channel coherence time
v	velocity
φ	Mean value of direction of arrival
φ_s	Angular spread in a multipath channel
Q	Eigenvector matrix
Λ	Eigenvalue matrix
$\lambda_{s,m}$	eigenvalues
I	Identity matrix
N_o	Noise PSD
ρ	Average signal-to-noise
J_0	zero-order Bessel function of the first kind
χ_M^2	Chi-Squared distribution with M DOF
Ω	Characteristic function
K	Number of samples
$s(t, \mathbf{p}(t))$	signal component of $r(t)$
T	Interval duration of the snapshot
t_m	starting instance of the m -th subinterval
$p(\mathbf{x} H_I)$	conditional PDF of \mathbf{x} given H_I
ρ_m	Required average SNR for the moving antenna
ρ_s	Required average SNR for the static antenna
$\mathbf{p}(t)$	Position vector of a moving antenna
$r(t)$	complex baseband signal received by an antenna
$s_o(t)$	Deterministic component of the received signal
$A(\mathbf{p}(t))$	Channel response to the signal at the antenna position of $\mathbf{p}(t)$
H_0	State that the received signal and replica are not synchronized
H_1	State that the received signal and replica are synchronized
x_m	Correlator output of the m -th subinterval

σ_A^2	Variance of the channel gain
\mathbf{C}_A	Spatial covariance matrix of the channel gains
\mathbf{C}_s	Signal covariance matrix
\mathbf{C}_n	Noise covariance matrix
ρ_T	Average SNR in T second interval
$\rho_{\Delta T}$	Average SNR in ΔT second interval
Ψ	Correlation coefficient matrix
z_{EC}	Test statistics of the EC process
z_{EG}	Test statistics of the EG process
ΔT	Snapshot subinterval in seconds
d	Normalized antenna displacement in T s interval
Δd	Normalized antenna displacement in ΔT s interval
G	Processing gain of the SA over the static antenna
M_{opt}	Optimum number of spatial samples
ρ_{EG}	Required average SNR in synthetic array case with the EG combiner
ρ_{EC}	Required average SNR in synthetic array case with the EC combiner
r	Correlation coefficient
\mathbf{E}_s	Eigenvectors of signal subspace
\mathbf{E}_N	Eigenvectors of noise subspace
\mathbf{R}_s	Signal correlation matrix

CHAPTER 1: INTRODUCTION

1.1 Background and Motivation

The problem of interest in wireless location applications is detecting and estimating signal parameters such as the Time Of Arrival (TOA) and the Angle Of Arrival (AOA) propagated over a wireless channel (Caffery & Stuber 1998a, 1998b, Caffery 2000). Direct Sequence Spread-Spectrum (DS-SS) systems have been extensively implemented in variety of positioning systems such as Global Positioning System (GPS) (Kaplan & Hegarty 2006). In a DS-SS system, the transmitted signal is modulated with a Pseudo Random Noise (PRN) code that is known to the receiver. The property of a PRN sequence is that its cross-correlation is almost zero except at the zero lag. The objective is to find the instance at which the correlation of the local PRN code and the received signal provides the maximum value denoted as a correlation peak. If a transmitter and a receiver are synchronized, the estimated correlation peak can be considered as the propagation delay between the transmitter and the receiver antennas. Hence, the corresponding receiver correlates the received signal with a known PRN sequence to estimate TOA (Misra & Ennge 2001). The PRN code acquisition is a procedure to determine the received signal code phase with respect to the known replica code. Therefore, to exploit the advantages of DS-SS techniques, a receiver must synchronize a locally generated code with the received one. The acquisition process involves searching through the uncertainty phases of the PRN code (Kim 2004, Shin & Lee 2003). The TOA

(equivalently ranging) estimation concept and the correlation function for a 7-chip sequence is shown in Figure 1-1.

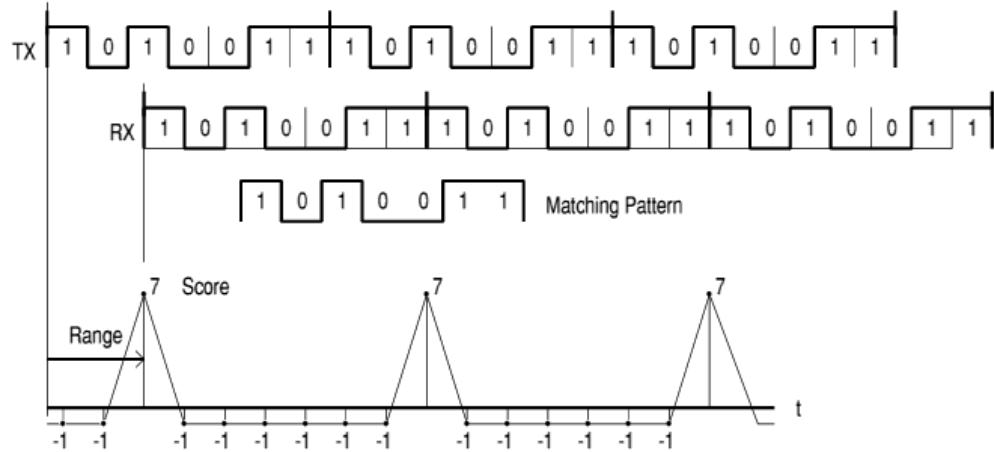


Figure 1-1: Correlation process and TOA (range) estimation utilizing a 7-chip sequence (from <http://www.amsat.org/amsat/articles/g3ruh/123.html>, last accessed 29June 2009)

TOA estimation of a signal is a fundamental observable in most positioning applications (Kaplan & Hegarty 2006, Sayed et al 2005). The position of a Mobile Station (MS) in a three-dimensional space can be estimated by four or more independent TOA measurements from transmitters that are spatially separated with known locations in the vicinity of the MS.

Multipath is a propagation phenomenon that causes the transmitted signal to be received by the receiver from different paths to be characterized by different AOAs, time delays and phases. In indoors or in dense multipath environments in the absence of the Line Of Sight (LOS) component, the multipath propagation causes deep fades in the received signal strength that makes the acquisition process and TOA estimation a challenging problem (Caini et al 2004a, 2004b). In urban canyon environments the

coexistence of the multipath components along with the desired LOS signal typically causes errors in the estimation of the TOA observables, which maps into significant position errors. To meet the requirements of applications that require accurate position estimation on the part of the MS, lower deviation and bias of the TOA observables is required. To achieve this requirement, mitigation of the distortions caused by the existence of the multipath components is necessary.

The use of multiple antennas that exploit the spatial dimension of wireless systems has generated much interest in improving the Signal-to-Noise Ratio (SNR) and spatial filtering. Multiple antennas are used either in the form of antenna arrays for AOA estimation and beamforming (Choi & Shim 2000, Fu et al 2003, Rensburg & Friedlander 2004a, Seco & Fernández-Rubio 1997) or in the form of antenna diversity systems to alleviate the fading loss in dense multipath propagation environments (Rensburg & Friedlander 2004b, Parsons 2000). Figure 1-2 shows the AOA estimation and the beamforming and null-steering concepts.

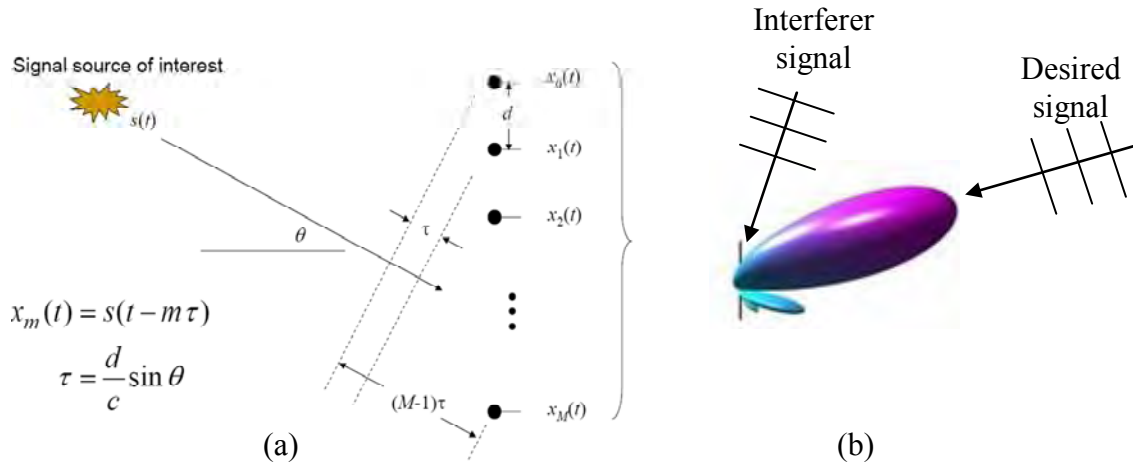


Figure 1-2: (a) AOA estimation, (b) beamforming concepts

In some particular applications such as position estimation with handheld receivers, the size and shape of the antenna array limit the applicability of AOA estimation and beamforming. In order to overcome the limitations of conventional antenna arrays, this thesis proposes a new method to synthesize an antenna array with one or two antennas. Instead of using multiple antennas with a multi-channel receiver, which increases the cost and complexity of the receiver, the antenna array can be synthesized by moving an antenna along an arbitrary spatial trajectory while snapshot data is being collected. The synthetic array concept may be implemented as a diversity system to enhance signal detection performance in dense multipath environments (Broumandan et al 2009a, 2009b) or in the form of AOA estimation and beamforming applications (Klukas 1993, Jong & Herben 1999, Broumandan et al 2007, 2008b, 2008c).

1.2 Applications of the antenna array in dense multipath fading environments

In terrestrial or indoor wireless location links, the signal typically propagates from the transmitter to the receiver over multiple reflective paths with a random variation in the complex amplitude of the received signal (Parsons 2000). When the antenna is located in a diffuse multipath scattering environment, fading appears to be a random function of the antenna location conforming approximately to the Rayleigh fading statistics with spatial decorrelation intervals of less than the signal carrier wavelength (Rensburg & Friedlander 2004b, Van Trees 2002, Saleh & Valenzula, 1987).

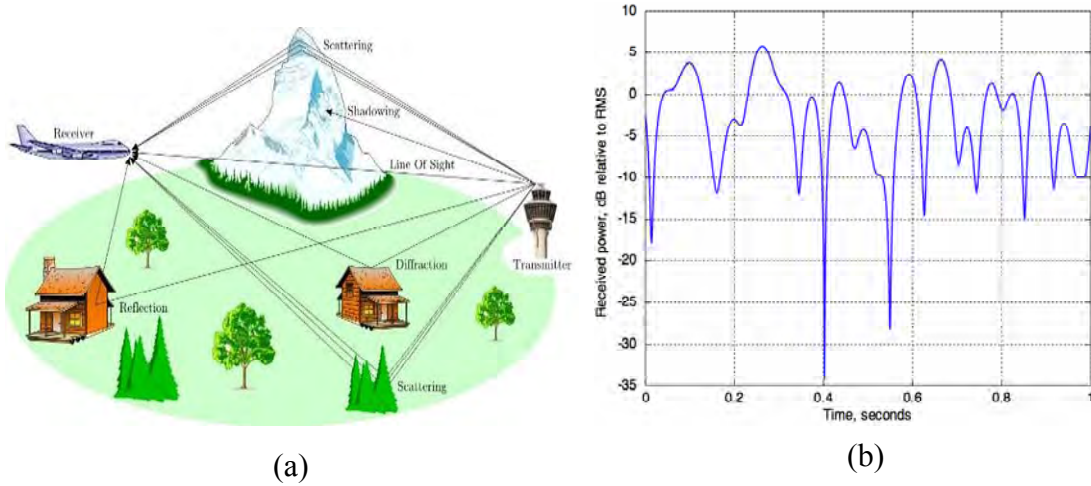


Figure 1-3: (a) Multipath phenomenon, (b) received signal power in multipath environments

The multipath scattering nature of the propagation medium causes the received power level to fluctuate when the receiver antenna moves as little as half the wavelength of the received signal. Hence, acquiring the signal in fading channels becomes a challenging problem. Figure 1-3 shows the multipath phenomenon and the received signal power by the antenna in a multipath fading channel.

If the receiver uses a single static antenna, then a substantial fading margin is required to ensure reliable signal detection. To reduce the fading margin required, the receiver can use multiple spatially separated antennas that exploit the spatial diversity (Kim 2004, Shin & Lee 2003, Friedlander & Scherzer 2004) that are inherent properties of discrete antenna arrays. Numerous papers have evaluated the detection performance of the antenna in a Rayleigh fading channel (e.g. Rensburg & Friedlande 2004b, Hyeon et al 2008). In (Hyeon et al 2008), a non-coherent combining called phase diversity system has been implemented to improve the detection performance of an antenna array for Code Division Multiple Access (CDMA) signals in indoor environments. The use of multiple

antennas can alleviate the fading problem to some degree by providing a means of diversity gain (Rensburg & Friedlander 2004b). Diversity techniques are established based on receiving statistically independent signals on each diversity antenna denoted as a diversity branch (Blaunstein & Andersen 2002). In practice, this may be implemented by utilizing spatially separated antennas in dense multipath environments, which results in spatial diversity (Colburn et al 1998, Kim 2004) or utilizing antennas with orthogonal polarization that maps into polarization diversity (Narayanan et al 2004). A comparison of the spatial diversity and the polarization diversity in the Rayleigh fading channel is investigated in (Valenzuela-Valdes et al 2006). The performance of the diversity system can be characterized by the correlation coefficient values among the diversity branches (Colburn et al 1998, Mahfuz 2008). In a multipath fading environment, the correlation coefficient decreases spatially where the decorrelation rate depends on the scatterer geometry and the array configuration. If multipath components arrive from a small sector in space, the antenna elements should have spacing of order of several wavelengths of the carrier frequency to yield spatial diversity gain, whereas in the ring of scatterers multipath model, half wavelength spacing is sufficient to ensure spatially uncorrelated samples. Hence, spatial correlation is a function of the channel model and the antenna spacing. The performance of diversity systems reduces by increasing the correlation coefficient among diversity branches (Rensburg 2001).

1.3 Application of antenna arrays for multipath and interference mitigation in specular multipath environments

Position estimation in interfered and multipath environments is susceptible to errors due to signal attenuation and biases in the TOA estimation (Broumandan et al 2008a). Consequently, multipath and interference mitigation techniques are essential for high accuracy positioning using TOA observations (Brown & Gerein 2001, Zoltowski & Gecan 1995). There are several methods for multipath mitigation. As an example, at the arrival of the incoming signals, spatial multipath limiting antennas such as choke rings and multiple beam antennas can be used to block the multipath signals from entering the receiver. However, the most common approach is the utilization of antenna arrays in the context of multipath and interferer cancellation. Because of the robustness of the spatial filtering and the beamforming techniques for interference and multipath mitigation, an antenna array with a set of multi-channel receivers can be used to enhance signal reception. The performance of the spatial filtering and the beamforming techniques in improving the TOA measurements have been investigated in many references (Fu et al 2003, Zoltowski & Gecan 1995).

The beamforming and null-steering techniques are based on the assumption that the array manifold, which is characterized by the direction of arrival of incoming signals and array response (phase, gain and sensor geometry), is completely known (Charndran 2006, Allen & Ghavami 2006). In this case, the beamforming weights can be estimated accordingly to have a desired response for each wave front. If the directions of arrival of incoming signals are not known *a priori*, the array response should be modified accordingly to have the capability of receiving signals from any direction. In this case,

the array gain approaches zero. Therefore, in the practical application of multipath and interference mitigation, the AOA and the array steering vector information should be known apriori. In view of computational simplicity and high-resolution performance requirements, eigen-decomposition AOA algorithms such as the Multiple Signal Classification (MUSIC) (Schmidt 1986) and the Estimation of Signal Parameters via Rotational Invariance Techniques (ESPRIT) (Roy & Kailath 1989) have received significant attention.

To overcome the portability issue of the antenna array, the latter can be synthesized by moving an antenna within a known trajectory (Jong & Herben 1999). The synthetic array concept has been an active research area for multipath and interference mitigation during recent years (Pany et al 2008, Soloviev & Van Graas 2009). Jong & Herben (1999) have shown an application of synthetic array with a Uniform Circular Array (UCA). They have used UCA-MUSIC to determine multipath contributions in wireless mobile propagation environments. In Jong (2001) a mechanical lever arm was used to synthesize a circular array by using a single rotating antenna with constant speed. In order to estimate the trajectory of the moving antenna, remove the hardware complexity and generalize the synthetic array signal processing problem for an arbitrary array geometry, Broumandan et al (2007) utilized auxiliary sensors called inertial measurement units (IMU), which consist of accelerometers and gyros. The problem of the previous work of AOA estimation and beamforming in the context of the synthetic array (e.g. Jong & Herben 1999, Jong 2001, Broumandan et al 2007) is that the antenna array is typically realized by using controllable moving motors or the antenna trajectory is estimated by utilizing external aiding sensors which indeed limits applicability of the synthetic array.

In this thesis, the advantages of the antenna array processing is sought but without the unwieldy hardware implications of a multi-antenna array. Hence, a synthetic array consisting of a single or two antennas conformal with the physical constraints of the handheld MS device is considered.

1.4 Objectives and novel contributions

As mentioned before, the size of a multi-element antenna array is incompatible with the small form factor of a handheld portable receiver, which is therefore typically limited to a single or two antennas. The only means of realizing the potential spatial processing gains is to physically translate the antenna as the signal is being captured by the receiver. This is equivalent to realizing a spatially distributed synthetic antenna array. The concept of a synthetic array based on a single moving antenna has been utilized in wireless signal parameter estimation and radar signal processing for many years (Stergiopoulos & Urban 1992, Jong & Herben 1999).

The primary objective of this thesis is to develop a practical signal processing method for handset-based location systems based on the synthetic array to enhance signal detection and parameter estimation in multipath environments. The synthetic array concept is considered for two different applications of the antenna array. In the first part, the detection performance of the synthetic antenna array in dense multipath fading channels where incoming signals are distributed over a large angular spread is considered. This problem is addressed in Chapters 3, 4 and 5. The second part deals with the AOA estimation problem utilizing the synthetic array where the transmitted source is

modeled as a point source. This problem is addressed in Chapters 3 and 6. The major original work is summarized as follows:

1.4.1 Signal detection enhancement in fading environments utilizing the synthetic array

In previous work relating to synthetic array implementation, the antenna trajectory has either been mechanically fixed or precisely measured during the signal snapshot using accurate inertial navigation devices (Jong & Herben 1999, Broumandan et al 2007). However, in the multipath fading scenario, the primary objective is to achieve diversity gain for which a rough approximation of the antenna trajectory is sufficient. Hence, mechanical constraint devices or precision inertial based sensors are not necessary. A low cost and physically small Micro Electro Mechanical Systems (MEMS) based accelerometer provides an adequate estimate of the antenna trajectory for the proposed method. The motion of the antenna during the signal sampling can be achieved by several means. There are two modes to be explored. In the first case, the user deliberately moves the receiver such that diversity gain results as described. Application of this would be when the user is attempting to acquire signals such as Global Navigation Satellite Systems (GNSS) or CDMA cellular network in environments subjected to multipath fading. In the second case, user generated motion through head or arm movements as well as walking or motion of a vehicle, can be exploited for diversity gain via the synthetic array. The user does not generate these motions deliberately to accommodate the synthetic array. Thus, the synthetic array in this context uses whatever motion of opportunity happens to be available.

This thesis proposes a new method for detecting a narrowband signal in a general case of the correlated Rayleigh fading (from uncorrelated to totally correlated fading) based on the synthetic array concept. The detection performance of a single moving channel receiver is compared to that of the equivalent receiver with a static antenna based on the diversity gain as a quantifiable metric. The synthetic array processing gain is defined as a reduction in the required average SNR for the moving antenna case to have the same detection performance as the static antenna. It is shown that if the antenna is held at a fixed position during the snapshot interval, then the signal is not subject to decorrelation as channel gain remains constant. However, the signal will be subject to fading losses, which are statistically large in the Rayleigh fading environment. Conversely, if the antenna is translated along some arbitrary trajectory during the snapshot interval, then the coherency of the signal will be compromised as the channel gain will change randomly but the snapshot data will contain spatial diversity that can effectively counter the spatial fading effects. Based on this, it is shown that the tradeoff between the increased diversity gain and the loss of signal coherency will result in an optimum processing gain.

The primary assumption of previous work related to spatial diversity is receiving uncorrelated samples at each diversity branch that results in the Equal-Gain (EG) combining process (Hyeon et al 2008, Wang & Cruz 2001). While this is an optimal process for uncorrelated Rayleigh fading, it is not optimal when the fading is spatially correlated. However, in the synthetic array context, the uncorrelated spatial sample assumption is valid when the trajectory of the moving antenna and channel statistics are known. In this thesis the detection performance of the synthetic array in the context of a

diversity system for a general correlated Rayleigh fading is investigated. Therefore, the achievable processing gain of a synthetic array antenna where the single antenna is translated through an arbitrary trajectory of the spatially correlated Rayleigh faded signal is analyzed. The net processing gain of the synthetic array based on the optimum Estimator-Correlator (EC) combining (Kay 1998) is contrasted with that of the static antenna in an equivalently faded propagation environment. The processing gain advantage of EC is also compared with the Equal Gain (EG) combining for a range of spatial correlation. The sensitivity of the proposed method in terms of trajectory estimation errors is also considered. The environment of interest is indoor and dense urban areas where there is no well-defined LOS component and the multipath is diffuse. In addition, the signal bandwidth is narrow such that it is assumed to be less than the coherence bandwidth resulting in unresolved multipath components. The quantitative metric that is used for comparison is the SNR required at the receiver to achieve specific detection performance goals. That is, target values of the probability of detection (P_D) and probability of false alarm (P_{FA}) are fixed. The required SNR to achieve this detection performance is compared for the synthetic array with the EG and EC combining and the static antenna. The required SNR is initially determined theoretically based on the assumption of Rayleigh fading. Two operating scenarios are considered for the synthetic array in this thesis. In the first case it is assumed that the antenna is almost static in each subinterval of data collection and there are some time gaps between different spatial samples. This mode is defined as a discrete synthetic array. In the second case, the receiver continuously collects data while the antenna is moving and sequentially combines received signals based on a specific process. This mode is defined as the

continuous synthetic array in this thesis. Subsequently, experimental measurements based on CDMA IS-95 and GPS signals received indoor are utilized to partially validate the theoretical achievements.

The main contributions of the signal detection enhancement utilizing the synthetic array are summarized as follows:

- Designing and analyzing detection algorithms for synthetic array processing in a Rayleigh fading channel.
- Evaluating the processing gain of the synthetic array over the static antenna in general Rayleigh fading environments.
- Assessing the detection performance of an optimal detection scheme based on the EC detector in fading environments characterized by a ring of scatterers model.
- Evaluating the detection performance of a sub-optimal detection approach based on the Equal-Gain (EG) combiner in a Rayleigh fading channel.
- Comparing the detection performance and processing gain of the synthetic array and the static antenna utilizing the EG and EC combiners for different values of the channel correlation coefficient.
- Determining an optimal extent of the synthetic array and the number of spatial samples that provide maximum synthetic array gain and the best detection performance.
- Evaluating the coherent integration loss due to antenna motion in a Rayleigh fading environment.
- Evaluating the channel correlation coefficient for the synthetic array case in the continuous mode.

- Determining an optimal velocity for the moving antenna in the continuous mode that provides the maximum processing gain over the static antenna.
- Considering the practical implementation issues of the synthetic array in term of the accuracy of the trajectory estimation unit.

1.4.2 AOA estimation utilizing the synthetic array

High-resolution AOA estimation is an important issue in many applications such as radar, sonar, spatial filtering and location estimation. The AOA information can be used in the form of beamforming or null-steering to enhance the TOA estimation in multipath and interference environments (Fu et al 2003, Zoltowski & Gecan 1995) or may be utilized to estimate the location of a mobile station (Broumandan et al 2008d). There have been several high-resolution AOA estimation methods including the MUSIC (Schmidt 1986) and ESPRIT (Roy 1987) algorithms. Although the MUSIC algorithm is widely used, it has certain practical implementation issues in comparison with ESPRIT. The MUSIC algorithm requires prior calibration of the antenna elements, namely the phase, gain and the positions of the elements. In addition, a computationally expensive search is required over the processed parameter space (Roy 1987).

To take advantage of the synthetic array concept and deal with the calibration and the moving antenna trajectory estimation problem, this thesis introduces an AOA estimation approach based on the synthetic array concept utilizing the ESPRIT algorithm. The ESPRIT array structure consists of different doublets, with each doublet composed of two identical pattern sensors (Roy & Kailath 1989). The array configuration of the ESPRIT

algorithm can be represented by two sub-arrays, with each doublet having a sensor in each sub-array. Therefore, each sub-array is the replica of the other one, separated by a known physical displacement d . In this scenario, each sub-array consists of sensors with arbitrary phase and gain characteristics. The ESPRIT algorithm for parameter estimation does not require the relative doublet position information. This structure can be utilized for the synthetic array implementation. The ESPRIT algorithm utilizes the rotational invariance property which is provided by an array of sensors with a translational invariance structure (Roy & Kailath 1989). Utilizing the ESPRIT algorithm in the context of the synthetic array, system complexity is reduced to a two-channel (doublet) receiver and removes the necessity of using any mechanical moving motors or external aiding sensors. However, the orientation of the antenna pair must be maintained as the handheld device is translated. This configuration can be installed in any rotationally invariant moving platform.

The main contributions of AOA estimation based on the ESPRIT algorithm utilizing the synthetic array are summarized as follows:

- Proposing a new approach for AOA estimation based on the ESPRIT algorithm which significantly reduces the complexity of the receiver.
- Evaluating the ESPRIT AOA estimation performance under practical implementation limitations.
- Demonstration of practicality of the proposed method.
- Experimental results of AOA estimation utilizing the synthetic array in urban environments.

1.5 Thesis Outline

The thesis consists of seven chapters that are related to each other in the manner shown in the Figure 1-4.

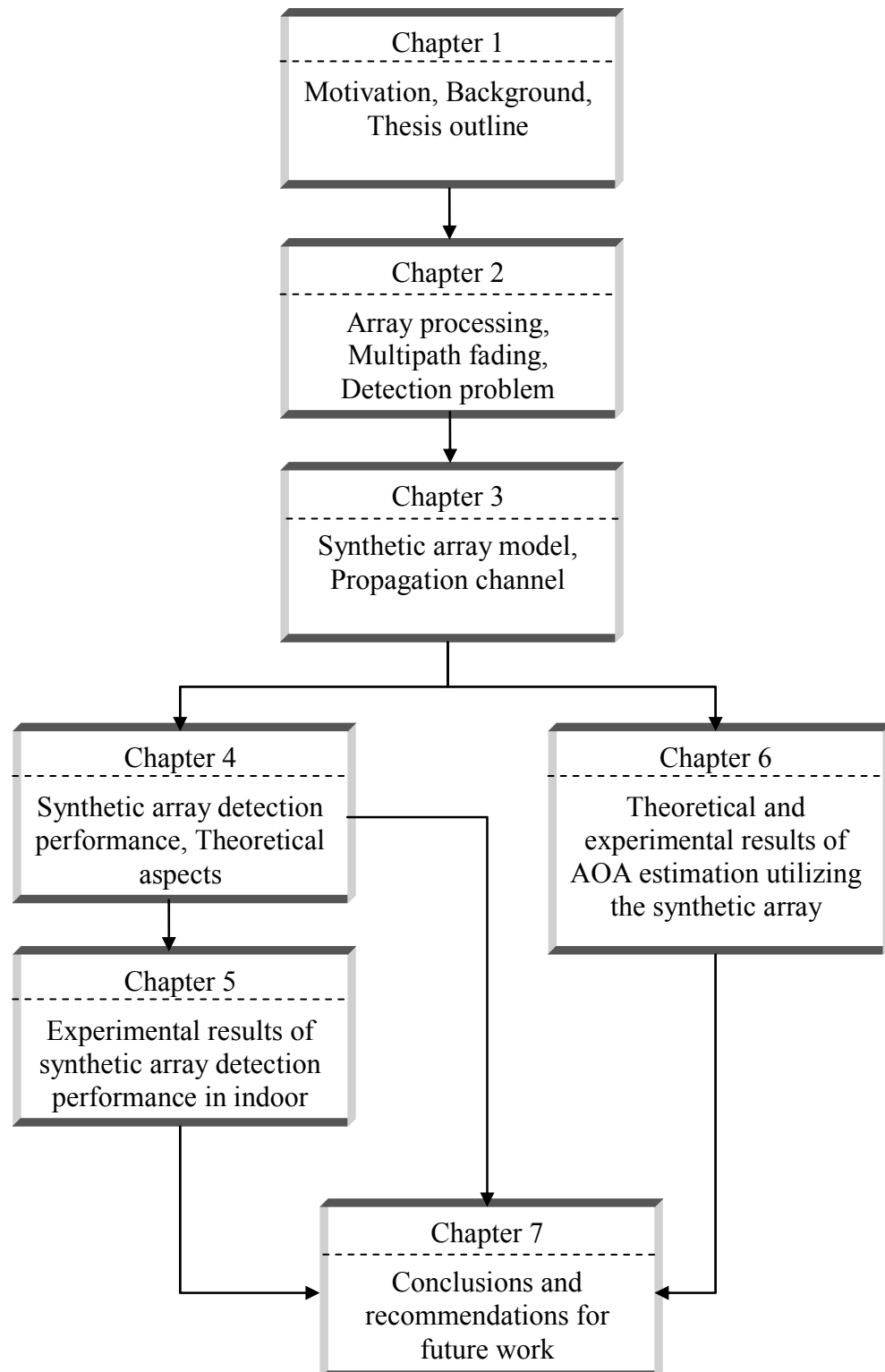


Figure 1-4: Thesis flow graph

The remainder of this thesis is organized in the following way:

In Chapter 2, the background knowledge for the spatial-temporal array processing problem including the signal model received by an antenna array and a beamforming approach are introduced. Signal propagation models in different multipath environments including the Rayleigh flat-fading channel are discussed. The performances of the beamforming technique in different multipath environments in terms of the array gain are analyzed. Diversity techniques are introduced as a remedy to alleviate the fading loss in dense multipath propagation environments. Finally, a brief overview of the detection problem of a complex signal embedded in circular white Gaussian noise is provided.

Chapter 3 describes the synthetic array system model and wireless propagation channels for different multipath scattering environments. The various covariance matrices derived for the different signal types that are used in conjunction with the EC detector are described. The performance of the EC process in different multipath propagation environments is also evaluated.

In Chapter 4, the detection performance of the moving receiver based on the synthetic array concept is compared to that of the equivalent receiver with a stationary antenna for the Rayleigh fading environment. Two operating scenarios for implementation of the synthetic array, namely discrete and continuous modes, are considered. The synthetic array detection procedure based on the EC and EG combiners is demonstrated. The processing gain advantage of the moving antenna is thereby quantified in uncorrelated and correlated environments. From this, the optimum spatial samples which maximize the processing gain of the synthetic array over the static antenna are evaluated. The

synthetic array practical implementation issues in terms of the accuracy of the trajectory estimation unit are also discussed in this chapter.

Chapter 5 experimentally verifies the theoretical findings presented in Chapter 4 for the discrete and the continuous synthetic array modes in indoor fading environments. Two different CDMA signal structures, namely IS-95 and GPS signals are utilized to evaluate the synthetic array detection performance in different indoor multipath environments. The objective of the experimental measurements in this chapter is to determine the processing gain of the synthetic array over the static antenna for a selection of typical indoor locations.

Chapter 6 considers signal detection performance in specular multipath environments where a plane wave has an unknown channel gain coefficient and an unknown AOA. An AOA estimation algorithm based on the synthetic array concept utilizing the ESPRIT algorithm is presented. Practical implementation issues including the array calibration and source number estimation are considered. Experimental results based on the reception of the downlink CDMA IS-95 pilot signals verify the applicability of the proposed method in the context of AOA estimation utilizing the synthetic array in specular multipath environments.

Chapter 7 concludes with the key findings of the above investigations. The limitations of the proposed algorithms and recommendations for further investigations are provided.

Finally, the appendices include some background information on selected relevant topics.

CHAPTER 2: ARRAY PROCESSING BACKGROUND

This chapter describes basic definitions and assumptions of the temporal-spatial array processing problem which will be referred to extensively in the remainder of this thesis. The material represented in this chapter may be found in different array processing literature such as Haykin (1985), Pillai (1989), Steinberg (1976), and Johnson & Dudgeon (1993). However, the array processing background presented in this chapter mainly follows the notation of Van Trees (2002).

An antenna array consisting of several sensors is utilized to filter signal and noise in a space-time field by exploiting its temporal-spatial characteristics and this filtering may be expressed as a function of the direction of arrival of impinging signals. The performance of an antenna array in terms of spatial filtering depends on several factors such as array geometry, number of sensors and signal-to-noise ratio (SNR). First of all, the response of an arbitrary geometry array to a plane wave far-field narrowband signal is described. Then the beamforming concept as a spatial filter and a main block of the array processing is explained. Antenna array performance metrics including array directivity and array gain are defined to quantify the beamformer performance in different propagation scenarios. In this chapter, signal propagation models in different multipath environments including the Rayleigh flat-fading channel which is widely referred to in this thesis are also introduced. Since the main focus of this research is dedicated to enhancing detection of a narrowband signal in multipath environments, the performance of beamforming techniques in different multipath environments are analyzed herein. To alleviate the

fading loss in dense multipath propagation environments diversity techniques have been widely used in practice. An overview of different antenna diversity techniques is also given in this chapter.

2.1 Signal model received by an antenna array

The coordinate system of interest is shown in Figure 2-1 where ϕ is the azimuth angle measured from the x axis, and θ is the polar angle with respect to the z axis. It will be assumed that the array will consist of M isotropic discrete sample points where the m -th sample point or antenna element is denoted as \mathbf{p}_m , which is a positional vector in the $\{\mathbf{x}, \mathbf{y}, \mathbf{z}\}$ coordinate frame. This scenario is shown in Figure 2-2.

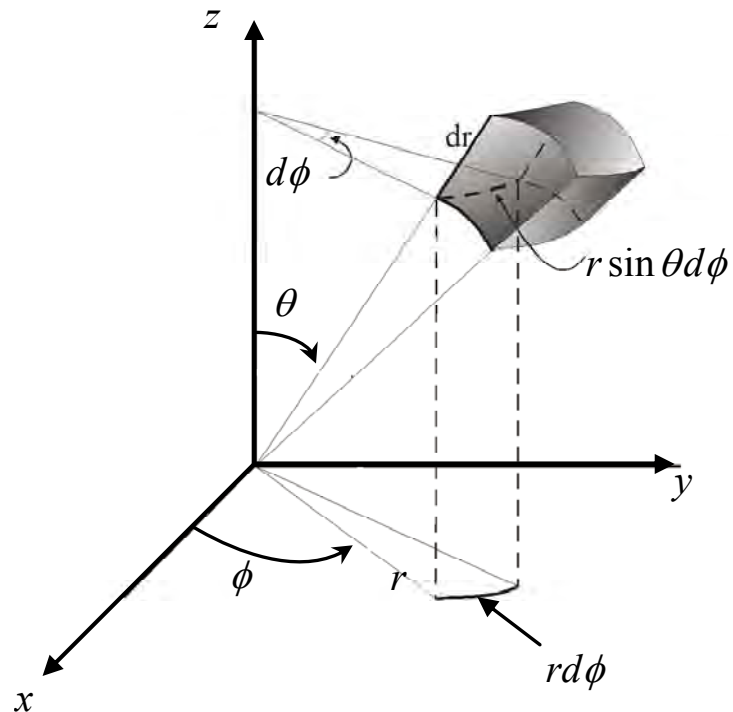


Figure 2-1: Spherical coordinate system

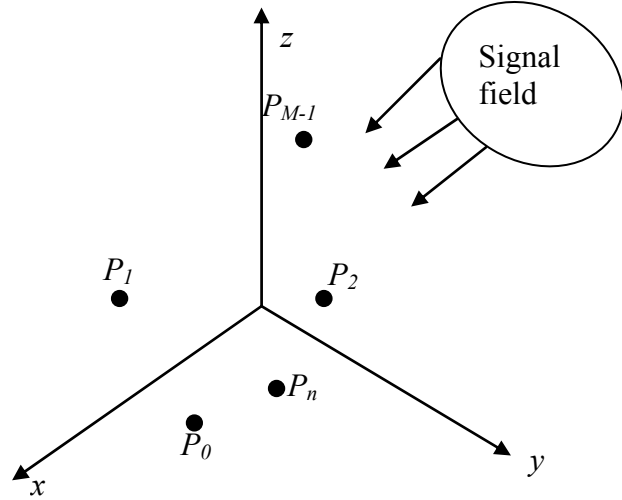


Figure 2-2: Spatial sampling by sensors (Van Trees 2002)

The set of M element positions is denoted as

$$\mathbf{p} = [\mathbf{p}_0 \dots \mathbf{p}_{M-1}]^T. \quad 2-1$$

The signal received at M spatial sampling points is denoted as

$$\mathbf{s}(t, \mathbf{p}) = \begin{bmatrix} s(t, \mathbf{p}_0) \\ \vdots \\ s(t, \mathbf{p}_{M-1}) \end{bmatrix}. \quad 2-2$$

Consider a plane wave propagation scenario in direction of \mathbf{a} with a temporal frequency of ω . If $s(t)$ is the signal received at the origin of the coordinate system, then Eq. 2-2 reduces to

$$\mathbf{s}(t, \mathbf{p}) = \begin{bmatrix} s(t - \tau_0) \\ \vdots \\ s(t - \tau_{M-1}) \end{bmatrix} \quad 2-3$$

where

$$\tau_m = \frac{\mathbf{a}^T \cdot \mathbf{p}_m}{c}. \quad 2-4$$

\mathbf{a} is a direction vector defined by

$$\mathbf{a} = -\begin{bmatrix} \sin(\theta)\cos(\phi) \\ \sin(\theta)\sin(\phi) \\ \cos(\theta) \end{bmatrix} \quad 2-5$$

and c is the propagation speed.

It is assumed that $s(t, \mathbf{p}_m)$ is a bandpass signal defined by

$$s(t, \mathbf{p}_m) = \sqrt{2} \operatorname{Re} \left\{ \tilde{s}(t, \mathbf{p}_m) e^{j\omega_c t} \right\}, \quad m = 0, \dots, M-1. \quad 2-6$$

$\tilde{s}(t, \mathbf{p}_m)$ is the complex envelope and ω_c is the carrier frequency. It is also assumed that

$\tilde{s}(t, \mathbf{p}_m)$ is bandlimited.

For the plane wave in Eq. 2-3, Eq. 2-6 becomes

$$s(t, \mathbf{p}_m) = \sqrt{2} \operatorname{Re} \left\{ \tilde{s}(t - \tau_m) e^{j\omega_c(t - \tau_m)} \right\}, \quad m = 0, \dots, M-1 \quad 2-7$$

In this thesis, it is assumed that incoming signals are narrowband implying that the reciprocal of a maximum propagation delay across the array is much greater than the signal bandwidth,

$$B_s \ll \frac{1}{\Delta T_{\max}} \quad 2-8$$

where B_s is the bandwidth of the complex envelope and ΔT_{\max} is the maximum propagation delay between two antennas in the array (Van Trees 2002). The narrowband assumption justifies

$$\tilde{s}(t - \tau_m) \approx \tilde{s}(t), \quad m = 0, 1, \dots, M-1. \quad 2-9$$

Hence, in the narrowband case, Eq. 2-7 reduces to

$$s(t, \mathbf{p}_m) = \sqrt{2} \operatorname{Re} \left\{ \tilde{s}(t) e^{j\omega_c t} e^{-j\omega_c \tau_m} \right\}, \quad m = 0, \dots, M-1. \quad 2-10$$

In the narrowband signal model, the sensor wise propagation delay is approximated by a phase shift.

A significant portion of the development in this thesis will involve plane waves with a propagation vector having a wavelength denoted as κ . It is more convenient to define a wavenumber vector \mathbf{k} as

$$\mathbf{k} = -\frac{2\pi}{\kappa} \begin{bmatrix} \sin(\theta)\cos(\phi) \\ \sin(\theta)\sin(\phi) \\ \cos(\theta) \end{bmatrix} = \frac{2\pi}{\kappa} \mathbf{a} \quad 2-11$$

where \mathbf{a} is a unit vector in the direction of the incoming plane wave. It can be shown that the propagation phase difference in Eq. 2-10 is a function of the wavenumber and the antenna position:

$$\omega_c \tau_m = \mathbf{k}^T \mathbf{p}_m. \quad 2-12$$

Thus, Eq. 2-10 becomes

$$s(t, \mathbf{p}_m) = \sqrt{2} \operatorname{Re} \left\{ \tilde{s}(t) e^{j\omega_c t} e^{-j\mathbf{k}^T \mathbf{p}_m} \right\}, \quad m = 0, \dots, M-1. \quad 2-13$$

Specifically for the incident plane wave, corresponding to a propagation vector \mathbf{k} , the signal outputs of the antenna elements are

$$\mathbf{s}(t, \mathbf{p}) = s(t) \mathbf{v}_k(\mathbf{k}) \quad 2-14$$

where $\mathbf{v}_k(\mathbf{k})$ is denoted as the array manifold vector and incorporates all spatial characteristics of the array, for the incident plane wave given as

$$\mathbf{v}_k(k) = \begin{bmatrix} \exp(-j\mathbf{k}^T \mathbf{p}_0) \\ \vdots \\ \exp(-j\mathbf{k}^T \mathbf{p}_{M-1}) \end{bmatrix}. \quad 2-15$$

2.2 Beamforming concept

The beamformer is a fundamental building block of an array processor. In beamforming techniques, the sensor outputs are weighted with specific complex weights to pass desired signals without distortion, while mitigating interference and undesired signals (Litva & Lo 1996). Figure 2-3 shows the concept of a narrowband beamformer where $\mathbf{w} = [w_0, w_1, \dots, w_{M-1}]^T$ is a complex beamformer weight vector.

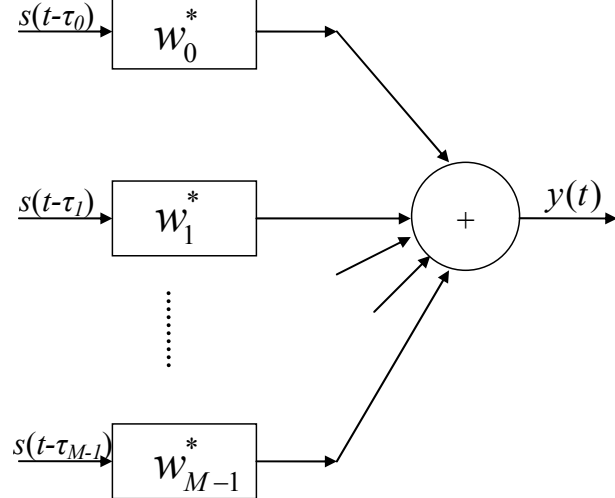


Figure 2-3: Narrowband beamformer block diagram

Basically, a beamformer adjusts the phase and the gain at the output of each sensor to provide desirable beam-patterns. Utilizing Eq. 2-14 the output of the array in vector form becomes

$$y(t, \mathbf{k}) = s(t) \mathbf{w}^H \mathbf{v}_k(\mathbf{k}). \quad 2-16$$

There are several common criteria used for setting the weights of the beamformer depending on constraints and the objectives of optimization (Van Trees 2002). The most straightforward application is when there are M antenna elements with simultaneous outputs and the objective is to maximize the SNR. A general assumption is that the noise entering each element is independent and white Gaussian. Therefore the beamformer is essentially a spatial matched filter. The weights of the filter are given by

$$\mathbf{w} = \mathbf{v}_k(\mathbf{k}). \quad 2-17$$

The beampattern of an array is a critical definition for evaluating the array performance. The array beampattern is given for the plane wave propagation scenario, which is defined by (Van Trees 2002) as

$$B(\theta, \phi) = \mathbf{w}^H \mathbf{v}_k(\mathbf{k}) \Big|_{k=\frac{2\pi}{\lambda} \mathbf{a}(\theta, \phi)}. \quad 2-18$$

An extremely useful concept with electro-magnetism is that of reciprocity whereby the beamformer can also be considered as a transmitting array. Consider a narrowband excitation with a frequency of c/λ . Define \mathbf{k}_T as the steering vector such that $\mathbf{w} = \mathbf{v}_k(\mathbf{k}_T)$. Hence, the beampattern generated by the antenna array defined in Eq. 2-18 can be considered as a transmitter radiation pattern. Note that it can also be referred to as the steering vector in the receiver mode such that the beampattern is given as

$$B_c(\mathbf{k} : \mathbf{k}_T) = \mathbf{v}_k(\mathbf{k}_T)^H \mathbf{v}_k(\mathbf{k}). \quad 2-19$$

Specifically, B_c is denoted as the conventional beampattern. The related power-pattern is denoted as

$$P(\mathbf{k} : \mathbf{k}_T) = |B_c(\mathbf{k} : \mathbf{k}_T)|^2. \quad 2-20$$

As it is more convenient to describe these in terms of azimuth and elevation angles the power pattern becomes

$$P(\theta, \phi) = |B_c(\theta, \phi)|^2 \quad 2-21$$

where the mapping from $(\mathbf{k} : \mathbf{k}_T)$ to (θ, ϕ) is related through the wavenumber vector \mathbf{k} defined earlier.

2.2.1 Array performance metrics

In this section, some array performance measures which characterize the response of the array to an incoming signal will be described.

2.2.1.1 Directivity

The directivity of an array is denoted as

$$D = \frac{P(\theta_T, \phi_T)}{\frac{1}{4\pi} \int_0^\pi d\theta \int_0^{2\pi} d\phi \sin\theta P(\theta, \phi)} \quad 2-22$$

where $P(\theta_T, \phi_T)$ is the power pattern in the steering direction of (θ_T, ϕ_T) . The numerator represents the power of the signal arriving from (θ_T, ϕ_T) . The denominator of Eq. 2-22 gives the noise power at the beamformer output due to isotropic noise. Hence, D can

represent the array gain in the presence of isotropic noise. For a uniform linear array with half-wavelength spacing the directivity becomes (Van Trees 2002)

$$D = (\mathbf{w}^H \mathbf{w})^{-1}. \quad 2-23$$

2.2.1.2 Array gain

The array gain is one of the most important array performance metrics which is defined by the SNR ratio at the output of the beamformer, SNR_{out} , to SNR before beamforming SNR_{in} and can be written as

$$AG \triangleq \frac{SNR_{out}(\omega)}{SNR_{in}(\omega)} \quad 2-24$$

where SNR_{in} is the signal spectrum-to-noise spectrum ratio defined by

$$SNR_{in}(\omega) = \frac{S_s(\omega)}{S_n(\omega)}. \quad 2-25$$

The output spectrum of the beamformer can be written as

$$S_y(\omega) = \mathbf{w}^H \mathbf{S}_x(\omega) \mathbf{w} \quad 2-26$$

where $\mathbf{S}_x(\omega)$ is spectrum of the correlation matrix at the output of each sensor. Hence, the output signal spectrum can be defined by

$$S_{y_s}(\omega) = \mathbf{w}^H \mathbf{v}_k(\mathbf{k}_s) S_s(\omega) \mathbf{v}_k^H(\mathbf{k}_s) \mathbf{w}. \quad 2-27$$

If the distortionless constraint is imposed, i.e.

$$\mathbf{w}^H \mathbf{v}_k(\mathbf{k}_s) = 1, \quad 2-28$$

which emphasizes that any signal arriving through \mathbf{k}_s will pass through the beamformer filter undistorted, then the output signal spectrum becomes

$$S_{y_s}(\omega) = S_s(\omega). \quad 2-29$$

The output spectrum due to noise is

$$S_{y_n}(\omega) = \mathbf{w}^H \mathbf{S}_n(\omega) \mathbf{w}. \quad 2-30$$

$\mathbf{S}_n(\omega)$ is the spectral matrix of the input noise. If the noise at the output of each sensor has identical spectra and is white then

$$S_{y_n}(\omega) = S_n(\omega) \mathbf{w}^H \mathbf{w}. \quad 2-31$$

Therefore, the output SNR is defined by

$$SNR_{out}(\omega) = \frac{1}{\mathbf{w}^H \mathbf{w}} \frac{S_s(\omega)}{S_n(\omega)}. \quad 2-32$$

By using Eq. 2-25 and Eq. 2-32 in Eq. 2-24, the AG, which is the improvement in SNR using an array, can be written as

$$AG = \frac{1}{\mathbf{w}^H \mathbf{w}}. \quad 2-33$$

Note that this result is valid for any arbitrary array geometry subject to a distortionless response. The maximum array gain possible is found by the Lagrange multiplier method based on the distortionless constraint

$$J = \mathbf{w}^H \mathbf{w} + \zeta (\mathbf{w}^H \mathbf{v}_k(\mathbf{k}_s) - 1) \quad 2-34$$

where ζ is Lagrange multiplier. Taking the complex gradient as zero, one gets

$$\frac{\partial J}{\partial \mathbf{w}^H} = \mathbf{w} + \zeta \mathbf{v}_k(\mathbf{k}_s) = 0 \quad 2-35$$

or

$$\mathbf{w} = -\zeta \mathbf{v}_k(\mathbf{k}_s). \quad 2-36$$

Satisfying the constraint gives

$$-\zeta \mathbf{v}_k(\mathbf{k}_s)^H \mathbf{v}_k(\mathbf{k}_s) = 1 \quad 2-37$$

such that

$$\zeta = \frac{-1}{\mathbf{v}_k(\mathbf{k}_T)^H \mathbf{v}_k(\mathbf{k}_T)} = \frac{-1}{M}. \quad 2-38$$

Hence, $\mathbf{w} = \frac{1}{M} \mathbf{v}_k(\mathbf{k}_T)$ and the maximum array gain is $AG_{\max} = M$. Of course the validity of this result depends on the noise being spatially white. If the noise is from radiated sources then as the elements get closer together, this assumption is no longer valid. The array gain defined in this section will be utilized to evaluate the performance of the beamformer in different multipath environments.

2.3 Multiple signal model in the presence of additive noise

Now consider N impinging signals with N discrete and distinct wavenumbers received by an arbitrary geometry M sensor array. Signals are assumed to be narrowband processes where source bandwidth is smaller than the reciprocal of the maximum propagation delay along the array. Far-field sources are assumed. The complex output of the k -th sensor at time t can be written as

$$x_k(t) = \sum_{i=1}^N v_k(\mathbf{k}_i) s_i(t - \tau_k) + n_k(t). \quad 2-39$$

where $v_k(\mathbf{k}_i)$ is defined in Eq. 2-15. The narrowband assumption leads to

$$x_k(t) = \sum_{i=1}^N v_k(\mathbf{k}_i) s_i(t) + n_k(t) \quad 2-40$$

where $\tau_k(\mathbf{k}_i)$ is the propagation delay between the k -th sensor and the reference point of the array, and $v_k(\mathbf{k}_i)$ is the phase and gain response of the k th element of the array. The output of the array in vector form can be written as

$$\mathbf{x}(t) = \mathbf{V}(\mathbf{k})\mathbf{s}(t) + \mathbf{n}(t) \quad 2-41$$

where $\mathbf{x}(t)$ is a $M \times 1$ observation vector, $\mathbf{s}(t)$ denotes the vector of a complex signal envelope at time t . $\mathbf{V}(\mathbf{k})$ is a $M \times N$ steering matrix and $\mathbf{n}(t)$ is a spatially and temporally white Gaussian circular complex noise vector with a variance of σ^2 .

2.3.1 Narrowband snapshot model

Consider a plane wave impinging on an array. The signal at the origin of the array coordinate is

$$s(t) = \sqrt{2} \operatorname{Re}\{\tilde{s}(t)e^{j\omega_c t}\}. \quad 2-42$$

The received signal at the m -th antenna can be represented by

$$s(t, \mathbf{p}_m) = \sqrt{2} \operatorname{Re}\{\tilde{s}(t)e^{j\omega_c t}e^{-j\omega_c \tau_m}\}. \quad 2-43$$

Prior to time-domain processing, receivers normally perform a quadrature demodulation as shown in Figure 2-4.

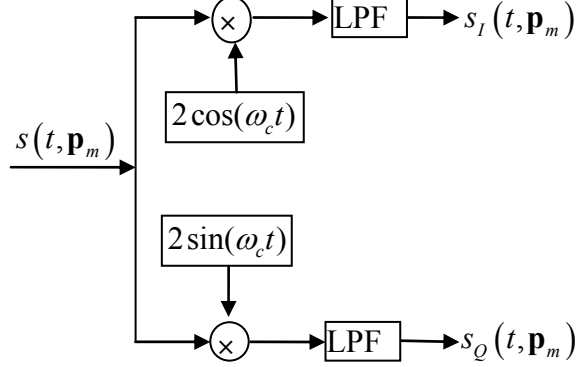


Figure 2-4: Quadrature demodulation

The complex output of the m -th antenna is

$$\tilde{s}(t, \mathbf{p}_m) = \tilde{s}(t) e^{-j\omega_c \tau_m}. \quad 2-44$$

Hence, the complex output of the array after quadrature demodulation becomes

$$\tilde{\mathbf{s}}(t) = \tilde{s}(t) \mathbf{v}(\mathbf{k}). \quad 2-45$$

where $\mathbf{v}(\mathbf{k})$ is an array steering vector as defined earlier and $\tilde{s}(t)$ is a zero-mean complex Gaussian random process. The signal covariance matrix can be defined as

$$\mathbf{R}_{\tilde{s}} = E[\tilde{\mathbf{s}}(t)\tilde{\mathbf{s}}^H(t)] = \mathbf{v}(\mathbf{k}) R_{\tilde{s}} \mathbf{v}^H(\mathbf{k}). \quad 2-46$$

where $R_{\tilde{s}}(0)$ is the signal power. The array output covariance matrix for N plane wave signals and additive noise is

$$\mathbf{R}_{\tilde{x}} = \mathbf{V}(\mathbf{k}) \mathbf{R}_{\tilde{s}} \mathbf{V}^H(\mathbf{k}) + \sigma_n^2 B_s \mathbf{I} \quad 2-47$$

where $\mathbf{V}(\mathbf{k})$ is a steering matrix, $\mathbf{R}_{\tilde{s}}$ is a signal correlation matrix, and B_s is the bandwidth of the Low-Pass Filter (LPF) shown in Figure 2-4. If $\tilde{s}(t)$ is bandlimited to

$-B_s/2 \leq s \leq B_s/2$ Hz, the time domain signal snapshots can be obtained by sampling $\mathbf{x}(t)$ in $1/B_s$ intervals. Hence, $\tilde{\mathbf{x}}(k)$, $k = 1, 2, \dots, K$ are snapshots of the complex envelope (Van Trees 2002).

2.4 Uniform linear array

The Uniform Linear Array (ULA) is an array configuration that has widely been used in practice. In this thesis, it will often be used. Figure 2-5 shows such an ULA configuration.

The M -element uniform spacing sensors are located on the z -axis with spacing d . The locations of elements are

$$\begin{aligned} p_{z_n} &= nd, \quad n = 0, 1, \dots, N-1 \\ p_{x_n} &= p_{y_n} = 0 \end{aligned} \quad . \quad 2-48$$

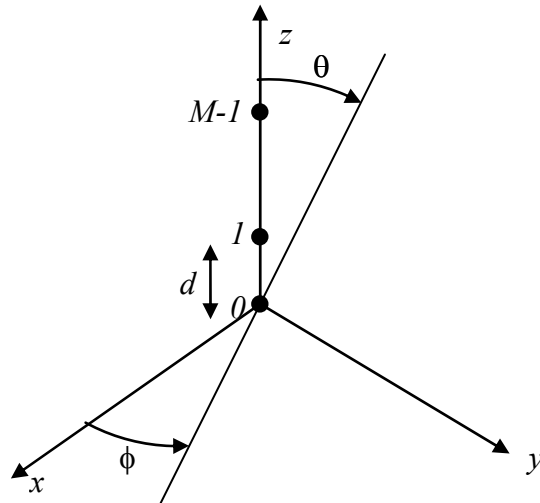


Figure 2-5: Uniform linear array configuration

Hence, the array manifold can be written as

$$\mathbf{v}_k(k_z) = [1, e^{-jk_zd}, e^{-j2k_zd}, \dots, e^{-j(M-1)k_zd}] \quad 2-49$$

where

$$k_z = -\frac{2\pi}{\kappa} \cos \theta. \quad 2-50$$

Figure 2-6 shows the beampattern of an ULA with 10 elements and half wavelength spacing $d = \kappa / 2$. The distance of the nulls adjacent to the main lobe is referred to as the array null-to-null beamwidth BW_{NN} . The BW_{NN} defines the ability of the array to resolve two different plane waves coming from different directions which is known as the Rayleigh resolution limit (Van Trees 2002). Based on this definition, two plane waves are resolvable if they have an angular separation more than $BW_{NN}/2$. The resolution of an array increases by increasing the number of sensors M and antenna spacing d .

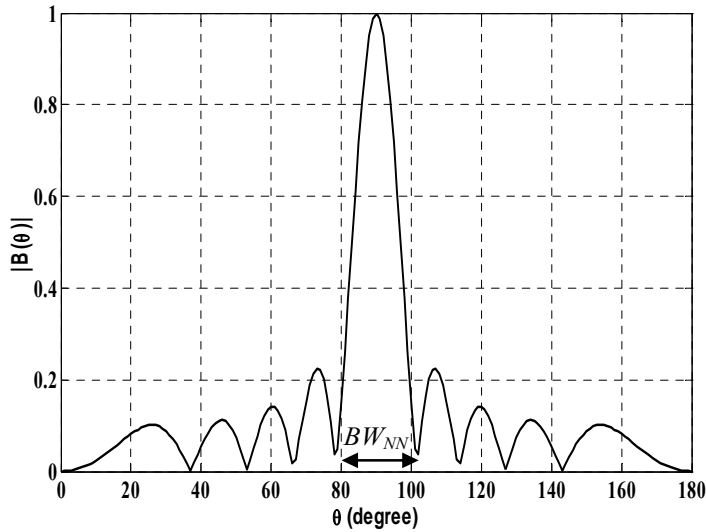


Figure 2-6: Beampattern of a ULA, $M=10$ and $d = \kappa / 2$

2.5 Signal propagation models in wireless channels

As mentioned earlier, the main contribution of this thesis is enhancing signal detection performance in indoor and dense multipath environments. Hence, it is necessary to analyze the behavior of different multipath propagation channels and to characterize the received signal model. The received signal transmitted over a wireless channel is affected by several factors which can be grouped into two categories: large-scale propagation loss and small-scale fading. As a mobile station moves away from the transmitter by several carrier wavelengths of the signal the local average received signal power will gradually decrease resulting in a large-scale propagation loss. This large-scale phenomenon is characterized by the distance between transmitter and receiver (path loss), and shadowing and attenuation of the received signal power. The large-scale loss predicts the mean signal strength for an arbitrary transmitter-receiver distance in a typical built up area and can be utilized to determine the coverage of a wireless system. However, in a multipath fading environment, as the result of moving a receiver over a small distance, the instantaneous received signal strength will fluctuate rapidly, an effect known as small-scale fading. This is due to the fact that in a dense multipath environment, the received signal is a contribution of several multipath components coming from different directions with different amplitudes. Hence, the received signal power may fluctuate up to four orders of magnitude (40 dB) in a typical fading environment when the receiver is displaced by a wavelength of the impinging signals (Rappaport 2002). Figure 2-7 shows small-scale fading.

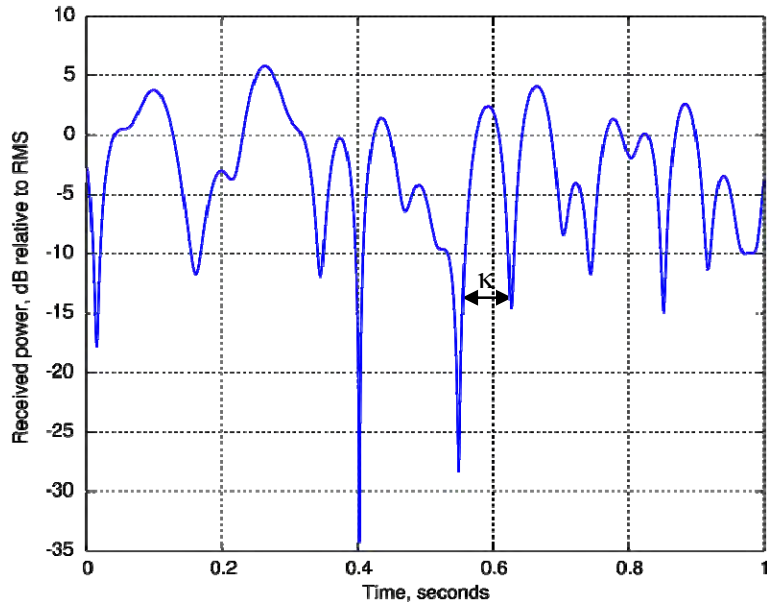


Figure 2-7: Small-scale fading in a multipath environment

In the following subsection the small-scale fading will be investigated in detail.

2.5.1 Small-scale fading

Small-scale fading or simply fading is a result of multipath propagation in a wireless channel. Multipath propagation received by a receiver antenna causes deep fades in the received signal strength, random frequency modulation due to Doppler spread on different multipath components and delay spread due to different times of arrival of multipath components. Hence, a received signal at any point in space in a multipath environment can be modeled by a combination of several plane waves resulting in a randomly distributed amplitude, phase and angle of arrival (Rappaport 2002).

An important factor influencing small-scale fading is the bandwidth of the transmitted signal. If the bandwidth of the transmitted signal is much greater than the coherence bandwidth of the channel, the received signal will be distorted. However, the received signal strength is not affected by small-scale fading. The coherence bandwidth of a channel is defined as the maximum frequency difference of the multipath channel where the amplitude of the received signal is noticeably correlated. On the other hand, if the transmitted signal bandwidth is smaller than the coherence bandwidth of the channel, the signal strength will change rapidly. However, the signal is not subject to distortion in time. Hence, the fading statistics depend on amplitude, phase and delay spread of multipath components which can be characterized by the geometry of reflectors as well as the bandwidth of the transmitted signal.

Multipath channels are usually characterized by the power delay profile defined by the energy received by a receiver over the time duration of the multipath propagation (Rappaport 2002). The coherence bandwidth of a channel and root mean square (rms) delay spread are inversely proportional where the rms delay spread is the square-root of the second central moment of the power delay profile. The coherence bandwidth of a channel is a statistical measurement where in that frequency range, the channel can be assumed flat. As a rule of thumb the relationship between the coherence bandwidth and the rms delay spread is defined by (Lee 1989)

$$B_c \approx \frac{1}{5\sigma_\tau} \text{ Hz} \quad 2-51$$

where B_c and σ_τ represent the coherence bandwidth and the rms delay spread, respectively. The coherence bandwidth in Eq. 2-51 is defined as a multipath channel

bandwidth where the frequency components have a correlation of more than 50 percent. The measurement results in (Saleh & Valenzula 1987) show that for a typical office building, the rms delay spread σ_τ is about 10-50 ns.

As an example, consider a multipath propagation channel with the multipath power delay profile shown in the Figure 2-8.

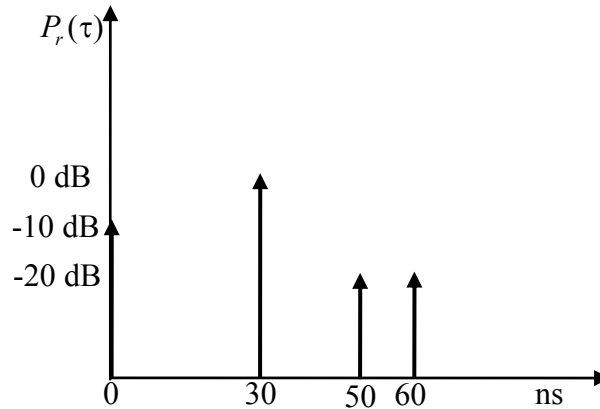


Figure 2-8: Multipath power delay profile

The delay of each profile is represented with respect to the delay of the first detectable signal. The mean excess delay can be calculated by

$$\bar{\tau} = \frac{0 \times 0.1 + 30 \times 1 + 50 \times 0.01 + 60 \times 0.01}{0.1 + 1 + 0.01 + 0.01} = 28 \text{ ns}. \quad 2-52$$

The second moment can be determined as

$$\tau^2 = \frac{0 \times 0.1 + (30)^2 \times 1 + (50)^2 \times 0.01 + (60)^2 \times 0.01}{0.1 + 1 + 0.01 + 0.01} = 858 \text{ ns}^2. \quad 2-53$$

Hence, the rms delay spread is

$$\sigma_\tau = \sqrt{\tau^2 - \bar{\tau}^2} = \sqrt{858 - 784} = 8.6 \text{ ns}. \quad 2-54$$

The coherence bandwidth B_c can be easily determined by

$$B_c \approx \frac{1}{5\sigma_\tau} = 23 \text{ MHz}. \quad 2-55$$

Any system with a signal bandwidth of less than 20 MHz can actually work without implementing an equalizer (Rappaport 2002). This is an example of a flat fading channel.

2.5.1.1 Doppler spread and coherence time

Channel coherence bandwidth and consequently delay spread are parameters which characterize the time dispersive nature of a wireless channel. However, these parameters do not provide any information about the time-varying nature of a wireless channel. Doppler spread and coherence time are parameters which take into account the time varying nature caused by changes in scatterer environment or relative motion between transmitter and receiver. Doppler spread denoted as B_D is a measure of frequency broadening of the received signal and it is defined by a frequency range where the Doppler spectrum is not zero. If a carrier frequency f_c is transmitted the received signal frequency has components in the range of $[f_c - f_d : f_c + f_d]$ where f_d is the Doppler frequency. Hence, B_D depends on the transmitter-receiver relative velocity and angle between direction of motion and angle of arrival. If the bandwidth of the transmitted signal is much higher than B_D , the effect of the Doppler spread is negligible, which is known as a slow fading channel (Rappaport 2002).

Channel coherence time, denoted as T_c , is inversely proportional to the Doppler spread which characterizes the frequency dispersive nature of a wireless channel in the time domain. Coherence time is a statistical measurement of a time period where two

received signals have a strong amplitude correlation. If the reciprocal signal bandwidth is greater than the coherence time, the received signal will be distorted. As a rule of thumb for modern digital communications, the relationship between maximum Doppler frequency $f_m = v / \kappa$ and coherence time can be defined by (Rappaport 2002)

$$T_c = \frac{0.423}{f_m} \text{ s.} \quad 2-56$$

As an example, consider a moving receiver capturing a signal in a fading environment. The carrier frequency is $f_c=1500$ MHz and the receiver velocity has two values, namely $v=1$ m/s and $v=50$ m/s. The problem of interest is determining the proper spatial sampling intervals in which consecutive samples are correlated in time. This may be equivalent to the time intervals where the receiver can perform coherent integration.

The coherence time can be easily calculated by using Eq. 2-56

$$\begin{aligned} T_{c_{v=1}} &= \frac{0.423}{f_m} = \frac{0.423c}{vf_c} = 0.0850 \text{ s} \\ T_{c_{v=50}} &= \frac{0.423}{f_m} = \frac{0.423c}{vf_c} = 0.0017 \text{ s} \end{aligned} \quad 2-57$$

where c is the propagation velocity. Taking time samples at half of the T_c ensures that the time correlation between spatial samples is preserved. Hence, the spatial samples for which received signal remains correlated in time can be determined by

$$\Delta D = \frac{T_c v}{2} = \frac{0.065}{2} = 4.25 \text{ cm} \quad 2-58$$

which is about a quarter of the carrier wavelength.

The Doppler spread can be calculated by

$$B_{D_v=1} = f_m = \frac{vf_c}{c} = 5 \text{ Hz} \quad . \quad 2-59$$

$$B_{D_v=50} = f_m = \frac{vf_c}{c} = 250 \text{ Hz}$$

Time dispersiveness of a wireless channel causes the transmitted signals to undergo flat fading or frequency selective fading. In flat fading channels, the amplitude of the received signals varies randomly in time however the spectral characteristics of the signal are preserved. The Channel Impulse Response (CIR) in the flat fading channel can be approximately modeled by a delta function without any excess delay. In the frequency selective fading channel, the channel impulse response has a delay spread which is greater than the reciprocal of the signal bandwidth. Thus, the channel induces Inter Symbol Interference (ISI).

Frequency dispersiveness of a wireless channel causes the transmitted signals to undergo slow or fast fading. In the fast fading channel the channel impulse response varies faster than the chip period of the signal. Hence, the chip period of the signal is larger than the coherence time. In slow fading, the CIR changes at a much slower rate than the signals change.

It is clear that the type of fading depends on the signal characteristics with respect to the nature of the wireless channel. Depending on the signal parameters such as bandwidth and channel parameters such as delay and Doppler spread, a received signal may experience the following four different types of fading:

1- Slow flat fading:

The bandwidth of the signal is much smaller than the coherence bandwidth of the channel and the channel also varies slower than the signal variations (low Doppler spread). This is

the typical model for indoor multipath environments with the signal bandwidth in the order of few MHz.

2- Fast flat fading:

The bandwidth of the signal is much smaller than the coherence bandwidth of the channel but there is high Doppler spread.

3- Slow frequency selective fading :

The bandwidth of the signal is greater than the bandwidth of the channel and the channel dynamics are smaller than the variations in the transmitted signal.

4- Fast frequency selective fading:

This fading type represents a situation where the signal bandwidth is greater than the bandwidth of the channel and the Doppler spread is high.

2.5.2 Rayleigh fading

In wireless radio systems Rayleigh fading is commonly used to describe the envelope of the received signal. Rayleigh fading is the envelope of the sum of two quadrature zero-mean Gaussian components (Parsons 2000). The envelope $r(t)$ of a complex signal $x(t) = I(t) + jQ(t)$ is

$$r(t) = \sqrt{I^2(t) + Q^2(t)} \quad 2-60$$

where $I \sim N(0, \sigma^2)$ and $Q \sim N(0, \sigma^2)$ and \sim denotes the Probability Density Function (PDF) of the left hand side variable and $N(0, \sigma^2)$ signifies a zero mean normal PDF with variance σ^2 . The PDF of $r(t)$ is defined by

$$p_r(r) = \begin{cases} \frac{r}{\sigma^2} \exp\left(-\frac{r^2}{2\sigma^2}\right) & 0 \leq r \leq \infty \\ 0 & r < 0 \end{cases} \quad 2-61$$

where σ^2 is the mean power and $r^2 / 2$ is the short-term signal power. The probability that the envelope does not exceed a value defined by R is given by

$$P_r(r \leq R) = \int_0^R p_r(r) dr = 1 - \exp\left(-\frac{R^2}{2\sigma^2}\right). \quad 2-62$$

The mean value of the Rayleigh distribution can be calculated by

$$E[r] = \int_0^\infty r p_r(r) dr = \sqrt{\pi/2} \sigma = 1.253\sigma. \quad 2-63$$

The variance of the Rayleigh distribution given as σ_r^2

$$\sigma_r^2 = E[r^2] - E^2[r] = 0.43\sigma^2. \quad 2-64$$

Figure 2-9 shows the Rayleigh PDF.

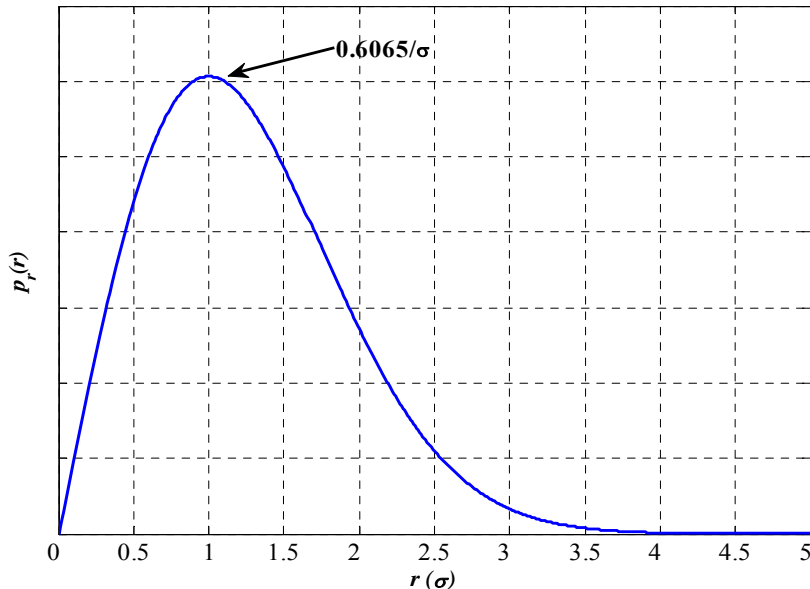


Figure 2-9: Rayleigh distribution

2.5.3 Signal model in fading environments

Now consider the signal reception model in a typical fading environment. The model represented in Eq. 2-41 can be modified to demonstrate the fading effect as

$$\mathbf{x}(t) = \xi(\phi, \theta) \mathbf{v}(\phi, \theta) s(t) + \mathbf{n}(t) \quad 2-65$$

where $\xi(\phi, \theta)$ models changes in the received signal amplitude from the source $s(t)$. In a multipath fading environment, each transmitted signal is received by the receiver antenna from different directions with a certain angular spread in space. Each multipath component is received with different directions of arrival, arrival time $\tau(\phi, \theta)$ and signal strength. Since the narrowband assumption is considered, a decomposition is made,

$$s(t - \tau(\phi, \theta)) = e^{\psi(\phi, \theta)} s(t) \quad 2-66$$

where the time delay is approximated by a phase shift ψ that is uniformly distributed over the interval $[-\pi, \pi]$, and the amplitude fading $\xi(\phi, \theta)$ is distributed according to the Rayleigh fading, which is an acceptable model for indoor and dense multipath environments. The total fading becomes

$$\alpha(\phi, \theta) = \xi(\phi, \theta) e^{\psi(\phi, \theta)} \sim CN(0, \sigma^2) \quad 2-67$$

which has a circularly complex normal distribution and $CN(0, \sigma^2)$ signifies a zero mean circular normal PDF with variance σ^2 ¹ (Rensburg 2001). Hence, the signal model in the fading environment is

$$x(t) = \int_0^\pi d\theta \int_0^{2\pi} \frac{\sin(\theta)}{4\pi} \alpha(\phi, \theta) \mathbf{v}(\phi, \theta) s(t) d\phi + n(t). \quad 2-68$$

The channel gain is defined as

$$A = \frac{1}{4\pi} \int_0^\pi \sin \theta d\theta \int_0^{2\pi} \alpha(\phi, \theta) \mathbf{v}(\phi, \theta) d\phi. \quad 2-69$$

Thus, the array response in a fading environment is

$$x(t) = As(t) + n(t). \quad 2-70$$

2.6 Performance of beamforming techniques in multipath fading channels

The performance of beamforming techniques based on the plane wave assumption was described in Section 2.2.1. The array gain metric was used to quantify the SNR improvement of a signal at the output of an array. However, in practice the desired signal may come from a sector in space where the angular size of the sector depends on the scatterer's geometry. As an example, Lee (1989) demonstrated that in cellular communication systems in urban environments where the BS antennas are about 1-2 km away, the angular spread is about 5 to 15 degrees. The problem of interest in this section

¹ Random variable $B = u + jv$ distributed according to circularly normal PDF with zero mean and variance σ^2 , $CN(0, \sigma^2)$, where u and v are independent zero mean normal random variables each with variance $\sigma^2/2$, $u \sim N(0, \sigma^2/2)$ and $v \sim N(0, \sigma^2/2)$

is to investigate the performance of an array in terms of output SNR improvement in a multipath environment. The signal spectrum at the output of an array is

$$S_{y_s}(\omega) = S_s(\omega) \mathbf{w}^H \mathbf{R}_A \mathbf{w} \quad 2-71$$

where $\mathbf{R}_A = E(\mathbf{A}\mathbf{A}^H)$ is the correlation matrix of the channel response and \mathbf{w} is the beamformer weight vector which is assumed to have unit norm, $\|\mathbf{w}^H \mathbf{w}\| = 1$. Hence the array gain becomes

$$AG = \mathbf{w}^H \mathbf{R}_A \mathbf{w}. \quad 2-72$$

In the case of independent fading where $\mathbf{R}_A = \mathbf{I}$ and \mathbf{I} is an identity matrix, the array gain AG become 1, emphasizing that there is no gain in beamforming in comparison with a single antenna. Whereas, in the case of a fully correlated fading channel, $\mathbf{R}_A = \mathbf{v}\mathbf{v}^H$ and $\mathbf{w} = \mathbf{v}/\|\mathbf{v}\|$. Hence, the array gain becomes $AG = \|\mathbf{v}\|^2 = M$. Thus, the array gain depends on the scatterer geometry and varies between 1 and M (Friedlander & Scherzer 2004).

To evaluate the performance of beamforming techniques in a multipath environment, a uniform linear array with half-wavelength element spacing is considered. It is also assumed that the array and incoming signals are located in the same plane and signals are coming from a sector with an angular spread of φ_s . Thus, the signal covariance matrix can be represented by

$$\mathbf{R}_A = \frac{1}{\varphi_s} \int_{-\varphi_s/2}^{\varphi_s/2} S(\varphi) \mathbf{v}(\varphi) \mathbf{v}(\varphi)^H d\varphi \quad 2-73$$

where $S(\phi)$ is the spatial distribution of fading signals. Hence, the spatial signal covariance matrix is a function of the array geometry and angular spread of the incoming signals. Figure 2-10 shows spatial correlation coefficients for different values of φ_s . In Figure 2-10, φ is the mean direction of arrival of the sector with an angle spread of φ_s . The spatial decorrelation is a function of angular spread and array geometry. Figure 2-11 shows the ULA array gain defined in Eq. 2-72 for different values of M versus multipath angular spread φ_s for $\varphi=0$. Figure 2-12 shows the ULA array gain for different values of M versus φ_s for $\varphi=45$. Figure 2-11 and Figure 2-12 show that, by increasing the angular spread, the achievable array gain is reduced. The rate of the gain degradation is severe for higher values of M . For example when the angular spread is at least 20 degrees, the array gain value for $M=16$ and $M=8$ becomes identical.

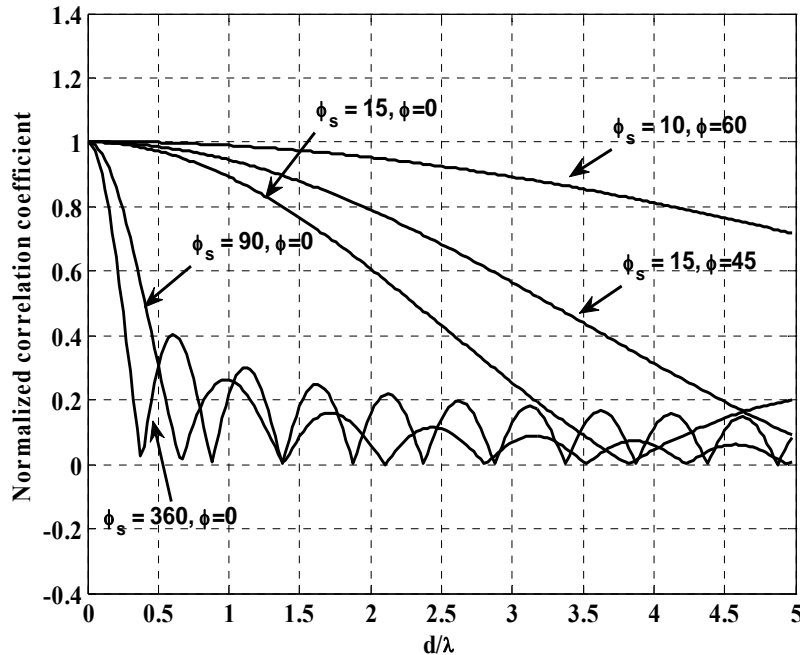


Figure 2-10: Spatial correlation coefficient for different values of φ_s and φ

However, the array gain for $M=2$ is almost insensitive to changes in angular spread and consequently to the correlation coefficient.

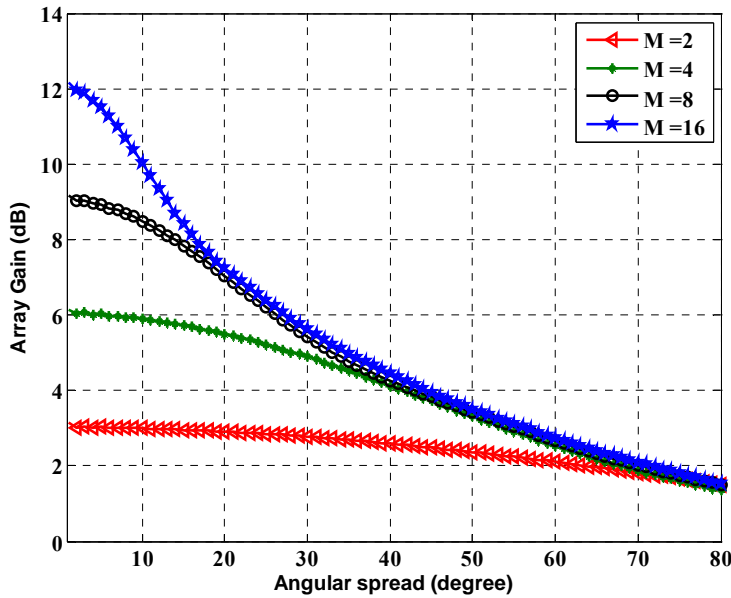


Figure 2-11: Array gain for different values of M vs multipath angular spread for $\varphi = 0$

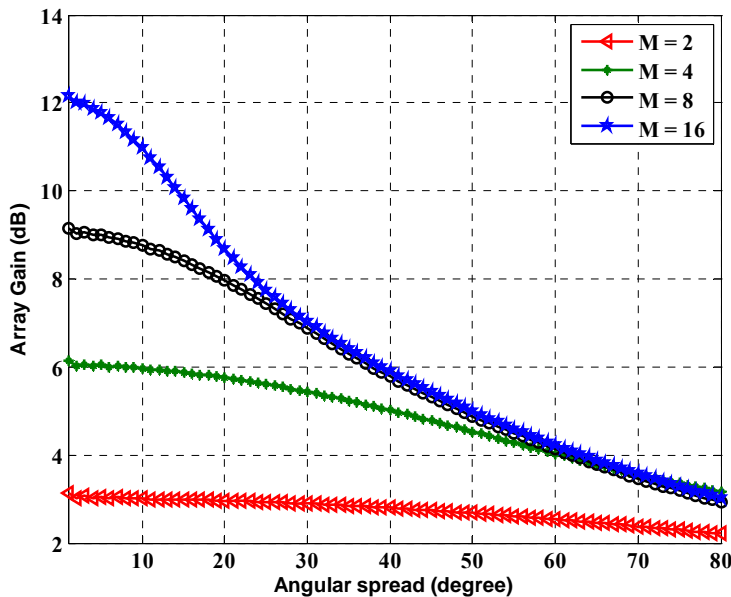


Figure 2-12: Array gain for different values of M vs multipath angular spread for $\varphi = 45$

Figure 2-13 shows the eigenvalues of the spatial covariance matrix defined in Eq. 2-73 for a 10-element ULA with half wavelength spacing versus different values of angle spread for $\varphi = 0$. When the angular spread is small, there is only one nonzero eigenvalue. The signal subspace is spanned by the eigenvector of the nonzero eigenvalue. Since the signal subspace is a one-dimensional space the beamformer can co-phase all received signals from different antennas and maximizes the array gain. By increasing the angular spread the number of nonzero eigenvalues and consequently the signal subspace dimension are increased. Hence, the array gain as it is shown in Figure 2-11 and Figure 2-12 is decreased.

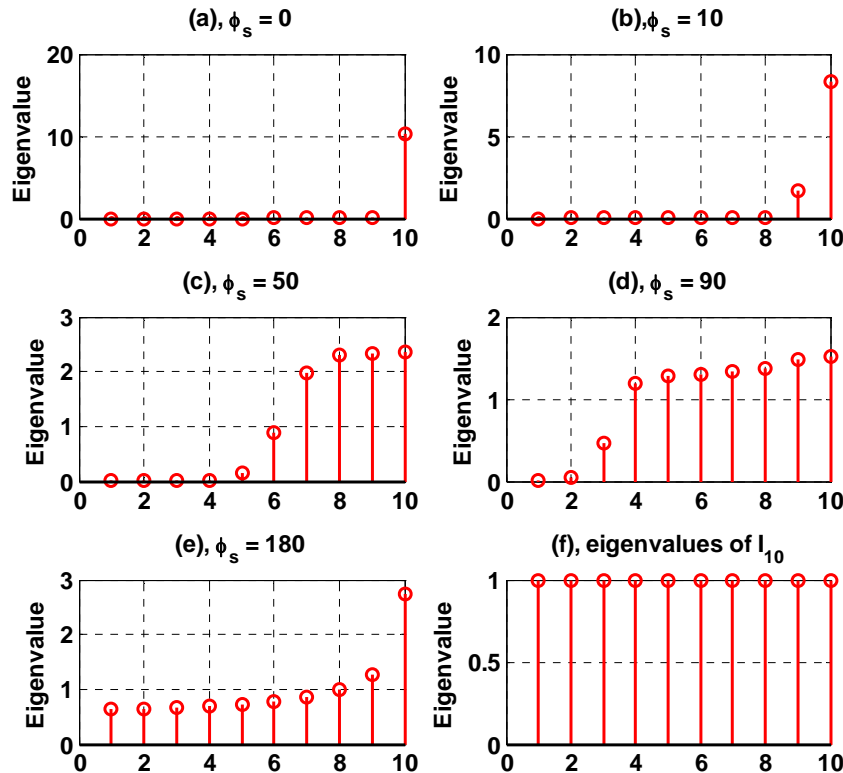


Figure 2-13: Eigenvalues of spatial covariance matrix for different values of φ_s

2.7 Diversity techniques

As shown in previous sections, in a multipath fading wireless channel the received signal envelope undergoes deep fades. If the receiver is using another independent source to process the received signal, the second path may have a strong signal which can strongly improve the detection procedure. The basic idea of the diversity system is to combine independent copies of the transmitted signal received by diversity branches. There are several methods to receive statistically independent faded signals and implement a diversity system which can be divided into three groups: time diversity, frequency diversity and antenna diversity systems (Parsons 2000).

In antenna diversity systems, a receiver uses multiple antennas known as diversity branches to capture independent copies of the transmitted signal. Different techniques have been utilized to capture statistically independent signals in the antenna diversity system. Among them, spatial diversity and polarization diversity are widely utilized in practice. Spatial diversity systems are established based on the fact that in a multipath fading environment received signals on the diversity branches decorrelate spatially. In polarization diversity systems, antennas with approximately orthogonal polarization can be considered as a diversity system (Rappaport 2002). After receiving independent signals the problem of interest is how to combine these signal copies efficiently. Figure 2-14 shows a general approach of the antenna diversity systems.

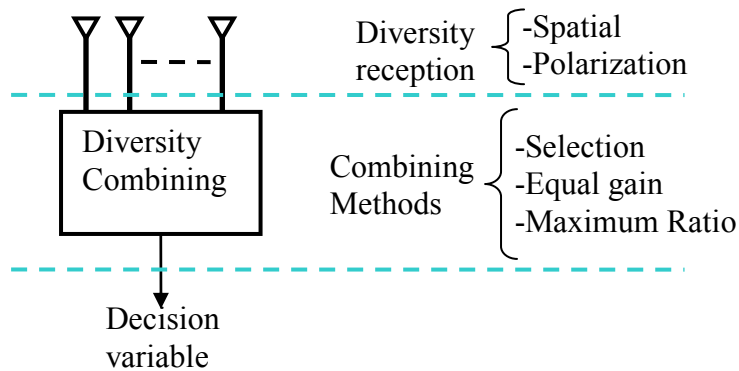


Figure 2-14: Block diagram of antenna diversity systems

After capturing independent signal samples from different diversity branches, the signals must be combined to mitigate fading effects. In general, different combining methods such as selection, equal gain, and maximum ratio combiners have been widely investigated in the literature such as Parsons (2000) and Rappaport (2002).

It is worthwhile to contrast the performance of the beamforming and diversity techniques. In the beamforming approach, the array gain is defined as an improvement in SNR at the output of the beamformer, however the diversity gain, which is an effect of multipath fading, is defined as the reduction in the required average SNR for given detection probability. The array gain is reduced by decreasing the channel correlation coefficient. However, the diversity gain which is a result of uncorrelated diversity branches is decreased by increasing the channel correlation coefficient.

2.8 Detection of a signal in noise

In this thesis, a statistical approach for evaluating the performance of a moving receiver for detecting a narrowband signal in multipath environments is presented. In this section, an overview of the detection problem of a complex signal embedded in circular white Gaussian noise is provided. A more detailed description can be found in Kay (1998) and Van trees (2001).

2.8.1 Matched filter

Consider a detection problem of a known circular deterministic signal embedded in a Circular White Gaussian Noise (CWGN). The objective is to maximize the probability of detection denoted as P_D subject to a constraint on the probability of false alarm P_{FA} .

The detector uses K uncorrelated samples to make a decision. The binary hypothesis test can be defined by

$$\begin{aligned} x(k)|_{H_1} &= s(k) + n(k) \quad k = 0, 1, \dots, K-1 \\ x(k)|_{H_0} &= n(k) \quad \quad \quad k = 0, 1, \dots, K-1 \end{aligned} \tag{2-74}$$

where $s(k)$ is a known circular signal and $n(k) \sim CN(0, \sigma^2)$. The optimum Likelihood Ratio Test (LRT) chooses the H_1 state if

$$L(x) = \frac{p(x; H_1)}{p(x; H_0)} > \gamma \tag{2-75}$$

where

$$\begin{aligned} p(x; H_1) &= \frac{1}{\pi^K \sigma^{2K}} \exp \left[-\frac{1}{\sigma^2} (\mathbf{x} - \mathbf{s})^H (\mathbf{x} - \mathbf{s}) \right] \\ p(x; H_0) &= \frac{1}{\pi^K \sigma^{2K}} \exp \left[-\frac{1}{\sigma^2} \mathbf{x}^H \mathbf{x} \right] \end{aligned} \quad 2-76$$

with $(\bullet)^H$ being a complex conjugate transpose operator. After some manipulation the test statistic becomes

$$\begin{aligned} z &= \operatorname{Re}(\mathbf{s}^H \mathbf{x}) > \gamma' \\ &= \operatorname{Re} \left(\sum_{k=0}^{K-1} s^*(k) x(k) \right) > \gamma'. \end{aligned} \quad 2-77$$

It can be easily shown that the test statistic is distributed as

$$z \sim \begin{cases} N(0, \sigma^2 \varepsilon / 2) & \text{under } H_0 \\ N(\varepsilon, \sigma^2 \varepsilon / 2) & \text{under } H_1 \end{cases} \quad 2-78$$

where ε is the signal energy defined as $\varepsilon = \mathbf{s}^H \mathbf{s}$. The performance of the matched filter can be written as

$$\begin{aligned} P_{FA} &= Q \left(\frac{\gamma'}{\sqrt{\sigma^2 \varepsilon / 2}} \right) \\ P_D &= Q \left(Q^{-1}(P_{FA}) - \sqrt{2\varepsilon / \sigma^2} \right) \end{aligned} \quad 2-79$$

Figure 2-15 shows the detection process of a matched filter (Kay 1998).

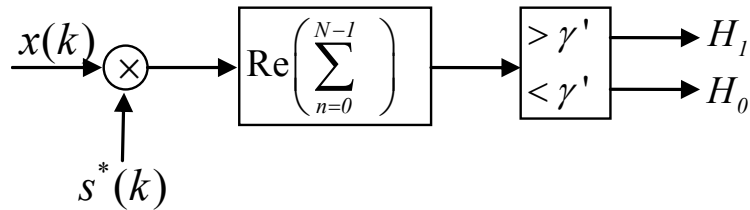


Figure 2-15: Detection process of a matched filter

2.8.2 Estimator-correlator

Consider a binary detection problem where the binary hypothesis test can be defined by

$$\begin{aligned} x(k)|_{H_1} &= s(k) + n(k) \quad k = 0, 1, \dots, K-1 \\ x(k)|_{H_0} &= n(k) \quad \quad \quad k = 0, 1, \dots, K-1 \end{aligned} \quad 2-80$$

where $s(k)$ is a zero-mean circular Gaussian random process with covariance matrix \mathbf{C}_s and $s(k) \sim CN(0, \mathbf{C}_s)$ and $n(k) \sim CN(0, \sigma^2)$. The optimum LRT chooses the H_1 state if

$$L(x) = \frac{p(x; H_1)}{p(x; H_0)} > \gamma \quad 2-81$$

where

$$\begin{aligned} p(x; H_1) &= \frac{1}{\pi^K \det(\mathbf{C}_s + \sigma^2 \mathbf{I})} \exp \left[-\mathbf{x}^H (\mathbf{C}_s + \sigma^2 \mathbf{I})^{-1} \mathbf{x} \right] \\ p(x; H_0) &= \frac{1}{\pi^K \sigma^{2K}} \exp \left[-\frac{1}{\sigma^2} \mathbf{x}^H \mathbf{x} \right] \end{aligned} \quad 2-82$$

After some manipulation the log LRT test reduces to the following statistic

$$z = \mathbf{x}^H \hat{s} > \gamma' \quad 2-83$$

where

$$\hat{s} = \mathbf{C}_s (\mathbf{C}_s + \sigma^2 \mathbf{I})^{-1} \mathbf{x} \quad 2-84$$

is the Minimum Mean Square Error (MMSE) estimator of s . Figure 2-16 shows the EC detection process (Kay 1998).

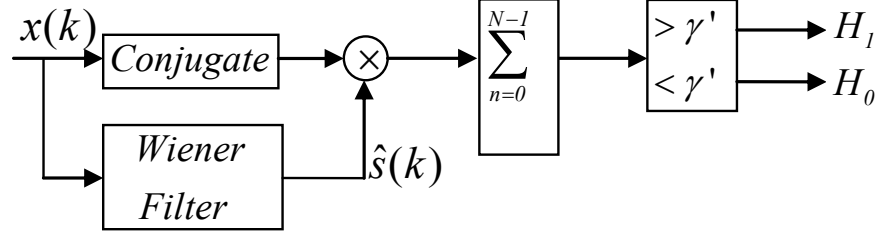


Figure 2-16: EC detection process

Consider a correlated signal case where the noise covariance is normalized such that

$$E[\mathbf{x}\mathbf{x}^H] = \begin{cases} \mathbf{C}_s + \mathbf{I} & H1 \\ \mathbf{I} & H0 \end{cases} \quad 2-85$$

where \mathbf{C}_s and \mathbf{I} are the signal and noise covariance matrices, respectively. The canonical form of Eq. 2-83 can be written in terms of the eigenvalues of \mathbf{C}_s based on the eigen-decomposition of $\mathbf{C}_s = \mathbf{Q}\Lambda\mathbf{Q}^H$ where Λ is the diagonal matrix of eigenvalues and \mathbf{Q} is the eigenvector matrix. Note that

$$\begin{aligned} z &= \mathbf{x}^H \mathbf{Q} \Lambda \mathbf{Q}^H (\mathbf{Q} \Lambda \mathbf{Q}^H + \mathbf{I})^{-1} \mathbf{x} \\ &= (\mathbf{x}^H \mathbf{Q}) \Lambda (\Lambda + \mathbf{I})^{-1} (\mathbf{Q}^H \mathbf{x}) \\ &= \mathbf{y}^H \Lambda (\Lambda + \mathbf{I})^{-1} \mathbf{y} \\ &= \sum_{m=1}^M |y_m|^2 \frac{\lambda_{s,m}}{\lambda_{s,m} + I} \end{aligned} \quad 2-86$$

where $\mathbf{y} = \mathbf{Q}^H \mathbf{x} = [y_1 \dots y_M]^T$ and $\lambda_{s,m}$ is the m th eigenvalue of \mathbf{C}_s . Note that

$$E[\mathbf{y}\mathbf{y}^H] = \mathbf{Q}^H E[\mathbf{x}\mathbf{x}^H] \mathbf{Q} = \begin{cases} \mathbf{Q}^H \mathbf{Q} \mathbf{I} \mathbf{Q}^H \mathbf{Q} = \mathbf{I} & \text{under } H_0 \\ \mathbf{Q}^H \mathbf{Q} (\Lambda + \mathbf{I}) \mathbf{Q}^H \mathbf{Q} = \Lambda + \mathbf{I} & \text{under } H_1 \end{cases} \quad 2-87$$

Hence, for either H_0 or H_1 , \mathbf{y} is a vector of independent CN random variables. The canonical form of the EC process is shown in Figure 2-17 (Kay 1998).

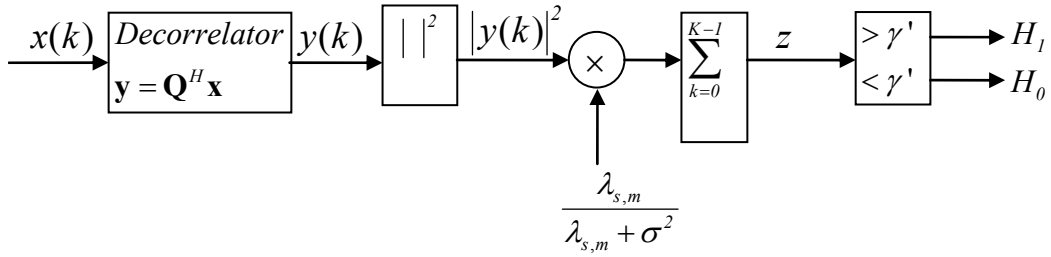


Figure 2-17: Canonical for of the EC process

2.9 Summary

This chapter described the background knowledge for the spatial-temporal array processing problem that will be used in the remainder of this thesis. The performance of the beamforming technique based on the plane wave assumption was described. The array gain metric was introduced to quantify the SNR improvement of a signal at the output of an antenna array. The array gain was evaluated for different scatterer angle spreads and array geometries. Signal propagation models in different multipath environments including the flat fading channel were described. To alleviate the fading loss and to enhance the detection performance of a narrowband signal in a dense multipath environment, different antenna diversity techniques were introduced. A brief overview of the detection problem of a complex signal embedded in circular white Gaussian noise including the Estimator-Correlator (EC) process was demonstrated.

CHAPTER 3: SYNTHETIC ARRAY MODEL AND CHARACTERIZATION OF THE PROPAGATION CHANNEL

This chapter discusses the synthetic array concept and the signal model received by a moving antenna. The statistical properties of the signal components of the snapshot signal will be considered in detail. Discussions of deviations from the assumed multivariate Gaussian approximation, which are primarily due to the LOS component of the signal at an unknown angle and a partially known antenna trajectory, will be given. The various covariance matrices derived for the different signal types will be used in conjunction with the Estimator-Correlator (EC) to clearly demonstrate the performance achievable with the synthetic array in different multipath environments. In indoors or dense multipath environments, where the amplitude of the received signal is modeled by a Circularly Normal (CN) random process and multipath is diffuse and arriving from any direction in space, the EC process introduced in Chapter 2 gives an optimal solution. The signal and covariance model presented in this chapter will be used in Chapter 4 and Chapter 5 where the detection performance of the synthetic array in a dense multipath environment is considered. When the received signal is a plane wave with an unknown direction of arrival, the EC becomes a suboptimal approach. In this situation, the Generalized Likelihood Ratio Test (GLRT) method as well as nonlinear detection/estimation schemes such as the MUSIC and the ESPRIT subspace methods can be used to enhance detection and estimation performance. The direction of arrival estimation based on the synthetic array will be discussed in Chapter 6 using the signal and noise characterization described in this chapter.

3.1 Synthetic array system model

Assume that the phase center of the moving single antenna is coincident with a point in a three-dimensional spatial coordinate system identified by the position vector $\mathbf{p}(t)$ which is a function of time t . The complex baseband signal representation of the antenna output received signal is denoted by $r(t)$. Under the H_1 state where the signal and noise are present, the signal component of $r(t)$ is denoted by $s(t, \mathbf{p}(t))$, which is a function of time t and the antenna position $\mathbf{p}(t)$ changing with time. The signal is assumed to be narrowband, which was explained in Section 2.2. The narrowband assumption justifies the decomposition of

$$s(t, \mathbf{p}(t)) = A(\mathbf{p}(t))s_o(t) \quad 3-1$$

which implies that small delay changes due to $\mathbf{p}(t)$ are insignificant in the context of $s_o(t)$. $A(\mathbf{p}(t))$ is the channel response to the incident signal at the antenna position of $\mathbf{p}(t)$ defined earlier in Section 2.5.3. The received signal is corrupted with additive noise which has an equivalent complex baseband representation denoted by $n(t)$. It is assumed that $n(t)$ is a circularly normal random process, independent of the signal and has a power spectral density (PSD) that is constant within the bandwidth of $s_o(t)$ with a level of N_o . The representations of $r(t)$ can then be written as

$$r(t) = A(\mathbf{p}(t))s_o(t) + n(t). \quad 3-2$$

To be rigorous, the additive noise component should also be written as a function of the position. However, as the noise is assumed to be decorrelated much faster temporally than spatially, the spatial correlation of the noise is negligible and therefore $n(t, \mathbf{p}(t)) \rightarrow n(t)$. An exception to this is where the noise is an interference signal from a jammer that closely represents the pilot signal $s_o(t)$ but has a different spatial correlation. Because of the latter, it is separable from the desired signal provided that the receiver has knowledge of the desired and jammer signal covariance matrices.

The receiver accumulates a temporal snapshot of $r(t)$ over an interval $t \in [t', T + t']$ where T is the interval duration of the snapshot and t' is an arbitrary time offset. There is no loss in generality by assuming that $t' = 0$ such that the snapshot interval extends over the interval $t \in [0, T]$. It is assumed that the signal snapshot of $r(t)$ is collected in M subintervals, each of duration ΔT such that $T = M \Delta T$. Consider that the signal is sampled over a subinterval of ΔT as shown in Figure 3-1.

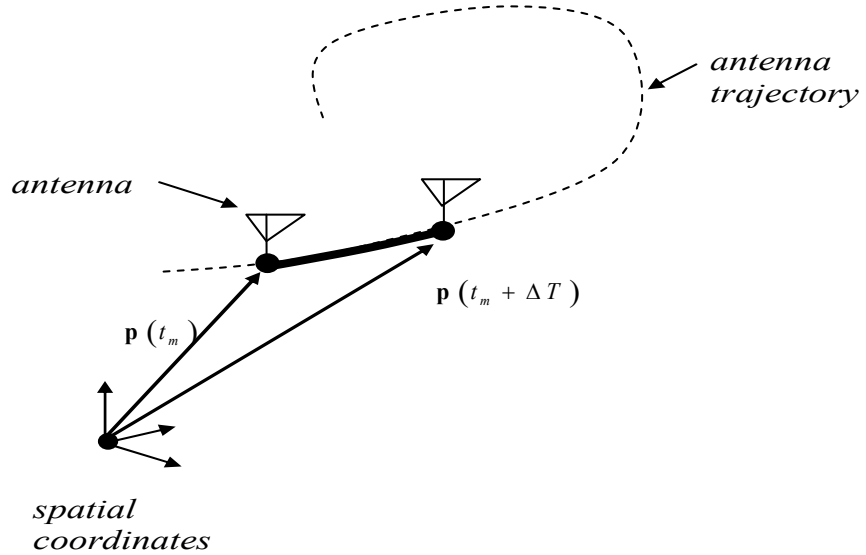


Figure 3-1: Diagram of moving antenna and positional vector definitions for snapshot collection for the m -th subinterval

Define t_m as the starting instance of the m -th subinterval that extends over the interval of $[t_m, t_m + \Delta T]$. Assume that $t_m > t_{m-1}$ and $t_m - t_{m-1} \geq \Delta T$ for $m \in 2, 3 \dots M$. The collection of signals over the m -th subinterval is shown in Figure 3-1. ΔT is considered to be sufficiently small such that $A(\mathbf{p}(t))$ can be approximated as a constant over the interval of ΔT such that

$$A(\mathbf{p}(t)) \approx A(\mathbf{p}(t_m)) \quad \text{for } t \in [t_m, t_m + \Delta T]. \quad 3-3$$

The signal captured in each subinterval is correlated with $s_0(t)^*$, resulting in a set of M spatial array samples denoted by x_m and given as

$$x_m = \int_{t_m}^{t_m + \Delta T} r(t) s_o(t)^* dt. \quad 3-4$$

x_m can also be expressed as

$$x_m = A(\mathbf{p}(t_m)) s_m + n_m \quad 3-5$$

where

$$\begin{aligned} s_m &= \int_{t_m}^{t_m + \Delta T} |s_o(t)|^2 dt \\ n_m &= \int_{t_m}^{t_m + \Delta T} n(t) s_o(t)^* dt \end{aligned} \quad 3-6$$

It follows that x_m forms a set of sufficient statistics of the accumulated snapshot signal in terms of optimal decoding between H_0 and H_1 . The vector forms of the signals are defined as $\mathbf{x} = [x_1 \dots x_M]^T$, $\mathbf{s} = [s_1 \dots s_M]^T$, $\mathbf{n} = [n_1 \dots n_M]^T$ and $\mathbf{A} = [A(\mathbf{p}(t_1)) \dots A(\mathbf{p}(t_M))]^T$.

Due to the Rayleigh fading assumption, the individual components of the vector \mathbf{A} are circularly normal such that $[A]_m = A(\mathbf{p}(t_m)) \sim CN(0, \sigma_A^2)$. With these definitions the detection problem is stated as

$$\begin{aligned} \mathbf{x} &= \mathbf{A} \odot \mathbf{s} + \mathbf{n} && \text{under } H_1 \\ \mathbf{x} &= \mathbf{n} && \text{under } H_0 \end{aligned} \quad 3-7$$

where \odot denotes the Hadamard vector product operator.

For convenience it will be assumed that

$$\int_{t_m}^{t_m + \Delta T} |s_o(t)|^2 dt \approx \Delta T. \quad 3-8$$

The validity of this approximation is based on ΔT being much longer than the reciprocal of the bandwidth of $s_o(t)$. For the CDMA signal this is easily justified as the chip rate is greater than 1 Mcps and ΔT will be on the order of milliseconds. Based on Eq. 3-8, the signal vector becomes

$$\mathbf{s} = \Delta T \mathbf{1}_M \quad 3-9$$

where $\mathbf{1}_M$ is a column vector of M 1's. With this, Eq. 3-7 is written as

$$\begin{aligned} \mathbf{x} &= \Delta T \mathbf{A} + \mathbf{n} && \text{under } H_1 \\ \mathbf{x} &= \mathbf{n} && \text{under } H_0. \end{aligned} \quad 3-10$$

The optimal detection processing scheme based on the Neyman-Pearson (NP) likelihood Ratio Test (LRT) is defined Section 2.8. The LRT chooses H_1 if

$$L(\mathbf{x}) = \frac{p(\mathbf{x} | H_1)}{p(\mathbf{x} | H_0)} > \gamma \quad 3-11$$

where $p(\mathbf{x} | H_1)$ and $p(\mathbf{x} | H_0)$ are the conditional PDFs of \mathbf{x} given H_1 and H_0 , respectively. If $p(\mathbf{x} | H_1)$ and $p(\mathbf{x} | H_0)$ are given, finding the optimal processing based on Eq. 3-11 is therefore trivial. If both $p(\mathbf{x} | H_1)$ and $p(\mathbf{x} | H_0)$ are multivariate Gaussian PDFs, then efficient linear or eigenvector based energy detection processing

results (Kay 1998). This is highly desirable as the implementation and the performance analysis can then take advantage of linear algebra constructs and formulations. When $p(\mathbf{x}|H_1)$ and $p(\mathbf{x}|H_0)$ are not multivariate Gaussian processes, then the processing implementation quickly becomes unwieldy and inefficient to implement. Hence, efforts are generally made to justify a Gaussian approximation to the conditional PDFs. For the synthetic array, it will be observed that $p(\mathbf{x}|H_0)$ can be construed as multivariate Gaussian. However, for $p(\mathbf{x}|H_1)$, typically only the marginal PDFs can be justified as being Gaussian. Approximating the joint components of \mathbf{x} as being Gaussian results in easily implementable detector processing but this is suboptimal, resulting in potential performance losses in some cases.

From Eq. 3-6, $n_m = \int_{t_m}^{t_m + \Delta T} n(t)s_o(t)^* dt$ which is a zero mean circular Gaussian random variable where $n(t)$ is independent of the signal. Essentially based on the spread spectrum nature of the despreading signal $s_o(t)$, it can be assumed that the various components of n_m are uncorrelated. Therefore, the noise covariance matrix, denoted as \mathbf{C}_n , is given as

$$\mathbf{C}_n = E[\mathbf{n}\mathbf{n}^H] = \frac{I}{M} \mathbf{I}_M \quad 3-12$$

where \mathbf{I}_M is the $M \times M$ identity matrix. The last step follows from $\int_{t_m}^{t_m + \Delta T} |s_o(t)|^2 dt \approx \Delta T$

and the normalization $\Delta T N_o = \frac{1}{M}$ where N_o is the PSD of $n(t)$ within the bandwidth of $s_o(t)$.

3.2 Characterization of the channel gain vector

In this section, the signal covariance matrix based on the synthetic array signal model presented in the previous section in different channel situations is described. The characterization of the channel gain vector \mathbf{A} is a function of the antenna trajectory and the multipath model. Meaningful results of the practical utilization of the synthetic array only emerge if different propagation scenarios are considered. In the following subsections, the following four different propagation scenarios and received signal models will be considered:

Case 1: Plane wave, known Angle Of Arrival (AOA) and known channel gain

Case 2: Plane wave, known AOA, and channel gain is circularly Gaussian

Case 3: Plane wave, unknown AOA and channel gain is circularly Gaussian

Case 4: Multiple plane wave, unknown AOA and channel gain is circularly Gaussian

3.2.1 Plane wave, known AOA and known channel gain

Here, it is assumed that the incident signal is a plane wave with a known unit magnitude direction vector denoted by \mathbf{a} (defined in Section 2.1) and the noise is coming from an isotropic source. Consequently, the signal component defined in Eq. 3-1 is shown by

$$\begin{aligned} s(t, \mathbf{p}(t)) &= A(\mathbf{p}(t)) s_o \left(t - \frac{\mathbf{a}^T \mathbf{p}(t)}{c} \right) \\ &\approx A(\mathbf{p}(t)) s_o(t) \\ &= A_o \exp(-jk_o \mathbf{a}^T \mathbf{p}(t)) s_o(t) \end{aligned} \quad 3-13$$

where the second step is a result of the narrowband assumption and $k_o = 2\pi/\kappa$.

Following the formulation introduced earlier,

$$A_m = A_o \exp(-jk_o \mathbf{a}^T \mathbf{p}_m(t)). \quad 3-14$$

Consequently, the channel gain vector \mathbf{A} becomes

$$\mathbf{A} = A_o \begin{bmatrix} \exp(-jk_o \mathbf{a}^T \mathbf{p}_1(t)) \\ \exp(-jk_o \mathbf{a}^T \mathbf{p}_2(t)) \\ \vdots \\ \exp(-jk_o \mathbf{a}^T \mathbf{p}_M(t)) \end{bmatrix}. \quad 3-15$$

x_m can be expressed as

$$x_m = A_m \Delta T + n_m. \quad 3-16$$

Note that $p(\mathbf{x} | H_0)$ and $p(\mathbf{x} | H_1)$ are both multivariate Gaussian, that is

$$\begin{aligned} \mathbf{x} | H_0 &\sim CN(\mathbf{0}_M, \mathbf{C}_n) = CN\left(\mathbf{0}_M, \frac{I}{M} \mathbf{I}_M\right) \\ \mathbf{x} | H_1 &\sim CN(\mathbf{A}, \mathbf{C}_n) = CN\left(\Delta T \mathbf{A}, \frac{I}{M} \mathbf{I}_M\right). \end{aligned} \quad 3-17$$

Hence, the LRT results in the matched filter defined in Section 2.8.1. This results in a standard beamformer at the direction of $-\mathbf{a}$. In this case, the motion of the antenna (spatial-temporal process) does not accomplish any gain relative to keeping the antenna stationary (temporal process). A signal space interpretation is that the additive noise is already uncorrelated based on the fact that the noise is sampled at different times. Hence, \mathbf{n} is already a white vector and moving the antenna cannot decorrelate it further as the signal is totally known. From a signal space perspective, it consists of space-time dimensions. A stationary antenna focuses the signal space in time but not spatially. A moving antenna focuses the signal space in terms of beamforming in the spatial dimensions. The resulting gain is the same. Note that if the noise was an interference source from a given direction, then moving the antenna would be more powerful than the stationary antenna as a null can be placed in the direction of the interference. In this case, the moving antenna allows the noise spatial correlation to be exploited to help segregate it from the deterministic signal.

3.2.2 Plane wave, known AOA and unknown channel gain

In this section, it is assumed that the incident signal is a plane wave with a known unit magnitude direction vector denoted by \mathbf{a} as before. However, the amplitude of the channel gain is random and unknown to the receiver. Consequently,

$$s_m = A_o \exp(-jk_o \mathbf{a}^T \mathbf{p}(t)) s_o(t) \quad 3-18$$

where

$$A_o \sim CN(0, \sigma_A^2). \quad 3-19$$

As defined previously, \mathbf{A} can be written as

$$\mathbf{A} = A_o \begin{bmatrix} \exp(-jk_o \mathbf{a}^T \mathbf{p}_1(t)) \\ \exp(-jk_o \mathbf{a}^T \mathbf{p}_2(t)) \\ \vdots \\ \exp(-jk_o \mathbf{a}^T \mathbf{p}_M(t)) \end{bmatrix} = A_o \mathbf{v}. \quad 3-20$$

Note that $p(\mathbf{x} | H_0)$ and $p(\mathbf{x} | H_I)$ are still multivariate Gaussian. However, without the deterministic mean, one obtains

$$\begin{aligned} \mathbf{x} | H_0 &\sim CN(\mathbf{0}_M, \mathbf{C}_n) = CN\left(\mathbf{0}_M, \frac{I}{M} \mathbf{I}_M\right) \\ \mathbf{x} | H_I &\sim CN(\mathbf{0}_M, \mathbf{C}_A + \mathbf{C}_n) = CN\left(\mathbf{0}_M, \sigma_A^2 (\Delta T)^2 \mathbf{v} \mathbf{v}^H + \frac{I}{M} \mathbf{I}_M\right). \end{aligned} \quad 3-21$$

The LRT temporally is no longer a matched filter. After some manipulations of the LRT and removing deterministic scaling and additive constants the LRT reduces to the EC formulation (Kay 1998), introduced earlier in Section 2.8.2, and resulting in a single sufficient statistic given as

$$z_{EC} = \mathbf{x}^H \mathbf{C}_s (\mathbf{C}_s + \mathbf{C}_n)^{-1} \mathbf{x}. \quad 3-22$$

In this case

$$\mathbf{C}_n = \frac{\mathbf{I}_M}{M}, \quad 3-23$$

and

$$\mathbf{C}_s = \sigma_A^2 (\Delta T)^2 \mathbf{v} \mathbf{v}^H. \quad 3-24$$

The test statistic by inserting Eq. 3-23 and Eq. 3-24 into Eq. 3-22 becomes

$$z_{EC} = \mathbf{x}^H \sigma_A^2 (\Delta T)^2 \mathbf{v} \mathbf{v}^H \left(\sigma_A^2 (\Delta T)^2 \mathbf{v} \mathbf{v}^H + N_o \Delta T \mathbf{I}_M \right)^{-1} \mathbf{x}. \quad 3-25$$

To simplify z_{EC} , $\mathbf{v} \mathbf{v}^H$ can be written by

$$\mathbf{v} \mathbf{v}^H = \mathbf{Q} \begin{bmatrix} M & & & \\ & 0 & & \\ & & \ddots & \\ & & & 0 \end{bmatrix} \mathbf{Q}^H = \mathbf{Q} \Lambda \mathbf{Q}^H \quad 3-26$$

where \mathbf{Q} is an eigenvector matrix and the first column is $\frac{\mathbf{I}}{\sqrt{M}}\mathbf{1}_M$. Then

$$z_{EC} = \mathbf{x}^H \sigma_A^2 (\Delta T)^2 \mathbf{Q} \Lambda \mathbf{Q}^H \left(\sigma_A^2 (\Delta T)^2 \mathbf{Q} \Lambda \mathbf{Q}^H + N_o \Delta T \mathbf{Q} \mathbf{Q}^H \right)^{-1} \mathbf{x} \quad 3-27$$

and

$$\begin{aligned} z_{EC} &= \mathbf{x}^H \mathbf{Q} \left(\sigma_A^2 (\Delta T)^2 \Lambda \right) \left(\sigma_A^2 (\Delta T)^2 \Lambda + N_o \Delta T \right)^{-1} \mathbf{Q}^H \mathbf{x} \\ &= \left(\mathbf{x}^H \frac{\mathbf{1}_M}{\sqrt{M}} \right) \left(\sigma_A^2 (\Delta T)^2 M \right) \left(\sigma_A^2 (\Delta T)^2 M + N_o \Delta T \right)^{-1} \left(\frac{\mathbf{1}_M^H}{\sqrt{M}} \mathbf{x} \right). \\ &= \left| \sum_{m=1}^M x_m \right|^2 \frac{\sigma_A^2 (\Delta T)^2}{\sigma_A^2 (\Delta T)^2 M + N_o \Delta T} \end{aligned} \quad 3-28$$

Ignoring the deterministic constant the test statistics becomes

$$z_{EC} = \left| \sum_{m=1}^M x_m \right|^2. \quad 3-29$$

The identical result is achievable by using Woodbury's identity (Kay 1998). Note that the EC in this case is the same as the matched filter magnitude squared. Again there is no advantage of moving the antenna if the noise vector \mathbf{n} is white and the signal is spatially correlated.

3.2.3 Single plane wave, unknown AOA and channel gain is circularly Gaussian

In this case it is assumed that the plane wave has an unknown channel gain coefficient and a completely unknown AOA. For the sake of simplicity in this subsection, a two-dimensional model is considered hence the direction vector \mathbf{a} becomes

$$\mathbf{a} = \begin{bmatrix} -\cos(\phi) \\ -\sin(\phi) \\ 0 \end{bmatrix} \quad 3-30$$

where ϕ is random being uniformly distributed over all azimuth such that

$$\phi \sim \frac{1}{2\pi} \quad 0 \leq \phi \leq 2\pi. \quad 3-31$$

It is interesting to note that the signal has three degrees of freedoms (DOF), namely two DOFs for the circular normal amplitude A_o and one DOF for the unknown ϕ . Now assuming that the trajectory is known, there can only be three DOFs associated with s_m . Clearly s_m is not jointly Gaussian but consider determining the covariance matrix \mathbf{C}_s .

Now consider $[\mathbf{C}_s]_{m,n}$ and define

$$\Delta \mathbf{p} = \mathbf{p}(t_m) - \mathbf{p}(t_n). \quad 3-32$$

Without loss of generality it is assumed that $\mathbf{p}(t_n) = \mathbf{0}$. Then,

$$[\mathbf{C}_s]_{m,n} = E \left[(A_o) (A_o^* \exp(-jk_o |\Delta\mathbf{p}| \cos(\phi))) \right]. \quad 3-33$$

Due to symmetry, Eq. 3-33 can be written as

$$[\mathbf{C}_s]_{m,n} = E \left[(A_o) (A_o^* \exp(-jk_o |\Delta\mathbf{p}| \cos(\phi))) \right]. \quad 3-34$$

Expanding the expectation one can write

$$\begin{aligned} [\mathbf{C}_s]_{m,n} &= E_\phi \left[E_{A_o|\phi} \left[(A_o) (A_o^* \exp(-jk_o |\Delta\mathbf{p}| \cos(\phi))) \right] \right] \\ &= E_\phi \left[\sigma_A^2 \exp(-jk_o |\Delta\mathbf{p}| \cos(\phi)) \right] \\ &= \sigma_A^2 \int_0^{2\pi} f_\phi(\phi) \exp(-jk_o |\Delta\mathbf{p}| \cos(\phi)) d\phi \\ &= \frac{\sigma_A^2}{2\pi} \int_0^{2\pi} \exp(-jk_o |\Delta\mathbf{p}| \cos(\phi)) d\phi \\ &= \sigma_A^2 J_o(k_o |\Delta\mathbf{p}|) \end{aligned} \quad 3-35$$

where J_0 is a zero-order Bessel function of the first kind. Suppose that the fact \mathbf{s} is not multivariate Gaussian is ignored. Then a detection scheme could be formulated based on the EC. However, for a given arbitrary AOA of a plane wave, \mathbf{C}_s is a full rank matrix implying $2M$ DOFs. The difference between the $2M$ DOF and the actual three DOFs is the information loss that makes the EC suboptimal in this case. A GLRT approach (Kay 1998) can be utilized to improve the detection performance since it tries to estimate the unknown AOA based on a Maximum Likelihood (ML) approach.

Suppose that the SNR is high such that $\sigma_A^2/\sigma_n^2 \gg 1$, then nonlinear estimation techniques such as MUSIC and ESPRIT can be utilized to estimate the unknown AOA

associated with the plane wave incident on the array. Based on this, beamforming can be performed in the direction of $-\mathbf{a}$ corresponding to the actual plane wave. The detection performance can be almost as good as the case of \mathbf{a} being known to the receiver.

The signal model explained in this section is a practical model of a channel in rural and suburban environments where the LOS component is available, the channel gain is modeled by a circular normal process and the direction of incidence is typically unknown. As it was explained, the EC process in this case suffers from the unknown AOA. The GLRT approach can alleviate this problem since it first tries to estimate the unknown AOA. The problem of AOA estimation based on the synthetic array will be discussed in Chapter 6.

3.2.4 Multiple plane wave, unknown AOA and channel gain is circularly Gaussian

In this case, it is assumed that the multipath consists of several plane waves, each with unknown channel gain coefficient and azimuth angle. This is the typical model of indoor and dense multipath environments. The channel characteristics and the signal covariance matrix for the synthetic array will be used in Chapter 4 to implement the EC formulation. Clearly as the number of independent plane waves increase, so does the joint Gaussianity of the signal vector. Now consider the case of diffuse multipath where there is a continuum of infinitesimal scattering reflection sources. From before, if the single plane wave at the known angle with CN random amplitude is propagated, then \mathbf{s} is jointly Gaussian. If the angle is random then \mathbf{s} is not jointly Gaussian. It follows that if

there is a multipath source with a given PDF, then the PDF of \mathbf{s} is not jointly Gaussian. However, if there is a continuous distribution of a large number of sources as in diffuse multipath, then \mathbf{s} approaches a jointly Gaussian distribution. This is an important distinction. Therefore, diffuse multipath from a finite angular sector that has a known PDF will lead to a jointly Gaussian signal. If there are finite possible angles of arrival and a random source at each angle with a CN amplitude PDF then \mathbf{s} is Gaussian. Hence, the EC formulation given in Eq. 3-22 becomes an optimal processing scheme.

Consider a model of diffuse multipath scatterers that comes from an equivalent sphere in the far field of the antenna array. Consider a differential patch of reflection, denoted by $ds_o(t, \theta, \phi)$ that is received by an antenna element of position vector \mathbf{p} such that

$$ds(t, \mathbf{p}) = ds_o(t, \theta, \phi) \exp(-jk_o \mathbf{a}^T(\theta, \phi) \mathbf{p}) \quad 3-36$$

where ϕ is the azimuth angle, θ is the polar angle and \mathbf{a} is the unit vector in the direction of the source patch to the center of the array. Note that, in this formulation, it has been assumed that the reflectors are in the far field of the array such that the component emanating from the signal patch is essentially a plane wave component when it arrives at the antenna array. A narrowband case is also assumed such that there is a single propagation constant k_o corresponding to the carrier frequency. The total received signal at the receiver element corresponding to position \mathbf{p} is then

$$s(t, \mathbf{p}) = \int_0^\pi d\theta \int_0^{2\pi} d\phi \frac{\sin(\theta)}{4\pi} ds_o(t, \theta, \phi) \exp(-jk_o \mathbf{a}^T(\theta, \phi) \mathbf{p}). \quad 3-37$$

The factor $\frac{4\pi}{\sin(\theta)}$ is introduced due to the use of spherical coordinates (Van Trees 2002).

Next consider the correlation of two antenna outputs due to spatially white distributed sources with corresponding position vectors \mathbf{p}_1 and \mathbf{p}_2 such that $\Delta\mathbf{p} = \mathbf{p}_2 - \mathbf{p}_1$:

$$\begin{aligned} C(\Delta\mathbf{p}) &= E[s(t, \mathbf{p}_1)s^*(t, \mathbf{p}_2)] \\ &= E\left[\left(\int_0^\pi d\theta_1 \int_0^{2\pi} d\phi_1 \frac{\sin(\theta_1)}{4\pi} ds_o(t, \theta_1, \phi_1) \exp(-jk_o \mathbf{a}^T(\theta_1, \phi_1) \mathbf{p}_1)\right) \cdot \right. \\ &\quad \left. \cdot \left(\int_0^\pi d\theta_2 \int_0^{2\pi} d\phi_2 \frac{\sin(\theta_2)}{4\pi} ds_o(t, \theta_2, \phi_2) \exp(jk_o \mathbf{a}^T(\theta_2, \phi_2) \mathbf{p}_2)\right)\right] \\ &= \int_0^\pi d\theta_1 \int_0^{2\pi} d\phi_1 \frac{\sin(\theta_1)}{4\pi} \exp(-jk_o \mathbf{a}^T(\theta_1, \phi_1) \mathbf{p}_1) \cdot \\ &\quad \int_0^\pi d\theta_2 \int_0^{2\pi} d\phi_2 \frac{\sin(\theta_2)}{4\pi} \exp(jk_o \mathbf{a}^T(\theta_2, \phi_2) \mathbf{p}_2). \\ &E[ds_o(t, \theta_1, \phi_1) ds_o^*(t, \theta_2, \phi_2)] \end{aligned} \quad 3-38$$

If the signals coming from different directions are uncorrelated,

$$E[ds_o(t, \theta_1, \phi_1) ds_o^*(t, \theta_2, \phi_2)] = \frac{4\pi\sigma_A^2}{\sin(\theta)} \delta(\theta_2 - \theta_1) \delta(\phi_2 - \phi_1). \quad 3-39$$

Hence,

$$\begin{aligned}
C(\Delta \mathbf{p}) &= \int_0^\pi d\theta_1 \int_0^{2\pi} d\phi_1 \frac{\sin(\theta_1)}{4\pi} \exp(-jk_o \mathbf{a}^T(\theta_1, \phi_1) \mathbf{p}_1) \\
&\quad \int_0^\pi d\theta_2 \int_0^{2\pi} d\phi_2 \frac{\sin(\theta_2)}{4\pi} \exp(jk_o \mathbf{a}^T(\theta_2, \phi_2) \mathbf{p}_2) \\
&\quad \frac{4\pi\sigma_A^2}{\sin(\theta)} \delta(\theta_2 - \theta_1) \delta(\phi_2 - \phi_1) \\
&= \frac{\sigma_A^2}{4\pi} \int_0^\pi d\theta_1 \int_0^{2\pi} d\phi_1 \sin(\theta_1) \exp(-jk_o \mathbf{a}^T(\theta_1, \phi_1) \Delta \mathbf{p})
\end{aligned} \tag{3-40}$$

Due to the symmetry of the problem, it can be arbitrarily assumed that $\Delta \mathbf{p}$ is along the z axis such that

$$\mathbf{a}^T(\theta, \phi) \Delta \mathbf{p} = |\Delta \mathbf{p}| \cos(\theta). \tag{3-41}$$

Then,

$$\begin{aligned}
C(\Delta \mathbf{p}) &= \frac{\sigma_s^2}{4\pi} \int_0^\pi d\theta \int_0^{2\pi} d\phi \sin(\theta) \exp(-jk_o |\Delta \mathbf{p}| \cos(\theta)) \\
&= \frac{\sigma_A^2}{2} \int_0^\pi \sin(\theta) \exp(-jk_o |\Delta \mathbf{p}| \cos(\theta)) d\theta \\
&= \sigma_A^2 \int_{-1}^1 \frac{1}{2} e^{-jk_o |\Delta \mathbf{p}| q} dq \\
&= \sigma_A^2 \frac{\sin(k_o |\Delta \mathbf{p}|)}{k_o |\Delta \mathbf{p}|}
\end{aligned} \tag{3-42}$$

Note the signals decorrelate with $|\Delta \mathbf{p}|$ on the order of half a wavelength of the carrier wavelength.

3.2.4.1 Ring of scatterers in the azimuth plane

Next consider a ring of scatterers in the azimuth plane and that the array is also in the $\theta = \pi/2$ plane. From earlier, one has

$$\begin{aligned} C(\Delta\mathbf{p}) &= \\ &\int_0^{\pi} d\theta_1 \int_0^{2\pi} d\phi_1 \frac{\sin(\theta_1)}{4\pi} \exp(-jk_o \mathbf{a}^T(\theta_1, \phi_1) \mathbf{p}_1) \\ &\int_0^{\pi} d\theta_2 \int_0^{2\pi} d\phi_2 \frac{\sin(\theta_2)}{4\pi} \exp(jk_o \mathbf{a}^T(\theta_2, \phi_2) \mathbf{p}_2) E[ds_o(t, \theta_1, \phi_1) ds_o^*(t, \theta_2, \phi_2)] \end{aligned} . \quad 3-43$$

However,

$$E[ds_o(t, \theta_1, \phi_1) ds_o^*(t, \theta_2, \phi_2)] = \frac{4\pi\sigma_A^2}{\sin(\theta)} \delta\left(\theta_2 - \frac{\pi}{2}\right) \delta\left(\theta_1 - \frac{\pi}{2}\right) \delta(\phi_2 - \phi_1). \quad 3-44$$

Due to the symmetry in scatterer geometry, there is no loss in assuming that

$$\Delta\mathbf{p} = |\Delta\mathbf{p}| \begin{bmatrix} 1 \\ 0 \\ 0 \end{bmatrix}, \text{ such that}$$

$$\begin{aligned} C(\Delta\mathbf{p}) &= \frac{\sigma_A^2}{2\pi} \int_0^{2\pi} \exp(-jk_o |\Delta\mathbf{p}| \cos(\phi_1)) d\phi_1 \\ &= \sigma_A^2 J_o(k_o |\Delta\mathbf{p}|) \end{aligned} . \quad 3-45$$

3.2.4.2 Angular sector of scatterers in the azimuth plane from known relative offset

Next consider an angular sector of scatterers in the azimuth plane, with the array also in the $\theta = \pi/2$ plane. There is no loss in generality by assuming that

$$\mathbf{p}_1 = \begin{bmatrix} 0 \\ 0 \\ 0 \end{bmatrix} \text{ and } \mathbf{p}_2 = \begin{bmatrix} |\Delta\mathbf{p}| \\ 0 \\ 0 \end{bmatrix}. \quad 3-46$$

Hence, based on the above formulation,

$$C(\Delta\mathbf{p}) = \frac{1}{4\pi} \int_0^{2\pi} d\phi_1 \int_0^{2\pi} d\phi_2 \exp(jk_o |\Delta\mathbf{p}| \cos(\phi_2)) E[ds_o(t, \phi_1) ds_o^*(t, \phi_2)]. \quad 3-47$$

However,

$$E[ds_o(t, \phi_1) ds_o^*(t, \phi_2)] = \sigma_A^2(\phi_1) \delta(\phi_2 - \phi_1) \quad 3-48$$

where $\sigma_A^2(\phi_1)$ is the spatial power density of the sectored multipath scattering which is assumed to be spatially white with respect to the angle. Substituting Eq. 3-48 into Eq. 3-47 yields

$$\begin{aligned} C(\Delta\mathbf{p}) &= \frac{1}{4\pi} \int_0^{2\pi} d\phi_1 \int_0^{2\pi} d\phi_2 \exp(jk_o |\Delta\mathbf{p}| \cos(\phi_2)) \sigma_A^2(\phi_1) \delta(\phi_2 - \phi_1) \\ &= \int_0^{2\pi} \exp(jk_o |\Delta\mathbf{p}| \cos(\phi_2)) \sigma_A^2(\phi_2) d\phi_2. \end{aligned} \quad 3-49$$

It is interesting to let the angular sector become very small. Consider a linear array such that ϕ_o is the angle between the linear array and the narrow sector of multipath. Then,

$$C(\Delta \mathbf{p}) \approx \sigma_f^2 \exp(jk_o |\Delta \mathbf{p}| \cos(\phi_o)). \quad 3-50$$

If the sector is sufficiently narrow then the rank of the covariance matrix will be one resulting in a beamformer. This situation becomes identical to the case of Section 3.2.2, a signal with known plane wave direction and complex normal amplitude.

3.3 Performance of EC in different multipath scenarios

As it was shown in previous sections, in indoor and dense multipath environments the test statistic reduces to the EC formulation. In this section, the performance of EC based on the EC beampattern concept and beamforming capability will be given. The array consists of a linear uniformly spaced array of M elements with inter-element spacing of d as normalized by the carrier wavelength. The array is along the axis corresponding to the polar angle $\theta = \pi/2$. The multipath is assumed to be distributed in azimuth with a angular spread denoted as φ_s and an offset of φ . In addition additive white Gaussian noise is assumed which is normalized such that the weighting of the estimator correlator eigenvector projections is $\frac{\lambda_s}{(\lambda_s + \sigma_n^2)}$ where λ_s denotes the eigenvalue of the signal covariance matrix and σ_n^2 is the variance of the additive noise.

In previous sections, different channel propagation models along with the covariance matrices were discussed. The radiation pattern, introduced in Chapter 2, can be considered as the array performance against an isotropic noise. In the known AOA of a plane wave, the principal eigenvector can be considered as a beamformer weight, where the principal eigenvector is the eigenvector corresponding to the largest eigenvalue (Van Trees 2002). However, in a dense multipath environment where scatterers are modeled by a ring, the covariance matrix becomes full rank and conventional beamforming based on the principal eigenvector becomes suboptimal. The problem of interest here is comparing the detection performance of EC with conventional beamforming techniques for different multipath scenarios as explained earlier.

In the following examples two superimposed plots for the radiation pattern are given. One is due to the principal eigenvector corresponding to the largest eigenvalue. This is given as

$$R_p(\varphi) = |\mathbf{v}^H \mathbf{q}_p|^2 \frac{\lambda_{s,p}}{\lambda_{s,p} + \sigma_n^2} \quad 3-51$$

where the subscript p denotes the principal eigenvector and \mathbf{v} is the steering vector given as

$$\mathbf{v} = \begin{bmatrix} 1 & e^{j2\pi d \cos(\varphi)} & \dots & e^{j2\pi(M-1)d \cos(\varphi)} \end{bmatrix}^T. \quad 3-52$$

The other radiation pattern is the EC pattern given as

$$R_{EC}(\varphi) = \sum_{m=1}^M |\mathbf{v}^H \mathbf{q}_m|^2 \frac{\lambda_{s,m}}{\lambda_{s,m} + \sigma_n^2}. \quad 3-53$$

The radiation plots are also normalized such that the maximum response is 1, which makes the comparison of the plots easier. The principal eigenvector radiation pattern in Eq. 3-51 only considers the principal eigenvalue and eigenvector, whereas the EC radiation pattern in Eq. 3-53 takes advantage of all available eigenvectors and eigenvalues. For the case of the known AOA of a plane wave propagation represented in Section 3.2.2, the rank of the signal covariance matrix becomes one, therefore the radiation patterns of the principal eigenvector and EC become identical. If the AOA of a plane wave is unknown, the case of Section 3.2.3, or the moving antenna receives signals in a dense multipath environment, the case of section 3.2.4, the signal covariance matrix becomes full rank and the radiation pattern of the principal eigenvector and EC are not identical anymore. In the following the principal eigenvector and EC radiation patterns will be compared for different propagation scenarios discussed earlier.

The first example is with $d = 0.5$, $M = 10$, $\varphi_s = 2$ degrees, $\varphi = 45$ degrees and $\sigma_n^2 = 1$. This is an example of plane wave propagation with CN amplitude represented in Section 3.2.2. The eigenvalues are plotted in Figure 3-2. Note that there is just one dominant eigenvalue.

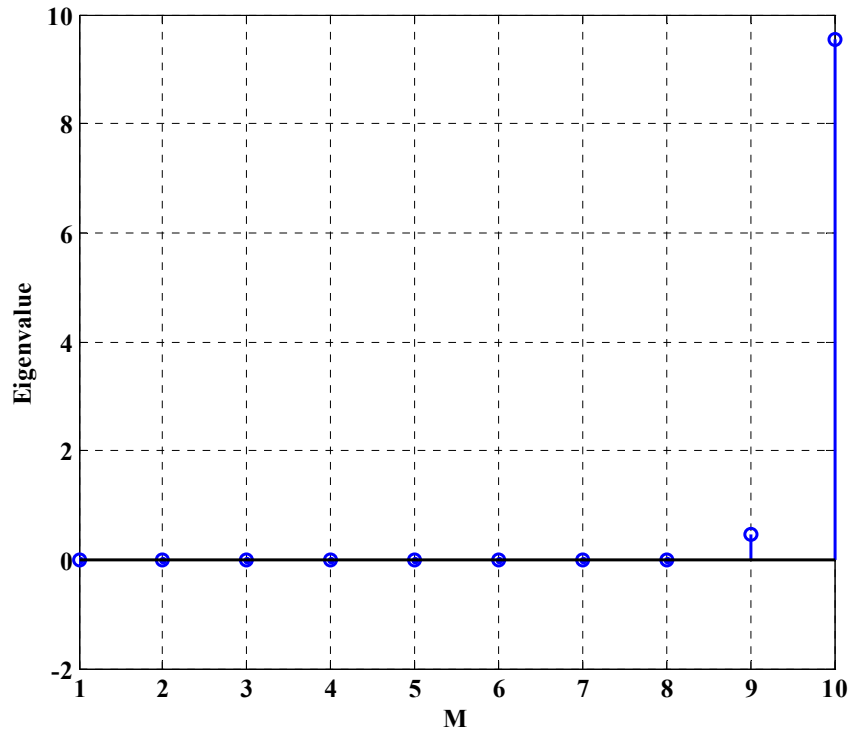


Figure 3-2: Eigenvalues for $d = 0.5$, $M = 10$, $\varphi_s = 2$ degrees, $\varphi = 45$ degrees and $\sigma_n^2 = 1$.

The compass plot of the principal eigenvector is shown in Figure 3-3. Note that the eigenvector is reasonable in that all of the values have a magnitude of 1 and essentially the phasing beamforms in the direction of the multipath source radiation.

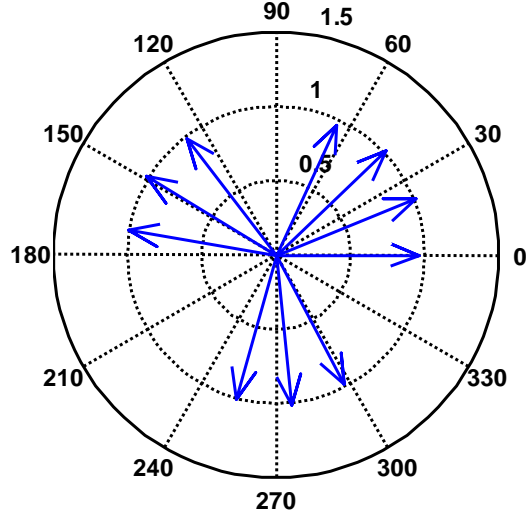


Figure 3-3 Compass plot of principal eigenvector for $d = 0.5$, $M = 10$, $\varphi_s = 2$ degree, $\varphi = 45$ degree and $\sigma_n^2 = 1$

Figure 3-4 shows the two superimposed radiation patterns, $R_{EC}(\varphi)$ and $R_p(\varphi)$. Note that now both $R_{EC}(\varphi)$ and $R_p(\varphi)$ beamform in the directions of 45 and -45 degrees. The reason for the split is that the linear array cannot discriminate between 45 and -45 degrees. That is the radiation pattern will always be symmetric about the line $\varphi = 0$. Note that, despite the value of σ_n^2 , the principal and EC radiation patterns are virtually the same. The reason for this is that the multipath spread is so small and the centroid angle of the PDF is known that only the principal eigenvalue has any value. The other eigenvalues are negligibly small. Note also that the EC or principal eigenvector beamforms in the direction of the desired signal. Next consider a situation where $\sigma_n^2 = 0.1$, implying an increased SNR. The emerging radiation patterns are shown in Figure 3-5.

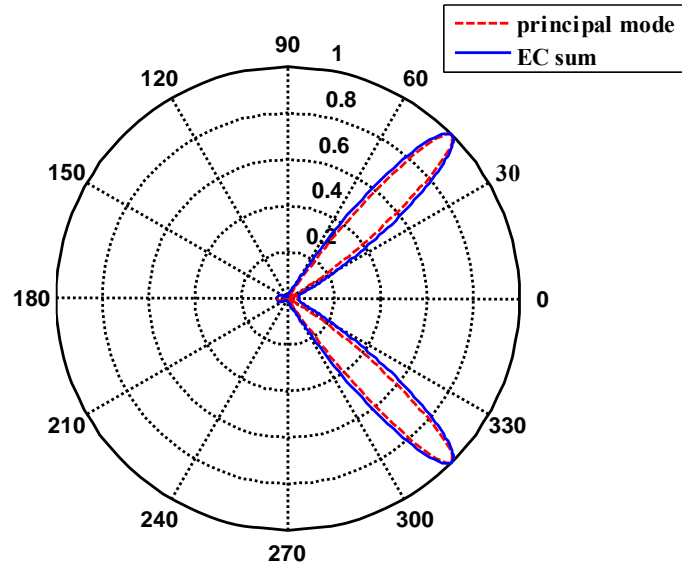


Figure 3-4: Radiation pattern for $\varphi_s = 2$ degree, $\varphi = 45$ degree and $\sigma_n^2 = 1$

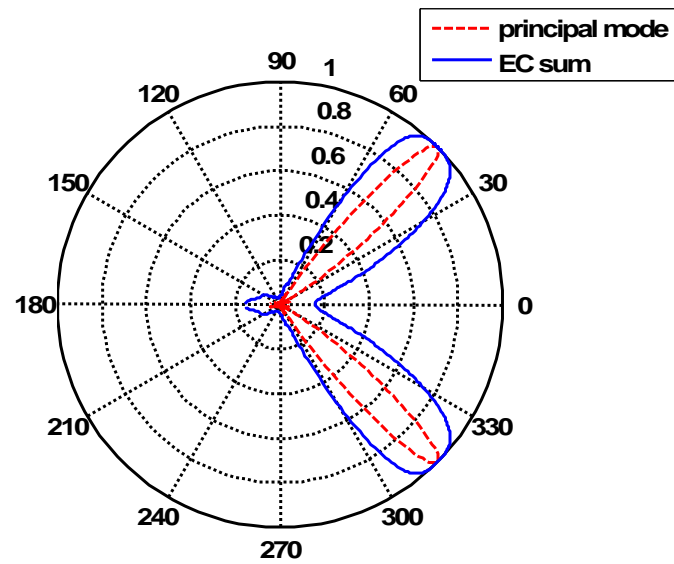


Figure 3-5: Radiation pattern for $\varphi_s = 2$ degree, $\varphi = 45$ degree and $\sigma_n^2 = 0.1$

Note that now both $R_{EC}(\varphi)$ and $R_p(\varphi)$ beamform in the direction of 45 and -45 degrees. Note also that the principal mode is a more focussed beam than the EC. The reason for this is that the noise is negligibly small and that the second largest eigenvalue, while being small relative to the principal eigenvalue, is still moderate relative to σ_n^2 such that the weighting coefficient $\frac{\lambda_{s,m}}{\lambda_{s,m} + \sigma_n^2}$ is non-negligible.

Next consider adding angular extent to the multipath radiation. For this example, $\varphi_s = 10^\circ$, $\varphi = 45^\circ$ degrees, $\sigma_n^2 = 1$. Figure 3-6 shows the eigenvalues of the signal covariance matrix. The principal eigenvector is shown in Figure 3-7 and the radiation pattern in Figure 3-8. Note that the principal eigenvector is no longer confined to the unit circle and hence it is not just purely beamforming in the direction of 45 degrees. The radiation pattern shows the EC pattern broadened with respect to the principal eigenmode pattern. However, each still beamforms in the direction of +45 and -45 degrees. If the noise is reduced further such that $\sigma_n^2 = 0.1$, then the plot in Figure 3-9 results. Note that the EC pattern is even broader as more eigenmodes contribute.

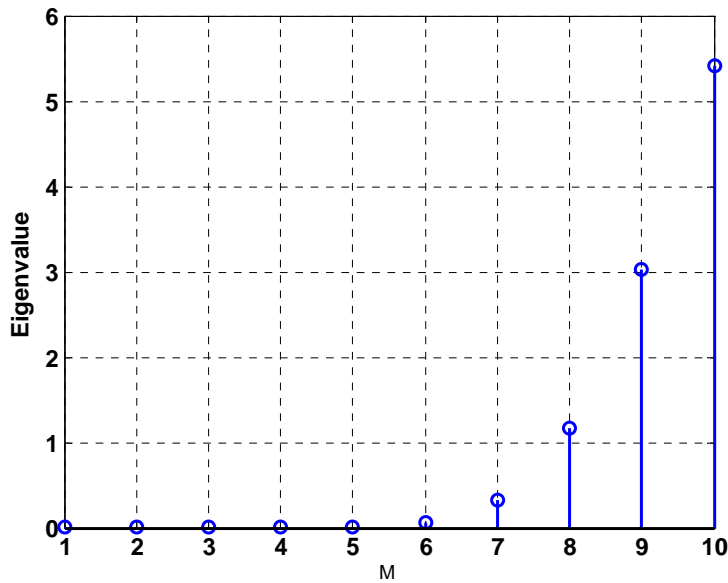


Figure 3-6: Eigenvalues of signal covariance matrix $\varphi_s = 10$ degree, $\varphi = 45$ degree and $\sigma_n^2 = 1$

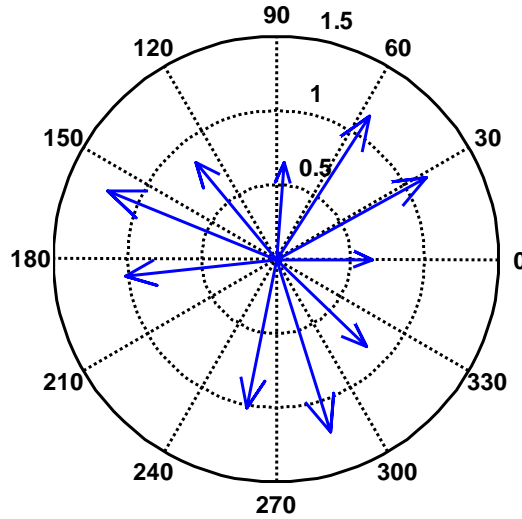


Figure 3-7: Principal eigenvector for $\varphi_s = 10$ degree, $\varphi = 45$ degree and $\sigma_n^2 = 1$

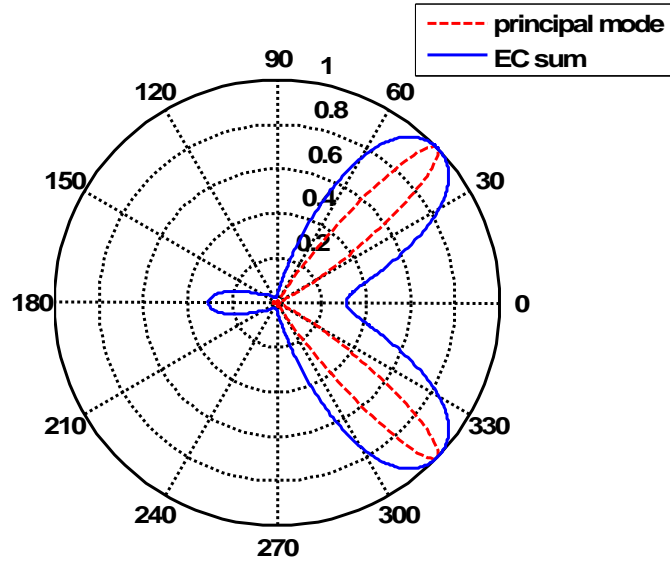


Figure 3-8: Radiation pattern for $\varphi_s = 10$ degree, $\varphi = 45$ degree and $\sigma_n^2 = 1$

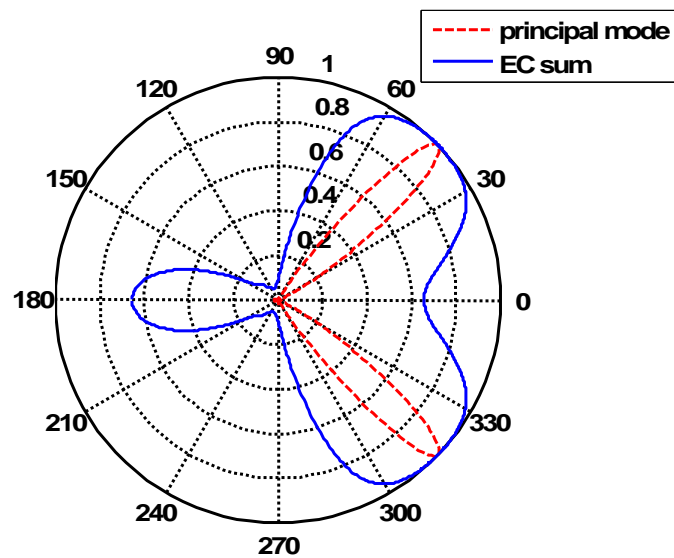


Figure 3-9: Radiation pattern for $\varphi_s = 10$ degrees, $\varphi = 45$ degrees and $\sigma_n^2 = 0.1$

As an additional example, consider the case when the angle spread is increased to $\varphi_s = 50$ degrees and the σ_n^2 is decreased further to 0.01. Then the pattern shown in Figure 3-10 emerges. Note that the EC radiation pattern is almost isotropic in azimuth. This occurs despite the fact that multipath only has an angle spread of 50 degrees. If the noise is increased substantially, in this case to $\sigma_n^2 = 10$, then the pattern in Figure 3-11 emerges. Note that the $R_{EC}(\varphi)$ pattern is converging towards the principal eigenmode pattern of $R_p(\varphi)$.

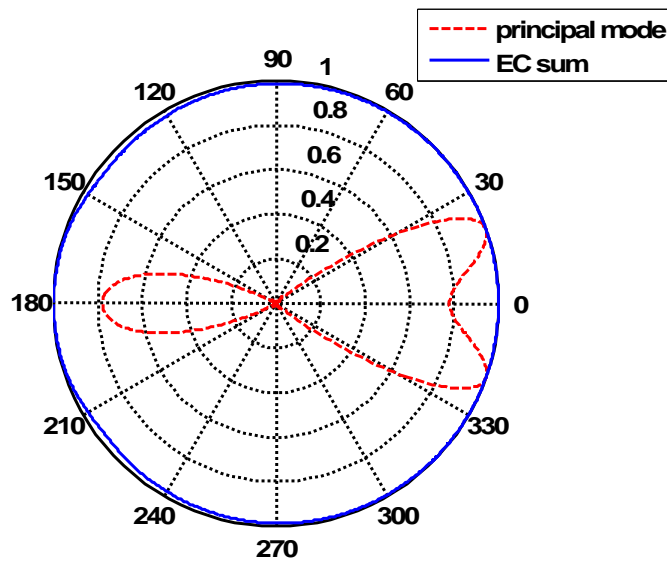


Figure 3-10: Radiation pattern $\varphi_s = 50$ degrees, $\varphi = 45$ degrees and $\sigma_n^2 = 0.01$

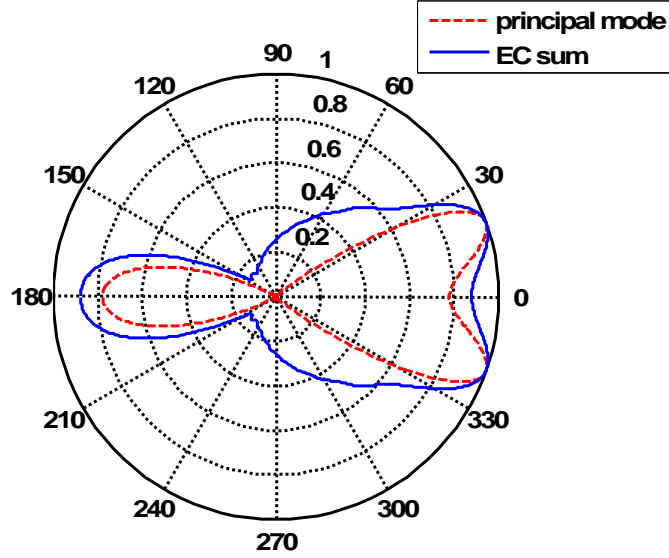


Figure 3-11: Radiation pattern $\varphi_s = 50$ degrees, $\varphi = 45$ degrees and $\sigma_n^2 = 10$

In conclusion then, for low SNR and small angular spread of multipath, the EC is essentially a beamformer in the direction of the multipath radiation. As the angular spread increases, the beamwidth of the EC becomes broader especially if the SNR increases. If the SNR decreases, then the EC beamwidth decreases and the pattern converges to that of the principal eigenmode. An important caveat is that the PDF of the multipath radiation is assumed to be known implying that the centroid angle of the radiation relative to the array is known by the receiver. As discussed earlier, the case of the multipath angular cluster of an unknown centroid angle does not reduce to a Gaussian PDF and hence performance degradation will occur.

CHAPTER 4: SIGNAL DETECTION PERFORMANCE IN RAYLEIGH FADING ENVIRONMENTS WITH A SYNTHETIC ANTENNA ARRAY

In the previous chapter, the synthetic array system model and detection scheme in different wireless propagation channels was described in detail. In this chapter, the detection performance of a moving receiver based on the Synthetic Array (SA) concept is compared to that of the equivalent receiver with a stationary antenna. In Chapter 2 and Chapter 3 it was shown that when a receiver is located in a diffuse multipath scattering environment such as indoors, fading appears to be a random function of the antenna location that spatially decorrelate in intervals of less than the carrier wavelength of the signal (Parsons 2000). The performance of beamforming techniques was also evaluated in Section 2.6. It was shown that in fading environments where wireless channels spatially decorrelates on the order of a carrier wavelength, the array gain decreases. Hence, in this chapter the diversity gain as a quantifiable metric is utilized to compare the detection performance of the static antenna with that of the synthetic array in fading environments. To simplify the analysis in order to obtain useful closed form expressions some assumptions regarding multipath fading are necessary. It will be assumed that the multipath is consistent with the Rayleigh fading model such that the channel gain becomes a circular Gaussian random process relative to the spatial dimensions. It is further assumed that the channel gain is static for the duration of the signal sampling which will be denoted here as the signal snapshot period. Based on these assumptions, if

the antenna is held at a fixed position during the snapshot interval, then the signal is not subject to decorrelation as channel gain remains constant. However, the signal will be subject to fading losses that are statistically large in a Rayleigh fading environment. Conversely, if the antenna is translated along some arbitrary trajectory during the snapshot interval then the coherency of the signal will be decreased as the channel gain will change randomly but the snapshot data will contain spatial diversity that can effectively counter the spatial fading effects. Based on this fact, it will be demonstrated that the trade-off between increased diversity gain and loss of signal coherency results in an optimum processing gain and number of spatial samples.

The design of the detection algorithm is based on target values of the probability of detection (P_D) and the probability of false alarm (P_{FA}) for the static and moving antennas. Assuming that the statistics of the signal and noise components are known, then the target detection performance requirements of $\{P_{FA}, P_D\}$ map into a specific required average signal-to-noise ratio denoted by ρ . A precise definition for ρ will be given in Section 4.1. Regardless of further algorithm details, the goal is to optimize the moving antenna processing such that the required ρ is minimized. In this chapter, the net processing gain for the moving antenna will be analyzed resulting in an optimum number of spatial samples. The resulting value of ρ , determined for the spatially translated antenna will be compared to the corresponding required value of ρ for the static antenna. The difference gives a quantitative indication of the performance advantage realized by moving the antenna during the signal snapshot.

Two operating scenarios are considered for the synthetic array. In the first mode it is assumed that the antenna is almost static in each subinterval of data collection and there are some time gaps between different spatial samples. This mode is defined as a discrete synthetic array (Broumandan et al 2009e, 2009f). In the second mode, the receiver continuously collects data while the antenna is moving and sequentially combines received signals based on a specific process. This mode is defined as continuous synthetic array in this chapter (Broumandan et al 2009d).

This chapter is organized as follows. In Section 4.1, a description of the single antenna receiver system is given along with the optimum processing for the static antenna. In Section 4.2 the synthetic array system model and signal statistics in discrete mode are discussed. Section 4.3 describes the synthetic array signal model in continuous mode. In Section 4.4, a detection procedure based on the Estimator-Correlator (EC) and Equal-Gain (EG) combiner is demonstrated. The processing gain advantage of the moving antenna is thereby quantified in uncorrelated environments. From this, the optimum number of spatial samples is evaluated. Section 4.6 and Section 4.7 provide the synthetic array performance and processing gain in Rayleigh fading channels for discrete and continuous modes respectively. Section 4.8 describes related practical implementation issues. Finally, conclusions are presented in Section 4.9.

4.1 System model and detection performance of the static antenna

Part of the initial acquisition of the received signal is a multi-hypothesis search typically performed over a pre-defined search window of unknown parameters (Caini et

al 2004a, 2004b). The design of the acquisition algorithm is generally based on target values of the P_D and the P_{FA} associated with each search hypothesis. If the locally generated signal matches that of the incoming signal, then the hypothesis being tested corresponds to a H_1 state where the signal is present and P_D can be evaluated. Likewise, if the parameters selected for the locally generated signal are mismatched with respect to those of the incoming signal, then the hypothesis being tested corresponds to a H_0 state where there is no signal present from which P_{FA} can be evaluated. To avoid complexities that obscure the essence of the comparison between the static and moving antennas, the multi-hypothesis process is idealized such that for the evaluation of P_D , the locally generated signal is assumed to be perfectly synchronized with the incoming signal. Wireless communication and GNSS signals typically consist of some known structure with unknown parameters used for signal acquisition and synchronization (e.g. GSM, IS-95, IS-136 and CDMA 2000). For instance the Global Positioning System (GPS) Coarse/Acquisition (C/A) code has essentially a deterministic structure except for unknown delay and Doppler frequency parameters and additional low rate unknown data bits. In this chapter, the desire was to focus specifically on the performance difference between a moving and a stationary antenna. Hence, a known structure signal is assumed with the despreading signal appropriately aligned in terms of delay and frequency offset (As in the GPS demodulation, this would be established by a multi-hypothesis search.).

The scenario considered is that of a single receiver antenna immersed in a Rayleigh fading environment, which is captured over a finite time interval of $t \in [0, T]$ where T denotes the duration of the signal snapshot. This signal snapshot is processed to decode

between the H_0 and H_1 states. It will be assumed that the multipath is temporally unresolvable and is constant over the snapshot duration of T (flat fading). This is a valid assumption for indoor environments for signals with a bandwidth of 1-2 MHz (Rappaport 2002). However, the multipath will vary randomly with the spatial position of the antenna. Thus, the channel gain between the transmitter and the receive antenna phase centre can be represented by a scalar variable denoted by A introduced in Chapter 2, which is a random process with regards to spatial variables but is static with regards to time (Friedlander & Scherzer 2004). As it was demonstrated in Section 2.5, flat fading is a reasonable model for indoor environments where multipath signals have unresolvable components.

The representation of the received signal $r(t)$ for a static antenna located at a position \mathbf{p} is expressed as

$$r(t) = A(\mathbf{p})s_o(t) + n(t) \quad 4-1$$

where $A(\mathbf{p})$ is the channel gain and $s_o(t)$ is the deterministic complex baseband component of the signal that is known to the receiver and $n(t)$ is circularly normal random additive noise, independent of the signal.

The receiver accumulates a temporal snapshot of $r(t)$ over the snapshot interval of $t \in [0, T]$ as introduced beforehand. Based on the Rayleigh fading assumption, $A(\mathbf{p})$ is a zero-mean circularly normal random variable (Rensburg & Friedlander 2004) such that $A(\mathbf{p}) \sim CN(0, \sigma_A^2)$ where \sim denotes the Probability Density Function (PDF) of the left

hand side variable². As $s_o(t)$ is known to the receiver, and $A(\mathbf{p})$ is circularly normal and $n(t)$ is spectrally white within the bandwidth of $s_o(t)$, the optimal Neyman-Pearson (NP) detection processing (Kay 1998) is a matched filter based on correlation with $s_o(t)^*$ followed by a magnitude squared operation as illustrated in Figure 4-1 where $(\bullet)^*$ represents the complex conjugate operator (refer to Section 2.8).

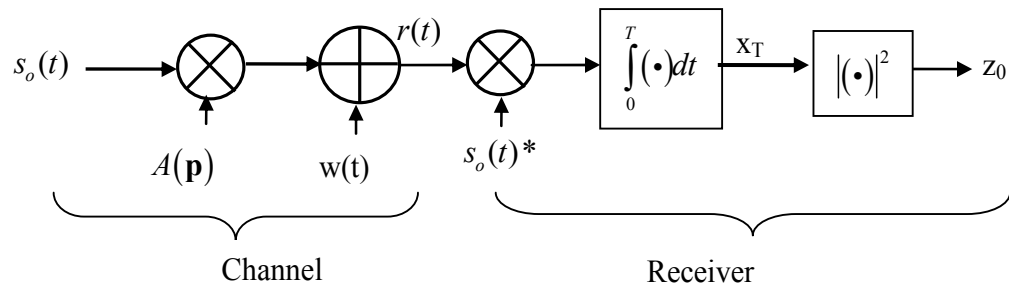


Figure 4-1 Static antenna channel model and subsequent NP processing

This processing results in the decision variable denoted as z_0 which is expressed as

$$\begin{aligned} z_0 &= |x_T|^2 \\ x_T &= \int_0^T r(t)s_o(t)^* dt \end{aligned} \quad 4-2$$

where the intermediate variable x_T is defined for convenience. The signal energy of $s_o(t)$ is normalized such that $\frac{1}{T} \int_0^T |s_o(t)|^2 dt = 1$. As $\int_0^T n(t)s_o(t)^* dt \sim CN(0, TN_0)$ it follows that the PDF of x_T conditioned on $A(\mathbf{p})$ is given as

² Random variable $B = u + jv$ distributed according to circularly normal PDF with zero-mean and variance σ^2 , $CN(0, \sigma^2)$, where u and v are independent zero-mean normal random variables each with variance

$$x_T | A(\mathbf{p}) \sim CN(TA(\mathbf{p}), TN_0). \quad 4-3$$

The SNR of x_T for a given T is denoted as ρ_T which conditioned on $A(\mathbf{p})$ is

$$\rho_T | A(\mathbf{p}) = \frac{TA(\mathbf{p})^2}{N_o}. \quad 4-4$$

Hence, the expected value of ρ_T is given as

$$E[\rho_T] = \frac{T\sigma_A^2}{N_o} \quad 4-5$$

where $E[\bullet]$ is the expectation operator. Based on this, it is convenient to define ρ as the average SNR as

$$\rho \equiv \frac{T\sigma_A^2}{N_o}. \quad 4-6$$

This definition will be used throughout the remainder of this chapter. Without loss of generality, the normalization of $TN_o = 1$ can be imposed such that $\rho = T^2\sigma_A^2$ which simplifies the expressions that follow.

4.1.1 Static antenna detection performance

In the static antenna case the antenna is located at a position \mathbf{p} throughout the interval $t \in [0, T]$. Based on the above definitions and normalizations, the PDF of x_T conditioned on H_0 and H_1 is

$\sigma^2/2$, $u \sim N(0, \sigma^2/2)$ and $v \sim N(0, \sigma^2/2)$ (Kay 1988).

$$x_T \sim \begin{cases} CN(0, I) & \text{under } H_0 \\ CN(0, I + \rho) & \text{under } H_1 \end{cases} . \quad 4-7$$

Consequently, the PDF of z_0 , defined in Eq. 4-2, conditioned on H_0 and H_1 is Chi-Squared central with two Degrees Of Freedom (DOF)³. Hence,

$$z_0 \sim \begin{cases} e^{-z_0} & \text{under } H_0 \\ \frac{I}{\rho+I} e^{-\frac{z_0}{\rho+I}} & \text{under } H_1 \end{cases} . \quad 4-8$$

Assuming that z_0 is compared with a threshold γ then the P_{FA} and P_D can be determined by

$$\begin{aligned} P_{FA} &= \exp(-\gamma) \\ P_D &= \exp\left(\frac{-\gamma}{I + \rho}\right). \end{aligned} \quad 4-9$$

Let ρ_s denote the value of ρ for the static antenna, which can be expressed explicitly in terms of the given target values of P_{FA} and P_D using Eq. 4-9 as

$$\rho_s = \frac{\ln(P_{FA})}{\ln(P_D)} - I. \quad 4-10$$

ρ_s is the average SNR required to meet the target values of P_{FA} and P_D for a static antenna assuming Rayleigh fading.

³ If $B \sim CN(0, \sigma^2)$, $|B|^2$ is distributed according to $f(|B|^2) = \frac{1}{\sigma^2} \exp(-|B|^2/\sigma^2)$ (Papoulis & Pillai 2002).

4.2 Synthetic array system model in discrete mode

The moving antenna is now considered whereby the antenna is translated along an arbitrary trajectory while the snapshot data is being collected. The position vector to the antenna location at time t from the origin is now denoted as $\mathbf{p}(t)$. The signal component of the complex baseband signal $r(t)$ is written as $s(t, \mathbf{p}(t))$, which is a function of time t , and the antenna position $\mathbf{p}(t)$, which in turn is a function of t . It is assumed that the signal snapshot of $r(t)$ is collected in M discrete subintervals, each of duration ΔT . For a direct comparison with the static antenna, the constraint $T = M \Delta T$ will be imposed. Define t_m as the starting instance of the m -th subinterval that extends over the interval $[t_m, t_m + \Delta T]$ for $m \in [1, 2, \dots, M]$. It is assumed that there are arbitrary time gaps between the subintervals such that $t_m - t_{m-1} > \Delta T$. These time gaps are selected based on the receiver velocity to capture statistically independent spatial samples and maximize diversity gain. The collection of signals over the m -th and $(m+1)$ -th subintervals in discrete mode is illustrated in Figure 4-2.

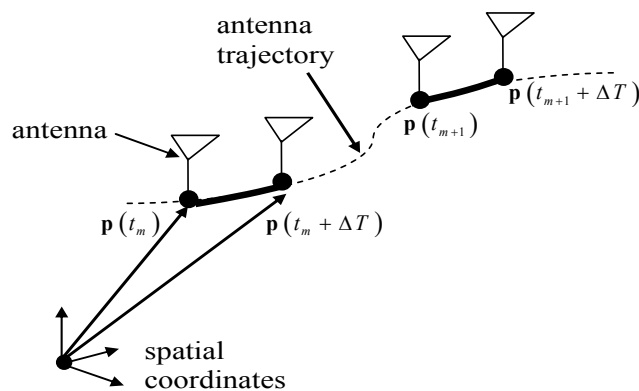


Figure 4-2: Moving antenna and positional vector definitions for snapshot collection for the m -th and $(m+1)$ -th sub-intervals each of duration ΔT in discrete mode

ΔT is considered to be sufficiently small such that $A(\mathbf{p}(t))$ can be assumed constant over the interval of ΔT such that

$$A(\mathbf{p}(t)) \approx A(\mathbf{p}(t_m)) \quad \text{for } t \in [t_m, t_m + \Delta T]. \quad 4-11$$

For this approximation to be valid, $|\mathbf{p}(t_m + \Delta T) - \mathbf{p}(t_m)|$ must be small relative to the wavelength of the carrier. This assumption places a limit on how large ΔT can be and also on how fast the antenna can be moved in the discrete synthetic array mode.

The signal reception model of the synthetic array was described in Chapter 3. For convenience here an overview of the synthetic array model is given. The signal captured in each subinterval is correlated with $s_o(t)^*$ resulting in a set of M spatial array samples denoted by x_m and given as

$$x_m = \int_{t_m}^{t_m + \Delta T} r(t) s_o(t)^* dt. \quad 4-12$$

x_m can also be expressed as

$$x_m = A(\mathbf{p}(t_m)) s_m + n_m \quad 4-13$$

where

$$\begin{aligned} s_m &= \int_{t_m}^{t_m + \Delta T} |s_o(t)|^2 dt \\ n_m &= \int_{t_m}^{t_m + \Delta T} n(t) s_o(t)^* dt \end{aligned} \quad 4-14$$

It follows that x_m forms a set of sufficient statistics of the accumulated snapshot signal in terms of optimal decoding between H_0 and H_1 . The vector forms of the signals

are defined as $\mathbf{x} = [x_1 \dots x_M]^T$, $\mathbf{s} = [s_1 \dots s_M]^T$, $\mathbf{n} = [n_1 \dots n_M]^T$ and $\mathbf{A} = [A(\mathbf{p}(t_1)) \dots A(\mathbf{p}(t_M))]^T$.

Due to the Rayleigh fading assumption, the individual components of the vector \mathbf{A} are circularly normal such that $[A]_m = A(\mathbf{p}(t_m)) \sim CN(0, \sigma_A^2)$. With these definitions the detection problem is stated as

$$\begin{aligned}\mathbf{x} &= \mathbf{A} \odot \mathbf{s} + \mathbf{n} && \text{under } H_1 \\ \mathbf{x} &= \mathbf{n} && \text{under } H_0\end{aligned}\quad 4-15$$

where \odot denotes the Hadamard vector product operator.

The optimal detection processing based on the NP Likelihood Ratio Test (LRT) (Kay 1998) chooses H_1 if

$$L(\mathbf{x}) = \frac{p(\mathbf{x}|_{H_1})}{p(\mathbf{x}|_{H_0})} > \gamma \quad 4-16$$

where $p(\mathbf{x}|_{H_1})$ and $p(\mathbf{x}|_{H_0})$ are the conditional PDF's of \mathbf{x} given H_1 and H_0 respectively and γ is a threshold. As both \mathbf{A} and \mathbf{n} are zero-mean multivariate circularly Gaussian random vectors, so is \mathbf{x} . Hence, $L(\mathbf{x})$ is a function of the covariance matrices of $\mathbf{A} \odot \mathbf{s}$ and \mathbf{n} . The noise covariance matrix is denoted \mathbf{C}_n and given as

$$\mathbf{C}_n = E[\mathbf{n}\mathbf{n}^H] = \frac{I}{M}\mathbf{I}_M \quad 4-17$$

where \mathbf{I}_M is the $M \times M$ identity matrix. The last step follows from the normalization

$TN_0 = 1$ and the relationship $\int_{t_m}^{t_m + \Delta T} |s_0(t)|^2 dt \approx \frac{T}{M} = \Delta T$. The signal covariance matrix is

denoted \mathbf{C}_s and is given as

$$\mathbf{C}_s = E \left[\mathbf{A} \odot \mathbf{s} (\mathbf{A} \odot \mathbf{s})^H \right] = \Delta T^2 \mathbf{C}_A \quad 4-18$$

where \mathbf{C}_A is the covariance matrix of \mathbf{A} .

As stated previously, the individual components of the vector \mathbf{A} are circularly normal such that $[\mathbf{A}]_m = A(\mathbf{p}(t_m)) \sim CN(0, \sigma_A^2)$. The signal covariance matrix in a Rayleigh fading environment with a ring of scatterer models was defined earlier in Section 3.2 by

$$\begin{aligned} \mathbf{C}_s &\approx \frac{\sigma_A^2 T^2}{M^2} \Psi = \frac{\rho}{M^2} \Psi \\ [\Psi]_{i,j} &= J_0 \left(\frac{2\pi}{\kappa} |\mathbf{p}_i - \mathbf{p}_j| \right) \end{aligned} \quad 4-19$$

where Ψ denotes the normalized correlation coefficient matrix which is a function of antenna position, J_0 is zero-order Bessel function of the first kind and κ is the carrier wavelength. Thus, the PDF of \mathbf{x} conditioned on H_I and H_0 is

$$\mathbf{x} \sim \begin{cases} CN\left(0, \mathbf{C}_s + \sigma_n^2 \mathbf{I}\right) = CN\left(0, \frac{\rho}{M^2} \Psi + \frac{I}{M} \mathbf{I}\right) & \text{under } H_I \\ CN\left(0, \sigma_n^2 \mathbf{I}\right) = CN\left(0, \frac{I}{M} \mathbf{I}\right) & \text{under } H_0 \end{cases} \quad 4-20$$

4.3 Synthetic array system model in continuous mode

The model discussed in the previous section was based on the assumption that the antenna movement in each subinterval is negligible and spatial samples are collected sufficiently apart that uncorrelated spatial samples can be assumed (Figure 4-2). Thus, this model puts a limit on how large ΔT can be and also how fast the antenna can be

moved. However, in some applications the stationarity assumption of the antenna in each subinterval cannot be considered. Hence, the proposed model should be adapted accordingly to accommodate this situation as well. For instance, if a receiver is moving with a velocity of 1 m/s, and 100 ms integration is required in each subinterval, for a carrier wavelength of 20 cm, antenna displacement during each subinterval becomes half of the wavelength and cannot be ignored.

In this section, the signal covariance model for continuous synthetic array mode is considered. The receiver accumulates a temporal snapshot of $r(t)$ over the snapshot interval $t \in [0, T]$. During the snapshot interval, the antenna moves with an approximately constant velocity. The signal snapshot of $r(t)$ is collected by the receiver and despread by the locally generated copy of $s_o(t)$. In the proposed method T is divided into M uniform subintervals, each of duration ΔT . As will be revealed later M is a function of the antenna velocity and the multipath model.

To facilitate the derivations, it is necessary to consider the signal snapshot as a set of discrete samples. Assume that each discrete sample is derived by despreading $r(t)$ with a locally generated signal for a subinterval duration of ΔT . It will be assumed that each subinterval is of the same duration as ΔT and that the total snapshot interval of T consists of M subintervals such that $T = M \Delta T$. Figure 4-3 represents the data collection scenario with M subintervals for T seconds for continuous mode synthetic array.

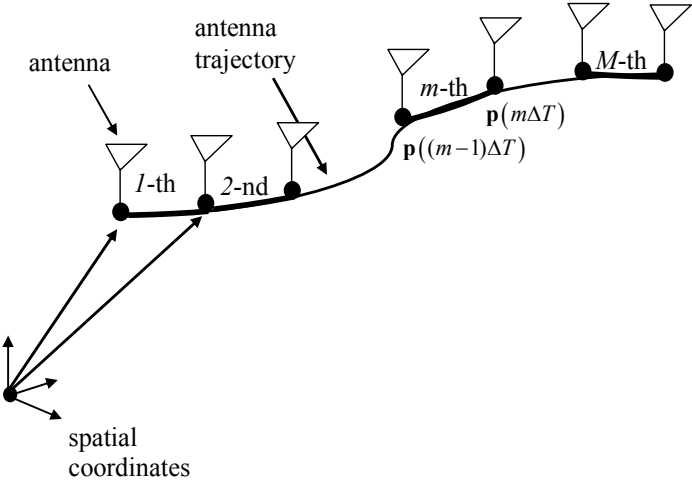


Figure 4-3: Moving antenna and positional vector definitions for snapshot collection for continuous mode synthetic array

Comparing Figure 4-2 with Figure 4-3 one can easily contrast the differences in discrete and continuous sampling modes. Define $(m-1)\Delta T$ as the starting instance of the m -th subinterval that extends over the interval of $[(m-1)\Delta T, m\Delta T]$. The signal captured in each subinterval is correlated with $s_o(t)$ resulting in a set of M spatial array samples denoted by x_m and given as

$$x_m = \int_{(m-1)\Delta T}^{m\Delta T} r(t) s_o(t)^* dt . \quad 4-21$$

x_m is expressed as

$$x_m = A(\mathbf{p}(t_m)) s_m + n_m \quad 4-22$$

where

$$\begin{aligned} s_m &= \int_{(m-1)\Delta T}^{m\Delta T} |s_o(t)|^2 dt \\ n_m &= \int_{(m-1)\Delta T}^{m\Delta T} n(t) s_o(t)^* dt \end{aligned} \quad . \quad 4-23$$

M is a function of the snapshot aperture and the multipath model which will be discussed in the next section. Clearly ΔT should be small enough that the decorrelation due to the changing $A(\mathbf{p}(t))$ over the subinterval should not be of significance.

To simplify the following development and notation it is assumed that

$$\int_{(m-1)\Delta T}^{m\Delta T} |s_o(t)|^2 dt = \Delta T \quad \text{for } m \in [1, 2 \dots M]. \quad 4-24$$

This is a valid assumption where a signal bandwidth is broad relative to ΔT^{-1} . Based on this assumption and that the PSD of the additive noise is N_o , the covariance matrix for the additive noise is defined as

$$\mathbf{C}_n \equiv E[\mathbf{n}\mathbf{n}^H]. \quad 4-25$$

The elements of \mathbf{C}_n are given as

$$\begin{aligned} [\mathbf{C}_n]_{m,m'} &= \frac{1}{\Delta T^2} E \left[\int_{t_m}^{t_m + \Delta T} n(t) s_o(t)^* dt \int_{t_{m'}}^{t_{m'} + \Delta T} n(t')^* s_o(t') dt' \right] \\ &= \frac{N_o}{\Delta T^2} \int_{t_m}^{t_m + \Delta T} |s_o(t)|^2 dt \\ &= \frac{N_o}{\Delta T} \delta_{m,m'} \end{aligned} \quad . \quad 4-26$$

Consequently, $\mathbf{C}_n = N_o / \Delta T \mathbf{I}_M$ where \mathbf{I}_M is the $M \times M$ identity matrix. The signal covariance matrix is a function of the scatterers' geometry as well as the antenna trajectory. Diffuse multipath is assumed and is considered a continuum of infinitesimal scattering reflection sources each of which results in a circularly normal random amplitude component. Results given here are adopted from the detailed derivation given

by Van Trees (2002). The covariance matrix is defined based on the multipath signal model in Eq. 4-15 as

$$\mathbf{C}_s \equiv E\left[\left(\mathbf{A} \odot \mathbf{s}\right)\left(\mathbf{A} \odot \mathbf{s}\right)^H\right] \quad 4-27$$

with elements given as

$$\begin{aligned} [\mathbf{C}_s]_{m,m'} &= \frac{1}{\Delta T^2} E\left[\int_{(m-1)\Delta T}^{m\Delta T} A(\mathbf{p}(t)) s_o(t)^* dt \int_{(m'-1)\Delta T}^{m'\Delta T} A(\mathbf{p}(t'))^* s_o(t') dt'\right]. \\ &= [\mathbf{C}_A]_{m,m'} \end{aligned} \quad 4-28$$

The last step follows from the normalization given in Eq. 4-24. Hence,

$$\begin{aligned} [\mathbf{C}_s]_{m,m'} &= \int_{(m-1)\Delta T}^{m\Delta T} \int_{(m'-1)\Delta T}^{m'\Delta T} E\left[A(\mathbf{p}(t)) A(\mathbf{p}(t'))\right] dt dt' \\ &= \sigma_A^2 \int_{(m-1)\Delta T}^{m\Delta T} \int_{(m'-1)\Delta T}^{m'\Delta T} J_0(2\pi v(t-t')) dt dt' \\ &= 2\sigma_A^2 \int_0^{\Delta T} (\Delta T - u) J_0(2\pi v(u + (m-m')\Delta T)) du \end{aligned} \quad 4-29$$

where J_0 is zero-order Bessel function of the first kind resulting from the ring of scattering model (Van Trees 2002, Fulghum et al 2002) and v is receiver velocity normalized by the carrier wavelength.

Define the distance between sample points normalized by the carrier wavelength as $\Delta d = v\Delta T$ such that

$$[\mathbf{C}_A]_{m,m'} = 2\sigma_A^2 \int_0^1 (1-q) J_0(2\pi \Delta d (q + (m-m'))) dq \quad 4-30$$

where $q = u/\Delta T$ is introduced for notational convenience.

For the numerical calculation it is convenient to normalize the signal and noise covariance matrices by $N_o/\Delta T$ such that $\mathbf{C}_n = \mathbf{I}_M$ and

$$[\mathbf{C}_s]_{m,m'} = \frac{2\Delta T \sigma_A^2}{N_o} \int_0^1 (1-q) J_0(2\pi\Delta d(q + (m - m'))) dq. \quad 4-31$$

Next, define the average SNR as the signal energy in the ΔT second interval to the noise PSD as $\rho_{\Delta T} = \Delta T \frac{\sigma_A^2}{N_o}$. Hence, the signal covariance matrix can be defined as

$$\begin{aligned} [\mathbf{C}_s]_{m,m'} &= 2\rho_{\Delta T} \int_0^1 (1-q) J_0(2\pi\Delta d(q + (m - m'))) dq \\ &= \rho_{\Delta T} [\Psi]_{m,m'} \end{aligned} \quad 4-32$$

where Ψ is the SA normalized signal correlation coefficient defined by

$$[\Psi]_{m,m'} = 2 \int_0^1 (1-q) J_0(2\pi\Delta d(q + (m - m'))) dq. \quad 4-33$$

This cannot be integrated in closed form and hence must be done numerically.

The PDF of \mathbf{x} conditioned on H_1 and H_0 is

$$\mathbf{x} \sim \begin{cases} CN(\mathbf{0}, \mathbf{C}_s + \mathbf{C}_n) = CN(\mathbf{0}, \rho_{\Delta T} \Psi + \mathbf{I}) & \text{under } H_1 \\ CN(\mathbf{0}, \mathbf{C}_n) = CN(\mathbf{0}, \mathbf{I}) & \text{under } H_0 \end{cases}. \quad 4-34$$

Equation 4-32 is the key relation in further analyses as it contains all the relevant information regarding the receiver motion and channel model. If the antenna is static then $\Delta d = 0$ and $J_0(0) = 1$ resulting in $[\Psi]_{m,m'} = 1$. Thus, the signal covariance matrix in the static case becomes

$$\mathbf{C}_s^{static} = \rho_{\Delta T} \mathbf{1}\mathbf{1}^T \quad 4-35$$

where $\mathbf{1}$ is the $M \times 1$ vector of ones.

4.3.1 Coherent integration loss due to antenna motion in Rayleigh fading

In this section for the static antenna case it is assumed that during the signal snapshot T the channel is stationary (other decorrelation effects such as oscillator instability are ignored). Hence, the optimum process is coherent integration for T seconds with $M=1$. In this case, the signal covariance matrix represented in Eq. 4-32 becomes a scalar equal to ρ_T . The problem of interest is assessing the coherent integration loss due to antenna motion relative to the static antenna when $M=1$.

By developing the signal covariance matrix in 4-32 it is possible to analyze the integration loss due to antenna movement in a Rayleigh fading environment. Assume a receiver that accumulates the received signal for a snapshot interval of T . Hence, the correlation coefficient matrix Ψ represented in Eq. 4-32 is a scalar and for the static antenna becomes one. Therefore, the signal covariance matrix in the static case can be considered as an average SNR during the signal snapshot ρ_T . If the signal covariance matrix in the moving case is defined as a function of the normalized velocity v and the snapshot interval T as $\rho_T \Psi(v, T)$, the coherent integration Gain Degradation (GD) due to the receiver motion with a constant velocity v can be defined as

$$GD = \frac{\rho_T \Psi(v, T)}{\rho_T} = \Psi(v, T). \quad 4-36$$

As seen in Eq. 4-36 the GD value is completely characterized by $\Psi(v, T)$. Figure 4-4a shows GD for different values of v when the receiver coherently integrates the signal snapshot for one second ($T=1$ s). Since $T=1$, the horizontal axis in Figure 4-4a may be considered as the antenna normalized aperture during the signal snapshot. As an example,

coherent integration for $T=1$ s and $v=0.5$ (half-wavelength aperture) results in a GD value being reduced to 0.8, implying a 20 percent loss relative to the ideal integration gain of the static antenna. Figure 4-4a shows observations that are relevant for system design issues. For instance, if the coherency of the channel during each snapshot should be preserved to within 95 percent, the spatial extent of the moving antenna should be kept to less than 0.25 of the carrier wavelength in a Rayleigh fading channel.

Next the receiver velocity is kept constant and T is varied. The Normalized Integration Gain (NIG) metric which is the ratio of the integration gain of a moving antenna to the integration gain of the static antenna for $T=1$ (defined as ρ_1)

$$NIG = \frac{\rho_T}{\rho_1} \Psi(v, T). \quad 4-37$$

Figure 4-4b shows the NIG value for $v=1$. As shown in Figure 4-4b, in the range of $T \in \{0, 0.5\}$, the integration gain is almost linearly increasing by T . Hence, increasing integration time enhances the process gain. However, due to receiver motion and signal decorrelation, increasing T further causes a decorrelation of signal samples. Thus, after approximately one second of coherent integration, the processing gain remains constant and becomes independent of T . Note that the integration gain of $T=1$ for the moving antenna with $v=1$ in the steady state case (after one second) is almost 30 percent of that of the static antenna. Note also that if the receiver is static, in the ideal case the NIG value given in the Figure 4-4b will linearly increase with a slope of one.

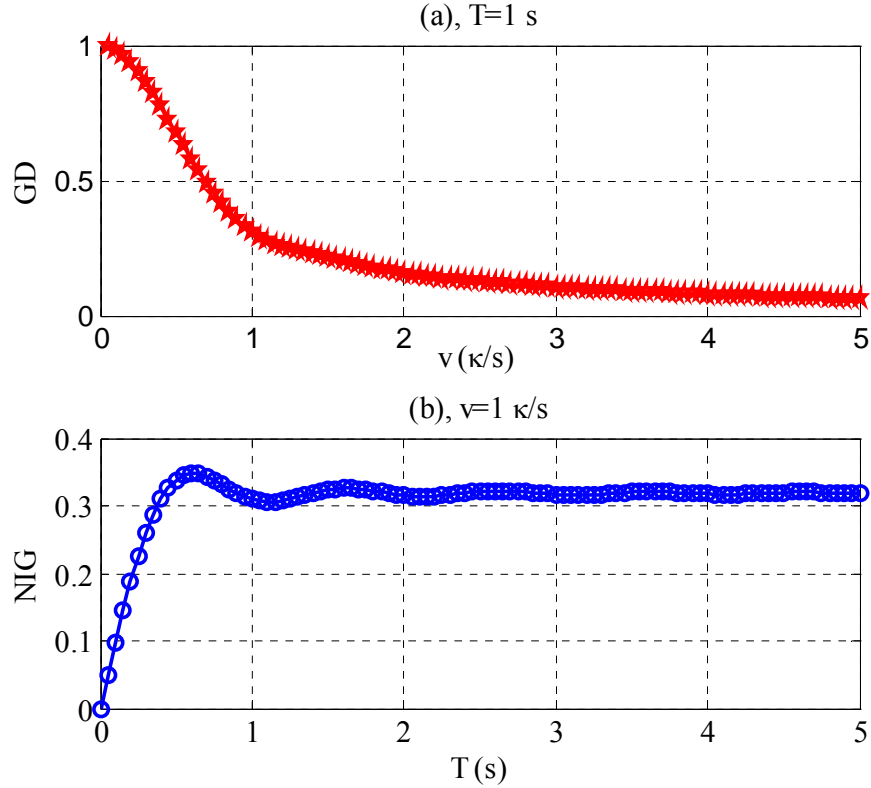


Figure 4-4: a) Correlation coefficient of a moving receiver versus receiver velocity for $T=1$ s and $M=1$, b) normalized integration gain versus T for constant $v=1$ and $M=1$

It is interesting to determine the limit of the NIG for different values of v when $T \rightarrow \infty$. In Appendix A, it is shown that

$$\lim_{T \rightarrow \infty} NIG = \frac{1}{\pi v}. \quad 4-38$$

Hence, the higher the velocity, the smaller the limit of NIG which is an intuitive result. For instance, if a vehicle navigation system is operating in a dense multipath environment with a velocity of 10 m/s (53 wavelength per seconds for GPS L1 signals), the

$$\lim_{T \rightarrow \infty} NIG \approx 0.006.$$

4.3.2 Selecting M for a given aperture in the Rayleigh fading model

An important issue in the development of the proposed method is the most favorable selection of M , which provides a good compromise between coherency loss and diversity gain. For a given extent of the moving antenna aperture normalized by the carrier wavelength d and a multipath model, if M becomes one, as shown previously the coherency of the channel will decrease resulting in an integration loss. On the other hand if M is too large, the matrix operations in the process becomes unwieldy. Hence, the optimal value of M may be selected that results in the diagonal elements of the correlation coefficient matrix Ψ being near one with negligible values for off-diagonal elements.

Assume a signal snapshot T and antenna velocity v so that the product of T and v provides the antenna aperture d by assuming linear motion. The problem of interest is to determine the signal correlation coefficient for a given aperture d and different values of M . Figure 4-5 shows the correlation coefficient Ψ for $d=1$ and different values of M . When $M=40$, the diagonal elements of the Ψ matrix become one. However, the adjacent samples are strongly correlated. By decreasing M the correlation of each snapshot by itself decreases which results in a coherent integration loss; however the adjacent samples become approximately uncorrelated and diversity gain can be achieved. Figure 4-5 also shows that for $M=4$ and $M=2$ the diagonal elements of the Ψ matrix are 0.91 and 0.68, respectively. Interestingly, the off-diagonal values for the two cases are almost the same. Hence, by comparing different correlation coefficients for different values of M , $M=4$ per wavelength can be considered as a practical choice since it has an autocorrelation value of greater than 0.9 and a cross correlation of less than 0.4.

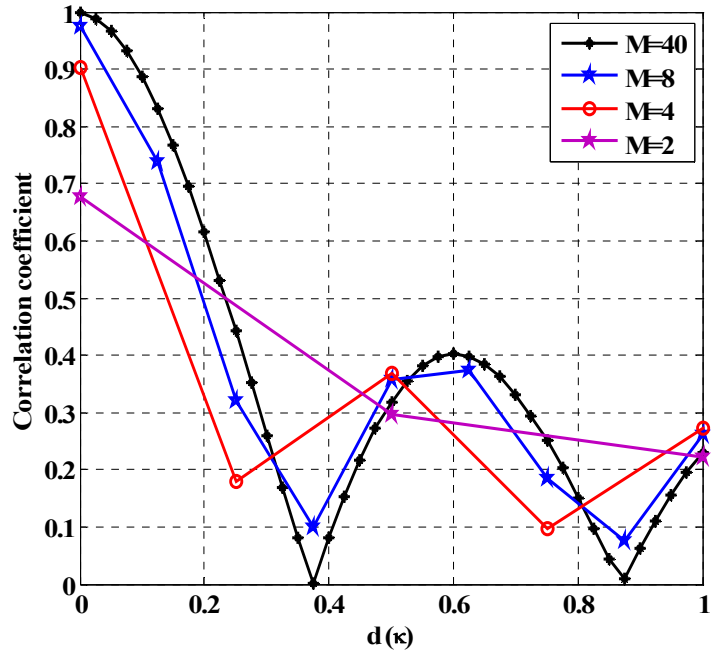


Figure 4-5: Correlation coefficient for different values of M

4.4 Detection process of a narrowband signal in Rayleigh fading

In this section, the narrowband signal detection performance in a Rayleigh fading environment is investigated. Two approaches are considered herein. The first method is based on the EC, which takes into account the signal covariance matrix and provides an optimum detection process in the Rayleigh fading channel introduced earlier. The second approach is developed based on the EG detector, which combines spatial samples with equal weights.

4.4.1 Optimum detection performance of a narrowband signal in Rayleigh fading based on the Synthetic Array

In Section 4.2 and Section 4.3 the signal covariance model \mathbf{C}_s of the discrete and continuous synthetic array were developed. In this section, \mathbf{C}_s is utilized for detecting a signal embedded in white Gaussian noise. Assuming that \mathbf{C}_s and \mathbf{C}_n are available, the PDF of \mathbf{x} conditioned on H_0 and H_1 can be written as

$$\begin{aligned} p(\mathbf{x}|_{H_1}) &= \frac{I}{\sqrt{|2\pi(\mathbf{C}_s + \mathbf{C}_n)|}} \exp\left[-\mathbf{x}^H ((\mathbf{C}_s + \mathbf{C}_n))^{-1} \mathbf{x}\right] \\ p(\mathbf{x}|_{H_0}) &= \frac{I}{\sqrt{|2\pi\mathbf{C}_n|}} \exp\left[-\mathbf{x}^H \mathbf{C}_n^{-1} \mathbf{x}\right] \end{aligned} . \quad 4-39$$

The optimal detection processing based on LRT was introduced in Section 3.2.2. It was shown that the LRT reduces to the EC formulation resulting in a sufficient statistic given as

$$z_{EC}(\mathbf{x}) = \mathbf{x}^H \mathbf{C}_s (\mathbf{C}_s + \sigma_n^2 \mathbf{I})^{-1} \mathbf{x} . \quad 4-40$$

Since \mathbf{C}_s is a Hermitian matrix, the eigen-decomposition of \mathbf{C}_s can be represented as

$$\mathbf{Q}^H \mathbf{C}_s \mathbf{Q} = \Lambda_s \quad 4-41$$

where $\mathbf{Q} = [\mathbf{q}_1, \mathbf{q}_2, \dots, \mathbf{q}_M]$ is the orthogonal matrix of columnwise eigenvectors and Λ_s is the diagonal matrix of eigenvalues where the m -th eigenvalue is denoted by λ_{s_m} . In Section 2.8.2 it was demonstrated that the EC test statistics can be shown as

$$z_{EC}(\mathbf{y}) = \sum_{m=1}^M \frac{\lambda_{s_m}}{\lambda_{s_m} + \sigma_n^2} |y_m|^2 \quad 4-42$$

where $\mathbf{y} = \mathbf{Q}^H \mathbf{x}$. The vector $\mathbf{y} = [y_1, y_2, \dots, y_M]^T$ consists of M independent circular Gaussian random variables such that

$$\mathbf{y} \sim \begin{cases} CN\left(0, \Lambda_s + \frac{\mathbf{I}}{M}\right) & \text{under } H_1 \\ CN\left(0, \frac{\mathbf{I}}{M}\right) & \text{under } H_0 \end{cases} \quad 4-43$$

Therefore, the test statistics represented in Eq. 4-42 z_{EC} becomes a scaled factor of Chi-Squared distribution. Figure 4-6 shows the EC processing model.

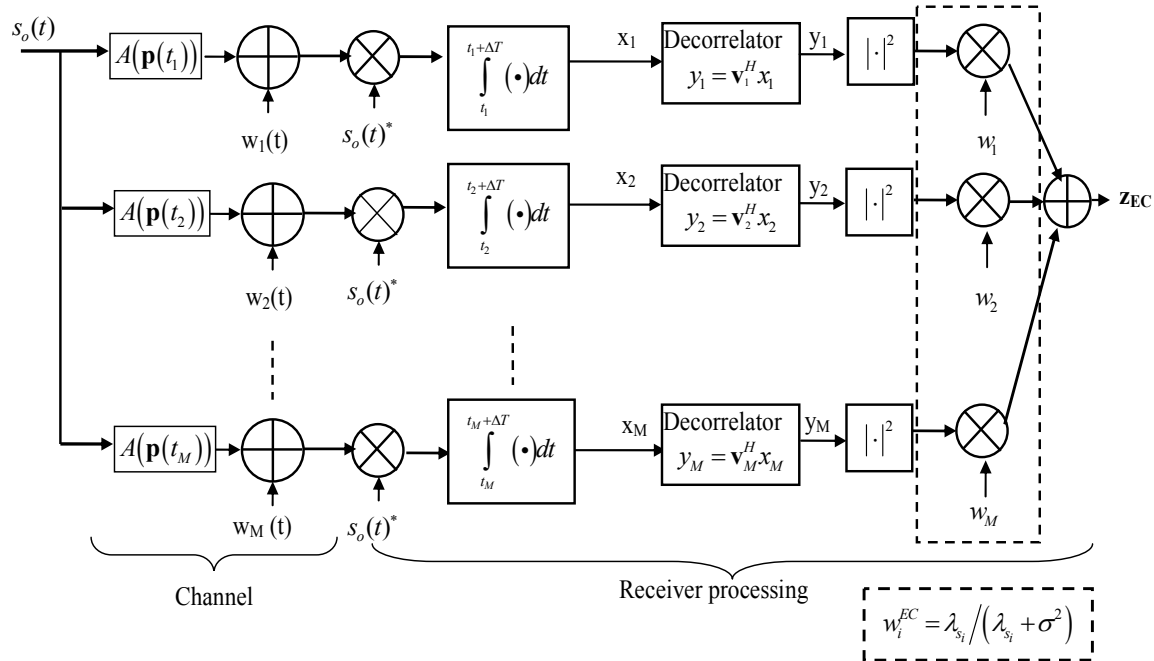


Figure 4-6: Synthetic antenna channel model and subsequent EC processing

Next consider the calculation of the P_{FA} and P_D . The characteristic function of z_{EC} conditioned on H_I and H_0 is given as

$$\begin{aligned}\Omega_{z|H_I}(\omega) &= \prod_{m=1}^M \frac{I}{I - j\alpha_m^{H_I}\omega} \\ \Omega_{z|H_0}(\omega) &= \prod_{m=1}^M \frac{I}{I - j\alpha_m^{H_0}\omega}\end{aligned}\quad 4-44$$

where

$$\begin{aligned}\alpha_m^{H_I} &= \lambda_{s,m} \\ \alpha_m^{H_0} &= \frac{\lambda_{s,m}}{M\lambda_{s,m} + I}\end{aligned}\quad 4-45$$

The values of P_{FA} and P_D can be determined by taking the Fourier transform of the characteristic functions. For a given threshold of γ applied to z_{EC} , the following is obtained:

$$\begin{aligned}P_D &= \int_{-\infty}^{\gamma} \int_{-\infty}^{\infty} \Omega_{z|H_I}(\omega) e^{-j\omega z} \frac{d\omega}{2\pi} dz \\ P_{FA} &= \int_{-\infty}^{\gamma} \int_{-\infty}^{\infty} \Omega_{z|H_0}(\omega) e^{-j\omega z} \frac{d\omega}{2\pi} dz.\end{aligned}\quad 4-46$$

To determine a closed form expression for P_{FA} and P_D in the case of distinctive eigenvalues of \mathbf{C}_s , using a partial fraction expansion, it can be shown that (Kay 1998)

$$\prod_{m=1}^M \frac{I}{I - j\alpha_m^{H_i}\omega} = \sum_{m=1}^M \frac{A_m^{H_i}}{I - j\alpha_m^{H_i}\omega} \quad i = 0, I \quad 4-47$$

where

$$A_m^{H_i} = \prod_{k=1}^M \frac{I}{I - \frac{\alpha_k^{H_i}}{\alpha_m^{H_i}}} \quad i = 0, 1 \quad 4-48$$

and $\alpha_m^{H_i}$ is defined in Eq. 4-45. For the general case of $z = \sum_{m=1}^M \alpha_m^{H_i} x_m^2$ where $\alpha_m^{H_i}$ are distinct with $\alpha_m^{H_i} > 0$, and x_m^2 are IID with PDF of Chi-Squared with two DOF, the PDF of z is given by

$$\begin{aligned} P_z(z) &= \int_{-\infty}^{\infty} \prod_{m=1}^M \frac{I}{I - j\alpha_m^{H_i}\omega} e^{-j\omega z} \frac{d\omega}{2\pi} dz \\ &= \begin{cases} \sum_{m=1}^M \frac{A_m^{H_i}}{\alpha_m^{H_i}} e^{-\frac{z}{\alpha_m^{H_i}}} & z > 0 \\ 0 & z < 0 \end{cases}. \end{aligned} \quad 4-49$$

Thus, the performance of EC can be represented in closed form as

$$\begin{aligned} P_{FA} &= \sum_{m=1}^M A_m^{H_0} \exp\left(\frac{-\gamma}{\alpha_m^{H_0}}\right) \\ P_D &= \sum_{m=1}^M A_m^{H_1} \exp\left(\frac{-\gamma}{\alpha_m^{H_1}}\right) \end{aligned} \quad 4-50$$

4.4.2 Detection performance of the EG combiner in the Rayleigh fading channel based on the synthetic array

As shown in Eq. 4-42 EC emphasizes the stronger signal components corresponding to those with larger eigenvalues. EC formulation requires approximate knowledge of the signal and noise covariance matrices in order to compute the eigenvalues. This may not be usable in many practical applications. When \mathbf{C}_n and \mathbf{C}_s are not known apriori, the EG combiner is a practical suboptimal alternative that may be applied. Note from Eq. 4-42

that the EG combiner becomes asymptotically optimal when the signal components become more uncorrelated. On the other hand, the EG combiner is an optimal approach for signal detection in an uncorrelated Rayleigh fading environment. This is because $\lambda_{s_m}/(\lambda_{s_m} + \sigma^2)$ in Eq. 4-42 becomes identical for all spatial samples and this leads to the EG formulation. The test statistic of the EG combiner can be represented by

$$z_{EG} = \mathbf{x}^H \mathbf{x} = \sum_{m=1}^M |x_m|^2 . \quad 4-51$$

As shown in Eq. 4-51, the test statistics of the EG combiner are independent of \mathbf{C}_s . The channel model and subsequent EG processing is shown in Figure 4-7.

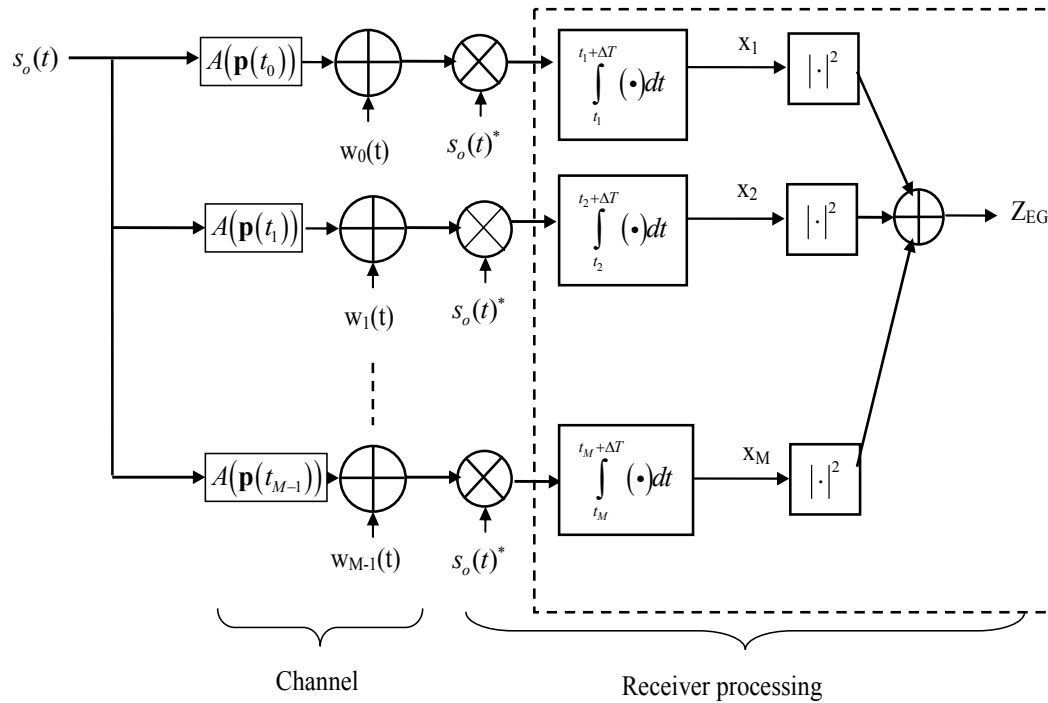


Figure 4-7: Channel model and equal-gain combining receiver processing for the moving antenna

4.4.2.1 EG combiner detection performance in uncorrelated Rayleigh fading

In this section, the detection performance of a discrete mode synthetic array in a Rayleigh fading environment is described. Note that if the subinterval sample points are sufficiently far apart such that $|\mathbf{p}(t_i) - \mathbf{p}(t_j)|$ for $i, j \in [1, 2, \dots, M]$ and $i \neq j$ is larger than the carrier wavelength then $\mathbf{C}_A \approx \sigma_A^2 \mathbf{I}_M$, and

$$\mathbf{C}_s \approx \frac{\sigma_A^2 T^2}{M^2} \mathbf{I}_M = \frac{\rho}{M^2} \mathbf{I}_M. \quad 4-52$$

\mathbf{C}_s is therefore available based on the assumption of the Rayleigh fading model and on the approximate estimate of the physical distance between the M spatial sampling points. As will be discussed further, the performance of the synthetic array is typically robust in terms of errors in these estimated distances. \mathbf{C}_n is based on the modeling of the noise which is typically construed as being spatially white. After some manipulation and the removal of deterministic scaling and additive constants, the LRT in uncorrelated Rayleigh fading reduces to the EG combiner defined as

$$z_{EG} = \mathbf{x}^H \mathbf{x} > \gamma \quad 4-53$$

where the scaling coefficient of $\frac{\rho}{M^2} / \left(\frac{\rho}{M^2} + 1 \right)$ has been ignored.

The decision variable output of the EG combiner, z_{EG} , has a PDF that is Chi-Squared central with $2M$ DOFs under both H_0 and H_1 . If the variance per DOF is taken as σ^2 then the PDF of the test statistics becomes (Hyeon et al 2008, Papoulis & Pillai 2002)

$$f_z(z) = \frac{1}{\sigma^{2M} 2^M \Gamma(M)} z^{M-1} e^{-\frac{z}{2\sigma^2}} \quad 4-54$$

where $\Gamma(M)$ is the Gamma function and for the integer M , $\Gamma(M) = (M-1)!$. The PDF of z_{EG} conditioned on H_0 and the assumption of spatial white channel noise with $\sigma^2 = \frac{1}{2M}$ is given by

$$f_z(z|_{H_0}) = \frac{2^M M^M}{2^M \Gamma(M)} z^{M-1} e^{-\frac{z2M}{2}} \quad 4-55$$

which simplifies to

$$f_z(z|_{H_0}) = \frac{M^M}{\Gamma(M)} z^{M-1} e^{-zM}. \quad 4-56$$

For H_I , $\sigma^2 = \frac{\rho}{2M^2} + \frac{1}{2M} = \frac{1}{2M} \left(\frac{\rho}{M} + 1 \right)$ such that

$$f_z(z|_{H_I}) = \frac{2^M M^M}{\left(\frac{\rho}{M} + 1 \right)^M 2^M \Gamma(M)} z^{M-1} e^{-\frac{zM}{\left(\frac{\rho}{M} + 1 \right)}}. \quad 4-57$$

The P_{FA} and P_D can be determined for a threshold γ as

$$P_{FA} = Q_{x_{2M}^2}(2M\gamma) \quad 4-58$$

and

$$P_D = Q_{x_{2M}^2} \left(\frac{2M\gamma}{\frac{\rho}{M} + 1} \right) \quad 4-59$$

where (Kay 1998)

$$Q_{x_{2M}^2}(v) = \exp\left(-\frac{I}{2}v\right) \sum_{k=0}^{M-1} \frac{(0.5v)^k}{k!}. \quad 4-60$$

The threshold can be scaled to simplify these expressions to

$$P_{FA} = Q_{x_{2M}^2}(\gamma) \quad 4-61$$

and

$$P_D = Q_{x_{2M}^2}\left(\frac{\gamma}{\frac{\rho}{M} + I}\right). \quad 4-62$$

The target detection parameter P_{FA} is used in Eq. 4-61 to determine the threshold γ .

This is used in Eq. 4-62 with the target parameter P_D to determine the average SNR ρ required. Let ρ_m denotes the average SNR required for the synthetic array.

4.4.2.2 EG combiner detection performance in correlated Rayleigh fading

To determine the performance of EG in correlated Rayleigh fading, it is convenient to perform the following transformation which decorrelates the signal covariance matrix:

$$\begin{aligned} z_{EG} &= \mathbf{x}^H \mathbf{x} = \mathbf{x}^H \mathbf{Q} \mathbf{Q}^H \mathbf{x} \\ &= \mathbf{y}^H \mathbf{y} = \sum_{m=1}^M |y_m|^2 \end{aligned} \quad 4-63$$

where $\mathbf{y} = \mathbf{Q}^H \mathbf{x}$, \mathbf{Q} being the eigenvectors of the signal covariance matrix defined earlier. The distribution of \mathbf{y} is given in Eq. 4-43. Consequently,

$$y_m \sim CN\left(0, \lambda_m^{H_i}\right) \quad i = 0, 1 \quad 4-64$$

$$|y_m|^2 \sim \frac{1}{\lambda_m^{H_i}} \chi_2^2\left(\frac{z}{\lambda_m^{H_i}}\right)$$

where $\lambda_m^{H_i}$ is the m-th eigenvalue of \mathbf{C}_x under the H_i state and χ_2^2 denotes a Chi-Squared distribution with two DOFs. For a general signal covariance matrix \mathbf{C}_s , the characteristic function of z_{EG} conditioned on H_1 and H_0 is given as

$$\Omega_{z|H_1}(\omega) = \prod_{m=1}^M \frac{I}{I - j\lambda_m^{H_1}\omega} \quad 4-65$$

$$\Omega_{z|H_0}(\omega) = \prod_{m=1}^M \frac{I}{I - j\lambda_m^{H_0}\omega}$$

where

$$\lambda_m^{H_1} = \lambda_{s_m} + \frac{1}{M} \quad 4-66$$

$$\lambda_m^{H_0} = \frac{1}{M}$$

The values of P_{FA} and P_D can be determined by replacing Eq. 4-65 and Eq. 4-66 into Eq. 4-46.

In summary the following points are made:

- In a correlated signal environment, if signal and noise are jointly circular Gaussian over the $2M$ dimensions the optimum detector reduces to the EC, for which the test statistic is given in Eq. 4-42. This procedure requires apriori knowledge of the covariance matrix and signal power. The EC performance was determined by inserting Eq. 4-44 into Eq. 4-46. The closed form expressions for the EC performance for distinctive eigenvalues of the signal covariance matrix were given in Eq. 4-50.

- When the multipath fading is such that the channel gains associated with the M samples of the synthetic array become uncorrelated then EC reduces to the EG combiner.

In this case, the test statistic becomes a random variable with a central Chi-squared PDF with $2M$ DOF, where M is the number of spatial samples.

- When the multipath fading is such that the channel gains associated with the M samples of the synthetic array become fully correlated, then the EC combining reduces to that of a matched filter followed by a magnitude squaring operation. In this case, the test statistic is random with a central Chi-square PDF of two DOF. The test statistic and performance are therefore equivalent to that of the static antenna as represented by Eq. 4-9 and Eq. 4-10.

- When \mathbf{C}_s and \mathbf{C}_n are unknown, a suboptimal solution is provided by the EG combiner. The performance of the EG combiner in correlated Rayleigh fading was demonstrated by inserting Eq. 4-65 into Eq. 4-46.

4.5 Discrete mode synthetic array detection performance and processing gain in uncorrelated Rayleigh fading

In previous sections, the detection performances of static and moving antennas were formulated. Given target detection parameters P_{FA} and P_D , the average SNR required for the static and the moving antenna, denoted as ρ_s and ρ_m respectively, can be evaluated. In this section, ρ_s and ρ_m are compared for various scenarios such that the advantage of moving the antenna can be quantified. Figure 4-8 shows ρ_s and ρ_m as a function of the target parameter P_D for $P_{FA} = 0.01$ and $M=4$.

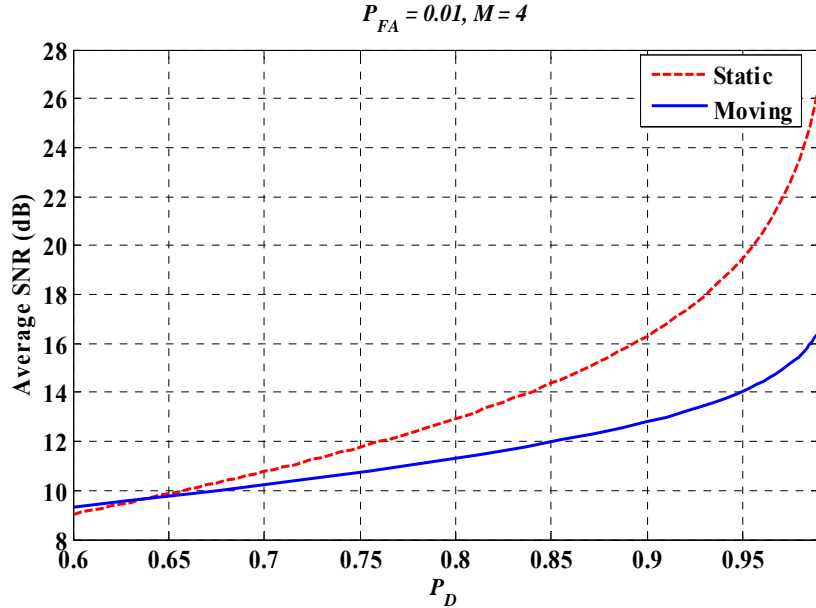


Figure 4-8: Required average SNR for a static and moving antenna versus P_D

For larger values of P_D , the required average SNR of the moving antenna is consistently less than that of static antenna, demonstrating the advantage of the moving antenna compared to the static one. Also evident in Figure 4-8 is that this advantage decreases as P_D is reduced. When P_D is sufficiently low, ρ_s is less than ρ_m indicating that the moving the antenna is actually detrimental. However, the range where $\rho_s < \rho_m$ is of negligible practical significance as P_D is low.

Figure 4-9a shows the required average SNR as a function of M for the static and the moving antenna cases with the interesting observation that there is a global minimum. Hence, there is an optimum value of M for which ρ_m is minimum, which is denoted as M_{opt} .

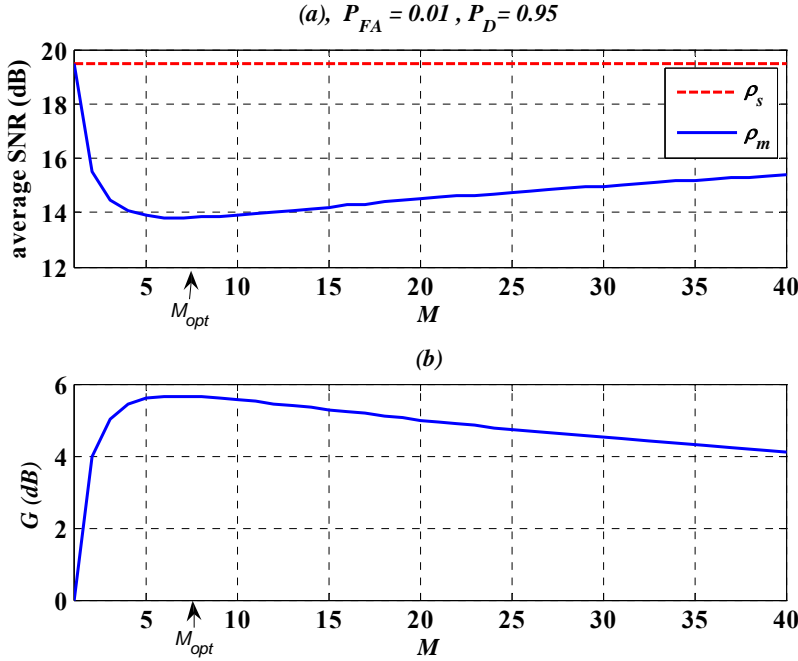


Figure 4-9: (a) Required average SNR for a static and moving antenna versus M (b) Achievable gain by moving antenna ($P_D=0.95$ and $P_{FA}=0.01$)

It is convenient to define $G = 10 \log(\rho_s / \rho_m)$ as the processing gain of the moving antenna process relative to the static antenna. In Figure 4-9b, G is plotted as a function of M for the corresponding case represented in Figure 4-9a. As expected, G has a global maximum at M_{opt} , emphasizing the optimum choice of M . For this analysis, uncorrelated samples of the channel gain were assumed which implies that the trajectory of the moving antenna is such that it can accommodate M_{opt} uncorrelated channel samples. As M is increased for the moving antenna, the diversity gain increases. However, the incremental diversity gain also decreases to small values as M becomes large. To satisfy the $T = M\Delta T$ constraint as M is increased, the coherency of the snapshot signal with coherent integration of ΔT seconds is reduced as each of the M subinterval components

constituting the overall snapshots are essentially noncoherently combined. This eventually becomes the dominant loss factor as M becomes larger. The consequence of these factors is the existence of an optimum value for M .

Figure 4-9a also demonstrates that for larger values of M , $\frac{d\rho_m}{dM} > 0$ which is proven in

Appendix B.

Figure 4-10 shows the required average SNR as a function of the P_D and the number of synthetic array elements M for a given $P_{FA} = 0.01$. $M=1$ indicates the static antenna case. By increasing M , the required SNR for target values of P_{FA} and P_D initially decreases which shows the advantage of utilizing a synthetic array. For larger values of P_D , the advantage of the synthetic array compared to the static antenna becomes dominant. In Figure 4-11, G is plotted as a function of M and P_D . As expected, G has a maximum at M_{opt} , emphasizing the optimum choice of M . The black curve in Figure 4-11 shows the corresponding value of M_{opt} for given P_D values with the interesting observation that M_{opt} increases for larger P_D values.

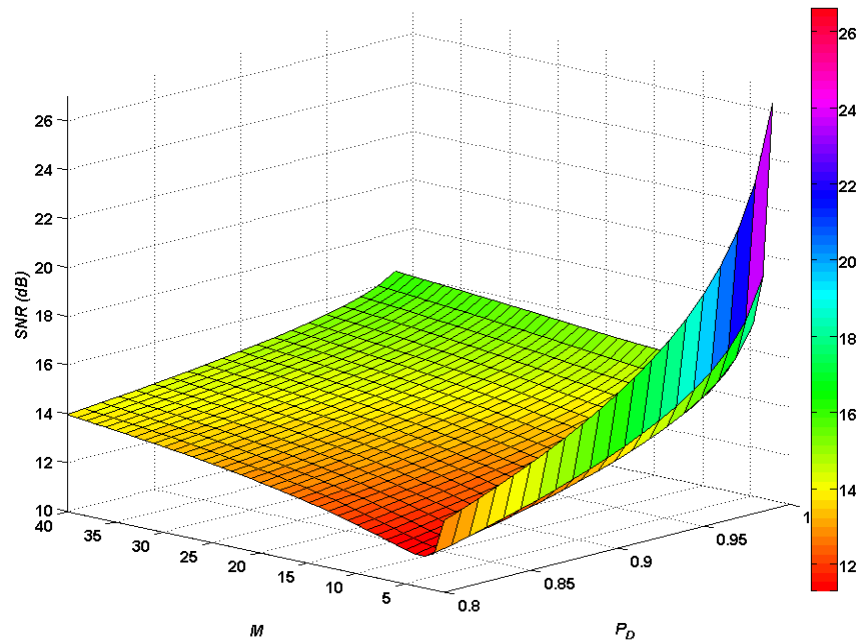


Figure 4-10: Synthetic array required average SNR versus P_D and M for $P_{FA}=0.01$

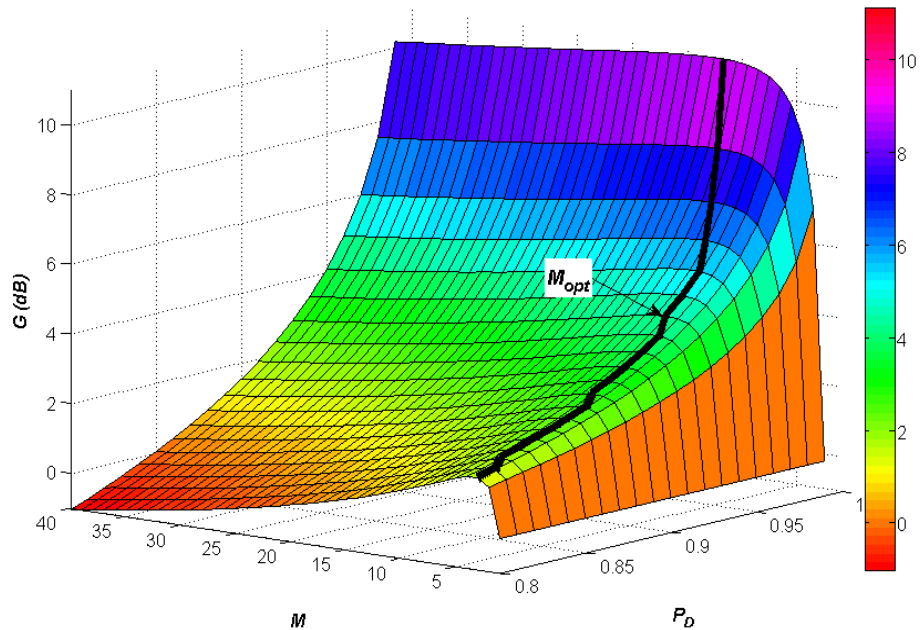


Figure 4-11: Synthetic array gain with respect to static antenna versus P_D and M for $P_{FA}=0.01$. The black line represents the optimum M as a function of P_D

Figure 4-12a shows the optimal value of G as a function of P_D for a given $P_{FA} = 0.01$. As indicated earlier, G increases as P_D is increased, which is due to the increased significance of diversity gain as the target P_D is increased.

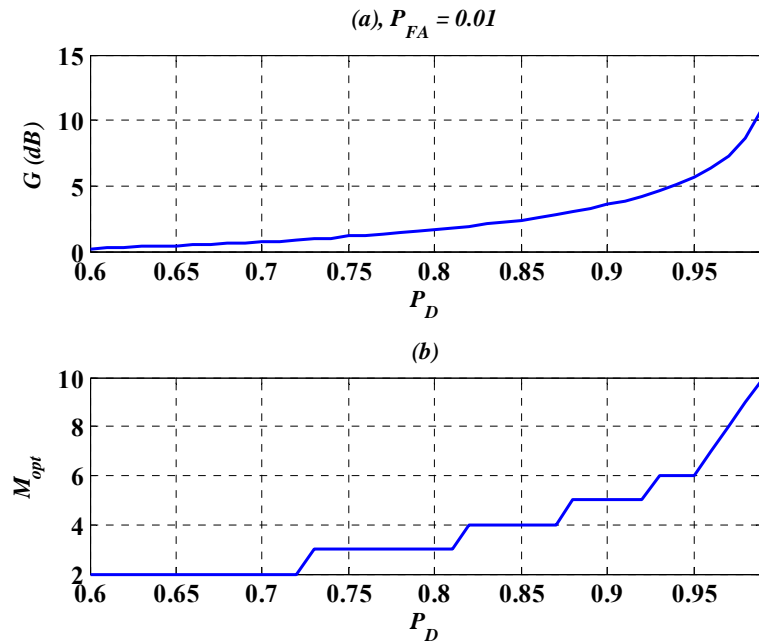


Figure 4-12: (a) Optimum processing gain versus P_D , (b) M_{opt} versus P_D ($P_{FA}=0.01$)

This is equivalent to the increased significance of the diversity gain for lower Bit Error Rate (BER) in communication systems (Proakis 2001). Figure 4-12b shows the corresponding value of M_{opt} with the interesting observation that M_{opt} increases for larger P_D . This implies that the trajectory of the antenna has to be larger to achieve more uncorrelated spatial samples of the channel gain. Note from Figure 4-12a that an optimal G of 11 dB gain is attainable when $P_D = 0.99$ which is a practical target specification.

M_{opt} for this case is 10, which maps into a reasonable trajectory size for carrier frequencies in the 1 to 2 GHz range.

The Mean-Acquisition Time (MAT) is a metric to evaluate the performance of acquisition systems. It is shown in Holmes & Chen (1977) that for a single dwell code searching system based on the flow graph method, the MAT, \bar{T} can be represented by

$$\bar{T} = \frac{2 + (2 - P_D)(q - 1)(1 + \Upsilon P_{FA})}{2P_D} T \quad 4-67$$

where q is the number of cells to be searched, Υ is a penalty factor due to false alarm and T is the integration or dwell time.

Consider fixed target values of P_D and P_{FA} for a synthetic array and a static antenna, respectively. Figure 4-11 showed the additional required SNR for the static antenna to meet these targets. Hence, by assuming a coherent signal model for the static antenna and uncorrelated noise samples in each snapshot, the static antenna has to increase the coherent integration time T by a quantity dictated by G in Figure 4-11 in order to have the same performance as a synthetic array. For example, if G is 3 dB, in order for the static antenna to achieve the same performance (in terms of P_D and P_{FA}) as the synthetic array, its integration time T needs to be increased by a factor of two, which increases the MAT by a factor of two. Hence, the processing gain represented in the Figure 4-11 can be directly used to compare MAT performances of the static antenna and synthetic array. For comparison, the ratio of the required processing time between the static antenna and

the synthetic array to have the same performance, $\bar{T}_{ratio} = \frac{\bar{T}_{static}}{\bar{T}_{synthetic}}$, is shown in Figure

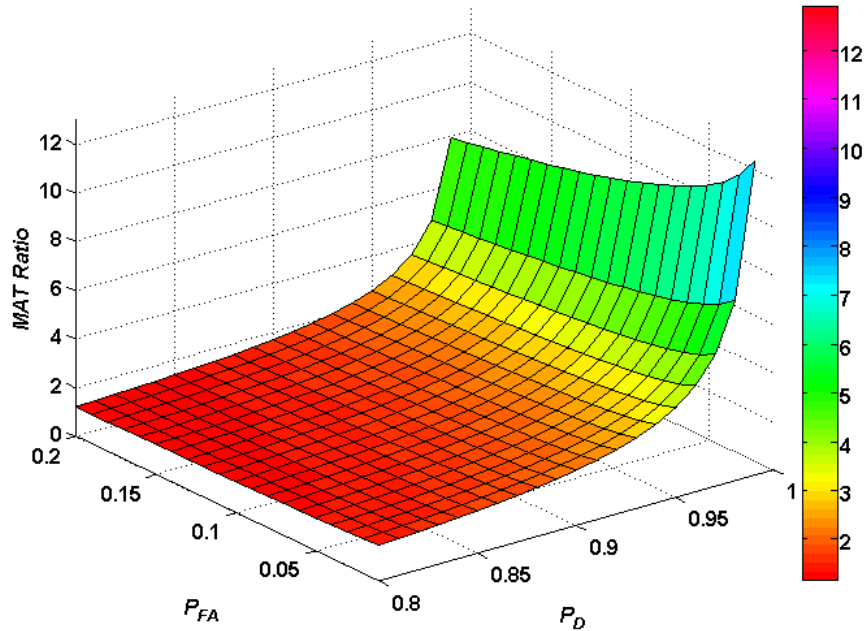


Figure 4-13: MAT ratio of static antenna to synthetic array

The Receiver Operating Characteristics (ROC) curve is a metric to evaluate the detection performance of a receiver. A ROC is a plot of P_D as a function of P_{FA} for specific values of ρ . Figure 4-14 shows the ROC curves for different values of M ($M=1$ represents the static antenna case) for a given $\rho=16$ dB. Figure 4-14 shows there is a significant gain in increasing M from one to 10, resulting in diversity gain. However, there is no advantage to increase M further because the coherency of the process becomes the dominant loss factor causing degradation in the processing performance.

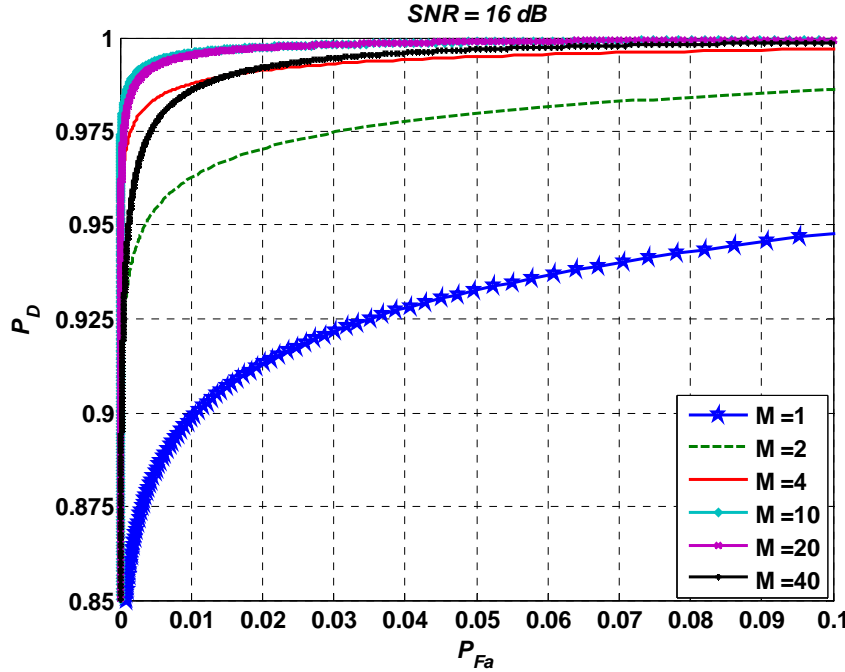


Figure 4-14: ROC curves for different values of M , SNR=16 dB

4.6 Discrete mode synthetic array detection performance and processing gain in correlated Rayleigh fading

In this section, the detection performances of a receiver using a static antenna and a discrete mode synthetic array are investigated for a correlated Rayleigh fading environment. Both the EG and EC combiners are considered for the synthetic array. The covariance matrix of the signal samples \mathbf{C}_s is assumed to be known. If the signal samples are totally correlated such that the rank of \mathbf{C}_s is one, then the EC processing results in the magnitude squared of the coherent sum over the M epoch samples resulting in the same performance as that of the static antenna. At the other extreme, if the M epoch samples are totally uncorrelated such that \mathbf{C}_s is full rank with equal magnitude eigenvalues, then the EC combining reduces to the EG combining.

The performance comparison of the static and synthetic array antennas receivers for correlated Rayleigh fading will be achieved using the following approach:

- Assume fixed target values for P_{FA} and P_D .
- Determine the average SNR, ρ , required to meet these target objectives. These will be denoted as ρ_s , ρ_{EG} , and ρ_{EC} for the static antenna, synthetic array with EG combining and synthetic array with EC combining, respectively.
- The performance advantage of the synthetic array with the EG or EC combining over the single static antenna is then given as $G_{EG} = 10 \log(\rho_s / \rho_{EG})$, $G_{EC} = 10 \log(\rho_s / \rho_{EC})$, respectively.

While the formulation presented thus far is for an arbitrary number of samples M of the synthetic array, the special case of $M=2$ is considered in detail as this is compatible with the experimental results given in Chapter 5. For $M=2$, using Eq. 4-19, the signal covariance matrix is given as

$$\mathbf{C}_s = \frac{\rho}{4} \begin{bmatrix} 1 & r \\ r & 1 \end{bmatrix} \quad 4-68$$

where r is the correlation coefficient which is a function of antenna spacing.

The left column of Figure 4-15 shows the average SNR required to achieve different target values of P_{FA} and P_D given the correlation coefficient, r , which varies between zero and one. The right column of Figure 4-15 also reveals the corresponding gain of the synthetic array processing schemes, G_{EC} and G_{EG} from which several significant observations can be made.

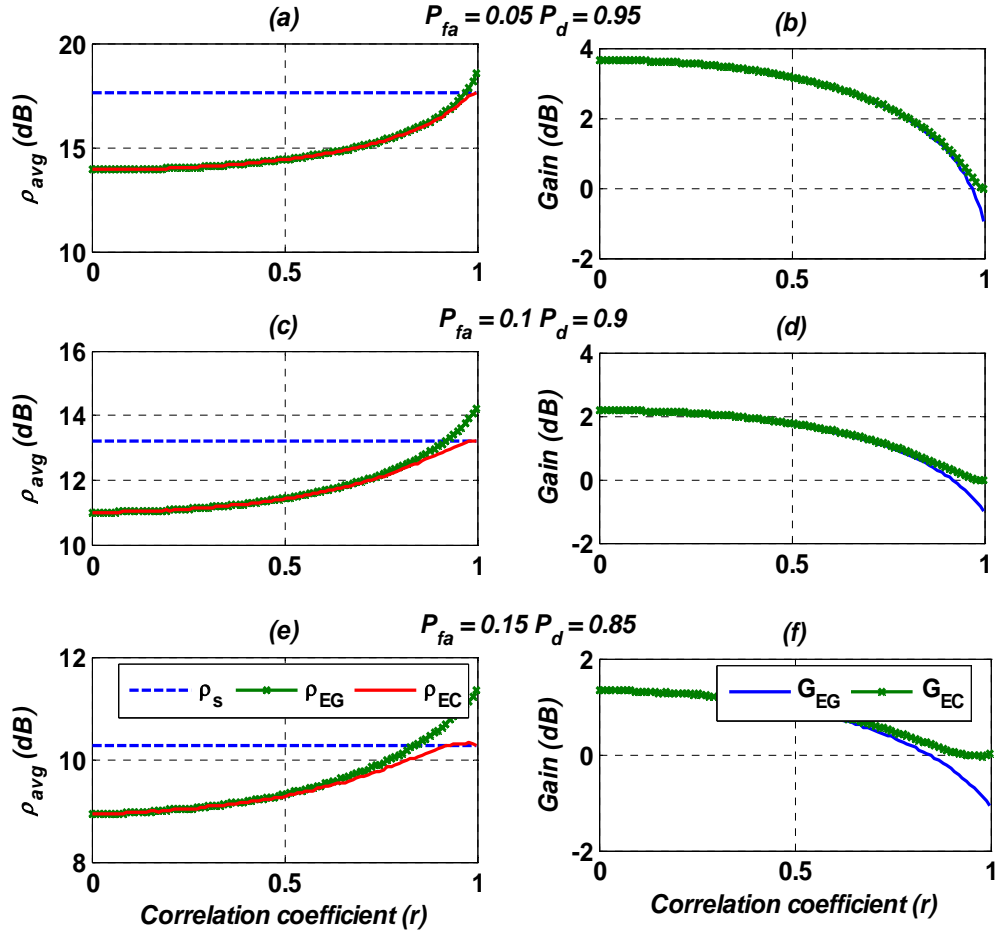


Figure 4-15:(a), (c) and (e) show the required SNR for the stationary and synthetic antenna with EC and EG for target values of P_{FA} and P_D ; (b), (d), and (f) show the processing gain of a synthetic array for the EC and EG combiner

The required average SNR for a single antenna is significantly higher than that of the synthetic array schemes. For the uncorrelated case, $r = 0$, the gain is about 4 dB for $P_{FA} = 0.05$ and $P_D = 0.95$. This is essentially a result of the diversity gain possible. Note that there is no suppression of the channel noise for the dual antenna schemes possible when $r = 0$ as the signal samples emerging from the antennas are uncorrelated. Hence,

the observed gain corresponding to $r = 0$ is strictly diversity gain. When r approaches 1, the signal components emanating from the pair of antennas are correlated and there is no diversity gain. In this case, there is identical gain on the EC scheme with a static antenna. This is a result of the averaging of the pair of uncorrelated noise samples due to the coherent combining of the EC. When high system performance is required there is a negligible advantage of the EC processing over the EG processing for realistically encountered values of the correlation coefficient. This phenomenon is shown in Figure 4-15a and b. Only when r becomes close to 1 there is an advantage in using EC over EG. This has a practical significance in that the parameters ρ and r do not have to be estimated by the receiver. By decreasing the probability of detection and increasing the probability of false alarm, the advantage of using EC becomes more evident. As it is shown in Figure 4-15c, d, e and f, the achievable gains from EC and EG are identical only when the correlation coefficient r is less than 0.8 and 0.7, respectively for ($P_{FA} = 0.1 P_D = 0.9$) and ($P_{FA} = 0.15 P_D = 0.85$). Figure 4-15 demonstrates that the performance of the synthetic array with the EC process is better or identical to that of the static antenna for all range of r .

Figure 4-16 represents ROC curves versus r for given values of SNR (16 dB) and $M=2$.

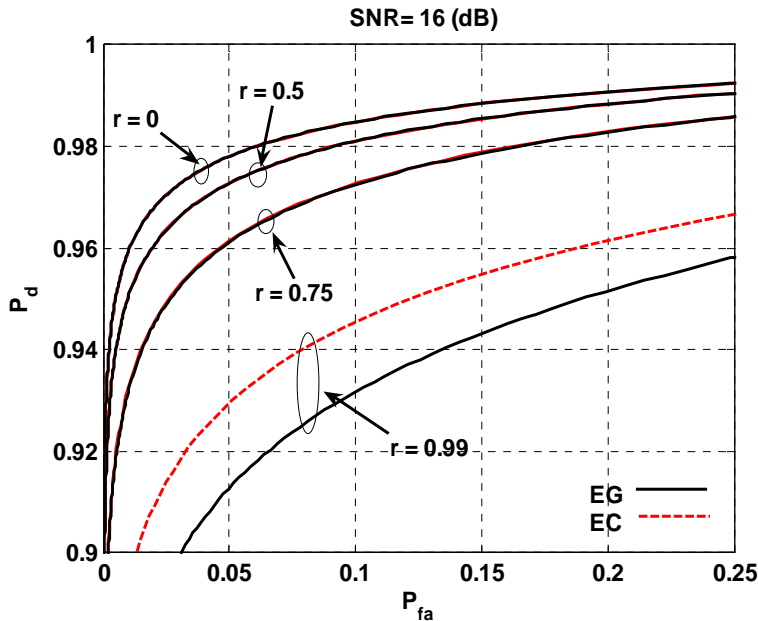


Figure 4-16: ROC curves for given SNR and r

By increasing the correlation coefficient r , the performance reduction due to correlation becomes more apparent. As expected in moderate correlated cases the performances of EC and EG are identical. Figure 4-16 also shows ROC curves for an almost coherent case where $r=0.99$. In this case the performance of EC is superior to that of the EG.

Figure 4-17 shows the synthetic array processing gain based on the EG combiner over the static antenna as a function of P_D and the correlation coefficient r for a given value of $P_{FA} = 0.01$ for $M=2$.

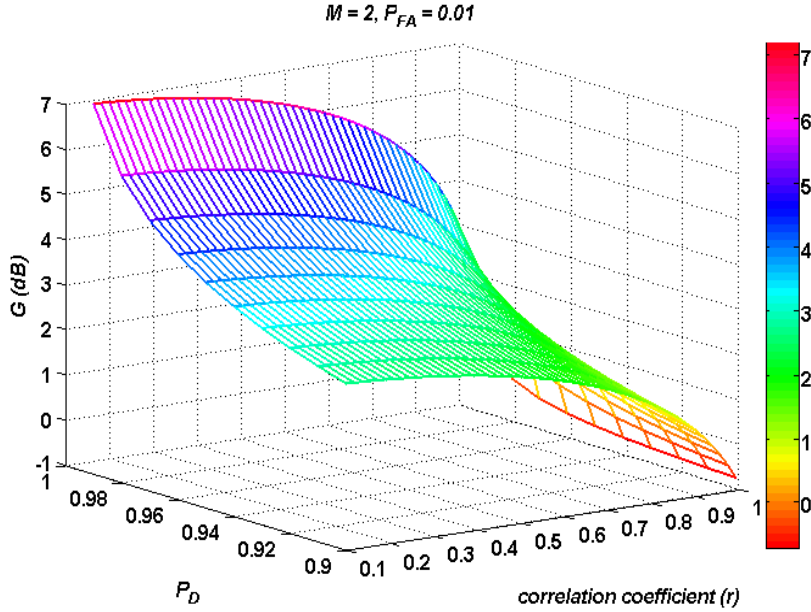


Figure 4-17: Synthetic array gain for $M=2$ versus different values of r and P_D

As expected there is a higher gain in the case of the synthetic array for higher values of P_D . For $r=0$ this gain is about 7 dB for $P_{FA} = 0.01$ and $P_D = 0.99$. When r approaches 1, the signal components emanating from the pair of antennas are correlated and hence, there is no diversity gain.

4.7 Processing gain of the synthetic array in the continuous mode

In Section 4.3, the continuous mode synthetic array signal model in a Rayleigh fading environment was demonstrated. The problem of interest in this section is quantifying the processing gain utilizing the SA method when the receiver has a process signal snapshot of T seconds.

The conditional probabilities of test statistics under H_0 and H_1 z , namely $p(z|H_0)$ and $p(z|H_1)$, will map into a detection performance measured by $\{P_{FA}, P_D\}$ which need to correspond to the given target specifications. In the analysis the value of average SNR for the static and the moving antenna, denoted here as ρ_s and ρ_m respectively, can be evaluated. Consequently, ρ_m can be expressed in terms of its functional dependence on these variables as $\rho_m(\Delta T, M, v, \mathbf{C}_s, P_{FA}, P_D)$. The value of ρ_m can then be compared for different detection schemes. Here, a performance comparison with respect to the stationary antenna with $\rho_s(T, \sigma_A^2, P_{FA}, P_D)|_{v=0, M=1}$ is of interest. Consequently, a specific metric denoted as the normalized processing gain, which is represented by G , is defined as

$$G = 10 \log \left(\frac{\rho_s(T, \sigma_A^2, P_{FA}, P_D)|_{v=0, M=1}}{\rho_m(\Delta T, M, v, \mathbf{C}_s, P_{FA}, P_D)} \right). \quad 4-69$$

If ΔT is too long, significant coherent integration losses will occur. M can be increased to avoid this but at the detriment of increased computational complexity on the part of the SA utilizing the EC (SAEC) process and performance loss in the SA utilizing the EG (SAEG) combiner. Of interest is to determine the appropriate size of M .

Figure 4-18a shows the required average SNR ρ_m for SAEC as a function of the target parameters $P_D = 0.95$ and $P_{FA} = 0.01$ versus a constant velocity of the receiver v with the interesting observation that there is a global minimum. Hence, there is an optimal value of v for which ρ_m is minimum. In Figure 4-18b, G is plotted as a function of v for the case represented in Figure 4-18a. As expected, G has a global maximum

emphasizing the optimum choice of v . In this performance investigation the value of M is chosen as $M = \lceil d/4 \rceil$ where d is the normalized aperture of the array and $\lceil \bullet \rceil$ rounds up to the nearest integer. Figure 4-18c shows M for different values of v . As v is increased for the moving antenna, the diversity gain increases. However, the incremental diversity gain also decreases to small values as v becomes large. To satisfy the $T = M\Delta T$ constraint and as M is increased, the coherency of the snapshot signal with coherent integration of ΔT seconds is reduced as each of the M subinterval components constituting the overall snapshots are essentially non-coherently combined. This eventually becomes the dominant degradation factor as M becomes larger. The result of these factors is the existence of an optimum value for v . It should be noted that the required average SNR ρ_m in the range of $v \in [0, 0.25]$ is slightly increased. This is due to the fact that in this range, M is 1. Hence, there is a coherency loss due to the antenna motion but the receiver does not take advantage of the potential diversity gain. The result of this is increasing in the ρ_m . As long as M becomes two at $v=0.25$, the ρ_m drops by 3 dB as a result of diversity gain.

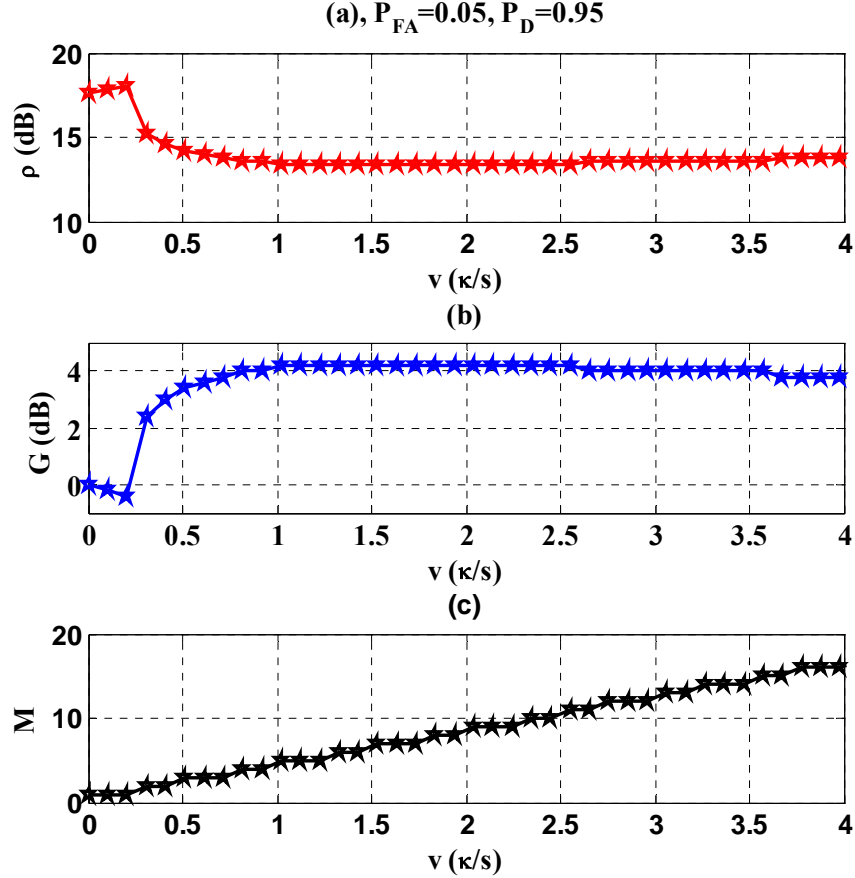


Figure 4-18: a) Required average SNR, b) Gain, and c) number of M versus different values of v

Figure 4-19 shows the P_D of SAEC process for $T=1$, $P_{FA} = 0.05$, and $\rho = 15$ dB versus receiver velocity and different values of M . As it is shown for $M=1$, by increasing the receiver velocity the detection performance degrades. This is due to the coherency loss. By increasing M the detection performance improves because the spatial snapshots now contain spatial diversity, which can enhance the detection performance.

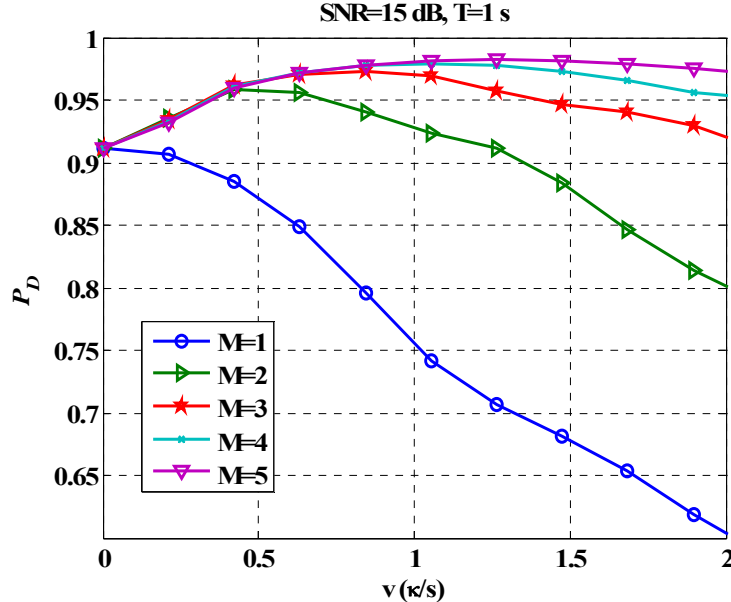


Figure 4-19: P_D of a moving receiver for given $T=1$, $P_{FA} = 0.05$, and $\rho = 15$ dB versus velocity of the receiver and different values of M

An interesting observation is that for each value of M there is a specific value of v that provides maximum P_D , which is approximately identical to $v = M/4T$. Figure 4-20 shows the probability of detection versus receiver velocity and SNR for a given $P_{FA} = 0.05$. As expected, P_D has a maximum for each value of SNR, emphasizing the optimum choice of v . The black curve in Figure 4-20 shows the corresponding value of v denoted here as v_{opt} for given P_{FA} values with the interesting observation that v_{opt} increases for larger SNR values.

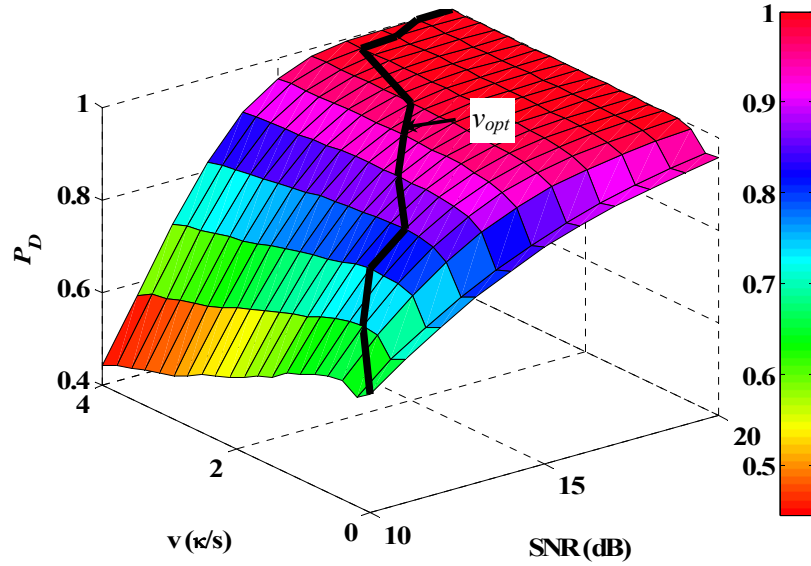


Figure 4-20: P_D versus receiver velocity and SNR for a given $P_{FA} = 0.01$ and $T=1\text{ s}$

Next consider that the target performance metrics are fixed at $P_{FA} = 0.01$ and $P_D = 0.95$. The problem of interest is determining the minimum value of T for different receiver velocities and SNR per second. Figure 4-21 shows required T versus v and SNR per second.

Consider a moving antenna scenario where a single antenna captures spatial-temporal samples. For a given trajectory of the antenna, it is insightful to compare the performance of the EC and the EG combining for different values of M . To this end, consider a multipath channel, which is characterized by the ring of scatterers model. Figure 4-22 shows the ROC curves of EC for different values of M .

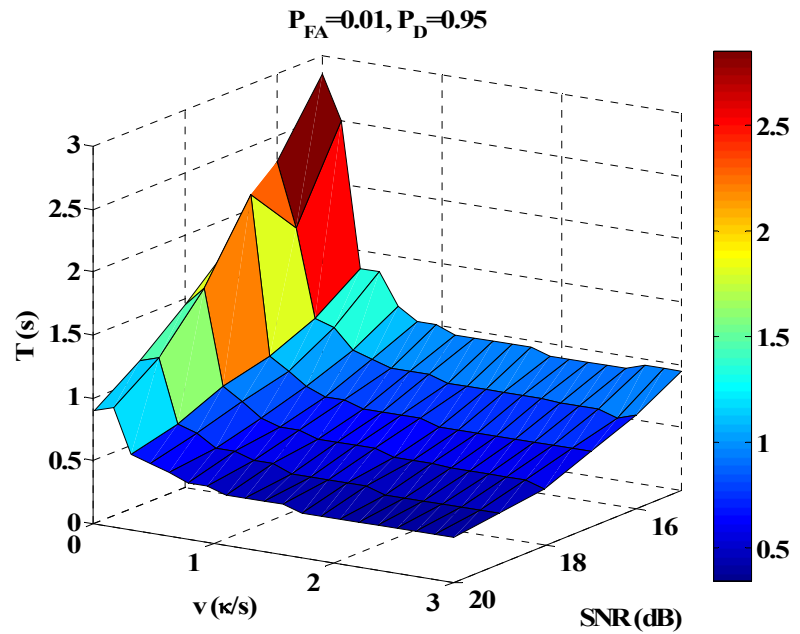


Figure 4-21: Required T versus v and SNR per second for detection targets of $P_{FA} = 0.01$ and $P_D = 0.95$

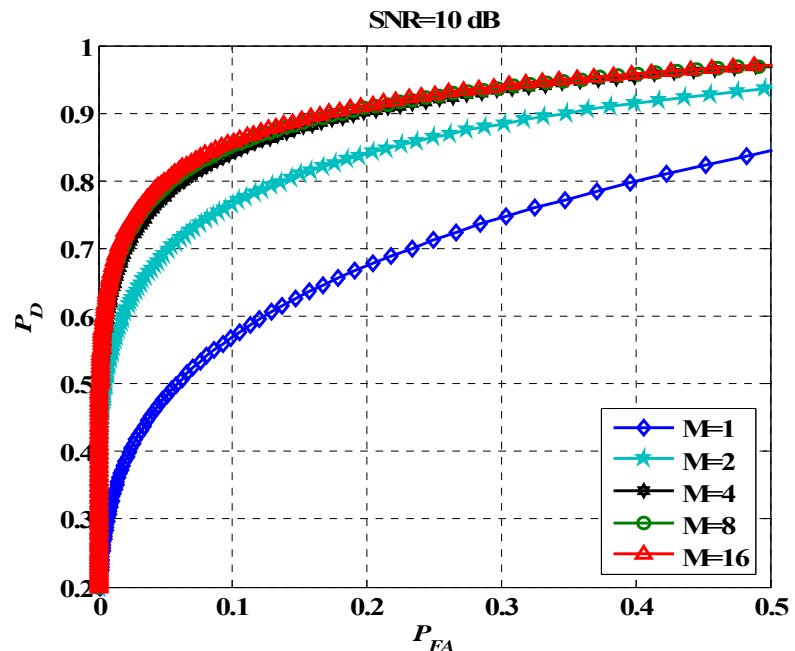


Figure 4-22: ROC curves of EC, SNR=10 dB and $d = \kappa$

As mentioned before, in the ring of scatterers model, the covariance matrix has approximately $4d$ non-zero eigenvalues and corresponding eigenvectors. When M is one, the EC process does not use all DOFs available in the signal snapshots, resulting in a performance loss. By increasing M the performance of EC becomes better as the number of spatial samples M approaches $4d$. As it is shown in Figure 4-22, the performance of EC does not change for $M > 4d$.

The PDF of the test statistics of EC for the given scenario presented in Figure 4-22 is shown in Figure 4-23. For a given trajectory size and signal covariance model, the PDF of the EC test statistics under H_0 and H_1 for $M=1$ to $M=4$ changes with a Chi-Squared distribution with 2 DOFs to 8 DOFs. This change provides diversity gain and hence enhancement in detection performance. However, by increasing the spatial samples M from 4 to 16, the PDF shape does not change. On the other hand, EC combines different spatial samples somehow to provide optimum diversity and coherency gain.

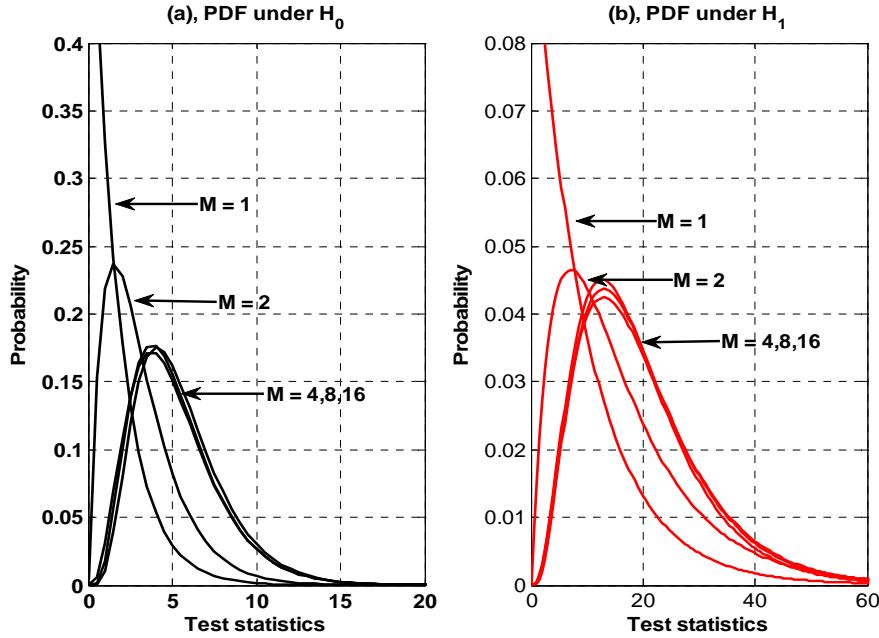


Figure 4-23: PDF of EC for different values of M

Figure 4-24 shows the performance of the EG combiner for a given trajectory and signal covariance model versus different values of M . When $M \leq 4d$, both EC and EG have the same performance. In this area, the performance of EC and EG combiner improves by increasing M . The best performance of the EG combiner is achievable when $M = 4d$. For $M > 4d$ the detection performance of EG decreases. The reason for this is that for a given trajectory and channel model, there is a maximum diversity gain characterized by the number of relevant eigenvalues of the signal covariance matrix. In this example, the rank of the signal covariance matrix does not go beyond four when increasing M . Hence, by increasing M not only there is no diversity gain but also the performance suffers from a loss of signal coherency. The PDF of test statistics of EG for average SNR 10 and $d = \kappa$ is shown in Figure 4-25.

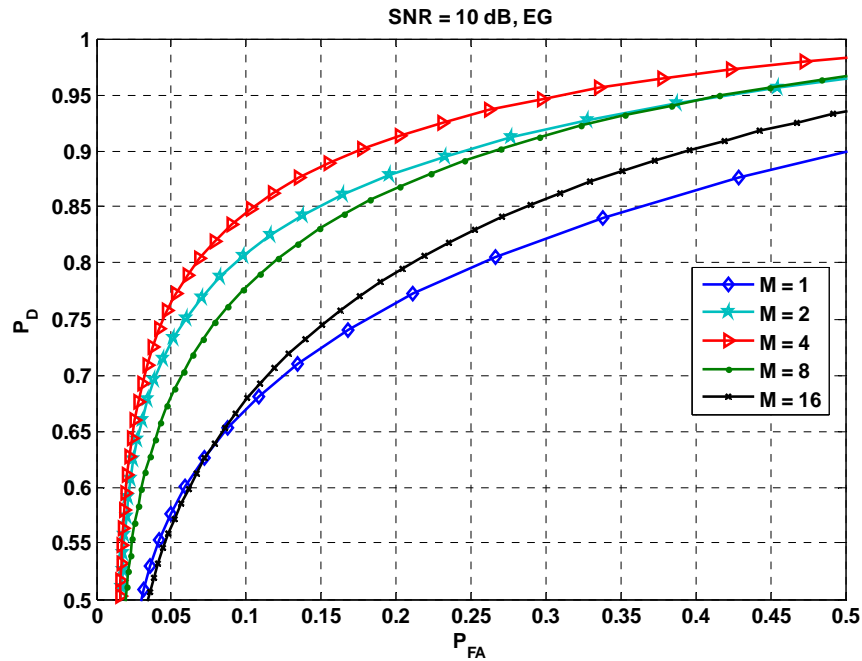


Figure 4-24: ROC curves of the EG combiner, $\text{SNR}=10 \text{ dB}$ and $d = \kappa$

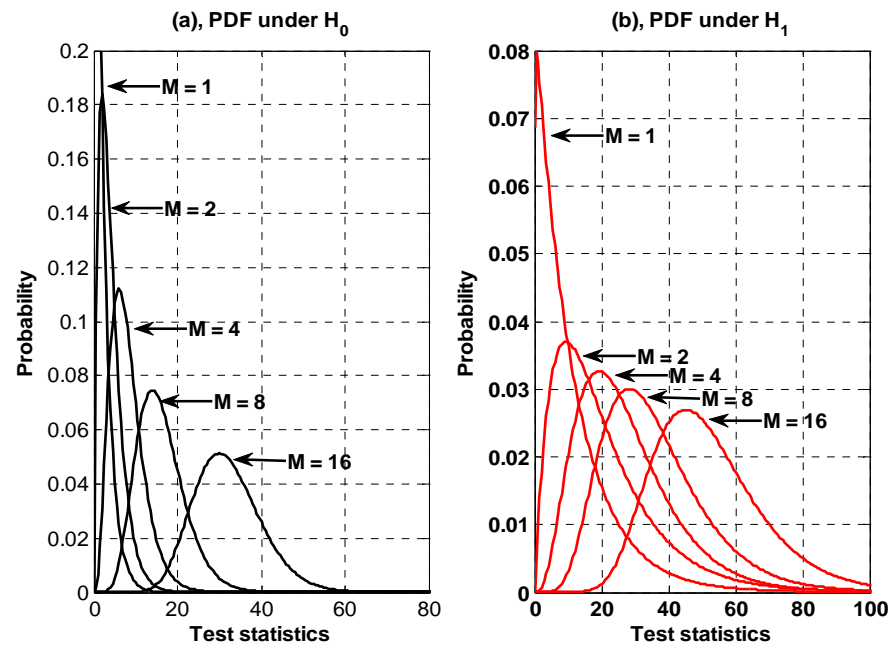


Figure 4-25: PDF of EG for different values of M

4.8 Synthetic array implementation considerations

The main assumption of a diversity system is the reception of statistically independent signals in each diversity branch. Thus, in a spatial diversity system the antenna spacing should be selected accordingly to satisfy this assumption. Based on this assumption, the optimum processing gain and the number of spatial samples for the moving antenna were determined. As it was revealed previously, the optimum processing based on the LRT with a Gaussian signal model results in the EC formulation of Eq. 4-42 that is completely defined by \mathbf{C}_s and \mathbf{C}_n , the signal and noise covariance matrices given by Eq. 4-17 and Eq. 4-18, respectively. In the Rayleigh fading channel, which is modeled by ring of scatterers, the signal covariance matrix is defined by Eq. 4-19. Hence, the \mathbf{C}_s depends only on pair wise distance between spatial sampling points, denoted here as d , which is determined by the approximate velocity and time interval between samples. Thus, no matter the array shape and configuration, as long as any pairs of spatial samples have a spacing more than approximately half of the wavelength (based on the signal covariance matrix model), the processing gain values presented in Section 4.1 are valid. Hence, the proposed method is applicable to an arbitrary geometry synthetic array with uniform and non-uniform spacing. This resolves the problem of precise trajectory estimation and array calibration, which are practical implementation difficulties associated with beamforming techniques (Van Trees 2002). However, in practice the receiver requires a rough estimate of the motion velocity such that it can reject highly correlated samples due to insufficient spatial separation. This can be accomplished by

using a consumer grade accelerometer device to estimate the spatial distance between samples by integrating the acceleration measurements twice.

To analyze the sensitivity of the SA method to a trajectory estimation error, a scenario with two antenna positions is considered. Since the signal correlation matrix is a function of the antenna spacing, considering some errors in the trajectory estimation unit, the processed spatial samples may become correlated. Hence, the EG detector is no longer an optimal process. However, the EG combiner has numerous implementation benefits and it is preferred for implementation in practice. The performances of the EC and the EG combiner for different correlation coefficient values of the Rayleigh channel were compared in Section 4.6. It was shown that for moderate correlation coefficient values, the performances of the EC and EG combiner are almost identical. Hence, the EG combiner is utilized herein. The EG combining detection performance for correlated channels was given in Section 4.4.2.2. Based on this, the processing gain of the moving antenna with respect to the static antenna can be evaluated for different channel correlation coefficients.

Normalized gain degradation (NGD) is defined as a designing metric to quantify the performance degradation of a diversity system due to correlated fading. NGD is defined by the percentage of the diversity gain difference between uncorrelated and correlated processes normalized by the diversity gain in the uncorrelated case

$$NGD = \left(\frac{G_{EG}^{r=0} - G_{EG}^{r=q}}{G_{EG}^{r=0}} \right) \times 100, \quad q \in [0, 1] \quad 4-70$$

where $G_{EG}^{r=0}$ is the EG combiner processing gain for the uncorrelated case.

Figure 4-26a shows the relative processing gain of the moving antenna with respect to the stationary one denoted as G for different values of the correlation coefficient r versus the probability of detection P_D . Figure 4-26b gives the NGD due to signal correlation.

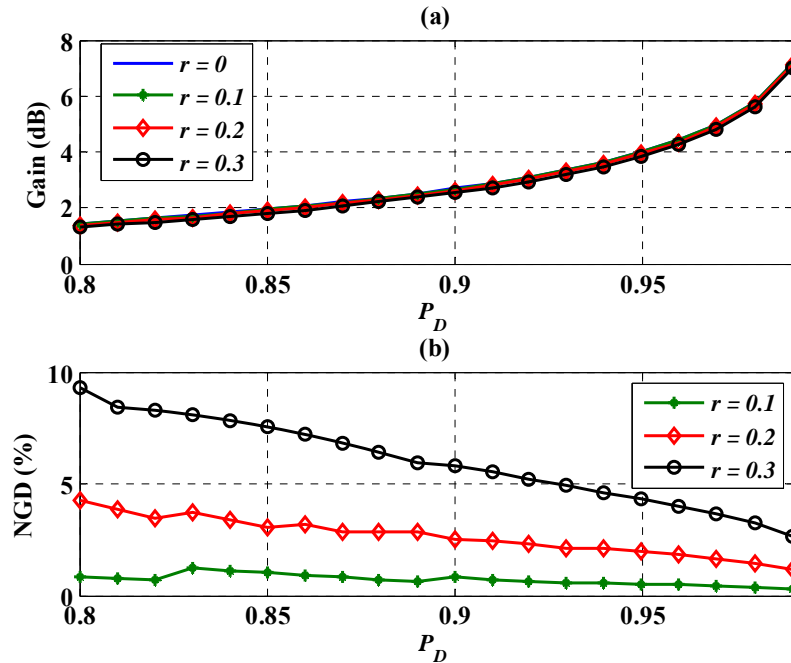


Figure 4-26: (a) Processing gain, and (b) normalized gain degradation for different values of r versus P_D

Figure 4-26, also shows that, by increasing r , the performance of the proposed method degrades. This performance reduction is more severe for low values of P_D . For nominal detection performances of $P_{FA} = 0.01$ and $P_D = 0.99$, NGD values are about 1, 2 and 3 percent for $r = 0.1, 0.2$, and 0.3 , respectively, which is negligible.

Figure 4-27 shows NGD for the desired range of P_D and correlation coefficients.

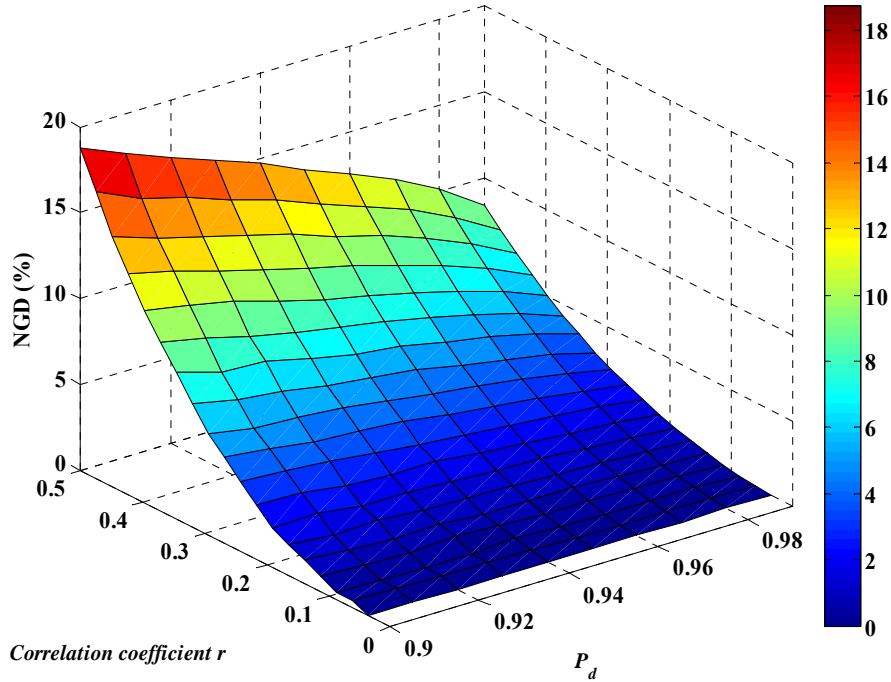


Figure 4-27: NGD for different values of correlation coefficients and P_D for $P_{FA}=0.05$

As it was expected, increasing r results in performance degradation. This performance reduction is more severe for low values of P_D . Figure 4-27 also gives a designing perspective regarding the performance degradation. As an example if a synthetic array diversity system must work within 90 % of the maximum diversity gain, the amount of the correlation coefficient, which the diversity system can tolerate, could be determined directly from the figure. For a nominal detection performance of $P_D = 0.98$, to have NGD value within 10 percent, the correlation coefficient should be less than 0.45, which means the antenna spacing should be more than one quarter of the carrier wavelength in a ring of scatterers model. Hence, by appropriate design of the

trajectory estimation unit, the gain degradation due to a trajectory estimation error can be minimized.

Although the performance of the EG combiner in moderate correlation cases has almost the same performance as the EC, in highly correlated circumstances the performance of the EG combiner becomes worse than that of the static antenna which means there is no advantage in moving the antenna. This happens when the processing gain of the EG combiner shown in Figure 4-15 goes below 0 dB. Thus, it is interesting to determine values of r for which zero crossing occurs. Figure 4-28 shows values of correlation coefficient for a range of target detection performance metrics $\{P_D, P_{FA}\}$ for which the detection performance of the synthetic array based on the EG combiner become worse than the use of a static antenna.

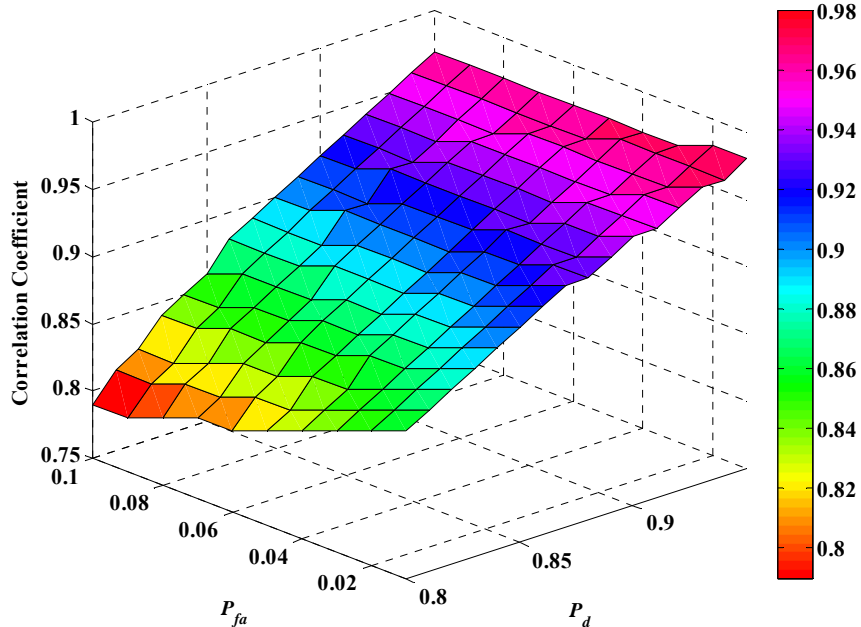


Figure 4-28: Values of the correlation coefficient where the performance of EG combiner becomes worse than static antenna

By requiring higher detection performance, the zero crossing occurs at higher values of the correlation coefficient. As an example when $P_D=0.99$ and $P_{FA}=0.01$ the zero crossing happens at $r=0.98$; however for $P_D=0.8$ and $P_{FA}=0.1$, the zero crossing occurs at $r=0.8$. Figure 4-28 shows upper boundaries of the correlation coefficient values for which the EG combiner provides the gain respect to the static antenna. Based on the results of the Figure 4-28, if the correlation coefficient is less than 0.8, the synthetic array utilizing the EG combiner provides some processing gain over the static antenna. To satisfy this condition in a Rayleigh fading environment with the ring of scatterers model, pair wise antenna spacing must be greater than 0.15 wavelength.

4.9 Conclusions

The detection performance of a narrow bandwidth wireless signal subjected to Rayleigh fading has been considered for a single antenna handheld receiver. Of specific interest was to determine the merits of moving the antenna while capturing a snapshot of the signal. This provides diversity gain but also incurs a loss due to the spatial decorrelation of the signal. Two operating modes for the synthetic array, namely discrete and continuous, were considered. It was shown that a substantial processing gain is possible by moving the antenna relative to maintaining the antenna in a static position. For a practical usage case, up to 11 dB processing gain relative to a static antenna was demonstrated as being achievable. Furthermore it was demonstrated that there is an

optimum spatial samples and receiver velocity to utilize that is a function of the target parameters P_{FA} and P_D .

The performance enhancement of a synthetic antenna array as compared to a static antenna subjected to a correlated Rayleigh fading environment demonstrated in Section 4.4.2.2. It was shown that, in such fading environments, a synthetic antenna with two elements for practical target performance values provides a net gain advantage of 4 dB, which is comprised essentially of diversity gain. More spatial samples would provide further gains due to further diversity gains. If the correlation of the signal samples is increased then the diversity gain diminishes eventually to the point where the moving antenna has no advantage over the static antenna. Of interest was the determination of the performance degradation of the EG combiner due to the correlation with respect to an optimal EC approach. The results show that in moderate correlation environments, the performance of EC and EG combiners are almost identical. The detection performance of the synthetic array in continuous mode was demonstrated in Section 4.7. In Section 4.8 the synthetic array sensitivity to trajectory estimation was investigated.

The synthetic array concept introduced in this chapter can be applied to the wireless locations systems to enhance signal detection and parameter estimation in indoor and dense multipath environments.

CHAPTER 5: EXPERIMENTAL RESULTS OF SIGNAL DETECTION ENHANCEMENTS IN INDOOR FADING ENVIRONMENTS

In the previous chapter, the theoretical gain of the synthetic array relative to the static antenna was determined based on the idealized Rayleigh fading model with the assumption that the channel gain $A(\mathbf{p})$ is a circular normal random process with respect to the antenna position \mathbf{p} but temporally static with respect to the snapshot interval T . This led to usable expressions for the relative processing gain G . The experimental measurements described in this chapter attempt to partially validate the application of these assumptions in the context of the synthetic array for indoor environments. The objective then is not the modeling of indoor fading environments, which has been aptly and extensively published (Rensburg & Friedlander 2004, Colburn et al 1998, Hyeon et al 2008). Rather, the objective of the experimental measurements is to determine the processing gain G for a selection of typical indoor locations (otherwise selected at random) and compare it with its theoretical value represented in Chapter 4. Experimental measurements involving indoor multipath scenarios are plagued with the issue of attaining statistical significance.

The theoretical aspects presented so far are developed for a general narrowband signal. In this chapter, the theoretical findings will be verified based on two different Code Division Multiple Access (CDMA) signal structures, namely the IS-95 (Liberti & Rappaport 1999) and Global Positioning System (GPS) (Kaplan & Hegarty 2006) signals. In Section 5.1 experimental results of the discrete mode synthetic array based on the CDMA IS-95 signals are presented. Section 5.2 gives experimental results of GPS

detection enhancement utilizing the discrete mode synthetic array. The field measurements results of GPS signals in indoor environments based on the continuous mode synthetic array are represented in Section 5.3.

5.1 Field measurements of the discrete mode synthetic array detection performance in indoor environments utilizing CDMA IS-95 signals

Experimental measurements represented in this section are based on indoor reception of CDMA IS-95 pilot signals. These signals are used to verify that the processing gain determined for the moving antenna based on the derived theoretical formulations are indeed representative of performance in typical indoor conditions.

5.1.1 CDMA IS-95 signal structure and receiver architecture

The CDMA IS-95 standard is one of the most widely deployed CDMA cellular technology in North America (Liberti & Rappaport 1999). This standard includes the IS-95A standard operating at 800 MHz and the JSTD-008 standard designed for 1900 MHz Personal Communications Service (PCS) systems. The forward channel of the IS-95 standard includes four sub-channels: Pilot channel, Sync channel, Paging channel, and Traffic channel. The pilot channel continuously broadcasts a known signal to provide mobile stations a robust time, frequency, and phase reference for demodulation in other channels (Liberti & Rappaport 1999). In the IS-95 cellular system all base stations (BS) transmit signals at the same frequency with the same Pseudo Random Noise (PRN)

sequence. However, each BS transmits pilot signals with a specific offset which is known to the MS receiver. This offset is a multiple of 64 chips. The length of the pilot sequence is 32768 chips with the chip rate of 1.2288 Mchip/s. Hence, each period of the pilot signal takes 26.67 ms. The pilot channel has no data modulation and consists of only in-phase and quadrature phase PRN codes. Typically, 15-20 % of the total BS power is allocated to the pilot channel. Due to strength and data-less property of the pilot channel, it is a desirable signal for channel parameter estimation and position estimation applications. All BSs in the IS-95 system are synchronized with the GPS 1 Pulse Per Second (PPS) signal. Table 5-1 provides the characteristics of the pilot CDMA IS-95 signals.

Table 5-1: CDMA IS-95 pilot characteristics

Chip rate	Bandwidth	Modulation	Code length	Code period
1.2288 Mch/s	1.25 MHz	QPSK	32768 chip	26.67 ms

The corresponding receiver correlates the received signal with a known PRN sequence to estimate signal parameters. The PRN code acquisition is a procedure to determine the received signal code phase with respect to the known replica code. The PRN code designed to modulate the transmitted signal is a periodic code with the length of L. One property of PRN sequences is that the cross-correlation of the PRN sequence is almost zero except in the zero lag. The objective is to find the instance at which the correlation of the local PRN code and the received signal provides the correlation peak. The estimated correlation peak gives an estimate of the Channel Impulse Response

(CIR). This searching procedure is often referred to as PRN code acquisition. The baseband received signal can be represented as

$$r(k) = \sqrt{P} s_o(k - \tau) e^{j2\pi\Delta f} + n(k) \quad 5-1$$

where P denotes the total average received power and Δf is the frequency difference between transmitted and received signals. This frequency offset may be due to a relative motion between the transmitter and receiver (Doppler effect) or to a difference in the transmitter-receiver local oscillators. This frequency offset can be removed by a maximum likelihood search over the range of the frequency offset. The received signal is correlated with the replica code to estimate the code phase. The m -th output of the correlator is

$$x(m) = \left| \frac{I}{L} \sum_{i=0}^{L-1} r(i) s_o^*(i-m) \right|^2 \quad 5-2$$

Figure 5-1 shows the block diagram of the IS-95 PRN acquisition scheme where s_{o_I} and s_{o_Q} represent two orthogonal pilot PRN sequences transmitted with QPSK modulation.

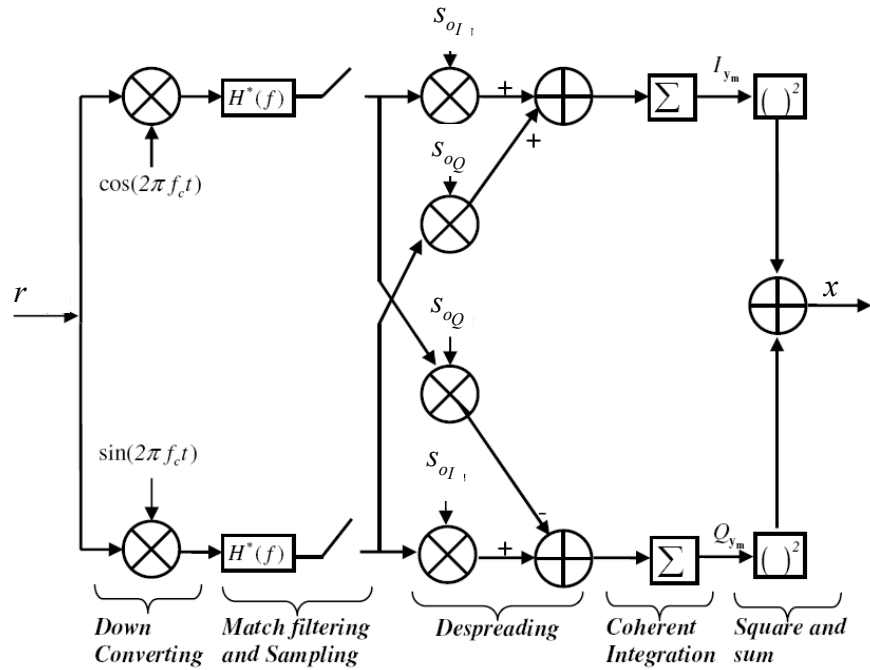


Figure 5-1: Down conversion and PRN code despreading

The acquisition process utilized in this thesis is based on the Fast Fourier Transform (FFT) approach which is shown in Figure 5-2 (Mogaddam 2007).

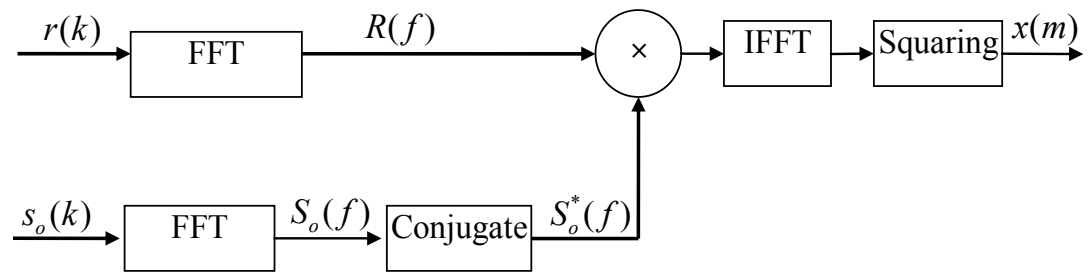


Figure 5-2: FFT based correlation method

The acquisition procedure in general is a two-dimensional search in both code and frequency. Figure 5-3 shows a typical output of the correlation function of actual CDMA IS-95 signals. It shows a two-dimensional space over code delay and frequency offset. The acquisition results shown in the figure are for the static receiver case. Hence, all BSs peak at approximately the same frequency offset $\Delta f = -25$ Hz and different time delays.

Figure 5-4 shows the normalized correlation output for one period of CDMA IS-95 signals. Each strong peak represents a distinct BS.

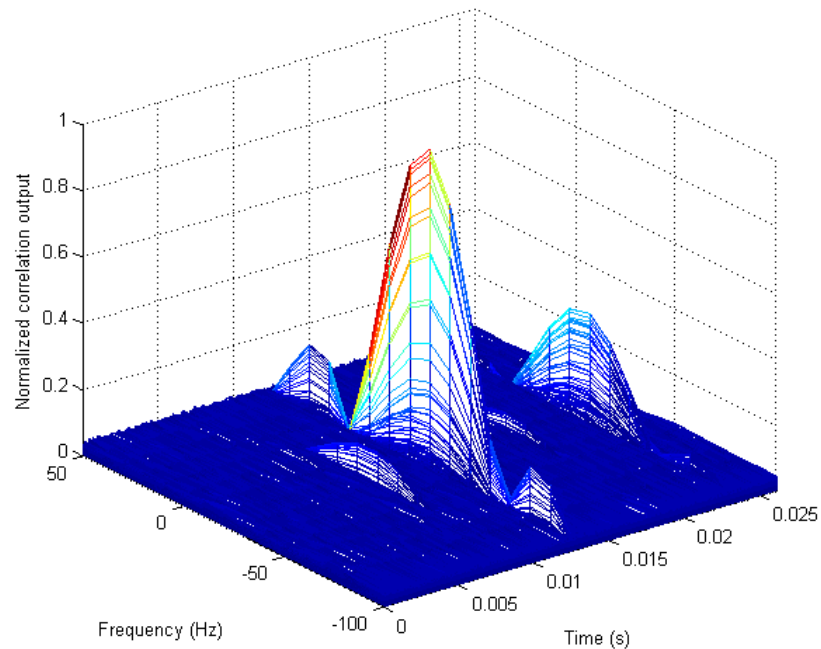


Figure 5-3: IS-95 correlation function over two-dimensional hypothesis search

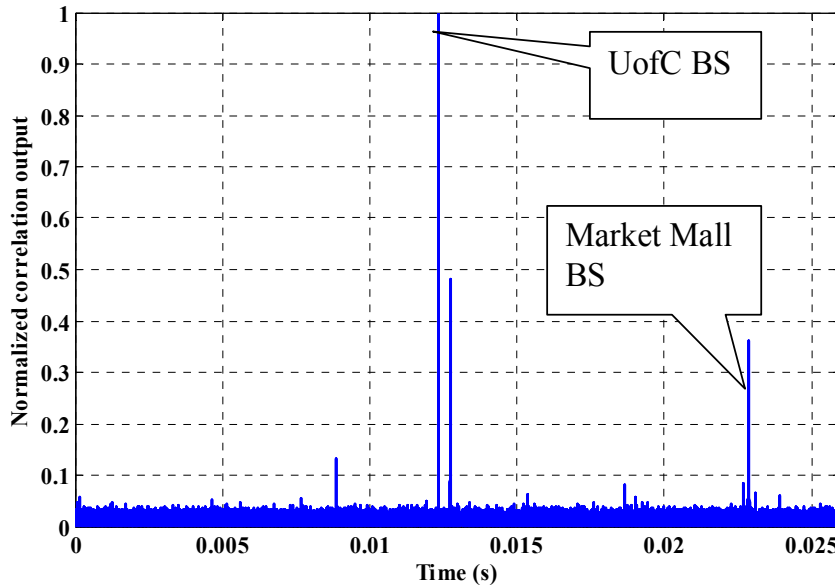


Figure 5-4: Normalized correlation outputs for a period of a CDMA IS-95 signal

As mentioned earlier, in the CDMA IS-95 systems all BSs are synchronized with a GPS 1PPS signal. Hence, after despreading by knowing the chip offset allocated to BSs, each BS can be uniquely identified. As shown in Figure 5-4, two strong BSs namely UofC (University of Calgary) and Market Mall near the data collection setup are detected.

5.1.2 Data collection and experimental results based on the CDMA IS-95 pilot signals

In this experiment a commercial receiver is tuned to capture CDMA signals at 1947.5 MHz. CDMA signals received at the antenna are amplified, filtered, down-converted and

sampled by a 10 MHz digitizer board. The utilized receiver is a National Instrument (NI) which down-converted the CDMA signals to an Intermediate Frequency (IF).

Figure 5-5 shows the data collection setup. A vertically polarized omni-directional antenna in the horizontal plane was mounted on a linear motion table to capture the CDMA pilot signals. Figure 5-6 represents the vertical pattern of the antenna. Theoretical findings presented in previous sections were based on the ring of scatterers model. Although in general the indoor propagation model may be characterized by a sphere of scatterers, due to the vertical pattern of the antenna shown in Figure 5-6, the scatterers geometry can be approximately characterized by a ring of scatterers model (Van Trees 2002).

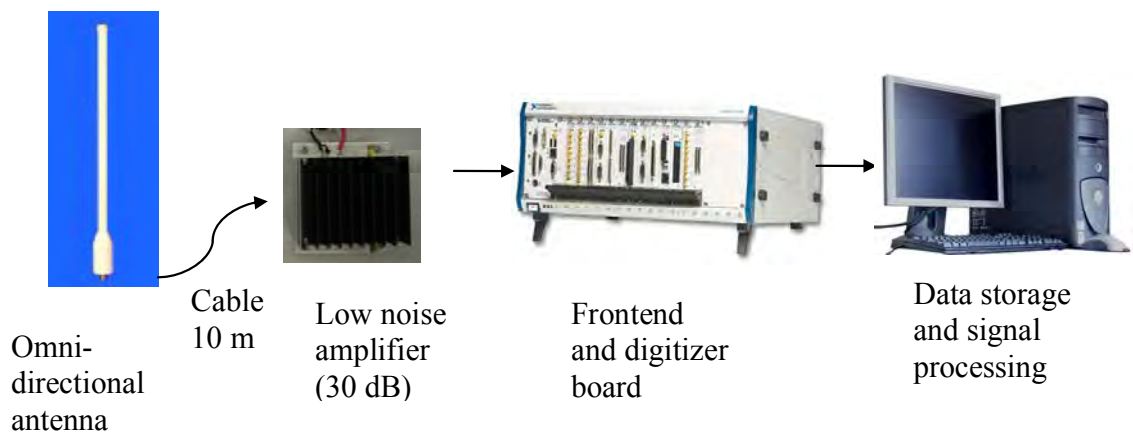


Figure 5-5: Data collection setup

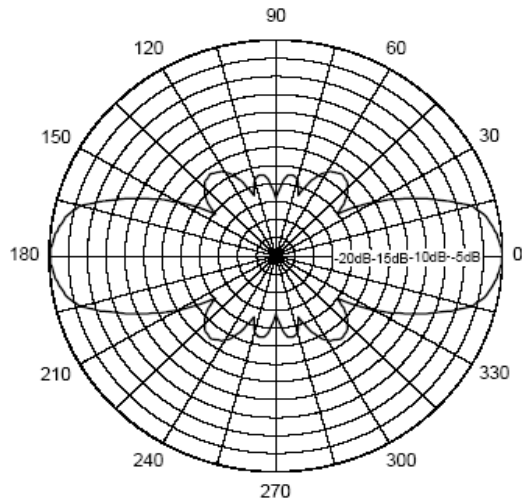


Figure 5-6: Vertical plane pattern of the antenna

Two sets of data were collected at different locations in a three-story office building on the University of Calgary campus, namely the CCIT building, which is an annex of the Schulich School of Engineering complex.

Figure 5-7 shows the data collection locations.

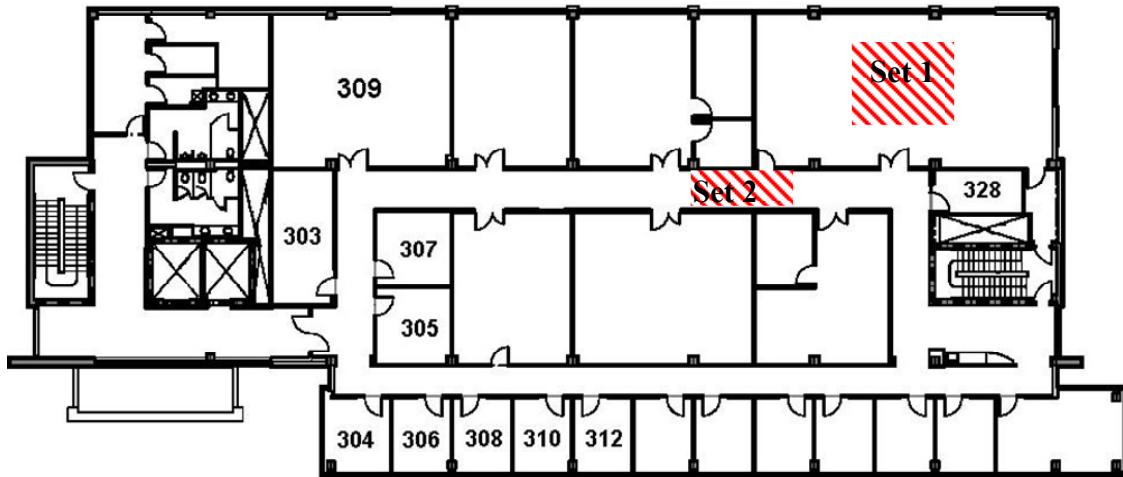


Figure 5-7: Layout of office floor with the hashed area indicating the locations used for collecting experimental data

Figure 5-8 shows a photograph of the data collection environments and measurement equipment used. Table 5-2 gives the characteristics of the data collection scenarios. The acquisition process for each code delay can be formulated as a binary hypothesis test problem where the objective is to determine the correct code phase between the received and replica signals and discarding all incorrect code phases under the constraint of a tolerable rate of false detections. The condition where the code phase of the locally generated despreading signal is different from that of the incoming signal corresponds to the H_0 state where equivalently there is no discernable signal.

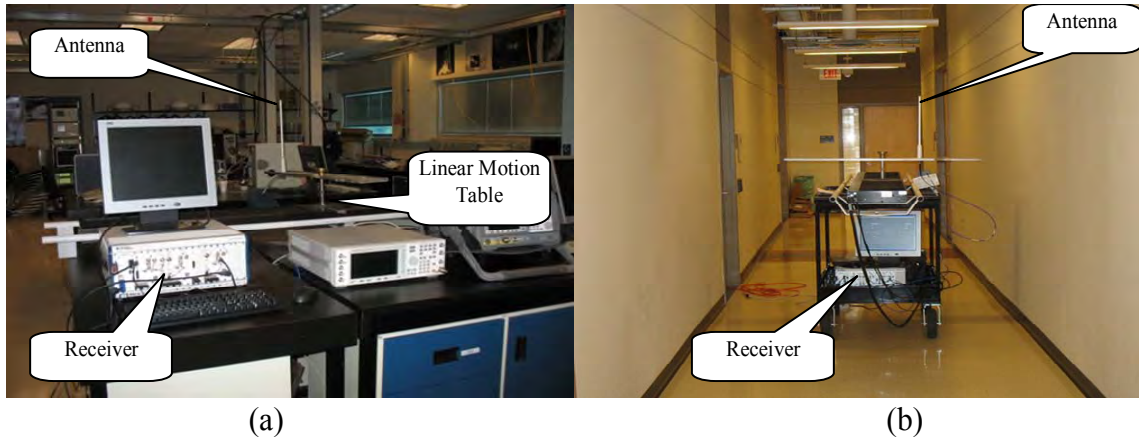


Figure 5-8: Data collection environment and measurement equipment (a) data set 1 (b) data set 2.

Table 5-2: Characteristics of IS-95 data collection scenarios

	Date	Sampling rate	IF Frequency	Data collection duration
Data set 1	1 June 2008	5 MHz	500 KHz	300 s
Data set 2	29 August 2008	10 MHz	3.5 MHz	300 s

In this state the P_{FA} can be evaluated. Likewise, if the code phase of the locally generated despreading signal is the same as that of the incoming signal, then it corresponds to the H_I state where the signal is present from which the P_D can be evaluated.

5.1.3 Experimental results of data set 1

The experimental measurements in this section are based on the indoor reception of a terrestrial CDMA IS-95 pilot signal emanating from the UofC BS shown in Figure 5-4. To conveniently obtain results from a variety of locations, a linear motion table, shown in Figure 5-8, was used. For each measurement set, the linear motion table was placed with a random orientation and location in the middle of the laboratory room of size 10 m by 30 m. The captured signals were amplified and down-converted to IF. The received signal is known to the emulated receiver processing with the exception of the code delay and a random channel gain coefficient. The code delay is determined by a standard search routine and applied to the despreading operation resulting in a set of despread and coherently integrated samples.

The aggregate set of measured signals was initially used to verify that there was no appreciable temporal decorrelation over the snapshot interval T and to determine that the spatial correlation complied with the expectation based on the Rayleigh fading model with the ring of scatterers. The second set of experimental measurements was aimed at producing the receiver operating characteristics (ROC). The results obtained for the static

and moving antennas were then compared with calculations based on the theoretical expressions for P_D and P_{FA} derived earlier.

The spatial samples were taken while the antenna was moving at a constant velocity of 0.1 m/s. Figure 9 shows a typical response of the correlation peak as a function of the code delay in indoor environment for $T=100 \mu\text{s}$.

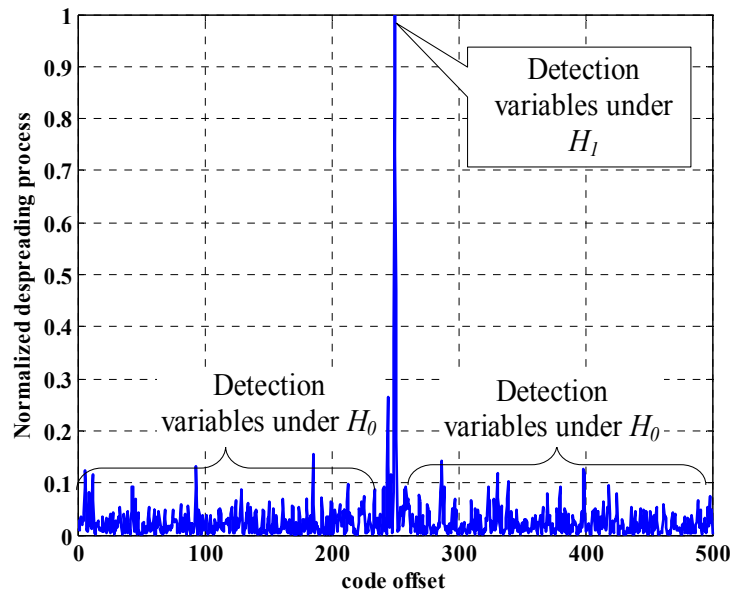


Figure 5-9: Typical code delay correlation function of the CDMA pilot signal processing

The peak corresponds to the correct code delay for which the statistics of the H_l case were extracted. The other mismatched code delays were used to generate statistics for the H_0 case.

As mentioned before, diversity gain is a result of receiving statistically independent signals at diversity branches. Thus, in a spatial diversity system the antenna spacing

should be selected accordingly to satisfy this assumption. In Figure 2.10 it was shown that spatial decorrelation is a function of the scatterers geometry. For the ring of scatterers model, the channel correlation coefficient was presented in Eq. 4.19. Figure 5-10 shows the spatial correlation results obtained, as averaged over a large number of measurements based on the experimental setup. The complex correlation coefficient for two despreading output samples x_1 and x_2 is defined by

$$r = \frac{E[x_1 x_2^*]}{\sqrt{E[x_1 x_1^*] E[x_2 x_2^*]}}. \quad 5-3$$

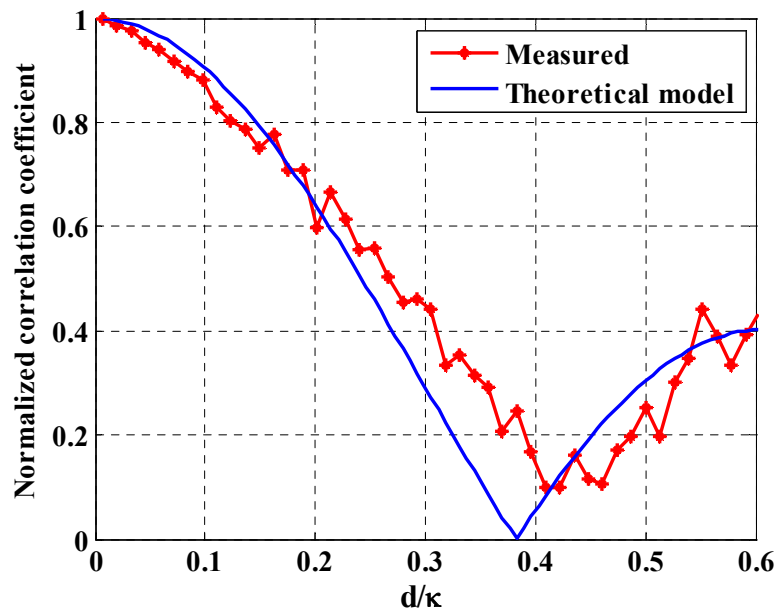


Figure 5-10: Indoor channel normalized correlation coefficient

These measured spatial correlation results are compared with the theoretical model presented in Chapter 3, and given by $J_0(2\pi d / \kappa)$ (Fulghum et al 2002) where d is the antenna spacing and κ is the carrier wavelength of the pilot signal. The reasonable agreement of the measured and theoretical results provides some degree of confidence in using the Rayleigh fading model for the analysis of the synthetic array antenna. Furthermore, the measurements indicate that the spatial samples used will be sufficiently uncorrelated provided that they are taken with a separation on the order of a half wavelength (or more) of the carrier. Figure 5-11 shows the measured and fitted Rayleigh PDFs of test statistics under the H_I state.

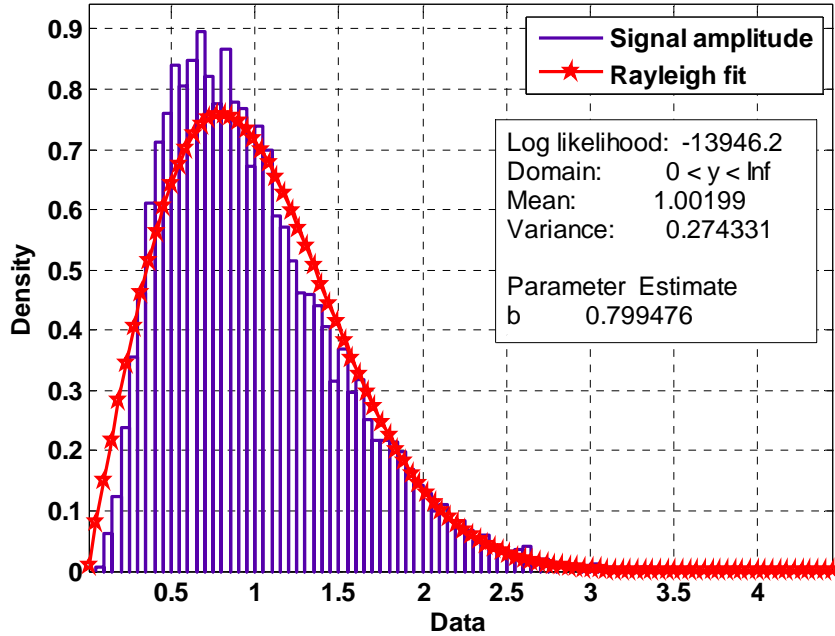


Figure 5-11: Measured and fitted PDF of the test statistics under H_I state

The MATLABTM dfittool toolbox was utilized to provide the best Rayleigh fit to the measured test statistic amplitude under the H_1 state. To evaluate the detection performance of a moving antenna, an extensive data set was collected at various locations in the laboratory and with the equipment shown in Figure 5-8 and the conditional PDFs corresponding to the H_0 and H_1 states were calculated. The experimental results represented in this part compare the performance of the static antenna with the moving antenna with two, four and eight spatial samples. Approximately 40,000 samples were utilized for statistical detection performance evaluation.

Figure 5-12 shows the measured PDFs of test statistics under H_0 and H_1 for the moving antenna case when $M=2$. For comparison, the PDF of a Chi-Squared central distribution with four DOF are overlaid.

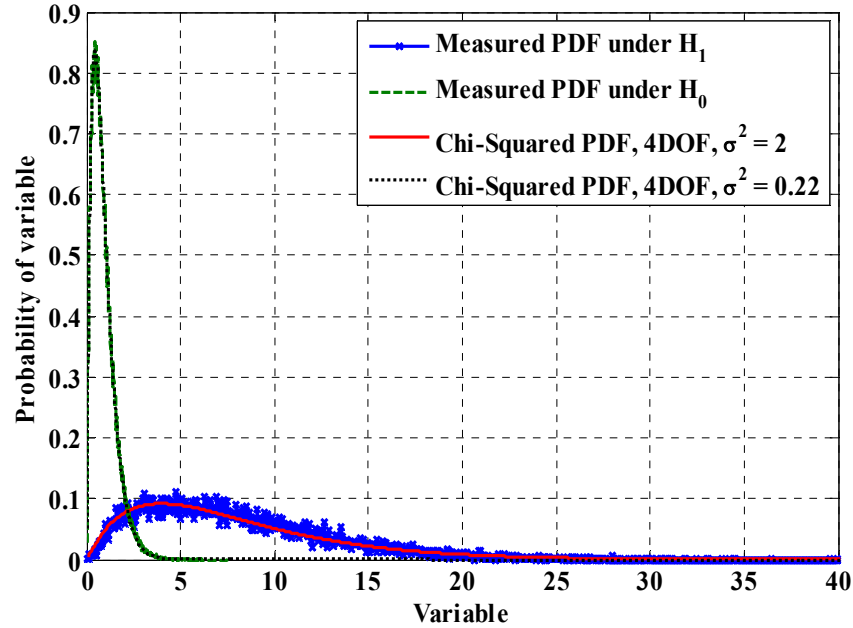


Figure 5-12: Estimated PDF under H_0 and H_1 states for moving antenna $M=2$

The Chi-Squared PDF and variance σ^2 was defined in Eq. 4-54. The match with the theoretical Chi-Squared density functions, which results from the Rayleigh fading assumption, is reasonable and provides further confirmation of the validity of the Rayleigh fading model used. The measured PDF of the test statistics for the static and moving antenna with four and eight spatial samples are evaluated similarly with similar close agreements to experimental results, although these were excluded from Figure 5-12 to avoid clutter.

The corresponding variance parameters under H_0 and H_1 can be estimated from the test statistics under H_0 and H_1 . These values can be normalized by $\sigma_{H_0}^2 = \frac{1}{M}$ and $\sigma_{H_1}^2 = \frac{1}{M} \left(\frac{\rho}{M} + 1 \right)$, respectively, as per (Eq. 4-20). It can be shown that $\frac{\sigma_{H_1}^2}{\sigma_{H_0}^2} = \left(\frac{\rho}{M} + 1 \right)$. Hence, the average SNR and ρ can be extracted from the estimated variances. Based on measurement results for the static and the moving antennas with two, four and eight spatial samples, the estimated average SNR is approximately $\rho = 12$ dB.

Figure 5-13 shows the numerically evaluated ROC curve resulting from the estimated PDFs of Figure 5-12. The theoretical ROC curve is also shown in the figure.

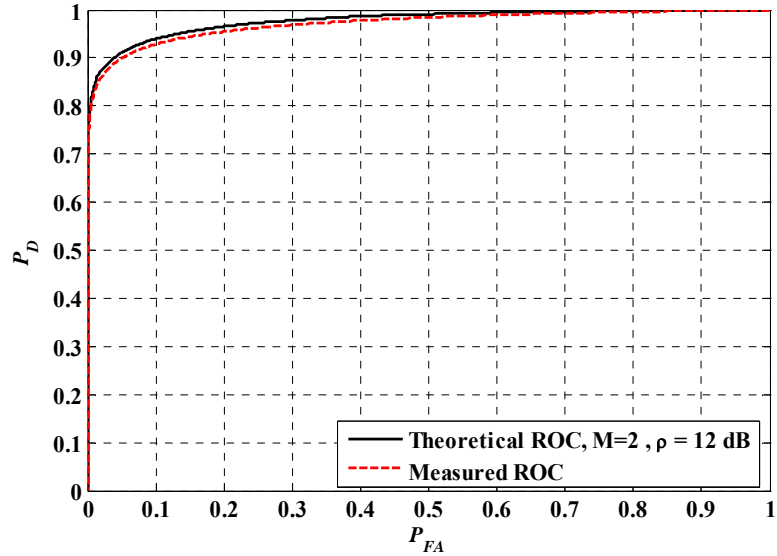


Figure 5-13: Theoretical and numerically evaluated ROC curves based on measurements for moving antenna $M=2$

An interesting observation is the comparison of the experimental measurement curves with the equivalent theoretical results given in Section 4.4.2. The theoretical ROC curves are based on matching the average SNR values with the experimental curves which corresponded to $\rho = 12 \text{ dB}$ for this set of measurements. The theoretical ROC curves can be evaluated utilizing Eq. 4.62 and Eq. 4.63.

Based on the measured sample set, the experimental output of the synthetic array two, four and eight spatial samples were calculated for the H_0 and H_1 cases. From this, the ROC curves shown in Figure 5-14 were generated. The corresponding ROC curve for the static antenna can be generated in a similar manner based on coherent summations. This curve is also shown in Figure 5-14. As expected, the synthetic array outperforms the static antenna.

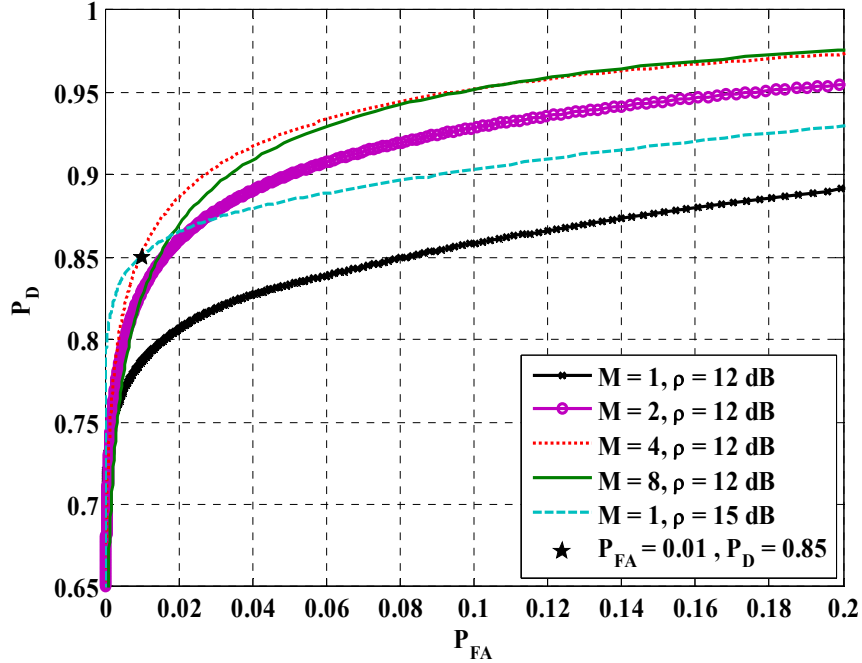


Figure 5-14: Measured ROC curves for the static and moving antenna

An interesting observation is that for the given target performance of $P_{FA}=0.01$, the moving antenna with four spatial samples ($M=4$) has the best performance relative to the static and the moving antennas with two and eight spatial samples. This is due to the fact that, by increasing the number of spatial samples, the diversity gain increases. However, as explained earlier, increasing spatial samples results in coherency loss. Hence, there is a compromise between increasing spatial samples and loss of signal coherency which results in the existence of an optimum processing gain and number of spatial samples. The experimental results in Figure 5-14 can be directly compared with the theoretical findings of Figure 4-12 for target performances of $P_{FA}=0.01$ and $P_D=0.85$. The optimum theoretical spatial sample, resulting from Figure 4-12b with $P_{FA}=0.01$ and $P_D=0.85$, is 4

which agrees with the experimental finding. For evaluating the processing gain, the average SNR of the static antenna is increased (by increasing T) to have the same target performances of $P_{FA}=0.01$ and $P_D=0.85$. This crossing point is shown in Figure 5-14. This was achieved by increasing by approximately 3 dB the average SNR of the static antenna. Hence, 3 dB of processing gain can be directly compared with the theoretical results of target detection performances of $P_{FA}=0.01$ and $P_D=0.85$ shown in Figure 4-12a. As observed, the theoretical and experimental results match very well. Table 5-3 summarizes the experimental detection performance and processing gain of the moving antenna for different P_{FA} values.

Table 5-3: Processing Gain of the moving antenna over static antenna for different spatial samples for data set 1

	ρ (dB)	P_D		Processing Gain (dB)	
		$P_{FA} = 0$	$P_{FA} = 0.01$	$P_{FA} = 0$	$P_{FA} = 0.01$
$M = 1$	12	0.79	0.86	0	0
$M = 2$	12	0.83	0.93	1.5	2
$M = 4$	12	0.86	0.95	3	4.5
$M = 8$	12	0.85	0.95	2	4.5

5.1.3.1 Synthetic array detection performance for different values of T

In this experiment, the detection performance of the synthetic array for different values of T was investigated. The statistical results presented in this part are based on the signal received by the UofC BS.

In the first experiment, the snapshot interval was $T=40 \mu\text{s}$, which is equivalent to 200 digitized samples (5 MHz sampling rate). In this case, the static antenna coherently integrates 40 μs . The synthetic array processor with two spatial samples, namely $M=2$, non-coherently integrates two spatial samples each with a coherent integration of 20 μs . Figure 5-15 and Figure 5-16 show the calculated PDFs based on measurements under the H_1 and the H_0 states for the static and synthetic array, respectively. For comparison, the PDFs of the test statistics of the static antenna with non-coherent combining are also shown in Figure 5-15b and Figure 5-16b, which are based on the same processing of the synthetic array. However, in the synthetic array case two spatial samples are statistically uncorrelated, whereas in the static non-coherent case two snapshots are fully correlated. The difference in the detection performance between the synthetic array and the static antenna with non-coherent process gives the synthetic array processing gain based on the equal-gain (EG) combiner for two extremes: uncorrelated and coherent channel situations. Figure 5-15 shows that the measured PDFs of the static coherent and the synthetic array have approximately a Chi-Squared distribution with two and four DOFs.

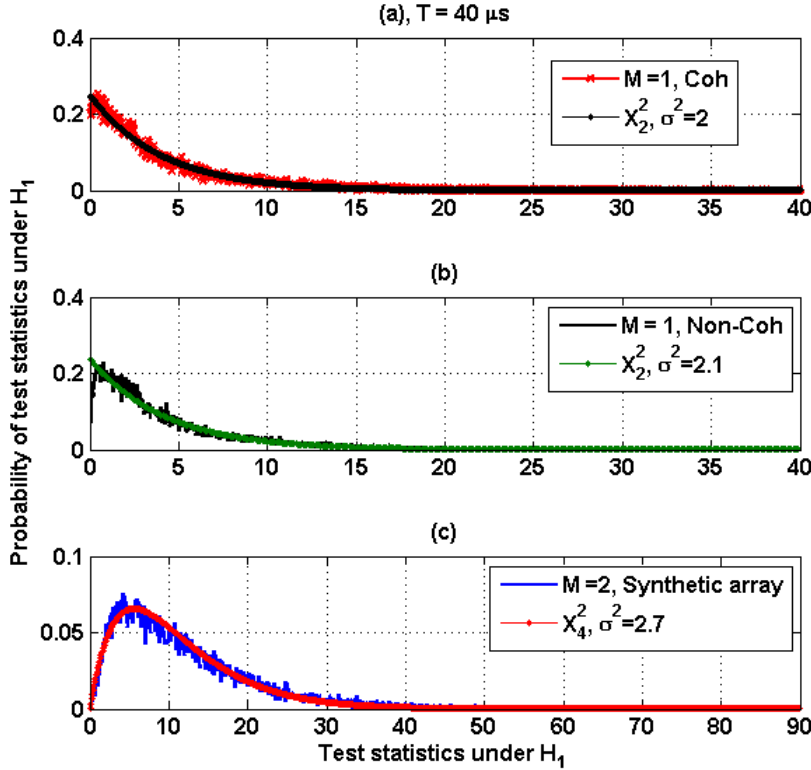


Figure 5-15: Calculated PDFs under H_1 state based on measurements of a) static, coherent integration b) static non-coherent integration c) synthetic array $M=2$

However, the test statistics under H_1 in the static case (Figure 5-15b) has a Chi-squared PDF with 2 DOFs implying that the non-coherent combining does not provide additional DOFs. However, in the synthetic array case (Figure 5-15c) non-coherent combining provides additional DOFs, a result of the diversity gain. Comparing Figure 5-16b with Figure 5-16c, one realizes that the test statistics of the static non-coherent process and the synthetic array conform to the Chi-Squared PDF with 4 DOFs. This result further confirms the decorrelation of noise samples temporally.

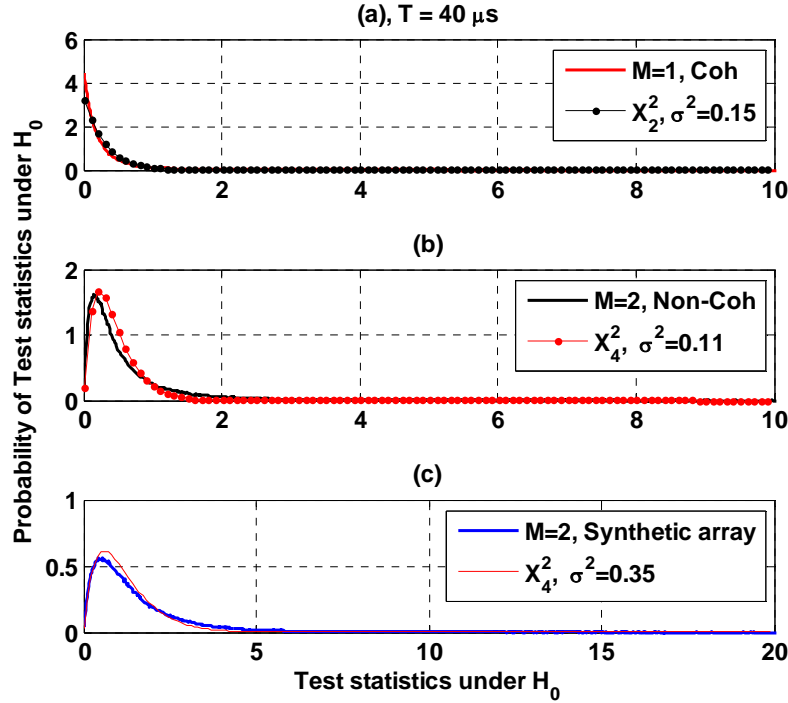


Figure 5-16: Calculated PDFs under H_0 state based on measurements of a) static, coherent integration b) static, non-coherent integration c) synthetic array $M=2$

Figure 5-17 shows ROC curves for the static and the synthetic array for $M=2$ and $T=40 \mu s$. As it is shown in Figure 5-17, the detection performance of the synthetic array for a given P_{FA} is better than that of the static antenna. Several interesting observations can be made from Figure 5-17. Section *a* in Figure 5-17 shows the trade-off between the coherency loss and the diversity gain. For the static non-coherent combining there is no diversity gain, hence section *b* signifies the coherency loss in non-coherent combining. Section *c* in Figure 5-17 shows the upper and the lower bounds of the synthetic array detection performance based on the EG combiner for $P_{FA}=0.1$ and given average SNR.

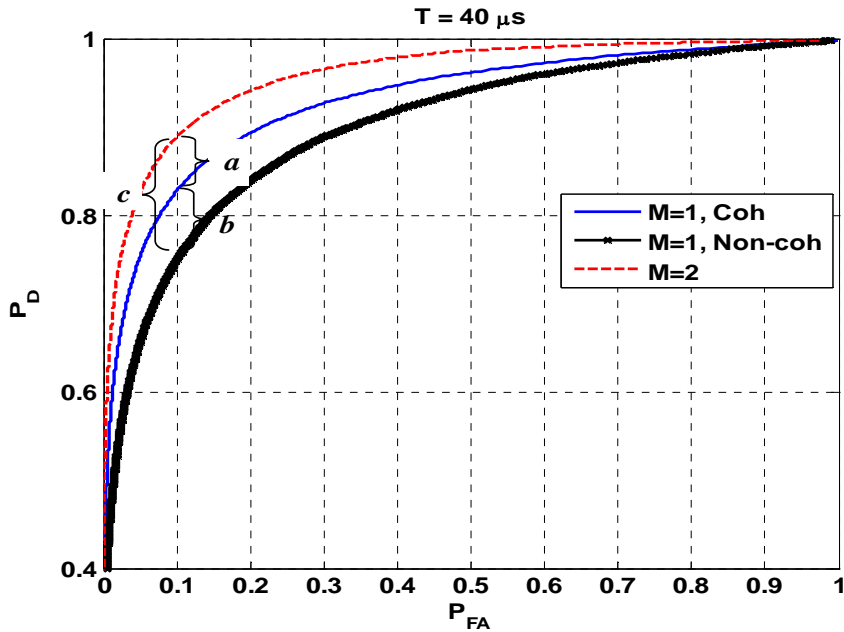


Figure 5-17: ROC curves for static coherent integration, static non-coherent process and the synthetic array, $T=40 \mu s$.

Table 5-4 gives the experimental detection performance and the processing gain of the moving antenna for different P_{FA} values.

Table 5-4: Processing Gain of the moving antenna over the static antenna for different spatial samples, UofC BS, $T= 40 \mu s$

	ρ (dB)	P_D		Processing Gain (dB)	
		$P_{FA} = 0$	$P_{FA} = 0.1$	$P_{FA} = 0$	$P_{FA} = 0.1$
$M = 1$, Coh	11	0.58	0.83	0	0
$M=2$, Static Non-coh	10	0.48	0.75	-	-
$M=2$, Synthetic	10	0.66	0.9	0.5	1.5

Next the case of $T=80 \mu\text{s}$ is considered. Figure 5-18 shows the ROC curves for the static antenna coherent process, static antenna non-coherent process and the synthetic array. Table 5-5 gives the experimental detection performance and processing gain for the static antenna and synthetic array for different P_{FA} values for $T=80 \mu\text{s}$.

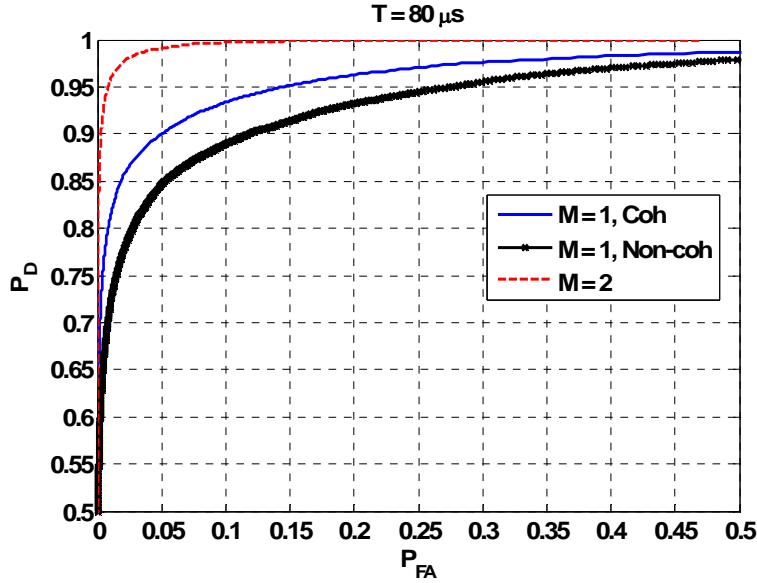


Figure 5-18: ROC curves of static coherent integration, static non-coherent process and the synthetic array, $T=80 \mu\text{s}$

Table 5-5: Processing Gain of moving antenna over static antenna for different spatial samples, UofC BS, $T=80 \mu\text{s}$

	ρ (dB)	P_D		Processing Gain (dB)	
		$P_{FA} = 0.01$	$P_{FA} = 0.1$	$P_{FA} = 0.01$	$P_{FA} = 0.1$
$M=1, \text{Coh}$	14	0.81	0.94	0	0
$M=2, \text{Static}$ Non-coh	13.1	0.72	0.88	-	-
$M=2,$ Synthetic	13.2	0.96	0.99	2	4

Figure 5-19 shows the ROC curves for the static antenna coherent process, static antenna non-coherent process and the synthetic array for the case of $T=160 \mu\text{s}$. Table 5-6 provides the experimental detection performance and processing gain for the static antenna and synthetic array for different P_{FA} values.

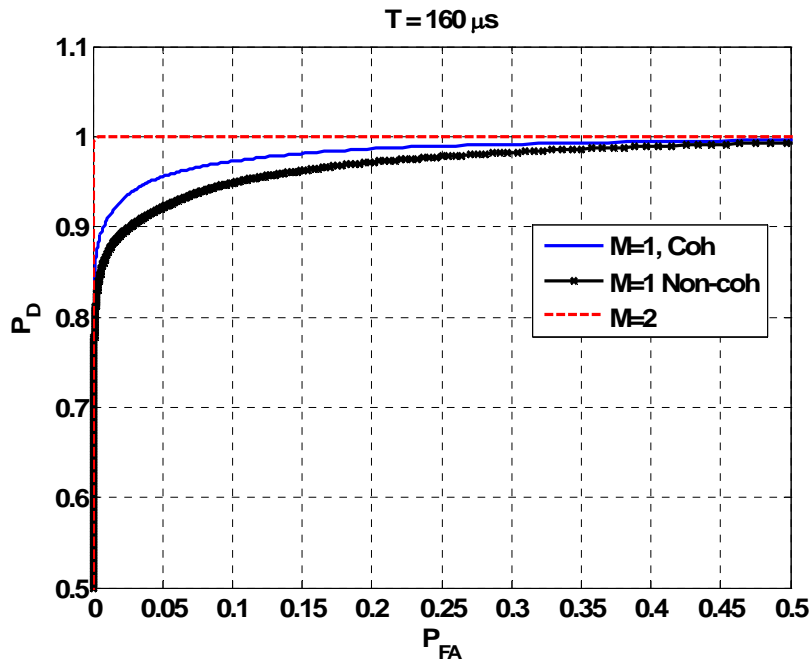


Figure 5-19: ROC curves of static coherent integration, static non-coherent process and the synthetic array, $T= 160 \mu\text{s}$

Table 5-6: Processing Gain of moving antenna over static antenna for different spatial samples, UofC BS, $T= 160 \mu\text{s}$

	ρ (dB)	P_D		Processing Gain (dB)	
		$P_{FA} = 0.01$	$P_{FA} = 0.1$	$P_{FA} = 0.01$	$P_{FA} = 0.1$
$M = 1, \text{Coh}$	17	0.92	0.97	0	0
$M=2, \text{Static Non-coh}$	16.6	0.87	0.95	-	-
$M=2,$ Synthetic	16.5	1	1	4	6

Comparing the synthetic array detection performance for the different values of T summarized in Table 5-4, Table 5-5 and Table 5-6, one observes that, by increasing T (or equivalently, increasing the average SNR), the processing gain of the synthetic array over the static antenna increases. This phenomenon was discussed in Chapter 4 and shown in Figure 4-8.

As mentioned before, the peak value of the correlation function is chosen as a detection variable under H_1 . Hence, the instantaneous SNR can be defined by the peak value to side level ratio. This metric can be used to represent the fading effect at different points of the indoor channel. The instantaneous SNR (ISNR) is defined as

$$ISNR = \frac{[E(T(x)|H_1) - E(T(x)|H_0)]^2}{\text{var}(T(x)|H_0)}. \quad 5-4$$

where $E(\bullet)$ defines the expectation operator, $E(T(x)|H_1)$ is the peak value of the correlation function, $E(T(x)|H_0)$ is the mean value of the test statistics under H_0 as it was shown in Figure 5-9 and $\text{var}(T(x)|H_0)$ gives the variance of the test statistics under H_0 . Figure 5-20 shows the cumulative distribution function (CDF) of ISNR for $T=160 \mu\text{s}$. Comparing the ISNR CDFs for the coherent and non-coherent processing of the static antenna, one observes that they have the same pattern with a shift in the mean value. Hence, the non-coherent process in the static case decreases the average SNR without providing diversity gain. Comparing the ISNR CDF of the moving antenna with the static antenna, one can see that the CDF shape is changed as a result of the diversity gain.

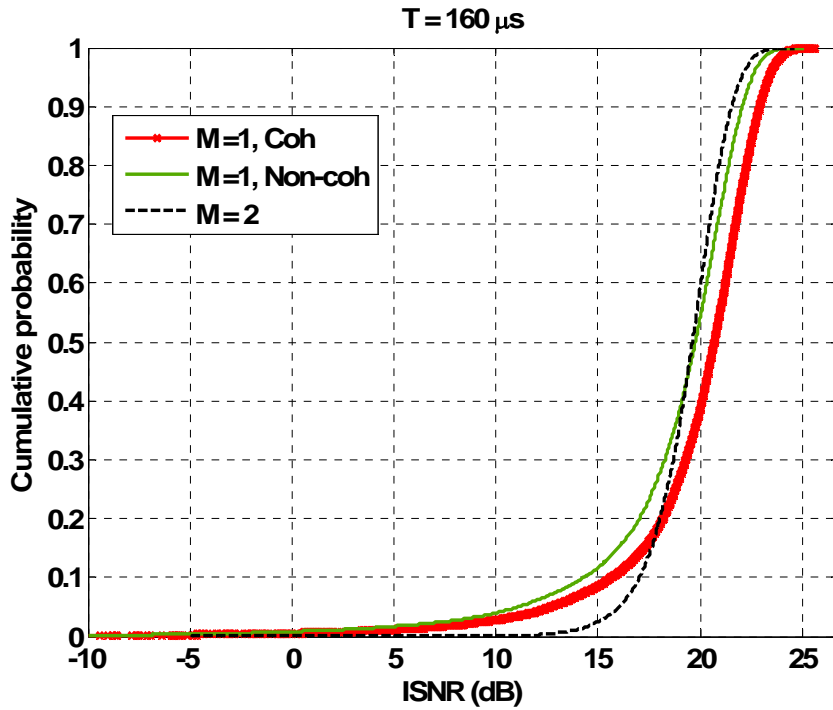


Figure 5-20: Instantaneous SNR for the static antenna and the synthetic array

Statistical results of the synthetic array represented so far were based on the signal reception of the UofC BS. A similar process was performed based on receiving signals transmitted from the Market Mall BS. The synthetic array detection performance utilizing signals from Market Mall BS is shown in Appendix C.

5.1.4 Experimental results of data set 2, synthetic array experimental results in a correlated Rayleigh fading

In Chapter 4 it was shown that the processing gain due to the synthetic array processing diminishes with an increasing correlation coefficient, the latter being a function of antenna spacing and diffuse multipath characteristics. It was also shown that the performance of the suboptimal EG is almost the same as that of the optimal EC combiner in cases where the channel gain is moderately correlated. In this section, the EG combiner is utilized to validate the theoretical results presented in Section 4.6. The objective of the experimental measurements is to determine the processing gain and the synthetic array performance for a selection of typical indoor locations and compare these with corresponding theoretical values.

The experimental measurements are based on the indoor reception of a terrestrial CDMA IS-95 pilot signal emanating from an outdoor base station. As mentioned earlier, diversity gain results due to the independency of spatially separated samples. Therefore, it is essential to evaluate the channel spatial correlation coefficients. To this end, the spatial covariance matrix is estimated based on all spatial samples measured on the linear moving table. The measurement results agree fairly well with the theoretical model of ring of scatterers defined in Chapter 4. Thus, based on the measurement results, arrival signals onto two spatial samples separated by half of a wavelength are approximately uncorrelated.

The second set of experimental measurements was aimed at producing ROC curves. The results obtained for the static antenna and the synthetic array for different antenna correlations, a process controlled by choosing different antenna spacings, were then compared with calculations based on the theoretical expressions for P_D and P_{FA} derived earlier. The spatial samples were taken while the antenna was moving with a constant speed of 0.1 m/s. To evaluate the detection performance of a moving antenna, comprehensive data collections at various locations in the hallway were performed and the conditional PDFs corresponding to the H_0 and H_1 states were numerically calculated based on the measured sample set. Figure 5-21 shows the measured PDFs of test statistics z_0 under H_0 and H_1 of the static antenna. For comparison, the PDF of central Chi-Squared distributions with two DOF (χ^2_2) are overlaid.

Figure 5-22 shows measured and theoretical PDFs of test statistics for the moving antenna (z_{EG}) under H_0 and H_1 when $M=2$ and $d = \kappa / 2$ where κ is the carrier wavelength. The theoretical PDFs in Figure 5-22 are Chi-Squared central distributions with four DOF (χ^2_4). The match with the theoretical Chi-Squared density functions, which results from the uncorrelated Rayleigh fading assumption, is reasonable and confirms the validity of the Rayleigh fading model. Based on the fitting to the Chi-Squared PDFs of Figure 5-21 and Figure 5-22, the average SNR can be extracted from the overlaid theoretical PDFs. Based on measurement results for the static and the moving antennas, the average SNRs are approximately $\rho_s = 10.2$ dB and $\rho_{EG} = 10$ dB, respectively. Figure 5-23 shows numerically calculated ROC curves based on measurements for the synthetic array and static antenna.

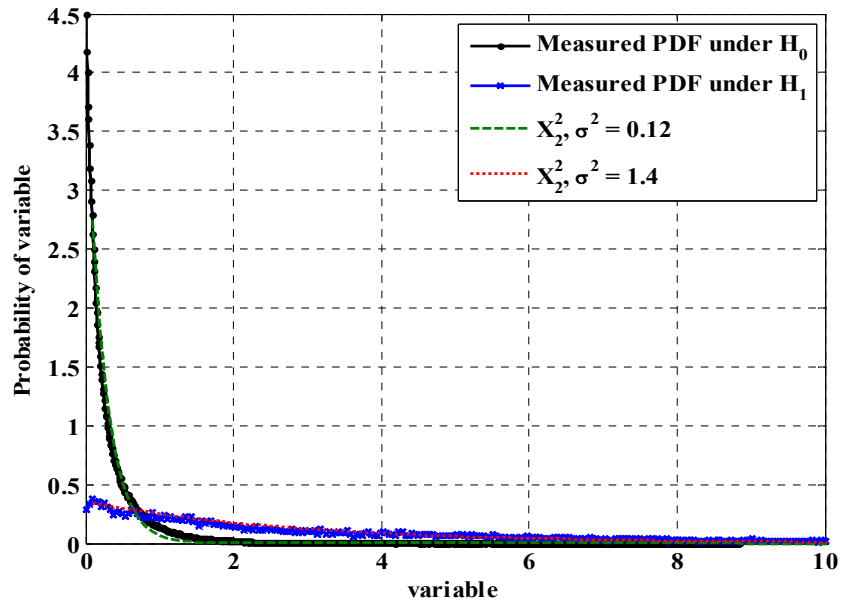


Figure 5-21: Numerically calculated PDFs under H_0 and H_1 states for a static antenna

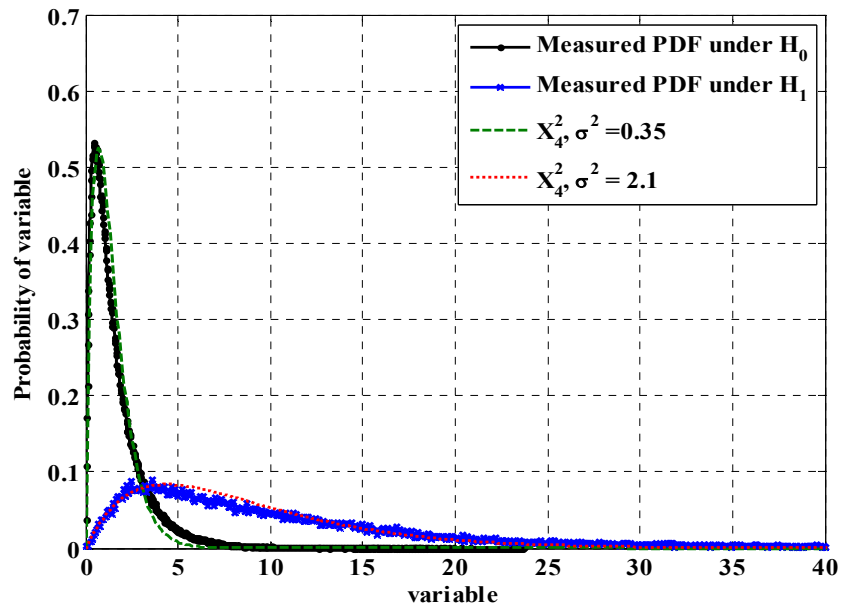


Figure 5-22: Numerically calculated PDFs under H_0 and H_1 states for a moving antenna

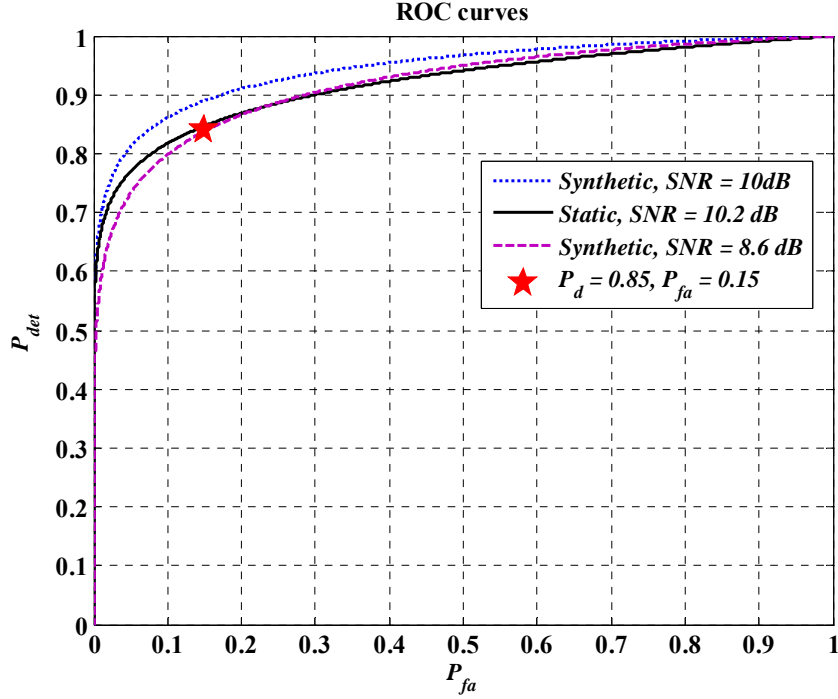


Figure 5-23: Numerically calculated ROC curves in an uncorrelated case

The detection performance of the synthetic array with two statistically uncorrelated sensors is significantly better than that of the static antenna. To determine the synthetic array gain over the static antenna in terms of the required average SNR, the measured ROC curves of a synthetic array with average SNR of $\rho_{EG} = 8.6$ dB are also plotted in Figure 5-23, which fits the ROC curves of the static antenna. The average SNR is decreased by adding noise to the process. From this, the synthetic array gain over the static antenna can be obtained and is about $G_{EG} = 1.6$ dB. The target performance of $P_{FA} = 0.15$ and $P_D = 0.85$ is nearly located on the ROC curve of the static antenna, as shown in Figure 5-23. The theoretical gain of the synthetic array with target values of $P_{FA} = 0.15$ and $P_D = 0.85$ was shown in Figure 4-15e and f. The theoretical gain for the

uncorrelated case ($r=0$) is about 1.6 dB, which agrees fairly well with the measurements results.

Figure 5-24 shows theoretical and measured PDFs for the synthetic antenna array under H_1 state for different antenna spacings d in terms of carrier wavelength κ . The theoretical PDFs can be evaluated based on the discussion given in Section 4.4.2.2.

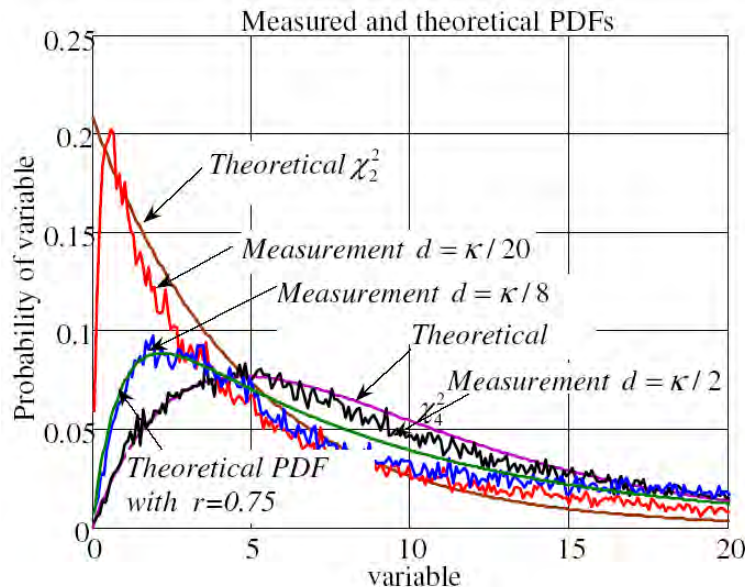


Figure 5-24: PDFs of the synthetic array under H_1 state for different antenna spacings.

Figure 5-24 shows that, by decreasing antenna spacing or increasing the correlation coefficient, the mean value of the detection variable decreases. This phenomenon causes a loss of the diversity gain. Figure 5-24 also shows that by increasing the correlation coefficient, the test statistics PDFs moves from a central Chi-Squared with four DOFs χ^2_4 toward a central Chi-Squared with two DOFs χ^2_2 which again results in a lower diversity

gain. Another observation is that the measured PDFs agree fairly well with theoretical PDFs for different correlation coefficients and antenna spacings.

Figure 5-25 shows ROC curves obtained with different synthetic antenna spacings d . The corresponding ROC curves for the static antenna are generated in a similar manner based on coherent summations of stationary samples and are also shown in the figure.

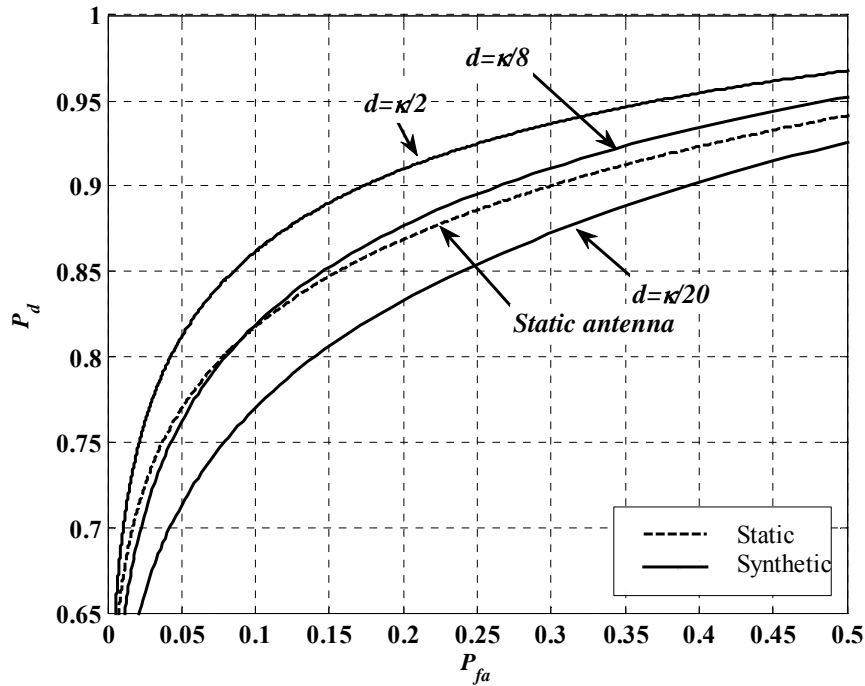


Figure 5-25: Measured ROC curves for static antenna and synthetic array

As expected the synthetic antenna with a synthetic element spacing of $\kappa/2$ with approximately uncorrelated samples outperforms all other scenarios. Figure 5-25 shows that, by decreasing antenna spacing, the performance of the EG combiner degrades due to the correlated signal covariance matrix. It is also shown that the performance of the coherent integration in the static case is almost the same as that of the synthetic antenna

array with a spacing of $\kappa/8$. By decreasing the antenna spacing to $\kappa/20$, the performance worsens, which demonstrates that there is no advantage in using a synthetic array in this case.

5.2 Experimental results on the detection performance of GPS signals in indoor environments based on the discrete synthetic array process

The objective of the experimental measurements in this section is to determine the processing gain for a selection of typical GPS indoor locations and compare these with corresponding theoretical values given in Chapter 4.

5.2.1 Signal model

GPS uses a Direct-Sequence Code Division Multiple Access (DS-CDMA) structure. Each satellite transmits a unique PRN with low cross-correlation with that of other satellites. The civilian GPS Coarse/Acquisition (C/A) code utilizes Gold codes with a code length of 1023 chips and a chipping rate of 1.023 MHz. Hence, each period of the GPS C/A code takes 1 ms. This structure allows all satellites to transmit signals at the same time and in the same frequency band. The PRN codes are known to the receiver, which correlates the received signal with the replica code to estimate the channel impulse response. The GPS L1 signal is modulated by 50 Hz navigation data bits. The navigation data includes timing and satellite orbital information (Kaplan & Hegarty 2006). Finally, the GPS C/A L1 signal is up-converted to the carrier frequency of 1575.42 MHz. For

more details on the GPS signal structure and receiver processing, readers are further referred to Kaplan & Hegarty (2006), Misra & Enge (2006) and Parkinson & Spilker (1996). Table 5-7 summarizes the GPS L1 C/A characteristics.

Table 5-7: GPS L1 C/A characteristics

Chip rate	Bandwidth	Modulation	Code length	Code period	Carrier frequency
1.023 MCPS	1.023 MHz	BPSK	1023Chip	1 ms	1575.42 MHz

Consider a GPS signal detection scenario in a flat Rayleigh channel (e.g. indoor). The complex signal received by an antenna position can be represented by

$$r(t) = A(\mathbf{p})s_o(t) + n(t) \quad 5-5$$

where

$$s_o(t) = e^{j(2\pi\Delta f t + \psi)} D(t - \tau) c(t - \tau). \quad 5-6$$

$A(\mathbf{p})$ is the complex channel gain as a function of the antenna position \mathbf{p} relative to a fixed coordinate system, $D(t)$ is the navigation data modulation, $c(t)$ is the PRN code and $n(t)$ is a complex additive white Gaussian noise. The received signal $s_o(t)$ is known to the receiver except for the navigation data, the code phase τ , the carrier frequency offset Δf and the initial phase offset ψ . Hence, successful signal detection includes navigation bit removal, Doppler and code phase estimation. Due to the signal attenuation and path loss, the received GPS signal is buried below the noise floor. Hence, it requires extensive processing to extract transmitted information from the weak signal.

As mentioned earlier, the acquisition process is the initial procedure for signal detection and coarse channel parameters estimation (e.g. propagation delay and Doppler frequency). This procedure is normally accomplished by a two-dimensional search over the code phase and Doppler domain. The searching range in the code domain is associated with the length of the code and the sampling frequency. The search range in the Doppler domain for the static receiver is typically ± 5 kHz with a step size of $2/(3T)$ where T signifies the coherent integration time (Kaplan & Hegarty 2006).

5.2.2 Data collection Setup

The experimental measurements are based on the indoor reception of GPS L1 C/A signals. An active patch Right-Hand Circular Polarization (RHCP) antenna mounted on the precise linear moving table described earlier is utilized to implement a synthetic array during raw GPS data collection. A commercial synchronized dual-channel RF front-end is exploited to down-convert GPS raw data to an intermediate frequency of 3.42 MHz. The data collection scenario consists of 45 minutes of IF GPS L1 data sampled by a 10 MHz digitizer with 8-bit quantization. A single stable Temperature Controlled Crystal Oscillator (TCXO) was utilized to provide reference frequencies for down-conversion and digitization (Broumandan et al 2009c).

Figure 5-26 shows the test setup and utilized equipment at the indoor and the reference stations.

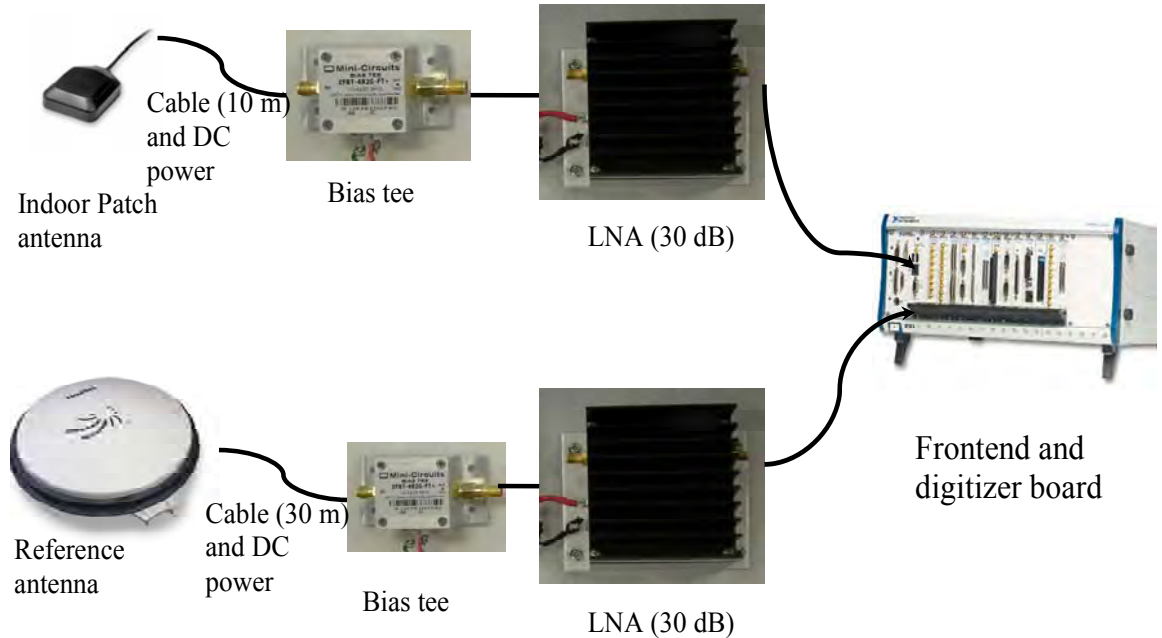


Figure 5-26: Reference and indoor data collection setup

The measurement setup and the geometry of the visible satellites and data collection location are shown in Figure 5-27. Shown in Figure 5-27 is the indoor measurement location, which was a hallway on the third floor of the CCIT building described earlier. The windows are covered with a conductive film resulting in an estimated 20-30 dB penetration loss of the received GPS signals.

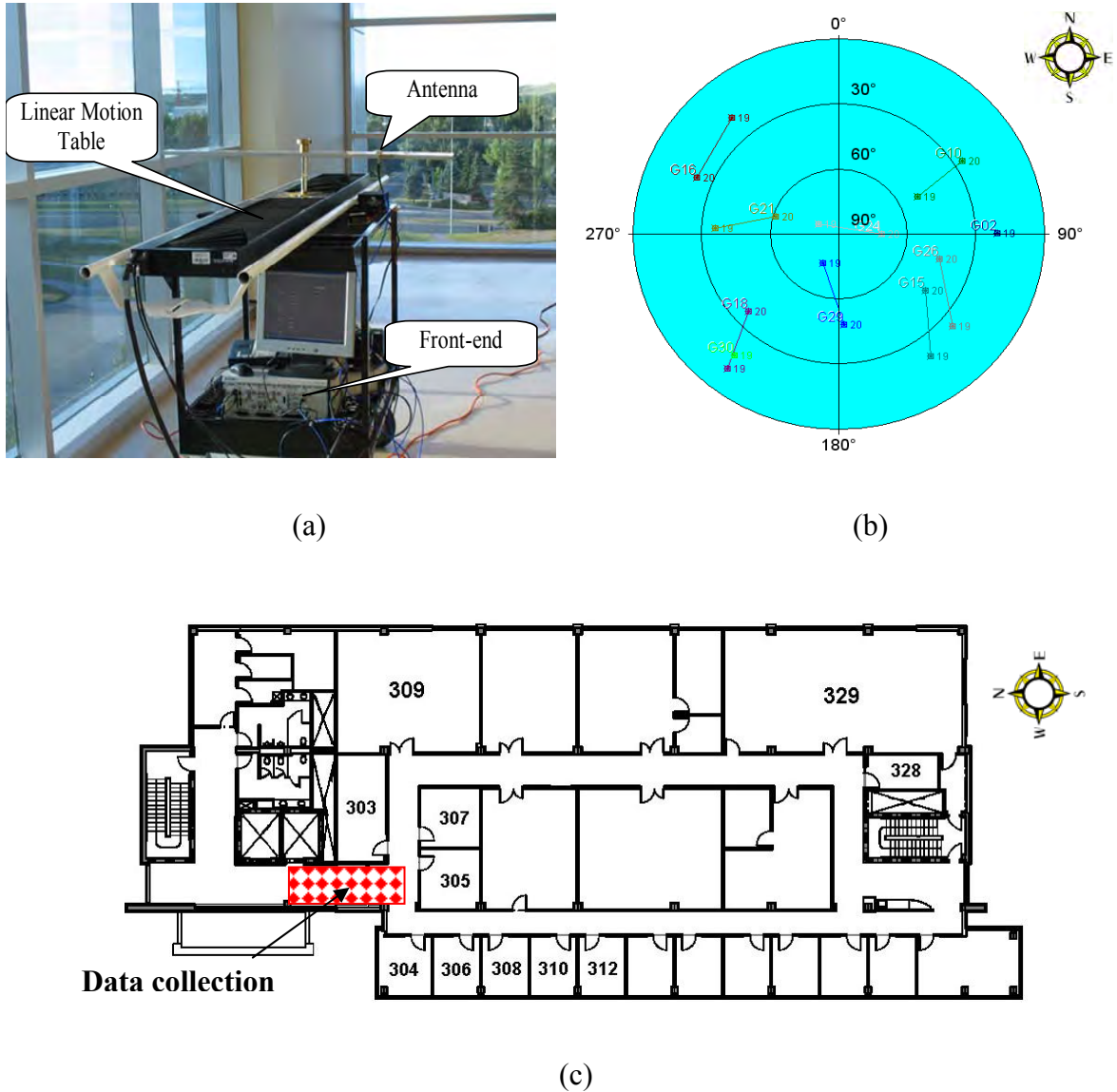


Figure 5-27: a) Measurement setup, b) geometry of visible satellites and data collection location, c) Layout of office floor with the hashed area indicating the area used for collecting experimental data

Hence, a coherent integration time more than 20 ms was required to overcome this loss. To conveniently account for the navigation data modulation, reference signals from a static antenna located on the rooftop directly above the measurement area of Figure

5-27a with a clear sky view of the GPS satellites were sampled in a synchronous fashion with the indoor signals.

Figure 5-28 shows the demodulation process utilizing the reference antenna. The estimated navigation data bits and Doppler frequency from the reference channel were used to demodulate the indoor GPS L1 signals.

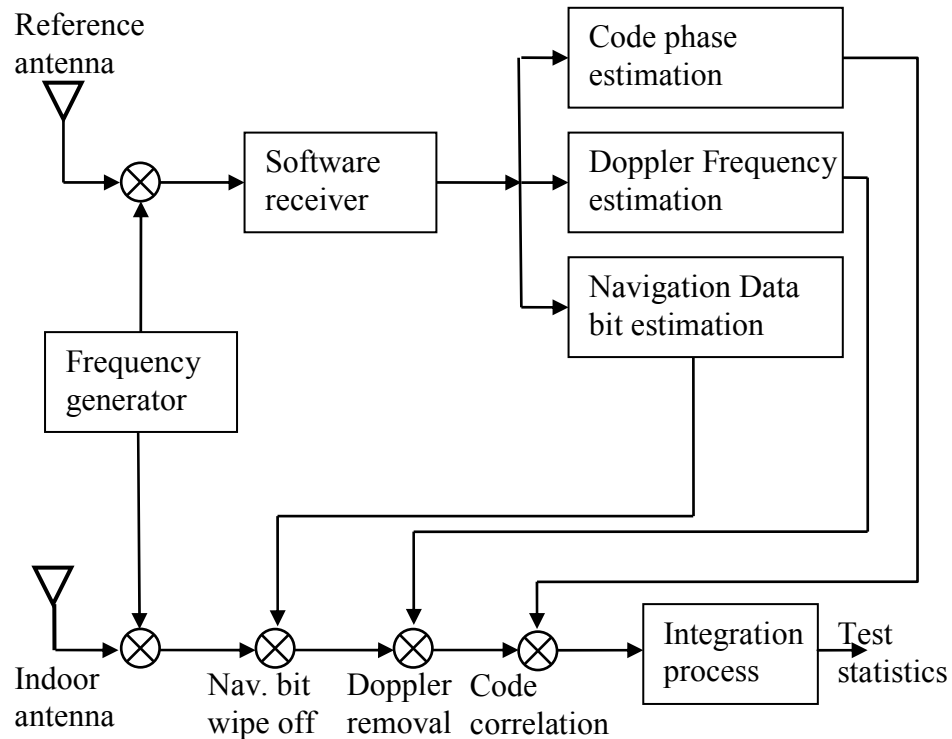


Figure 5-28: Demodulating process utilizing the reference signal

5.2.3 Measurement results

As demonstrated in Section 4.6, if the spatial samples are relatively uncorrelated, the EC process can be approximated by the EG combiner. Hence, in this section the performance of the EG combiner will be investigated. The experimental results presented in this section compare the performance of the static antenna with the synthetic array for $M=2$ and $M=4$. Each output sample of the measurement results is based on 400 ms of processing of the GPS PRN 18, 21 and 24 L1 C/A code. Thus, the static antenna coherently integrates 400 ms signal samples whereas the synthetic array with two and four antenna positions non-coherently integrates two and four spatial samples, each processed with 200 ms and 100 ms coherent integration times. The statistical results represented in this section are based on the processing of 45 minutes of data. Hence, the statistical results are based on 7000 samples under H_I . In the sequel, the measurement results of PRN 21, which are representative of all PRN, will be discussed in detail. The measured processing gain of PRN 18 and 24 are tabulated at the end of the section. Table 5-8 shows the characteristics of data collection scenarios.

Table 5-8: Characteristics of indoor GPS data collection scenarios

Date	Sampling rate	IF Frequency	Data collection duration	Antenna velocity
7 Oct 2008	10 MHz	3.42 MHz	45 min	2 cm/s

Figure 5-29 shows a typical response of the GPS correlation process as a function of the code delay. The peak corresponds to the correct code delay for which the statistics of the H_I case were extracted. The other mismatched code delays were used to generate

statistics for the H_0 case. The first experiment was performed to measure the indoor channel characteristics.

Figure 5-30 shows the numerically evaluated PDF envelopes based on the indoor GPS measurements and theoretical Rayleigh PDF. As shown in Figure 5-30, the GPS indoor signal reception agrees well with the Rayleigh distribution.

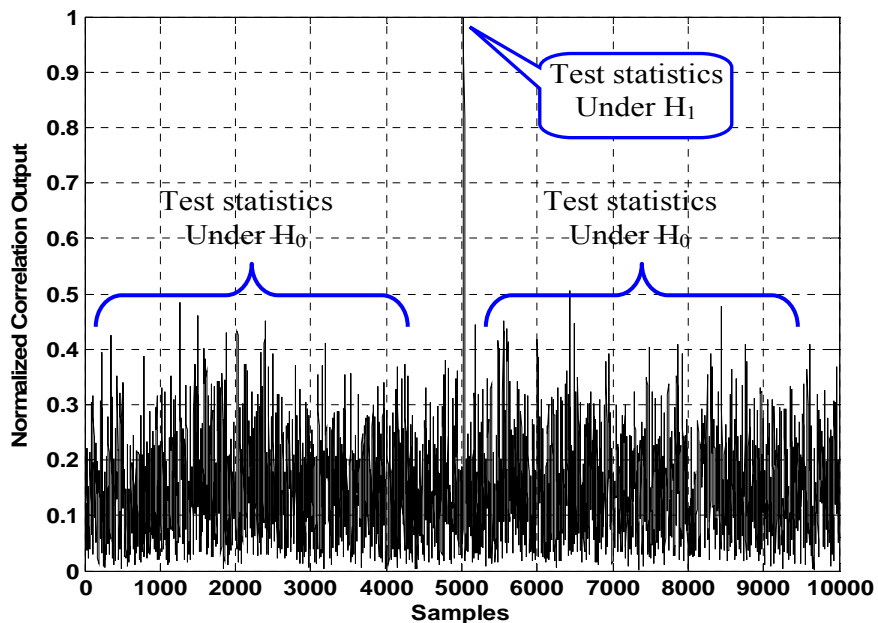


Figure 5-29: Correlation outputs and test statistics under H_0 and H_1 for GPS PRN 21

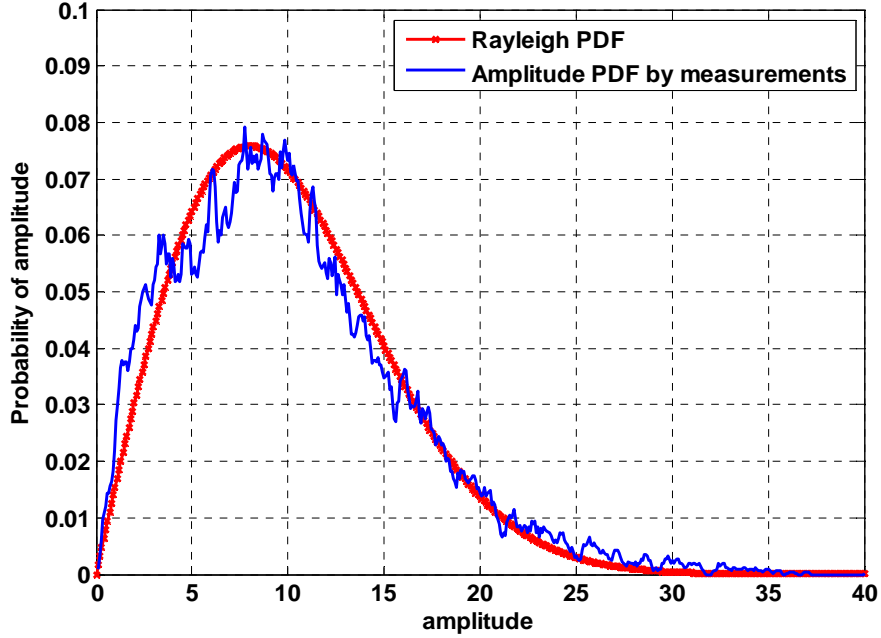


Figure 5-30: Measured amplitude PDF and theoretical Rayleigh PDF for GPS measurements

To evaluate the detection performance of the synthetic array, comprehensive data was collected with the linear table at various locations and the conditional PDFs corresponding to the H_0 and H_1 states were numerically calculated based on the measured samples. Figure 5-31 shows the measured PDFs of test statistics under H_0 and H_1 for the static antenna ($M=1$) and the synthetic array ($M=2$ and $M=4$). For comparison, the PDF of Chi-Squared central distributions are overlaid. The theoretical PDF shown in Figure 5-31 is a Chi-squared density function with $2M$ DOF defined by

$$f_z(z) = \frac{1}{\sigma^{2M} 2^M \Gamma(M)} z^{M-1} e^{-\frac{z}{2\sigma^2}}. \quad 5-7$$

The match with the theoretical Chi-Squared density function provides further confirmation of the validity of the Rayleigh fading model used and confirms the theoretical processing gain presented in Chapter 4.

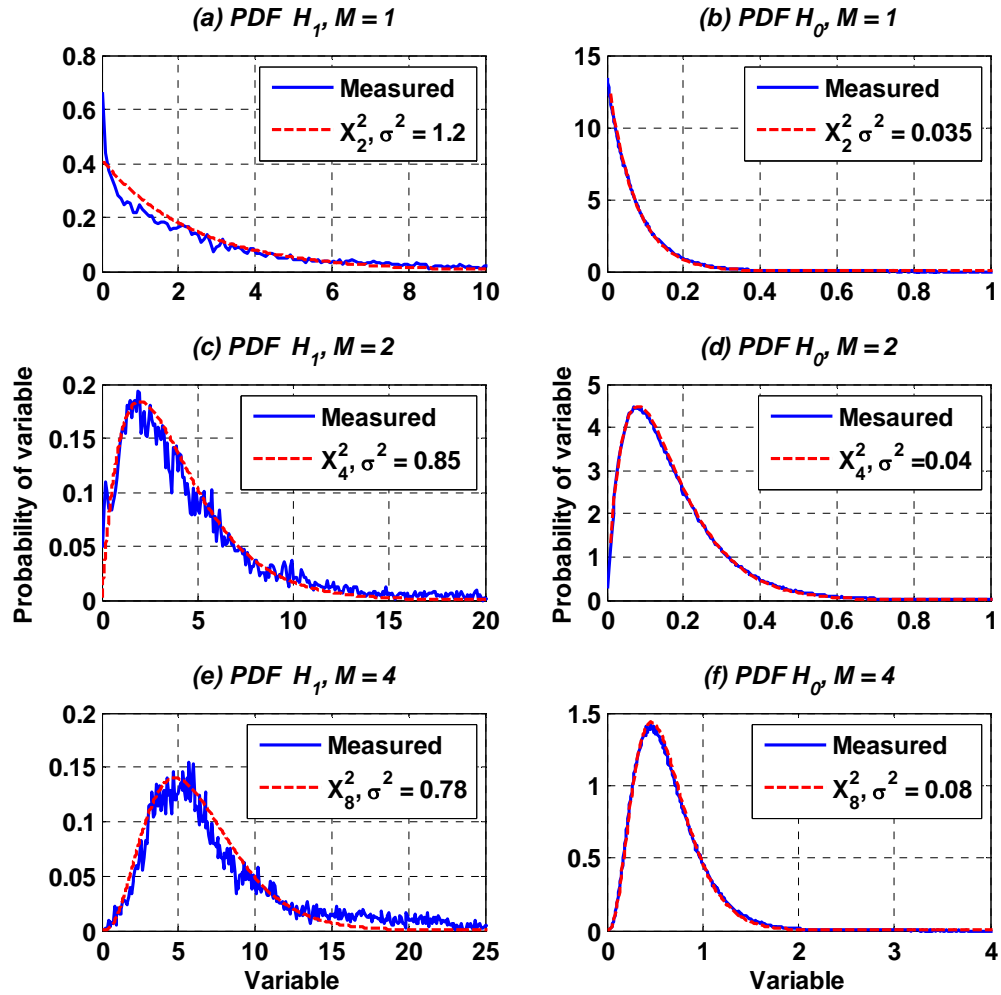


Figure 5-31: Estimated PDFs under H_1 (a, c and e) and H_0 (b, d and f) states for GNSS static antenna (a and b) and synthetic array with $M=2$ (c and d) and synthetic array with $M=4$ (e and f)

Based on the experimental output of the EG combiner for a static antenna, a synthetic array with $M=2$ and $M=4$, half wavelength spacing between sample points ($r=0$), P_D and P_{FA} was evaluated for the H_0 and H_1 cases. From this, the ROC curves shown in Figure 5-32 were generated.

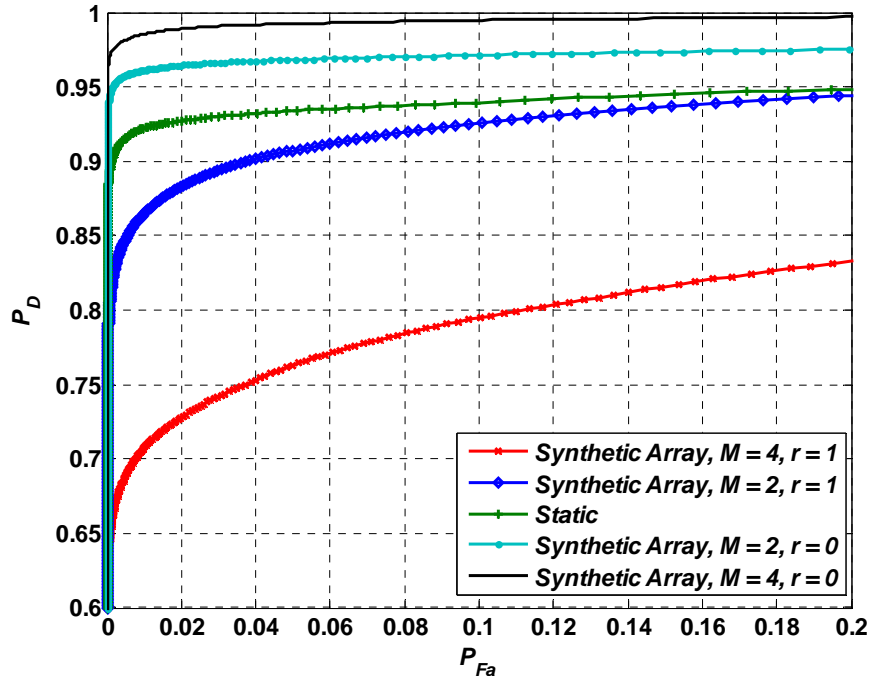


Figure 5-32: Estimated ROC curves based on GNSS measurements for the static antenna and the synthetic array with 2 and 4 elements for uncorrelated and coherent cases

As expected, the synthetic array outperforms the static antenna. The ROC curves for the fully correlated case ($r=1$) for the synthetic array with $M=2$ and $M=4$ are also shown in Figure 5-32. Based on the results of Figure 5-32 for a given $P_{FA}=0.01$, the P_D for the static antenna and synthetic array with $M=2$ and $M=4$ are 0.92, 0.96 and 0.98, respectively. By comparing these experimental results with the theoretical results of

Section 4.5, the achievable gain with the use of a synthetic array is found to be about 4 and 8 dB for $M=2$ and $M=4$ respectively, which is indeed significant.

Figure 5-33 shows the measured ISNR values (defined in Eq. 5-4) for the static antenna and a synthetic array with $M=2$ and $M=4$ for a 100-second signal processing interval. From Figure 5-33 it is evident that the static antenna has higher maximum ISNR values as expected. However, the ISNR values are susceptible to deep fades and lost peak detection. By increasing M , the ISNR mean decreases although the ISNR values are immune to deep fades. Figure 5-34 shows the Cumulative Density Function (CDF) of the ISNR values with the interesting observation that the slope of the CDF curves becomes steeper when increasing M , which leads to the removal of fading effects.

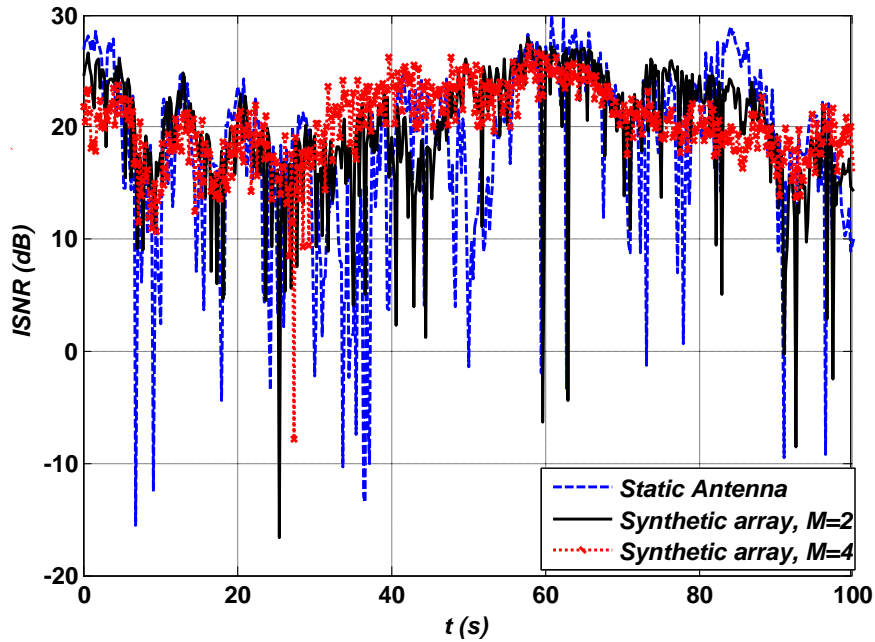


Figure 5-33: Instantaneous SNR for static antenna and synthetic array with $M=2$ and $M=4$

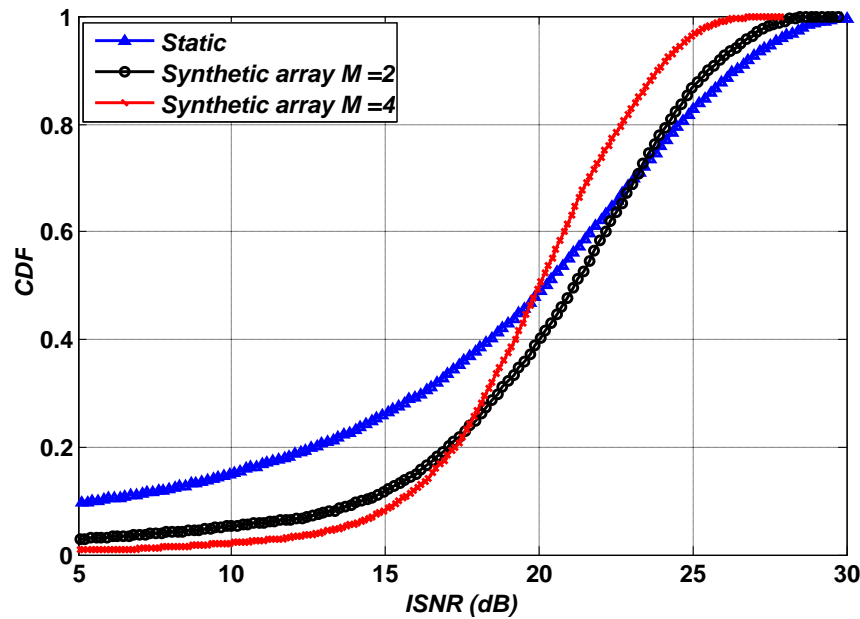


Figure 5-34: Instantaneous SNR cumulative density functions

Table 5-9 shows the P_D and processing gain of the synthetic array for two and four antenna positions for a given $P_{FA}=0.01$ based on the measurement results of PRN 18, 21 and 24. The measured average SNR for a 400 ms integration time is also given. These results further verify the theoretical findings of Chapter 4.

Table 5-9: Processing Gain and MAT ratio of the synthetic array over the static antenna for different PRNs

	Average SNR (dB)	P_D		Processing Gain (dB)	
		$M=2$	$M=4$	$M=2$	$M=4$
PRN 18	15	0.9 2	0 .96	3.5	7
PRN 21	16	0.9 6	0 .98	4	8
PRN 24	17.5	0.9 7	0 .99	5	11

5.3 Experimental results of detection performance of GPS indoor signals based on the continuous synthetic array

In Section 4.7 the gain advantage of the SA algorithm in the continuous mode was determined based on the Rayleigh fading model with the assumption that the signal channel gain $A(\mathbf{p})$ is a circular normal random process with respect to the antenna position \mathbf{p} but temporally static with respect to the snapshot interval. This resulted in practical expressions for establishing the relative processing gain. The experimental measurements described in this section validate these assumptions in the context of GPS signal detection in indoor environments. The objective of these experimental measurements is to determine the processing gain of the synthetic array in continuous mode for a selection of typical indoor locations and compare these with corresponding theoretical evaluations.

5.3.1 Data collection setup

Two indoor environments were considered for data collection. The first data set was collected in the same laboratory as described earlier and as shown in Figure 5.35a. The second data collection was performed in a larger laboratory, as shown in Figure 5.35b. The utilized equipment and data collection parameters were described in Section 5.2.2. Table 5-10 shows the GPS data collection parameters for the continuous synthetic array.

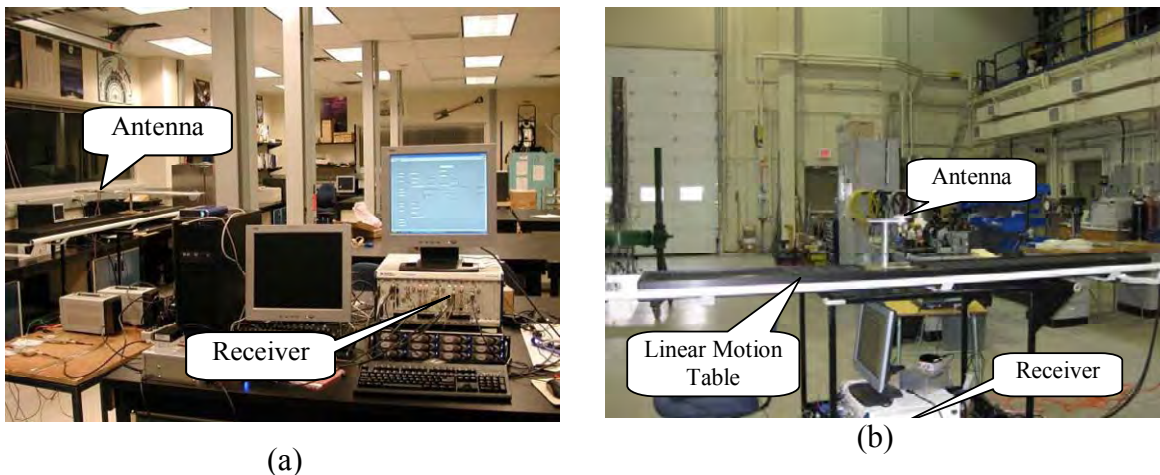


Figure 5-35: Measurements setup a) in the medium size laboratory b) in the large size laboratory

Table 5-10: Characteristics of indoor GPS data collection scenarios in continuous mode

		Date	Sampling rate	IF Frequency	Data collection duration	Antenna velocity
Mid size Lab (Section 5.3.2)		7 March 09	10 MHz	3.42 MHz	30 min	50 cm/s
Large size lab (Section 5.3.3)	Set 1	20 May 09	10 MHz	3.42 MHz	10 min	2 cm/s
	Set 2	20 May 09	10 MHz	3.42 MHz	10 min	1 m/s

5.3.2 Measurement results of data collection in medium size laboratory

The experimental results presented in this section compare the performance of the moving antenna for different values of M . During data collection, the antenna was moving with a constant velocity of 50 cm/s. Each output sample of the measurement results are based on 400 ms processing of the GPS PRN 7, 8 and 19 L1 C/A codes. Hence, in 400 ms the antenna moved about a wavelength of the GPS L1 signal. Thus, based on the discussion of Section 4.7, $M=4$ is a proper choice which provides maximum SA gain. In this section, the detection performance of the moving antenna with $M=1$, $M=2$ and $M=4$ is compared. The statistical results presented herein are based on the processing of 30 minutes of data. Hence, the statistical results shown in this part are the results of 4500 samples under the H_1 state. As a consequence, the PRN 8 measurement results, which are representative of other PRNs, will be discussed in details. The measured processing gain of PRN 7 and 19 are tabulated at the end of this section.

As mentioned in previous sections, the receiver correlates the received signals with the known replica codes through the correlation process. The peak of the correlation process corresponds to the correct code delay and Doppler for which the statistics for the H_1 case were extracted. The other mismatched code delays were used to generate statistics for the H_0 case. Figure 5-36 shows the measured PDFs of the test statistics under H_0 and H_1 for different values of M . For comparison, the PDFs of Chi-Squared central distributions are overlaid.

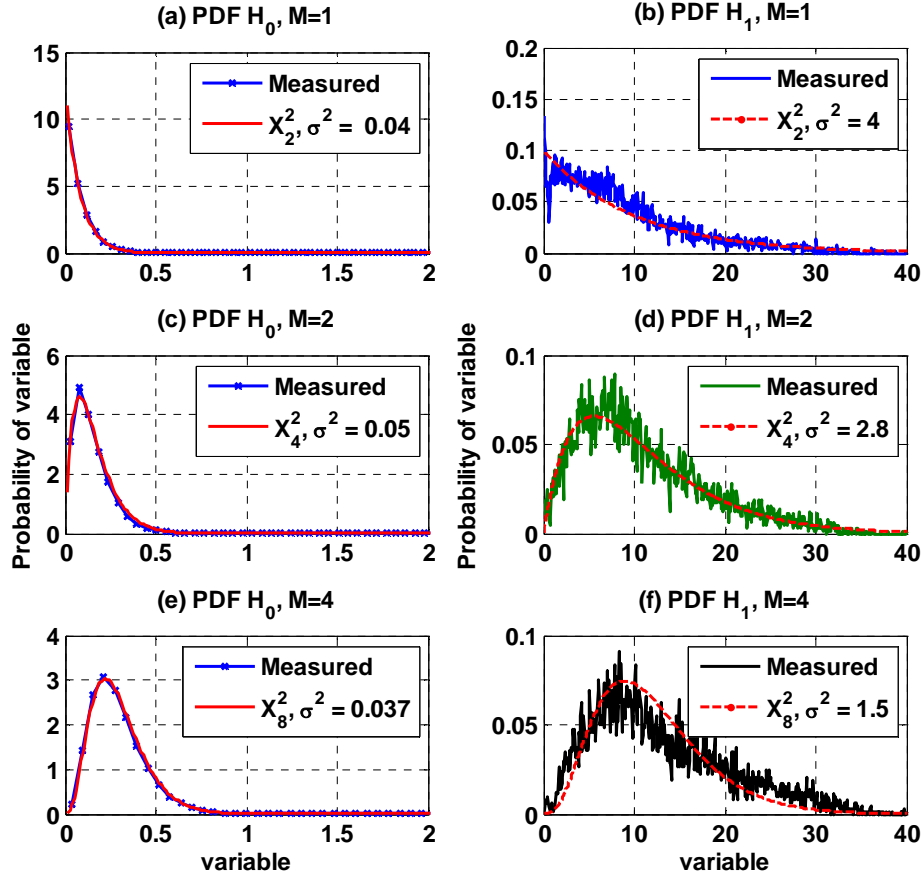


Figure 5-36: Measured PDF under H_0 (a, c and e) and H_1 (b, d and f) states for $M=1$ (a and b), $M=2$ (c and d) and $M=4$ (e and f)

The theoretical PDF shown in Figure 5-36 is a Chi-squared density function with $2M$ DOFs defined in Eq. 5-7. The match with the theoretical Chi-Squared density function provides further confirmation of the validity of the Rayleigh fading model. The variance parameters of the measured test statistics under H_0 and H_1 can be estimated based on the maximum likelihood approach. Then, the corresponding variance parameters under H_0 and H_1 can be normalized by $\sigma^2_{H_0} = 1$ and $\sigma^2_{H_1} = \left(\frac{\rho}{M} + 1\right)$ respectively such that

$\frac{\sigma^2_{H_1}}{\sigma^2_{H_0}} = \left(\frac{\rho}{M} + 1 \right)$. Hence, the average SNR, ρ , is extracted from the measurements. The

estimated average SNR values for $M=1$, $M=2$ and $M=4$ are 20 dB, 21.5 dB and 22.5 dB, respectively. As it is clear, increasing M enhances the SNR values. Note that the match of measurement results with the Chi-squared PDF with two DOFs under H_0 and H_1 for $M=1$ shown in Figure 5-36 a and b confirms the Rayleigh fading assumption. In addition, matching experimental PDFs with the theoretical Chi-squared PDF with four (Figure 5-36c, d) and eight DOFs (Figure 5-36e, f) for $M=2$ and $M=4$ confirms signal decorrelation and multipath model used. After calculating the PDFs under H_0 and H_1 based on measurements, the ROC curves were generated and are shown in Figure 5-37.

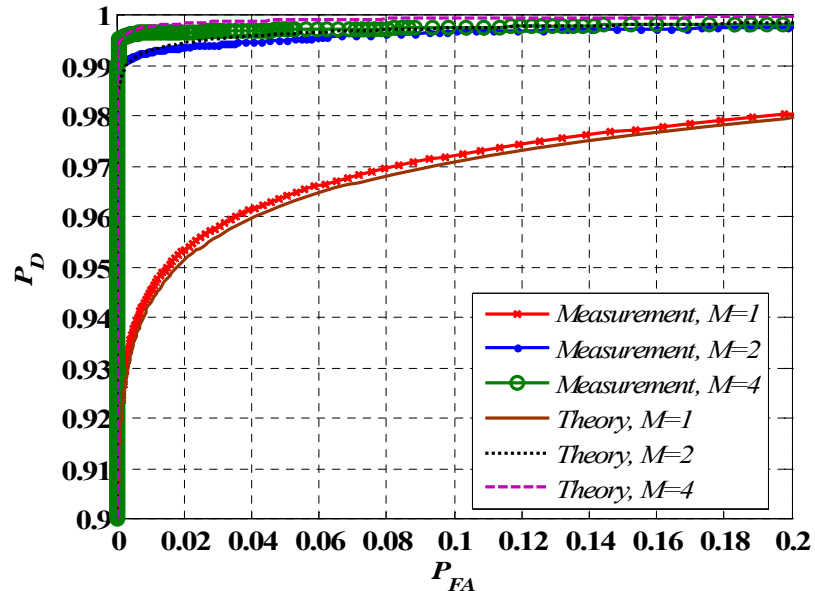


Figure 5-37: Estimated ROC curves based on measurements for the moving antenna for different values of M

As expected, increasing M improves the detection performance. However, a more interesting observation is the comparison of the experimental measurement curves with

the equivalent theoretical results. As observed, the theoretical and experimental results match very well, which further confirms the theoretical analysis presented earlier in Section 4.3 and Section 4.7. Figure 5-38a shows the measured ISNR for a moving antenna with different values of M for a 16-wavelength antenna displacement. It is evident that the moving antenna with $M=1$ has the lowest ISNR values as a result of coherency loss. In addition, ISNR values are susceptible to deep fades and loss of peak detection. By increasing M , the ISNR mean value increases and the ISNR values become resistant to deep fades. Figure 5-38b shows the CDF of ISNR with the interesting observation that the slope of the CDF curves becomes steeper by increasing M , which leads to the removal of fading effects.

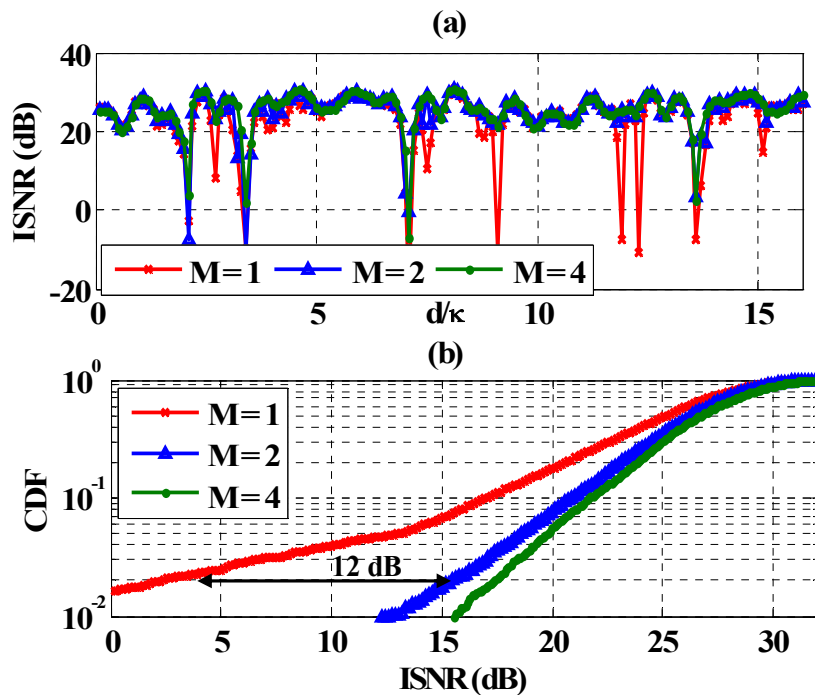


Figure 5-38: a) ISNR for the moving antenna for different values of M , b) CDF of ISNR for different values of M

For instance, the probability of ISNR values which goes below 15 dB for the $M=4$ case is one order of magnitude less than that for $M=1$.

Table 5-11 summarizes the detection statistics of the moving antenna for different values of M for GPS PRNs 7, 8, and 19. The table also provides measured average SNR values for a 400 ms processing interval, number of misdetections, percentage of misdetections and P_D for two different values of P_{FA} . A misdetection occurs when the maximum value of the correlation function based on the measurements is not in the correct cell. Table 5-11 shows that, utilizing the synthetic array process for different PRNs with different target detection performances, the misdetection percentage can be considerably reduced.

Table 5-11: Moving antenna detection statistics for PRN 7, 8 and 19

P RN	ρ (dB)	Num ber of miss detection	Percenta ge of misdetection (%)	P_D	
				$P_{FA} = 0.1$	$P_{FA} = 0.01$
7	1	12.5	1295	28	0.71
	2	14	730	16	0.84
	4	14.7	582	13	0.85
8	1	20	218	5	0.965
	2	21.5	45	1	0.992
	4	22.5	20	0.5	0.995
19	1	15.5	1002	22	0.78
	2	17.4	504	11	0.89
	4	18.3	367	8	0.92

5.3.3 Measurement results of data collection in large size laboratory

In Section 5.3.2, the detection statistics of the synthetic array in continuous mode were compared with the theoretical values presented in Section 4.7 for different values of M in a medium size laboratory. In this section, the detection performance of the moving antenna will be compared with that of the static antenna for different values of M in a large size laboratory. Data collection consisted of two sets: set1 in a pseudo static mode and set2 in a moving mode. In the case of set1, the antenna was moving with a constant velocity of 2 cm/s. In the moving scenario, set2, the antenna was moving 1 m/s. For each data collection set, the test statistics and detection performances were calculated for $T=100$ ms and $T=200$ ms using the C/A code of PRN 31. Hence, in the set2 case, the antenna was displaced 10 cm ($T=100$) and 20 cm ($T=200$) respectively, which is either a half or one full wavelength of the GPS L1 carrier. In this part, the detection performance of the static and moving antennas are compared for $M=1$, $M=2$ and $M=4$. Figure 5-39 shows ROC curves for set1 and set2 for different values of M and for $T=200$ ms. In set1, increasing the number of spatial samples M results in performance degradation. This phenomenon is tagged as *a* in Figure 5-39. Hence, as expected $M=1$ provides the best detection performance in this case. However, when the antenna moves with a displacement of a wavelength of the carrier in each snapshot, $M=1$ gives the worst detection performance. This is due to coherency loss of the channel, tagged as *b* in Figure 5-39. Increasing M while the antenna is moving increases the detection performance. This detection enhancement relative to the static antenna is tagged as *c* in Figure 5-39. Figure 5-40 shows the ISNR CDFs for set1 and set2. In the case of set1, increasing M reduces the ISNR values.

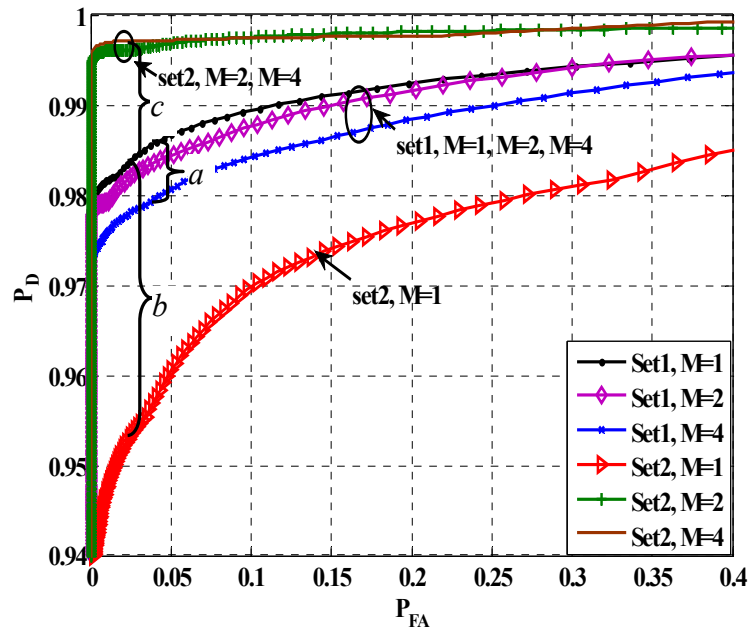


Figure 5-39: ROC curves of the static set1 and moving set2 antenna for $T=200$ ms

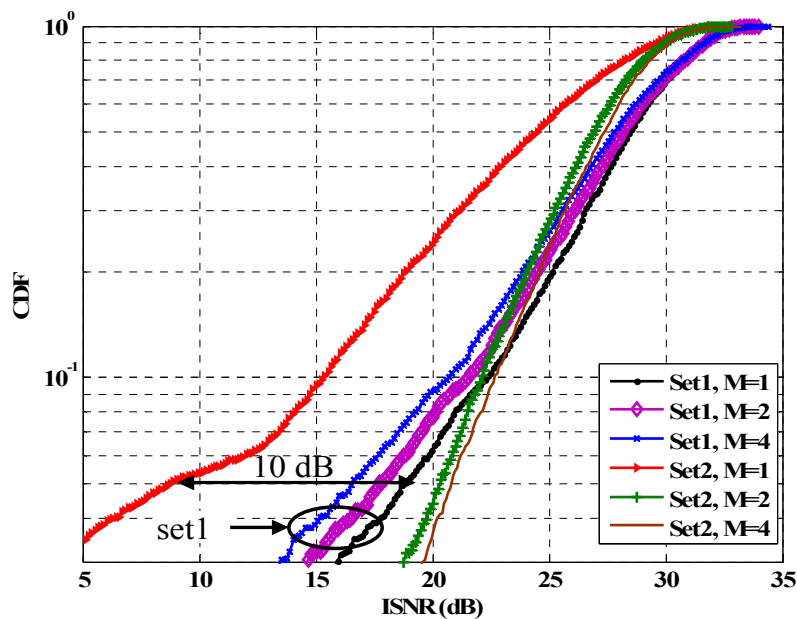


Figure 5-40: ISNR CDFs for (set1) and moving (set2) antennas for $T=200$ ms

However, the patterns of the ISNR CDF for different values of M are almost identical and they all have the same slope. In set2 when $M=1$, ISNR suffers from a channel coherency loss. By increasing M , the detection process takes advantage of the diversity gain and counteracts the fading effect. Hence, the patterns of the ISNR CDF in the set2 with $M=2$ and $M=4$ have steeper slopes than those for the static antenna case.

Table 5-12 and Table 5-13 summarize the detection statistics of the static and the moving antenna tests for different values of M , PRN 31 for $T=100$ ms and $T=200$ ms. The measured average SNR values for a 100 ms processing interval, percentage of misdetection and P_D for two different values of P_{FA} are also given.

Table 5-12: Detection statistics of the moving antenna for PRN 31 ($T=100$ ms)

	M	ρ (dB)	Percentage of misdetection	P_D	
				$P_{FA} = 0.1$	$P_{FA} = 0.01$
Set 1	1	20. 55	3.6	0.971	0.982
	2	20. 4	4.1	0.965	0.977
	4	20. 4	5	0.96	0.972
Set2	1	19	5	0.962	0.978
	2	20	2.1	0.986	0.992
	4	20. 1	2.5	0.982	0.99

Table 5-13: Detection statistics of the moving antenna for PRN 31 ($T=200$ ms)

	M	ρ (dB)	Percentage of misdetection	P_D	
				$P_{FA} = 0.01$	$P_{FA} = 0.001$
Set1	1	23. 5	0.53	0.982	0.989
	2	23. 4	0.55	0.98	0.987
	4	23. 3	0.7	0.975	0.984
Set2	1	20	1.5	0.95	0.97
	2	22	0.12	0.995	0.997
	4	22. 5	0.08	0.996	0.998

Based on the results of Table 5-12, for $M=2$ the detection performance of the moving antenna (set2) is maximum and has the lowest misdetection rate. This phenomenon is expected since, for 100 ms signal snapshots, the antenna was displaced by about half of the carrier wavelength. For the moving antenna when $T=200$ ms (Table 5-13, set2), the lowest misdetection and the highest P_D occur when $M=4$.

Comparing the average SNR values ρ for the static antenna in Table 5-12 and Table 5-13, a 3 dB difference occurs. This is due to the use of two times more data with 200 ms signal snapshots. This result ensures that in this case the channel remains coherent and coherent integration gain can be achieved.

To compare the processing gain of the EG algorithm relative to that of the static antenna, the ROC curves for the moving antenna with $M=2$ and $T=100$ ms compared with the static one with different T values are shown in Figure 5-41.

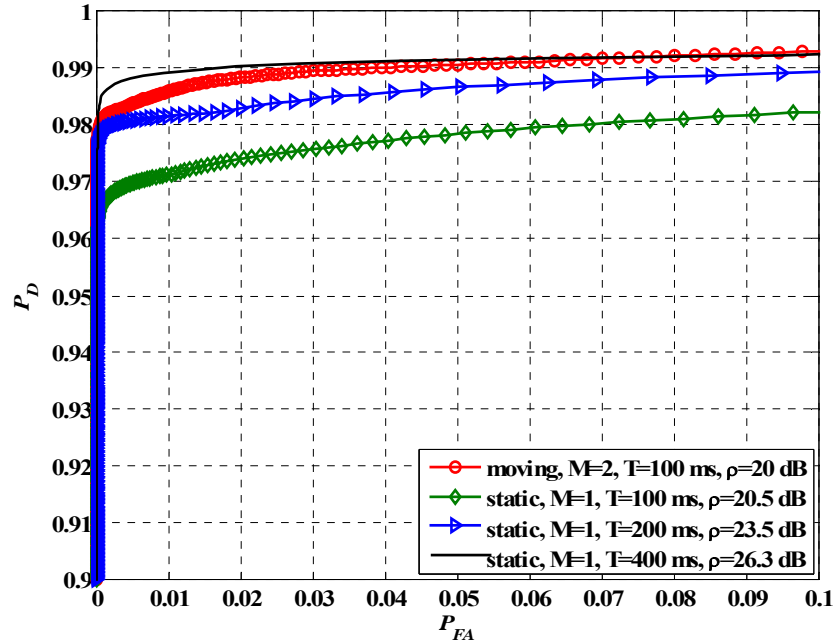


Figure 5-41: ROC curves of the static and moving antennas for different values of T

The performance of the moving antenna with $M=2$ and $T=100$ ms is superior to that of the static antenna. The P_D performances of the moving and the static antenna with $T=400$ ms in the range of $P_{FA} \in [0.04 : 0.1]$ are identical. The estimated average SNR ρ for each experiment is also shown. Based on these, for detection target parameters of $P_D=0.99$ and $P_{FA} \in [0.04 : 0.1]$ there is a gain of about 6 dB. This gain could significantly reduce the mean acquisition time of GPS receivers. For instance, based on the experimental results of Figure 5-41, the performance of the moving antenna utilizing the

EG process becomes identical to the static antenna using four times less data. This may be considered as a reduction in the mean acquisition time performance by a factor of four.

5.4 Conclusions

In this chapter, experimental results of the detection performance of the synthetic array in different indoor fading environments were presented. Two different signals, namely CDMA IS-95 and GPS, were utilized to verify the theoretical findings presented in Chapter 4. The comprehensive set of measured signals was used to verify the Rayleigh fading and spatial correlation models.

The detection performance of the discrete synthetic array under uncorrelated Rayleigh fading was discovered and compared with the theoretical values represented in Chapter 4. It was shown experimentally that, for given target detection parameters in terms of P_{FA} and P_D , there is an optimum number of spatial samples that provides maximum processing gain of the synthetic array over the static antenna. The detection performance of the discrete mode synthetic array was also investigated under correlated fading environments and verified with the theoretical values. A good agreement between the experimental and theoretical results was obtained.

In Section 5.3, experimental results of the detection performance of GPS signals utilizing continuous mode synthetic array were demonstrated. It was shown experimentally that there exists an optimum antenna velocity that provides maximum processing gain. Experimental results reveal that for a practical range of P_D and P_{FA} the synthetic array receiver results into a 6 dB gain advantage relative to the static receiver case. This significant gain translates in a reduction of the mean acquisition process by a

factor of four, which is very important when tracking attenuated GPS signals in urban canyons and indoor.

Table 5-14 summarizes the synthetic array field measurement experiments for different signal structures.

Table 5-14: Summery of field measurement experiments

Signal	Data set	Objectives
IS-95 (Section 5.1)	Data set 1	<ul style="list-style-type: none"> - Verification of Rayleigh fading assumption - Channel correlation coefficient estimation - Evaluation of processing gain of the synthetic array over the static antenna for different values of T in uncorrelated fading environments - Verification of the existence of an optimum value of M
	Data set 2	<ul style="list-style-type: none"> - Analysis of the synthetic array gain in correlated Rayleigh fading - Verification of the test statistics PDFs with different spatial spacing and comparison with theoretical values
GPS in discrete mode (Section 5.2)		<ul style="list-style-type: none"> - GPS indoor channel statistics and correlation coefficient measurements - Evaluation of processing gain of the synthetic array over the static antenna in uncorrelated indoor GPS environments based on the discrete mode synthetic array
GPS in continuous mode (Section 5.3)	Data set 1	<ul style="list-style-type: none"> - Analysis of the detection performance of the indoor GPS utilizing the synthetic array in the continuous mode - Comparison of the detection statistics with the theoretical values
	Data set 2	<ul style="list-style-type: none"> - Comparison of the detection performance of the synthetic array in continuous mode for different receiver velocities - Verification of the existence of the optimum velocity and M which provides maximum gain

Chapter 6: AOA ESTIMATION BASED ON THE SYNTHETIC ANTENNA ARRAY

The approach for detecting a narrowband signal utilized in Chapter 4 and Chapter 5 was based on the assumption that the received signal consists of diffuse multipath where there is a continuum of infinitesimal scattering reflection sources. This is a typical model of the indoor and dense multipath environments. Based on this the signal covariance matrix for the multipath Rayleigh fading model described in Section 3.2.4 and the detection performance and processing gain based on the Estimator-Correlator (EC) detector were investigated theoretically and practically in Chapter 4 and Chapter 5 respectively.

However, in specular multipath environments (described in Section 3.2.3) where a plane wave has an unknown channel gain coefficient and an unknown Angle Of Arrival (AOA), the detection algorithm presented in Section 4 utilizing the EC formulation is not optimal. In this case, a Generalized Likelihood Ratio Test (GLRT) approach (Kay 1998) can be utilized to improve the detection performance since it attempts to estimate the unknown AOA based on a Maximum Likelihood (ML) approach. If the SNR is high, a nonlinear estimation technique such as MULTiple Signal Classification (MUSIC) (Schmidt 1986) and Estimation of Signal Parameters via Rotational Invariance Techniques (ESPRIT) (Roy & Kailath 1989, Rao & Hari 1989) may be utilized to estimate the unknown AOA associated with the plane wave incident on the array. Based on the estimated AOA, the beamforming and null steering approaches can be implemented to

improve detection performance of the desired signal and reject multipath and interference signals.

In this chapter, an approach for AOA estimation based on the synthetic array utilizing the ESPRIT algorithm is described and tested with actual CDMA IS-95 signals. Physical size constraints of handheld devices typically exclude the possibility of using multiple antennas. By taking advantage of the rotational invariance property of the ESPRIT algorithm, an antenna array can be synthesized by moving a single doublet (a two-channel receiver) (Broumandan et al 2008b). The advantages of the proposed method compared to the previous work of AOA estimation based on the synthetic array (Jong & Herben 1999, Jong 2001, Broumandan et al 2007) is that the synthetic array trajectory estimation, which is normally performed by using controllable moving motors or external aiding sensors, is relaxed. This configuration can be used with any rotational invariance moving platforms (i.e. during the data collection the doublet does not rotate) such as moving vehicles. With this configuration, system complexity is considerably reduced.

6.1 AOA estimation problem

In this section the problem of AOA estimation of impinging signals on an antenna array is considered. Assume N signals from distinctive spatial locations are received by an arbitrary geometry array consisting of M sensors. Signals may be samples of a stationary random stochastic process or deterministic function of time (Roy & Kailath 1989). Signals are assumed to be narrowband processes which implies the source bandwidth is much smaller than the reciprocal of the maximum time delay across the

array. Far-field sources which are not coherent (perfectly correlated) are assumed. Consequently, the received signal is a combination of the LOS and reflected plane wave signals. It is also assumed that the number of incoming signals is less than the number of sensors ($N < M$). The transmission-reception medium is assumed to be isotropic and non-dispersive such that the propagated signals are received by the receiver via a straight line (Roy 1987). Hence, signals received are a combination of plane wave signals.

The complex output of the k -th sensor at time t is represented by

$$x_k(t) = \sum_{i=1}^N v_k(\theta_i) s_i(t - \tau_k) \quad 6-1$$

where τ_k is the propagation delay between the k -th sensor and the reference point of the array coordinate, N is the number of signals and $v_k(\theta_i)$ is the phase and gain response of the k -th element of the array to the signal coming from direction θ_i . The narrowband assumption leads to

$$x_k(t) = \sum_{i=1}^N \mathbf{v}_k(\theta_i) s_i(t). \quad 6-2$$

The output of the array in vector form can be written by

$$\mathbf{x}(t) = \mathbf{V}(\theta) \mathbf{s}(t) + \mathbf{n}(t) \quad 6-3$$

where $\mathbf{x}(t)$ is a $M \times 1$ observation vector, $\mathbf{s}(t)$ denotes a $N \times 1$ vector of complex signal envelope at time t . $\mathbf{V}(\theta)$ is a $M \times N$ steering matrix for signals coming from directions $\theta = \{\theta_1, \theta_2, \dots, \theta_N\}$ and

$$\mathbf{V}(\theta) \stackrel{\text{def}}{=} [\mathbf{v}(\theta_1), \mathbf{v}(\theta_2), \dots, \mathbf{v}(\theta_N)]. \quad 6-4$$

It is assumed that the matrix $\mathbf{V}(\boldsymbol{\theta})$ is a full rank matrix and the incoming signals are not coherent. $\mathbf{n}(t)$ is spatially and temporally white Gaussian noise with a variance of σ^2 .

6.1.1 Array manifold and signal subspace

Consider the noise free signal model defined by

$$\mathbf{x}(t) = \mathbf{V}(\boldsymbol{\theta})\mathbf{s}(t). \quad 6-5$$

The columns of $\mathbf{V}(\boldsymbol{\theta})$, $\mathbf{v}(\boldsymbol{\theta}_i)$, are elements of a set which are composed of array responses for the entire range of incoming signals. This set is known as an array manifold. The array manifold is completely defined by the array phase and gain response from all possible signal directions and the array geometry. To evade the ambiguity in the AOA estimation, the mapping from $\boldsymbol{\theta} = \{\theta_1, \dots, \theta_N\}$ to the range of $\mathbf{V}(\boldsymbol{\theta})$ should be one to one, which can be accomplished by proper array design (Roy 1987). The received signal vector in the absence of noise is constrained to the N -dimensional subspace known as signal subspace, which is spanned by the columns of $\mathbf{V}(\boldsymbol{\theta})$.

The signal subspace can be determined by the intersection of the measured signal subspace and calibrated array manifold. In the absence of noise, the outputs of the array span a N -dimensional subspace by the columns of the array manifold. Once the signal subspace is known, the intersection of the array manifold and signal subspace gives a set of vectors from the array manifold that spans the signal subspace.

In practical applications where noise is present, the signal subspace is not known *a priori* and has to be estimated based on the noisy samples. Assuming an unknown deterministic signal embedded in white Gaussian noise, a Maximum Likelihood (ML)

estimator can be applied (Roy 1987). The problem with the ML estimator is that it requires multidimensional search over entire parameters which for most practical applications is computationally prohibitive. Instead, Schmidt (1986) developed a two-step approach for this problem. First, an unconstrained estimate of the signal subspace based on N vectors that best fits the measurements is found. Then the projection of the space spanned by this vector into the array manifold is determined. It is shown that the Schmidt's suboptimal approach is asymptotically an unbiased estimator (Roy 1987).

The objective is to define N linearly independent vectors from noisy measurements which span the signal subspace. Such vectors can be estimated from the eigenvectors of the received signal covariance matrix. The covariance matrix of the signal is given by

$$\mathbf{R}_x \stackrel{\text{def}}{=} E\{\mathbf{x}\mathbf{x}^H\} = \mathbf{V}\mathbf{R}_s\mathbf{V}^H + \sigma^2\mathbf{I} \quad 6-6$$

where \mathbf{R}_s is the signal covariance matrix. The N eigenvectors of \mathbf{R}_x corresponding to the N largest eigenvalues given by $\mathbf{E}_s = [\mathbf{e}_1, \mathbf{e}_2, \dots, \mathbf{e}_N]$, provides N independent vectors which spans the signal subspace. In real applications, the covariance matrix is not known and must be estimated from measurements. An estimate of the measured signal covariance matrix may be defined by

$$\hat{\mathbf{R}}_x = \frac{1}{K} \sum_{k=1}^K \mathbf{x}(k)\mathbf{x}^H(k) = \frac{1}{K} \mathbf{X}\mathbf{X}^H \quad 6-7$$

where K is the number of snapshots and \mathbf{X} is the $M \times K$ data matrix. In this case the $M-N$ smallest eigenvalues of the covariance matrix are not exactly equal to σ^2 but are only clustered around it. In this situation, sophisticated algorithms based on the Likelihood Ratio Test (LRT) can be used to estimate the signal and noise dimensions. For more

details of array manifolds and the signal and noise subspaces, readers are referred to Van Trees (2002).

6.1.2 AOA estimation based on the MUSIC algorithm

In the absence of noise, signal parameters (e.g. AOA) can be determined by finding the intersection of the array manifold with the signal subspace. The signal parameters can also be determined by finding elements of the array manifold which are orthogonal to the noise subspace. In the absence of noise, finding the intersection of the array manifold and signal subspace is computationally costly and requires a multi-dimensional search. However, in the presence of noise, this procedure becomes even worse due to the fact that there is no intersection between the signal subspace and the array manifold. Hence, vectors of array manifolds, which are closest to the signal subspace should be taken as a potential solution. Schmidt (1986) proposed the following criterion for defining the elements of array manifold which are closest to the signal subspace:

$$P_{MUSIC}(\theta) = \frac{\mathbf{v}^H(\theta)\mathbf{v}(\theta)}{\mathbf{v}^H(\theta)\mathbf{E}_N\mathbf{E}_N^*\mathbf{v}(\theta)} \quad 6-8$$

where $\mathbf{E}_N = [\mathbf{e}_{N+1}, \dots, \mathbf{e}_M]$ are the $M-N$ eigenvectors of \mathbf{R}_x corresponding to the $M-N$ smallest eigenvalues of \mathbf{R}_x . This relation is known as the MUSIC spectrum. In the absence of noise, for the correct AOA Eq. 6-8 goes to infinity. In the presence of noise, the MUSIC spectrum gives some peaks for the closest approach of the array manifold to the signal subspace (Schmidt 1986).

6.1.3 ESPRIT angle of arrival estimation algorithm

This section briefly describes the Total Least Squares (TLS) ESPRIT algorithm. For simplicity consider a planar array consisting of M doublets with an arbitrary geometry, phase and gain response. The ESPRIT array geometry for three doublets is shown in Figure 6-1.

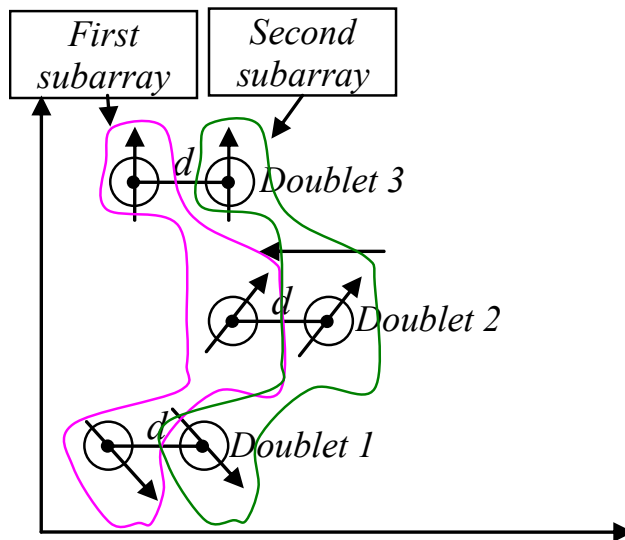


Figure 6-1: ESPRIT array geometry

d is the distance between two sensors in each doublet and is identical for all doublets. Sensors in each doublet have the same phase and gain characteristics. However, different doublets may have different phase and gain responses. In addition, doublet sensors connection axes are parallel for all doublets (translation invariance property). Shown in Figure 6-1 is the ESPRIT array structure which consists of different doublets, with each doublet composed of two identical pattern sensors (Roy & Kailath 1989, Swindlehurst et al

1992, Ottersten et al 1991). The array configuration of the ESPRIT algorithm can be represented by two sub-arrays, with each doublet having a sensor in each sub-array. Therefore, each sub-array is the replica of the other one, separated by a known physical displacement d . In such case, each sub-array consists of sensors with arbitrary phase and gain characteristics. Doublets and sub-arrays are shown in Figure 6-1.

The output of each doublet can be represented by

$$\begin{aligned}\mathbf{x}_1(t) &= \mathbf{Vs}(t) + \mathbf{n}_1(t) \\ \mathbf{x}_2(t) &= \mathbf{V}\Psi\mathbf{s}(t) + \mathbf{n}_2(t)\end{aligned}\quad 6-9$$

where $\mathbf{s}(t)$ is the $N \times 1$ received signal vector and $\mathbf{n}_1(t)$ and $\mathbf{n}_2(t)$ are $M \times 1$ noise vectors at the output of each sub-array. Ψ is defined as a $N \times N$ matrix that relates the measurements from the first sub-array to the second. Ψ is defined as

$$\Psi = \text{diag} \left\{ e^{\frac{j2\pi d}{\kappa} \sin \theta_1}, \dots, e^{\frac{j2\pi d}{\kappa} \sin \theta_N} \right\} \quad 6-10$$

where κ is the wavelength of the impinging signals and θ_i is the AOA of the i th signal relative to the doublets connection vector. Combining the outputs of the sub-arrays in a single vector yields

$$\begin{aligned}\mathbf{z}(t) &= \begin{bmatrix} \mathbf{x}_1(t) \\ \mathbf{x}_2(t) \end{bmatrix} = \begin{bmatrix} \mathbf{V} \\ \mathbf{V}\Psi \end{bmatrix} \mathbf{s}(t) + \begin{bmatrix} \mathbf{n}_1(t) \\ \mathbf{n}_2(t) \end{bmatrix} \\ &= \mathbf{V}'\mathbf{s}(t) + \mathbf{n}'(t)\end{aligned}\quad 6-11$$

The ESPRIT algorithm similarly to the MUSIC AOA estimator relies on the estimation of the signal subspace. The signal subspace can be estimated through an eigen analysis of the covariance matrix defined by

$$\mathbf{R}_z = \mathbf{V}'\mathbf{R}_s\mathbf{V}'^H + \sigma^2\mathbf{I}. \quad 6-12$$

The N eigenvectors corresponding to the N largest eigenvalues span the signal subspace denoted as $\mathbf{E}_s = \{\mathbf{e}_1, \mathbf{e}_2, \dots, \mathbf{e}_N\}$. The range of \mathbf{E}_s is equal to the range of \mathbf{V}' (Roy & Kailath 1989). Hence, there is a nonsingular matrix \mathbf{T} to satisfy $\mathbf{E}_s = \mathbf{V}'\mathbf{T}$. \mathbf{E}_s can be decomposed as (Roy 1987)

$$\mathbf{E}_s = \begin{bmatrix} \mathbf{E}_{x_1} \\ \mathbf{E}_{x_2} \end{bmatrix} = \begin{bmatrix} \mathbf{V}\mathbf{T} \\ \mathbf{V}\Psi\mathbf{T} \end{bmatrix} \quad 6-13$$

where the ranges of \mathbf{E}_{x_1} and \mathbf{E}_{x_2} are equal to the range of \mathbf{V} . Since the ranges of \mathbf{E}_{x_1} and \mathbf{E}_{x_2} are the same, the rank of matrix $[\mathbf{E}_{x_1} \ \mathbf{E}_{x_2}]$ becomes N . This implies that there is a $2N \times N$ matrix, namely

$$\mathbf{P} = \begin{bmatrix} \mathbf{P}_{x_1} \\ \mathbf{P}_{x_2} \end{bmatrix} \quad 6-14$$

with rank N that spans the null-space of $[\mathbf{E}_{x_1} \ \mathbf{E}_{x_2}]$, which implies

$$\begin{aligned} 0 &= [\mathbf{E}_{x_1} \ \mathbf{E}_{x_2}] \mathbf{P} \\ &= \mathbf{E}_{x_1} \mathbf{P}_{x_1} + \mathbf{E}_{x_2} \mathbf{P}_{x_2} \\ &= \mathbf{V}\mathbf{T}\mathbf{P}_{x_1} + \mathbf{V}\Psi\mathbf{T}\mathbf{P}_{x_2} \end{aligned} \quad 6-15$$

Eq. 6-15 can be written as

$$\mathbf{V}\mathbf{T}\mathbf{F} = \mathbf{V}\Psi\mathbf{T}. \quad 6-16$$

where $\mathbf{F} = -\mathbf{P}_{x_1} \mathbf{P}_{x_2}^{-1}$, which assumes that \mathbf{P}_{x_2} is full rank. From Eq. 6-13 and 6-16 $\mathbf{F} = -\mathbf{E}_{x_1} \mathbf{E}_{x_2}^{\#}$ where $(\bullet)^{\#}$ is the pseudo inverse operator. Hence, it can be shown that (Roy 1987)

$$\Psi = \mathbf{T} \mathbf{F} \mathbf{T}^{-1}$$

6-17

Eq. 6-17 shows that Ψ and \mathbf{F} are similar and they have the same eigenvalues, which are the diagonal elements of Ψ . Therefore, the AOA can be estimated from the eigenvalues of \mathbf{F} . In the following, steps toward AOA estimation by the TLS ESPRIT algorithm are described (Roy & Kailath 1989):

- 1) Estimate the correlation matrix from K independent measurements
- 2) Calculate the signals subspace dimension
- 3) Estimate the signal subspace \mathbf{E}_s from partitioning the eigenvectors
- 4) Compute the eigenvectors of

$$\begin{bmatrix} \mathbf{E}_{x_1}^* \\ \mathbf{E}_{x_2}^* \end{bmatrix} \begin{bmatrix} \mathbf{E}_{x_1} & | & \mathbf{E}_{x_2} \end{bmatrix} = \mathbf{E} \Lambda \mathbf{E}^* \quad 6-18$$

and partition \mathbf{E} as

$$\mathbf{E} = \begin{bmatrix} \mathbf{E}_{11} & \mathbf{E}_{12} \\ \mathbf{E}_{21} & \mathbf{E}_{22} \end{bmatrix} \quad 6-19$$

- 5) Estimate eigenvalues $\hat{\phi}_k$ of $\Phi = -\mathbf{E}_{12}\mathbf{E}_{22}^{-1}$
- 6) The AOA can be estimated by

$$\hat{\theta}_k = \sin^{-1} \left\{ \frac{\arg(\hat{\phi}_k)\lambda}{2\pi d} \right\} \quad 6-20$$

6.1.4 AOA estimation based on the synthetic array utilizing the ESPRIT algorithm

Eq. 6-17 revealed that, for AOA estimation with the ESPRIT algorithm, array manifold information is not required. This property has several benefits in the context of the synthetic array including:

1) Array calibration is a critical procedure in high-resolution AOA estimation. Several articles (e.g. Pierre & Kaveh 1991, See 1994, 1995) have discussed methods to mitigate phase and gain differences among different channels of the sensor array. In the ESPRIT algorithm context, the calibration process is reduced to the doublet phase and gain adjustment. Experimental results showed that AOA estimation by the ESPRIT algorithm is not sensitive to gain differences which decrease the number of parameters to be estimated (Li & Vaccaro 1992, Soon & Huang 1992).

2) Eq. 6-17 is the key relationship in the development of the ESPRIT algorithm which suggests that eigenvalues of $\mathbf{F} = \mathbf{E}_{x_1}^H \mathbf{E}_{x_2}$ are equal to the diagonal elements of Ψ . Utilizing the ESPRIT algorithm, the AOA is estimated relative to the vector d shown in Figure 6-1. Hence, the calibration process of doublet geometry is relaxed. This property increases the flexibility of the array geometry and aperture extension with a fixed number of sensors.

The specific properties of the ESPRIT algorithm make it a proper candidate for AOA estimation with the synthetic antenna array. In this case, just one doublet is required for synthesizing the whole array. During the data collection, the receiver collects spatial and temporal samples. The only constraint in the synthetic array realization utilizing the ESPRIT algorithm is the rotational invariance displacement. Neither a rotating arm with mechanical motor nor external sensors is required to estimate the trajectory of the antenna.

6.2 Simulation results of AOA estimation based on the synthetic array

In this section Monte-Carlo simulations are carried out to determine the performance of the ESPRIT algorithm in the context of AOA estimation. The problem of interest is estimating the AOA of far field narrowband sources. Various scenarios considering implementation issues of the ESPRIT AOA estimator based on the synthetic array including source correlation, and source number estimation, are considered. Throughout the simulations, it is assumed that each antenna in the doublet has a constant gain and phase response in the range of interest (omni-directional pattern).

6.2.1 Baseline simulation

In all simulations, M denotes the number of sensors in each sub-array, N is the number of sources, and K is the number of snapshots used to estimate the signal covariance matrix. It is assumed that the number of sources N is known unless stated to the contrary. Since ESPRIT does not depend on the location of doublets, the arbitrary geometry array shown in Figure 6-2 is utilized. As a baseline case, two uncorrelated sources at 50 and 60 degrees with equal powers (SNR=20 dB) are assumed. The sensor array is shown in Figure 6-2 where the doublet spacing is half of the wavelength. Figure 6-3 shows AOA estimation based on the ESPRIT algorithm for 5000 independent runs where $K=20$.

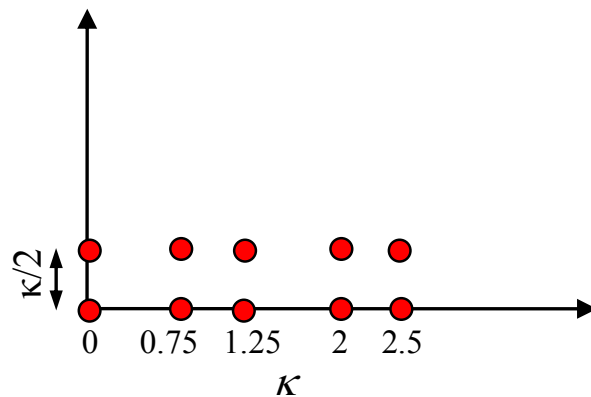


Figure 6-2: Array configuration utilized in the simulation

Figure 6-4 shows the estimated AOA PDF and overlaid Normal fit for the scenario presented in Figure 6-3. Figure 6-4 also shows the mean and variance values of AOA estimation utilizing the ESPRIT algorithm.

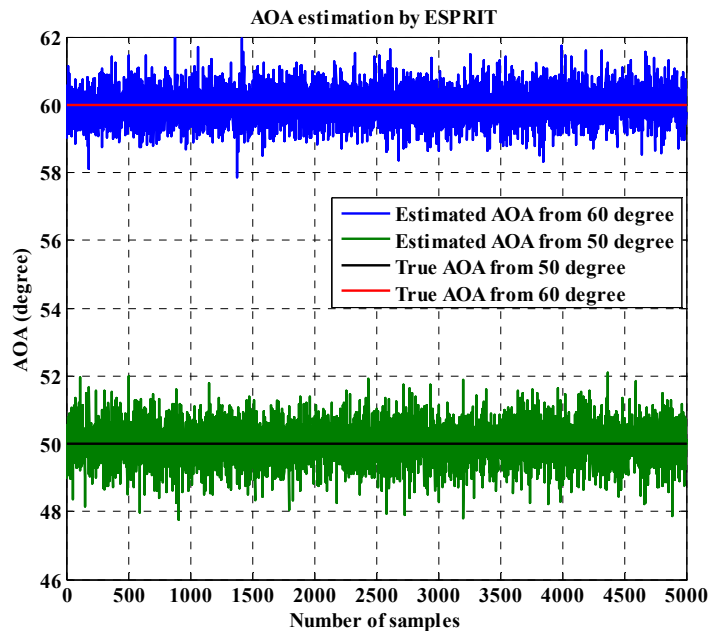


Figure 6-3: AOA estimation by the ESPRIT algorithm for 5000 runs

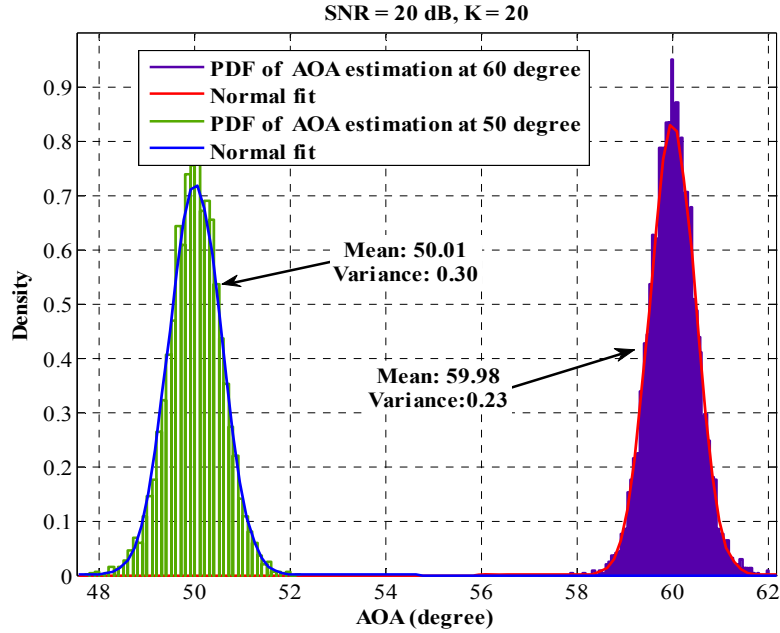


Figure 6-4: Estimated and fitted PDFs of AOA estimation

6.2.2 Sensitivity of the ESPRIT algorithm to the model order estimation

In the baseline simulation, it was assumed that the number of sources is known. However, in practical cases the number of sources should be estimated from the received signal. This subsection examines the performance of the ESPRIT AOA estimator in the presence of errors in model order estimation. The scenario considered here is the same as that of the baseline simulation except for the assumption of the number of sources. Figure 6-5 shows the histogram of AOA estimation for the situation when just one incoming signal is assumed (signal subspace is one).

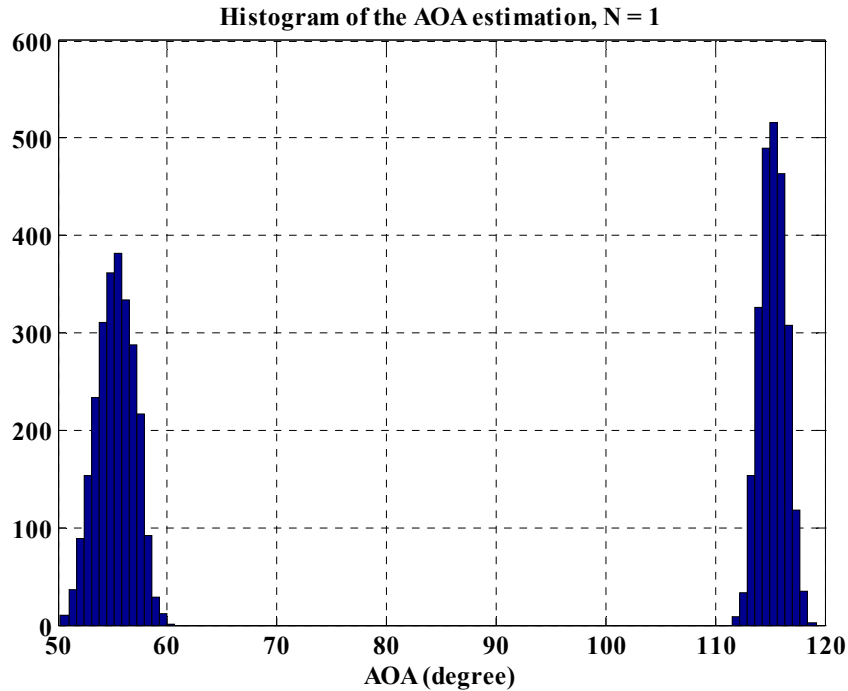


Figure 6-5: Histogram of AOA estimation by the ESPRIT algorithm, model order is underestimated (true angles are 50 and 60 degrees)

The actual directions of arrivals are 50 and 60 degrees. In this scenario the ESPRIT algorithm cannot correctly estimate even one direction.

Figure 6-6 shows the AOA estimation for the situation where the ESPRIT algorithm is assuming three impinging signals (overestimated case).

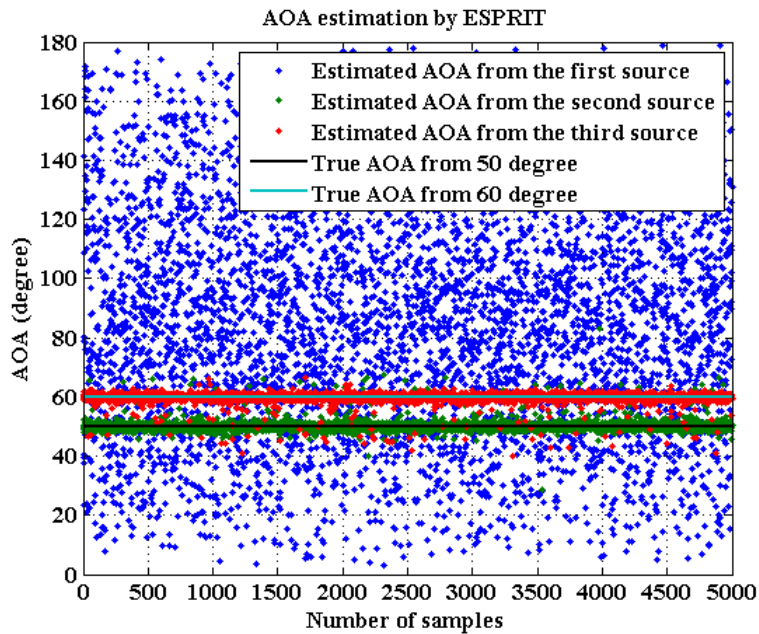


Figure 6-6: AOA estimation by the ESPRIT algorithm, model order is over estimated

Simulation results showed that, when the number of incoming signals is underestimated, the ESPRIT algorithm cannot correctly estimate even one direction. However, in the over estimation case (results of Figure 6-6), the actual AOA of the impinging signals can be correctly estimated. This phenomenon is also reported in (Jong 2001).

6.2.3 AOA estimation in correlated signal environments

One issue which limits the accuracy and performance of the high resolution AOA estimation algorithms is source correlations. If some signals impinging on the antenna array are correlated, the signal covariance matrix tends to be ill conditioned (near singular

in correlated cases and singular in coherent cases) and cannot be used to estimate the AOAs of the signals (Reddy et al 1987). In wireless communication, correlated or coherent signals exist due to multipath propagation (Haykin 1985). In this section, the performance of the ESPRIT AOA estimation in correlated signal environments is considered.

Figure 6-7 shows the PDFs of the estimated AOA for a signal correlation coefficient of $r = 0.9 \exp(-j\pi/4)$.

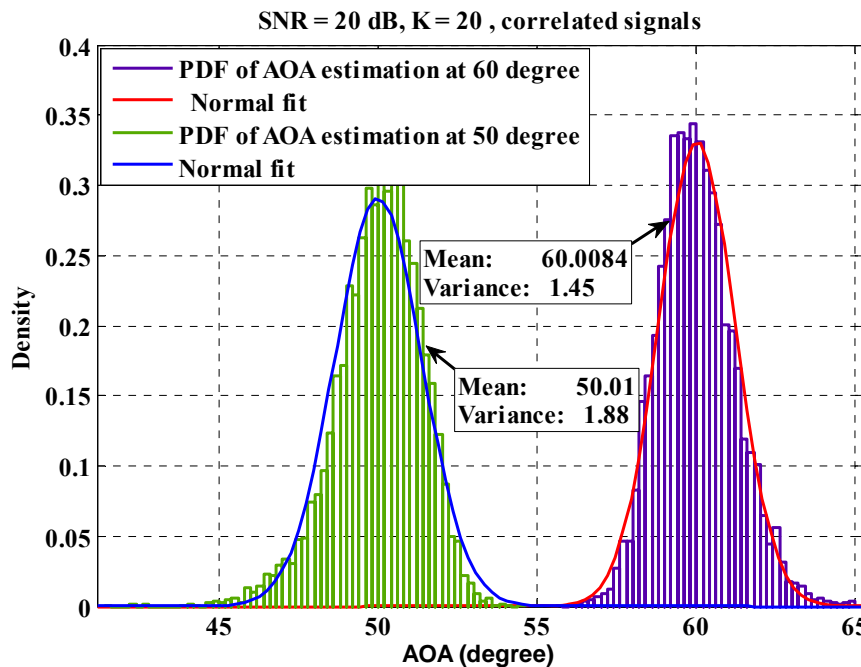


Figure 6-7: PDFs of the estimated AOA in correlated signal environment

By increasing the correlation coefficient, one observes that the variance of the AOA estimation increases (compared to the results of Figure 6-4). Table 6-1 summarizes the means and variances of AOA estimation for different values of signal correlations for the same scenario of the baseline example.

Table 6-1: Means and variances of AOA estimation for different values of signal correlations

Correlation	Mean		Variance	
	True AOA=50	True AOA=60		
$r=0.25$	50	60	0.32	0.26
$r=0.5$	50	60	0.41	0.33
$r=0.75$	50	60	0.72	0.56
$r=0.9$	50	60	1.9	1.5
$r=0.99$	48.9	64	120	280

The results show that, by increasing the correlation coefficient, the variance of the ESPRIT AOA estimator increases. However, for moderate and high correlation coefficient cases ($r \leq 0.9$) and for the given scenario, the ESPRIT algorithm provides an unbiased estimation.

6.3 Practical considerations and experimental results

In this section, practical considerations and implementation issues of AOA estimation utilizing ESPRIT including signal subspace dimension estimation and calibration process are explained. Then, experimental results of AOA estimation of the synthetic array with actual CDMA IS-95 pilot signals are demonstrated.

6.3.1 Estimation of signal subspace dimension

High-resolution subspace-based AOA estimation algorithms rely on the estimation of signal subspaces (or equivalently noise subspaces). In an ideal case, the $M-N$ smallest eigenvalues of the sensors output covariance matrix are all identical and equal to σ^2 . Based on this fact the signal/noise subspace can be easily estimated. However, in practice the covariance matrix is estimated by a finite number of samples. In such a case, all eigenvalues of the covariance matrix become different. Hence, it is difficult to estimate the signal subspace size. Simulation results in Section 6.2.2 revealed the importance of correct estimation of the signal subspace dimension. In this section, a principle based on Akaike's Information Criterion (AIC) (Wax & Kailath 1985) is used to estimate signal subspace dimension. The AIC principle is defined by

$$AIC(N) = -K(M-N) \ln \left[\frac{\left(\prod_{l=N+1}^M \hat{\lambda}_l \right)^{1/(M-K)}}{\frac{1}{M-N} \sum_{l=N+1}^M \hat{\lambda}_l} \right] + N(2M-N) \quad 6-21$$

where M , N , and K are the number of sensors, incoming signals and snapshots, respectively. $\hat{\lambda}_i$ is the i -th eigenvalue of the estimated covariance matrix. The estimated number of source signals (\hat{N}) is chosen to minimize the AIC criterion as

$$\hat{N}_{AIC} = \arg \min_N \{ AIC(N) \}. \quad 6-22$$

6.3.2 Calibration process

Although high-resolution techniques for AOA estimation such as MUSIC and ESPRIT have superior accuracy over conventional parameter estimation algorithms and less complexity over the Maximum-Likelihood (ML) approach, these algorithms are sensitive to array perturbation errors in the array manifold. As a result, to achieve a super-resolution performance, array calibration is required. These deviations from an actual array manifold are the result of gain and phase differences between different channels of a multi-channel receiver, mutual coupling between antennas, and I/Q imbalance in quadrature receivers.

With array manifold parameterization, the array calibration procedure can be approached as an estimation problem (Kay 1993). Different approaches for array calibration based on ML and subspace algorithms are proposed in the literature (Ng et al 1996, Pierre & Kaveh 1991). Experimental results in Soon & Huang (1992) have shown that the ESPRIT algorithm, as opposed to the MUSIC estimator, is not sensitive to the sensor gain errors. Hence, phase calibration is sufficient. In this section, a phase estimator is utilized to compensate for the element phase differences in each doublet.

6.3.2.1 Phase estimator

In Section 6.1.3 it was shown that, by taking advantage of the ESPRIT algorithm, the antenna array can be synthesized by moving a single doublet without using controllable moving motors or external aiding sensors. This property reduced the array configuration

into a two-channel receiver. However, as discussed in Section 6.1.3 the sensors in each doublet should have the same phase response. Hence, before implementing the synthetic array utilizing the ESPRIT algorithm, one should calibrate the two-channel receiver.

In Section 5.1 it was mentioned that the correlation function of the PRN codes provides sufficient statistics for estimating signal parameters received by the array. Hence, the complex value at the peak position of the correlation function denoted here as x is utilized for the calibration process. The correlation function for one period of CDMA IS-95 signals was shown in Figure 5-4. The phase estimation may be defined by

$$\phi_i = \tan^{-1} \left\{ \frac{\text{imag}(x_i)}{\text{real}(x_i)} \right\} \quad i = 1, 2 \quad . \quad 6-23$$

ϕ_i gives the estimated phase of each channel at the output of the correlation function (Kay 1993). The calibration process adjusts the phase differences of the two-channel receiver with respect to the calibration source. For example if the calibration source is perpendicular to the doublet connection axis, the calibration process equalizes phases at the output of two sensors.

6.3.3 Experimental results

Experimental measurements represented in this chapter are based on reception of the downlink CDMA IS-95 pilot signals. The characteristics of the CDMA IS-95 signals were described in Section 5.1.1. The utilized synthetic array method based on the ESPRIT algorithm consists of a two-channel receiver. Due to using different electrical components in different channels, each channel has a distinctive phase and gain response. In the AOA

estimation concept, the directions of incident signals are estimated based on the phase differences among different antennas. Therefore, the relative measured phase of sensors with respect to that of a reference sensor is utilized for the calibration process. Hence, in the calibration process the first channel was considered as the reference antenna and the phase of the second channel adjusted accordingly.

The data collection site was the roof of the CCIT building at University of Calgary where access to LOS signals from two CDMA BSs, namely Market Mall and UofC, is possible. The measurement site and experimental setup are shown in Figure 6-8. In CDMA wireless communication systems, signals received by the antenna are normally below the noise floor. To extract signal parameters, an acquisition process is required. The acquisition process of the CDMA IS-95 signal was described in Section 5.1.1. Signals at the peak of the correlation function are used for the calibration process and AOA estimation. The true angle of incidence was estimated by knowing the exact position of the BSs, measurement location and doublet orientation. This information then was used to verify the AOA estimation results. Two sensors with half wavelength spacing were placed on the linear moving table shown in Figure 6-8 to synthesize the antenna array. Table 6-2 shows the characteristics of data collection scenarios.

Table 6-2: Characteristics of indoor GPS data collection scenarios

Date	Sampling rate	IF Frequency	Data collection duration	Antenna velocity
11 Sep 2008	10 MHz	500 KHz	10 min	5 cm/s



Figure 6-8: Measurement setup on the roof of the CCIT building

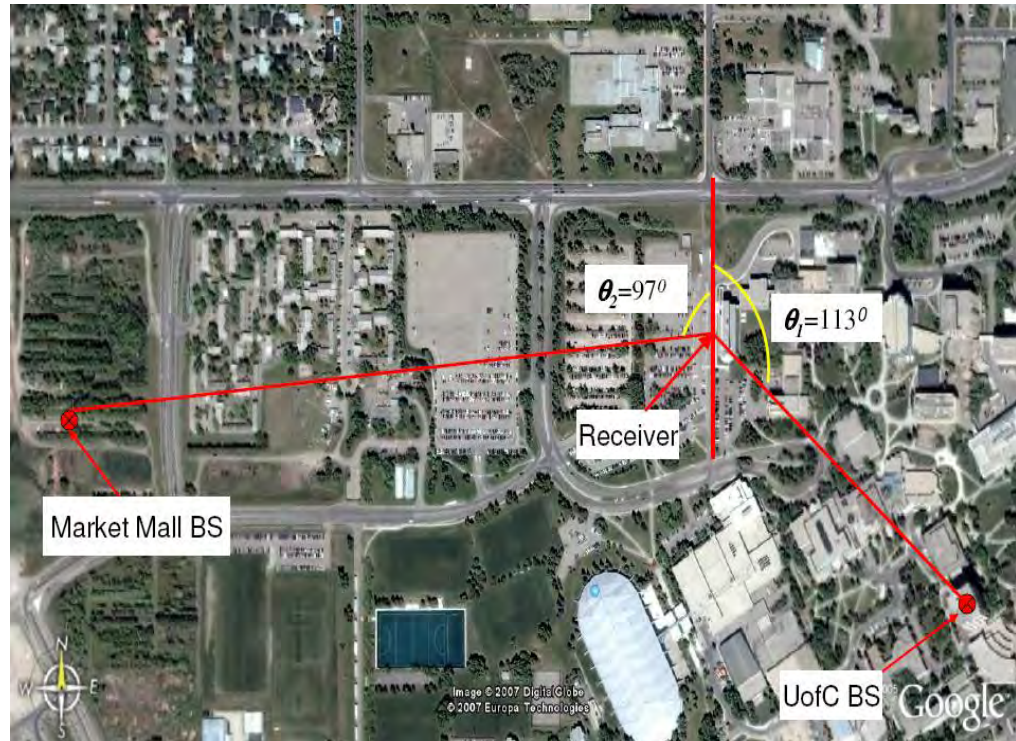


Figure 6-9: Topology of the receiver and BSs

Before estimating the AOA of incoming signals, the receiver was calibrated based on the phase estimation and compensation method described in Section 6.3.2. Calibration in the field due to the multipath propagation in the presence of noise is not a deterministic process. Figure 6-10 shows unwrapped estimated phase values at the output of each antenna element for signals arriving from the UoFC BS. During the data collection, the doublet was moving with a velocity of 5 cm/s.

Figure 6-11 shows phase differences of two antennas at the output of the correlation peak for 45,000 signal snapshots.

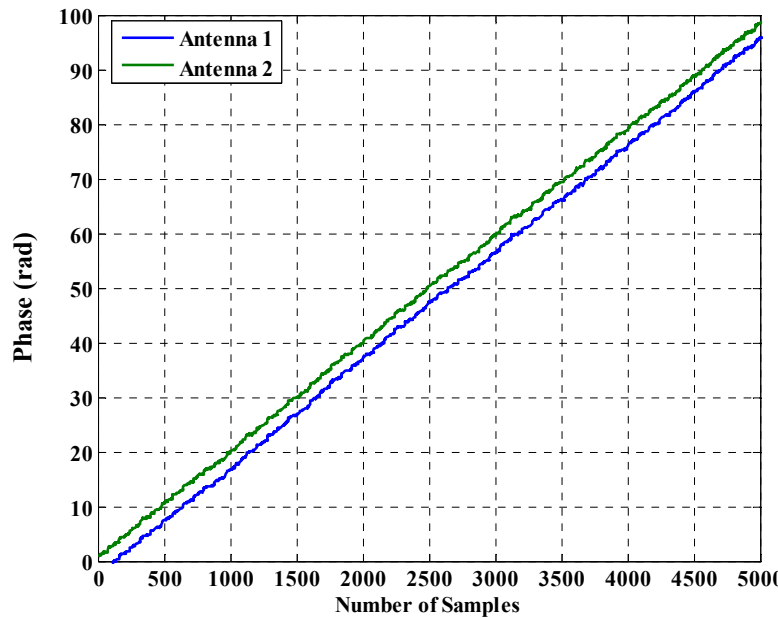


Figure 6-10 Estimated phase values of two antennas at the calibration point

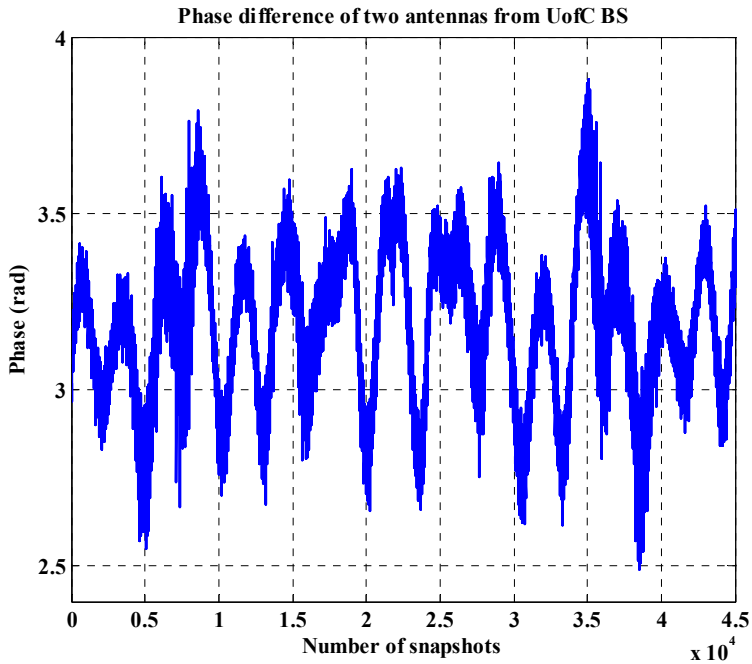


Figure 6-11: Phase differences of estimated phase values between two antennas at the output of the correlation function

The mean value of the phase differences shown in Figure 6-11 is utilized as the estimate of the phase difference. The PDF of the estimated phase differences of the doublet is shown in Figure 6-12, which also shows the Normal fit to the PDF of the measured phase differences.

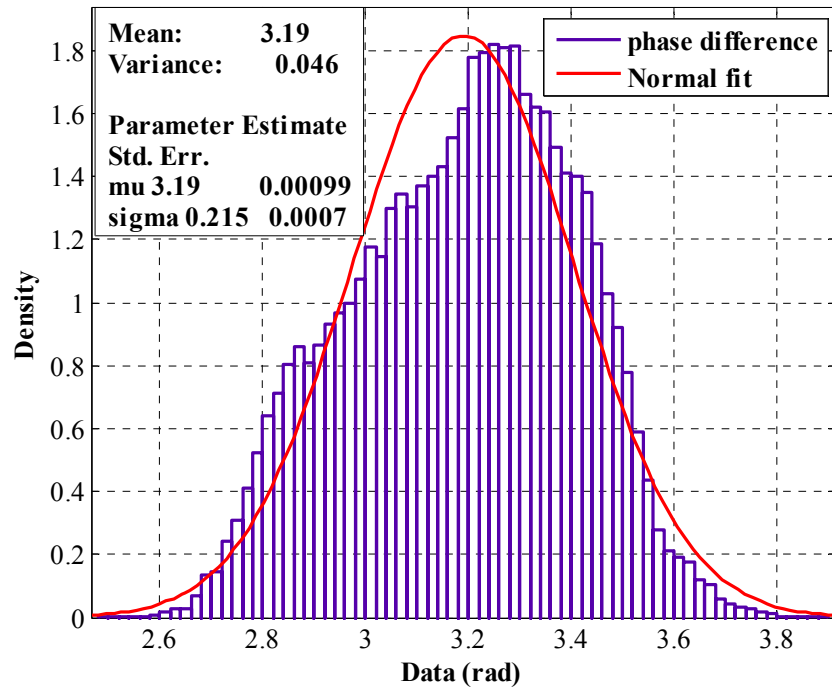


Figure 6-12: PDF of phase differences between two channels and normal fit

It is interesting to analyze the AOA estimation degradation due to phase calibration errors which can be modeled by an uncorrelated random process. In Soon & Huang (1992) is shown that the MSE of AOA estimation for two incoming signals can be simplified by

$$E\left\{|\Delta\theta_k|^2\right\} \approx \frac{2}{M} \left(\frac{\kappa}{2\pi d \cos\theta_k} \right)^2 \sigma_\phi^2 \quad 6-24$$

where M is the number of sensors, σ_ϕ^2 is the variance of the phase mismatch error, d is doublet spacing and κ is the carrier wavelength.

Figure 6-13 shows the root MSE of AOA estimation by the ESPRIT algorithm for a given variance in the phase estimation.

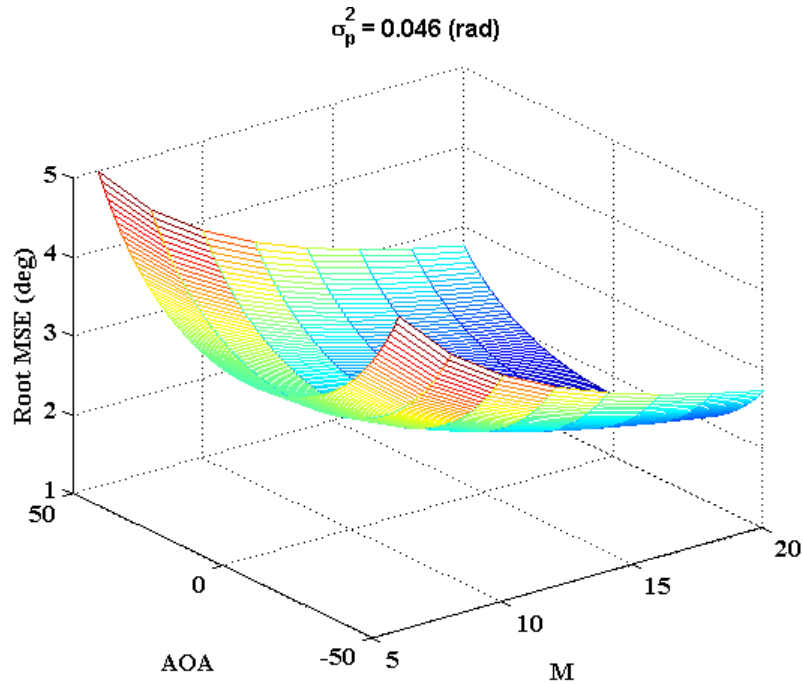


Figure 6-13: Root MSE for AOA estimation degradation due to phase mismatches in the calibration process

As mentioned in the previous section, the ESPRIT AOA estimator assumes that the number of incoming signals is known or can be estimated. In Section 6.3.1 the AIC criterion was introduced to estimate the number of sources and signal subspaces. Figure 6-14 shows the output of the AIC criterion for real data measurements. Based on the results of Figure 6-14, the minimum of the AIC function occurs at 1, which emphasizes the number of incoming signals.

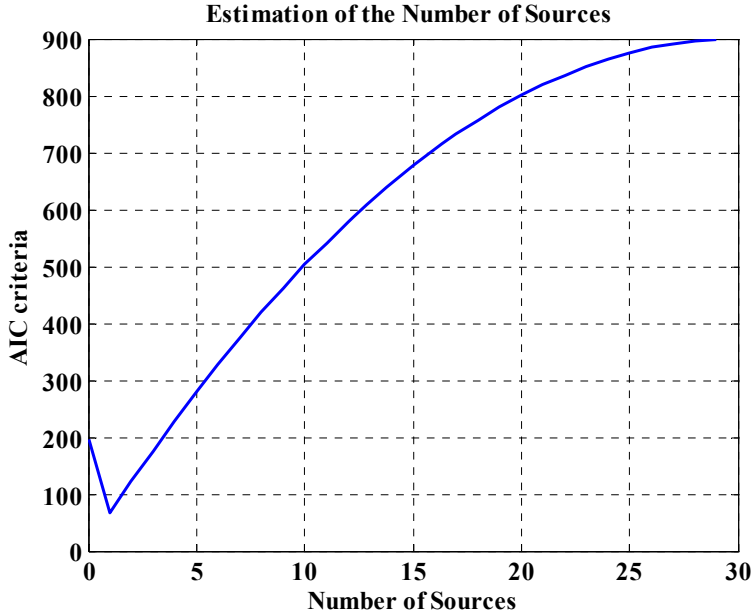


Figure 6-14: AIC criterion as a function of the number of sources

The topology of the receiver and BSs were previously shown in Figure 6-9. Based on this, the correct AOAs can be compared with the estimated ones, which for the Market Mall and UofC BSs, are 97 and 113 degrees respectively. Figure 6-15 shows AOA estimation results of Market Mall BS for $M=30$ and $K=20$ for 18,000 snapshots. Figure 6-16 shows the PDF of AOA estimation for the results given in Figure 6-15. For comparison a normal fit is also overlaid. The statistics of the AOA estimation are also given in Figure 6-16. Based on the averaging of 18,000 independent snapshots, the mean value of AOA estimation is 97.8 degrees with a standard deviation (STD) of 0.28 degrees.

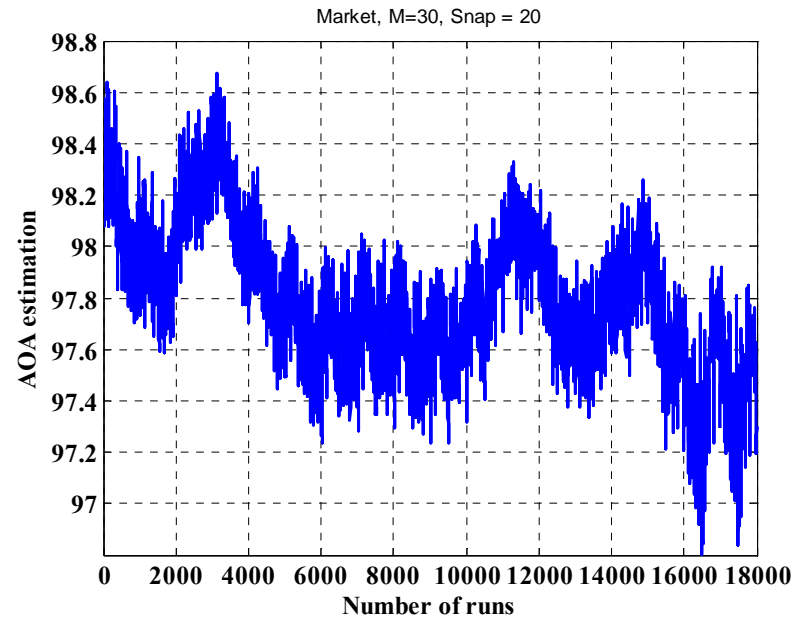


Figure 6-15: Estimated AOA from Market Mall BS, $M=30, K=20$

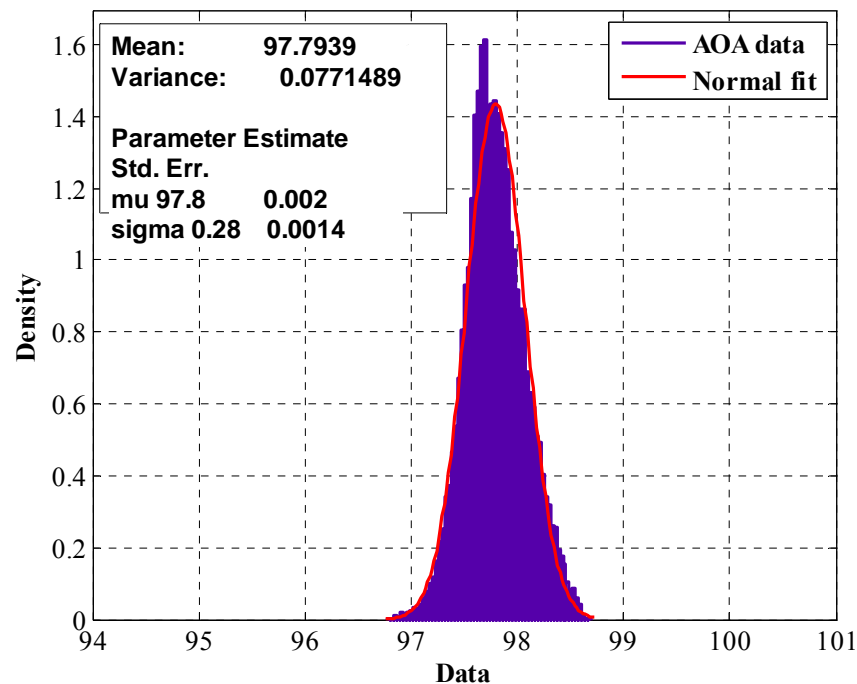


Figure 6-16: AOA estimation PDF and normal fit for 18000 snapshots

Figure 6-17 shows the PDF of AOA estimation for the UofC BS signals for $M=10$, $K=1$.

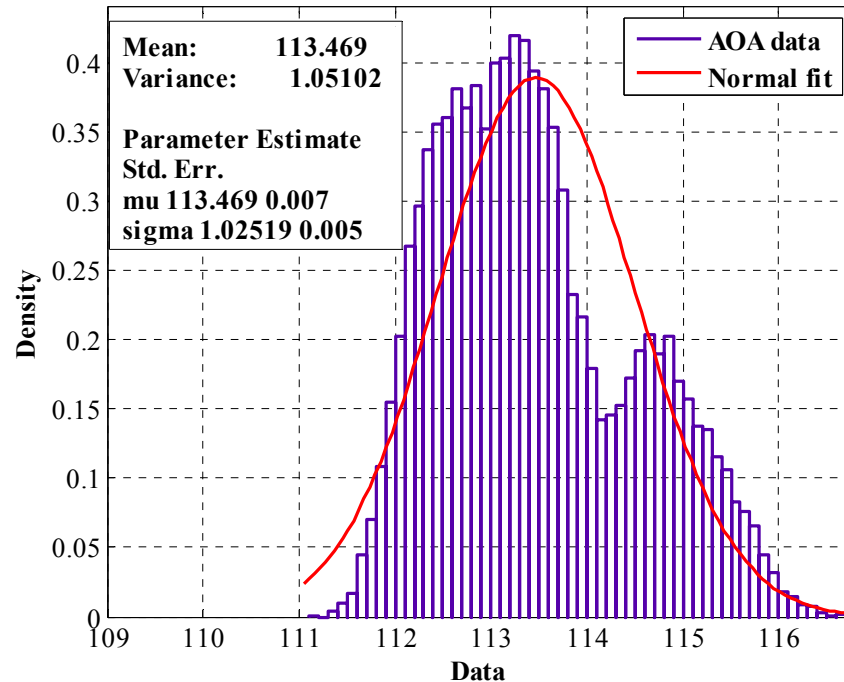


Figure 6-17: AOA estimation PDF and normal fit for 18000 snapshots, UofC BS,

$M=10, K=1$

Figure 6-18 show the PDF of AOA estimation for UofC BS signals when $M=20, K=1$.
The corresponding PDF when $M=30, K=1$ is shown in Figure 6-19.

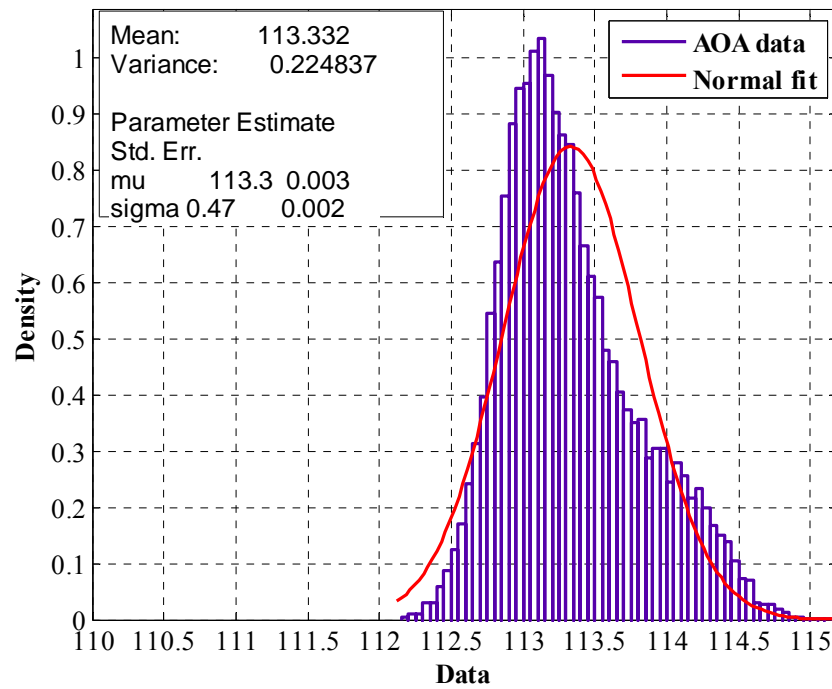
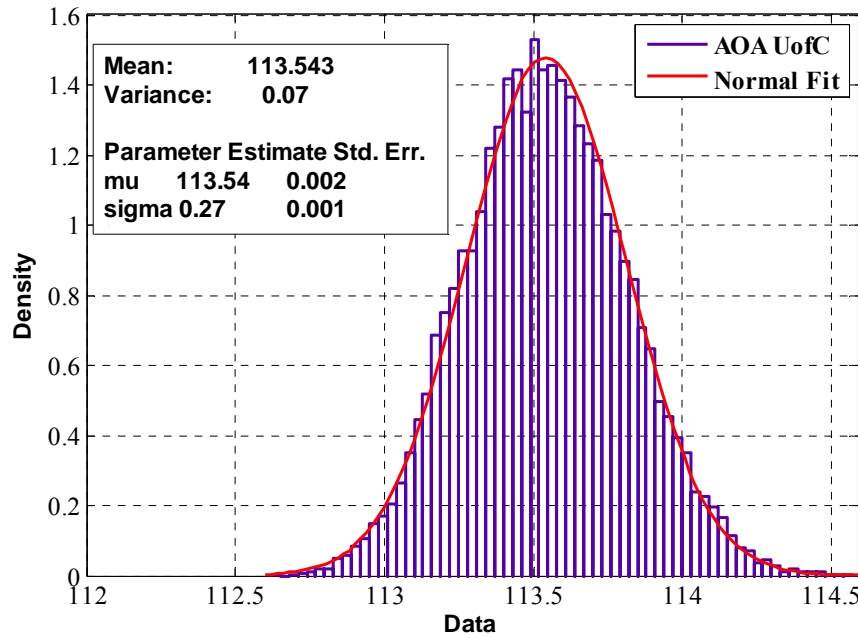


Figure 6-18: AOA estimation PDF and normal fit for 18000 snapshots

Figure 6-19: PDF of estimated AOA from UofC BS, $M=30$, $K=1$

By comparing the results of Figure 6-16 to Figure 6-19, one sees that the variance of AOA estimation decreases when increasing the number of spatial samples M .

Figure 6-20 shows the PDF of AOA estimation for the UofC BS signals for $M=20$ and $K=20$.

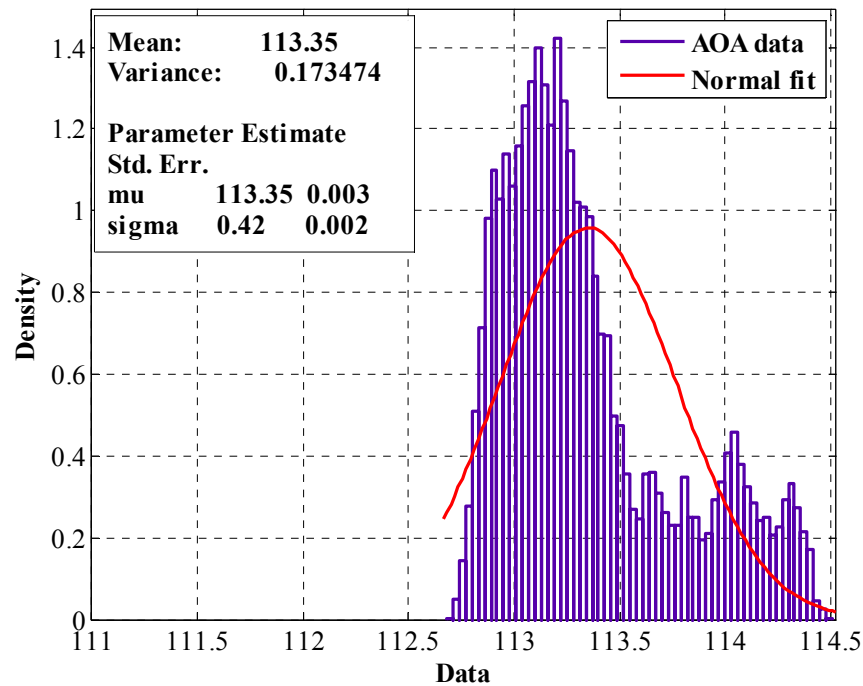


Figure 6-20: PDF of Estimated AOA from UofC BS, $M=20$, $K=20$

Figure 6-21 shows the PDF of AOA estimation results of UofC BS signals for the case of $M=30$ and $K=20$.

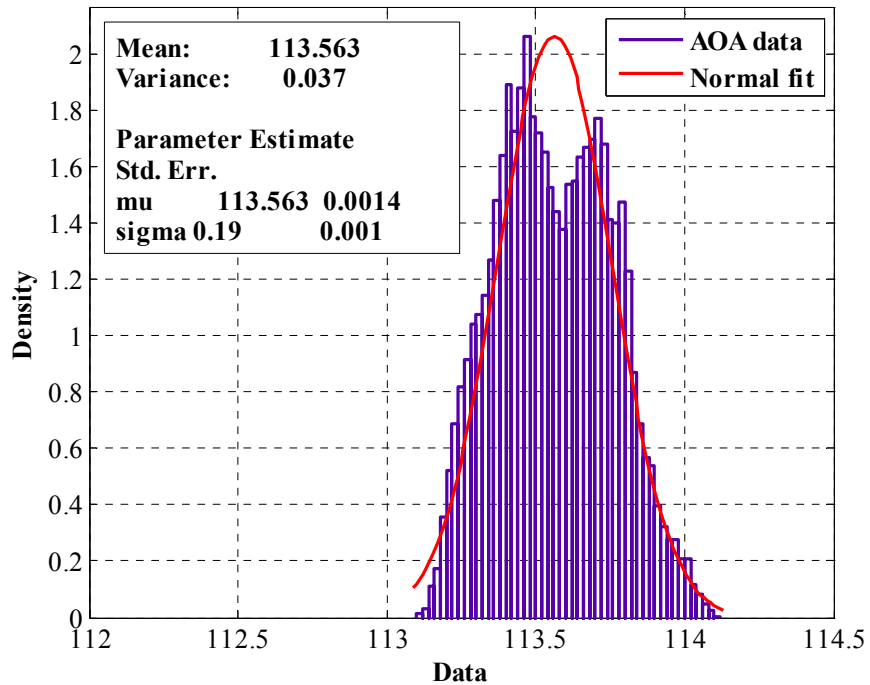


Figure 6-21: PDF of estimated AOA from UofC BS, $M=30$, $K=20$

Comparing the results of Figure 6-20 and Figure 6-21, one sees that increasing the number of snapshots K decreases the variance of AOA estimation. Table 6-3 summarizes the AOA estimation results utilizing the synthetic array for the Market Mall and UofC BSs.

For more experimental results based on the synthetic array concept utilizing the ESPRIT algorithm readers are further referred to (Broumandan et al 2008b)

Table 6-3: Summary of experimental results of AOA estimation

BS	Snapshots	M	K	Mean	Variance
Market Mall	18,000	30	20	97.8	0.08
UofC	18,000	10	1	113.5	1.05
UofC	18,000	20	1	113.3	0.25
UofC	18,000	30	1	113.5	0.07
UofC	18,000	20	20	113.35	0.17
UofC	18,000	30	20	113.5	0.04

6.4 Conclusions

In this chapter, a high-resolution AOA estimation methodology based on the ESPRIT concept was developed and tested. During data collection, a doublet was moved to create a synthetic array. Utilizing this method the previous constraints including array trajectory estimation could be relaxed. Neither a mechanical moving motor with constant speed nor auxiliary sensors are required. The synthetic ESPRIT algorithm is highly suitable for rotational invariance movements such as vehicle AOA estimation. Experimental results based on the actual CDMA IS-95 signals revealed that the proposed method is usable for high-resolution AOA estimation.

Chapter 7: CONCLUSIONS AND RECOMMENDATIONS

This chapter provides conclusions pertaining to the synthetic array signal detection and parameter estimation performance in different multipath environments presented in the thesis. This is followed by recommendations for future work.

7.1 Conclusions

The detection performance of the static and moving antennas in multipath fading environments characterized by Rayleigh fading was investigated. Two operating scenarios for implementation of the synthetic array, namely discrete and continuous modes, were demonstrated. It was shown that a substantial processing gain is possible by moving the antenna relative to maintaining the antenna in a static position. For a practical application case, more than 10 dB of processing gain relative to a static antenna was demonstrated as being achievable. Furthermore it was demonstrated that there is an optimum spatial sample and receiver velocity to utilize, which is a function of the target detection parameters P_{FA} and P_D . The detection performance and processing gain of the synthetic antenna array were compared to that of the static antenna subject to correlated Rayleigh fading. It was shown that if the correlation of the signal samples is increased then the diversity gain diminishes, eventually to the point where the moving antenna does not provide any gain over the static antenna. The performance degradation of the EG combiner due to correlated fading with respect to an optimal EC approach was determined. The results showed that in moderate correlated signal environments, the performance of the EC and EG combiners are almost identical. The detection

performance of the synthetic array in continuous mode was also demonstrated based on the EC and EG combiners. The coherent integration loss due to antenna motion in the Raleigh fading channel was characterized. A limit for the coherent integration gain versus the velocity of the receiver in Rayleigh fading environment was presented. The synthetic array sensitivity to the trajectory estimation error and practical implementation issues were discussed.

Experimental measurements were used to validate the theoretical findings in the context of the discrete and continuous modes of the synthetic array in indoor fading environments. The objective of the experimental measurements was to determine the processing gain advantage of the synthetic array over the static antenna. Two different CDMA signal structures, namely IS-95 and GPS signals were utilized to evaluate the synthetic array detection performance in different indoor multipath environments. Experimental measurements were performed to verify the assumption of Rayleigh fading and the channel correlation coefficient. The detection performance of the discrete synthetic array under the correlated Rayleigh fading was investigated and compared with the theoretical values. It was empirically demonstrated that for the given target detection parameters in terms of P_{FA} and P_D , there is an optimum number of spatial samples that provides maximum processing gain and detection probability of the synthetic array over the static antenna. It was shown experimentally that there is an optimum antenna velocity to use that provides the maximum processing gain. Experimental results of the synthetic array in the continuous mode revealed that for a practical range of P_D and P_{FA} the processing gain advantage of the synthetic array over the static antenna is of the order of

6 dB. This significant gain translates in a reduction of the mean acquisition process by a factor of four.

AOA estimation results utilizing the synthetic array based on the ESPRIT algorithm was introduced and tested. Practical implementation issues including the array calibration and source number estimation were considered. Experimental results based on the reception of the downlink CDMA IS-95 pilot signals verified the applicability of the proposed method in the context of the AOA estimation utilizing the synthetic array in specular multipath environments.

7.2 Recommendations

Owing to the broad nature of the synthetic array concept, the research presented herein primarily focused on specific aspects of signal detection and parameter estimation for particular signal and channel models. Considering the theoretical and experimental results presented, the following recommendations are made to extend the scope of this research and identify the limitations of the proposed methods.

7.2.1 Signal detection performance in dense multipath environments

- The assumption utilized herein was based on Rayleigh fading where there is not a well defined Line Of Sight (LOS) signal component. Based on this assumption the synthetic array processing gain over the static antenna was determined. The results presented herein may be generalized by considering the presence of the LOS component and taking into consideration Rician type fading.

- It was assumed that received signals are narrowband relative to the coherence bandwidth of the propagation channel. This is reasonable as the coherence bandwidth of indoor channels is typically several MHz in excess of the equivalent bandwidth of the pilot CDMA IS-95 and GPS L1 C/A signals. Consequently, it can be assumed that the signal undergoes flat fading which implies that multipath is unresolvable. If the coherence bandwidth becomes less than the bandwidth of the signal, which is typical of dense outdoor urban propagation environments, then multipath becomes frequency selective. In this case, there are several resolvable components of the multipath which tend to fade independently. This result in additional diversity could be exploited to further enhance signal detection performance. The analysis presented herein could be generalized to include the possibility of resolvable multipath.
- The temporal clock instability which effectively reduces the equivalent channel coherence time was ignored. The finite channel coherence time degrades the processing performance of the stationary antenna more than that of the synthetic array. Hence, the relative processing gain of the synthetic array actually increases if the clock instability is taken into account in the analysis. Thus, the synthetic array gain over the static antenna may be generalized by considering the clock instability for low cost handheld receiver applications.
- Although the synthetic array concept presented herein was basically introduced for a spatial diversity system where the antenna motion provides the diversity gain, the synthetic array formulations, the detection performance and the processing gain may be applied to other antenna diversity systems such as

polarization diversity. For instance, in a polarization diversity system utilizing the synthetic array concept, instead of using several orthogonally polarized antennas, diversity gain may be realized by changing the orientation of a single antenna.

- Comparing to the spatial diversity where the antenna spacing is the limiting factor to receive independent signals, two closely spaced antennas with orthogonal polarization can receive independent signals. To enhance signal detection performance in dense multipath environments utilizing a handheld receiver one may extend the synthetic array concept investigated herein to a system with a dual-polarized antenna. In this case, the signal detection performance and robustness of the diversity system will be further improved.

7.2.2 AOA estimation and signal detection performance in specular multipath environments

- The field measurement results of AOA estimation presented herein were based on data collection on the roof top of a building with access to LOS signals. Further data collection is required to evaluate the performance of the proposed method for different multipath scenarios.
- The AOA estimation concept utilizing the synthetic array presented here was established based on the rotational invariance property of the ESPRIT algorithm. However, in practical applications of the synthetic array utilizing the ESPRIT method, the doublet orientation may change. This phenomenon can be investigated to further evaluate the performance of the proposed method in the

presence of doublet alignment errors. A rate gyro may be considered to estimate the doublet rotation and compensate for this effect.

- Since AOA estimation utilizing the ESPRIT algorithm does not require any array manifold information, it can be used to estimate the synthetic array manifold. It would be of interest to analyze the accuracy of the array manifold estimation utilizing the proposed method.
- Once the array manifold is estimated, the beamforming and null-steering approaches may be implemented to enhance signal parameter estimation (e.g. TOA) and remove multipath and interference. One can take this into account and evaluate the beamforming and null-steering performances in the presence of the synthetic array manifold estimation errors.

REFERENCES

- Allen, B., and M. Ghavami (2006) *Adaptive Array Systems*, John Wiley & Sons, Ltd
- Blaunstein, N., and J. B. Andersen (2002) *Multipath Phenomena in Cellular Networks*, Artech House
- Broumandan, A., T. Lin, A. Moghaddam, D. Lu, J. Nielsen, and G. Lachapelle (2007) “Direction of Arrival Estimation of GNSS Signals Based on Synthetic Antenna Array,” *Proceedings of ION GNSS07*, Fort Worth, TX, 25-28 September
- Broumandan, A., and T. Lin (2008a) “Performance of GNSS Time of Arrival Estimation Techniques in Multipath Environments,” *Proceedings of ION GNSS08* (Savannah, GA, 16-19 Sep, Session C2), The Institute of Navigation
- Broumandan, A., J. Nielsen, and G. Lachapelle (2008b) “Practical Results of High Resolution AOA Estimation by the Synthetic Array,” *IEEE VTC Fall Conference*, Calgary, Alberta, Canada September
- Broumandan, A., J. Nielsen, and G. Lachapelle (2008c) “TOA Estimation Enhancement based on Blind Calibration of Synthetic Arrays,” *IEEE VTC Fall Conference*, Calgary, 22-25 September
- Broumandan, A., T. Lin, J. Nielsen, and G. Lachapelle (2008d) “Practical Results of Hybrid AOA/TDOA Geolocation Estimation in CDMA Wireless Networks,” *IEEE VTC Fall Conference*, Calgary, 22-25 September
- Broumandan, A., J. Nielsen, and G. Lachapelle (2009a) “Narrowband Signal Detection with a Moving Antenna under Correlated Rayleigh Fading,” *International Journal of Antennas and Propagation*, submitted for publication
- Broumandan, A., J. Nielsen, and G. Lachapelle (2009b) “Signal Detection Performance in Rayleigh Multipath Fading Environments with a Moving

Antenna," *IET signal Processing Journal*, accepted for publication

Broumandan, A., J. Nielsen, and G. Lachapelle (2009c) "Indoor GNSS Signal Acquisition Performance Using a Synthetic Antenna Array," *IEEE Transactions on Aerospace and Electronic Systems*, submitted for publication

Broumandan, A., J. Nielsen, and G. Lachapelle (2009d) "Enhanced Detection Performance of Indoor GNSS Signals based on Synthetic Aperture," *IEEE Transaction on Vehicular Technology*, submitted for publication

Broumandan, A., J. Nielsen, and G. Lachapelle (2009e) "Signal Detection Performance in Indoor Environments with a Synthetic Antenna Array," *proceedings of 13th International Symposium on Antenna Technology and Applied Electromagnetics (ANTEM) and the Canadian Radio Sciences Meeting (URSI/CNC)*, Banff, Canada, 15-18 February

Broumandan, A., J. Nielsen, and G. Lachapelle (2009f) "Narrowband Signal Detection in Correlated Rayleigh Fading with a Moving Antenna," *proceedings of 13th International Symposium on Antenna Technology and Applied Electromagnetics (ANTEM) and the Canadian Radio Sciences Meeting (URSI/CNC)*, Banff, Canada, 15-18 February

Brown, A., and N. Gerein (2001) "Test Results of a Digital Beamforming GPS Receiver in a Jamming Environment," *Proceedings of ION GPS*, Salt Lake City, September

Caffery, J. J. (2000) *Wireless Location in CDMA Cellular Radio Systems*, Kluwer Academic Publishers, Boston

Caffery, J. J., and G. Stuber (1998a) "Overview of Radiolocation in CDMA Cellular Systems," *IEEE Communications Magazine*, pp. 38-45, April

Caffery, J. J., and G. Stuber (1998b) "Subscriber Location in CDMA Cellular Networks," *IEEE Transactions on Vehicular Technology*, vol. 47, no. 2, May

Caini, C., G. E. Corazza, and A. Vanelli-Coralli (2004a) "DS-CDMA Code Acquisition in the Presence of Correlated Fading-Part I: Theoretical Aspects," *IEEE Transaction on Communications*, vol. 52, no. 7, pp. 1160-1167, July

Caini, C., G. E. Corazza, and A. Vanelli-Coralli (2004b) "DS-CDMA Code Acquisition in the Presence of Correlated Fading-Part II: Application to Cellular Networks," *IEEE Transaction on Communications*, vol. 52, no. 8, pp. 1397-1407, August

Charndran, S. (2006) *Advances in Direction of Arrival Estimation*, Artech House

Choi, S., and D. Shim (2000) "A Novel Adaptive Beamforming algorithm for a smart antenna system in a CDMA mobile communication environment," *IEEE Transaction on Vehicular Technology*, vol. 49, no. 5, pp. 1793–1806, September

Colburn, J. S., Y. Rahmat-Samii, M. A. Jensen, and G. J. Pottie (1998) "Evaluation of Personal Communications Dual-Antenna Handset Diversity Performance," *IEEE Transaction on Vehicular Technology*, vol. 47, pp. 737–744, August

Friedlander, B., and S. Scherzer (2004) "Beamforming Versus Transmit Diversity in the Downlink of a Cellular Communications Systems," *IEEE Transaction on Vehicular Technology*, vol.53, no. 4, pp. 1023-1034, July

Fu, Z., A. Hornbostel, and A. Konovaltsev (2003) "Suppression of Multipath and Jamming Signals by Digital Beamforming for GPS/Galileo Applications," *GPS Solutions*, vol 6, no 4, pp. 257-264

Fulghum, T. L., K. J. Molnar, and A. Duel-Hallen (2002) "The Jakes Fading Model for Antenna Arrays Incorporating Azimuth Spread," *IEEE Transaction on*

- Vehicular Technology*, vol. 51, no. 5, pp. 968-977, September
- Haykin, S. (1985) *Array Signal Processing*, Prentice-Hall, Englewood Cliffs, New Jersey
- Holmes, J. K., and C. C. Chen (1977) "Acquisition Time Performance of PN Spread-Spectrum Systems," *IEEE Transaction on Communications*, vol. COM-25, no. 8, August
- Hyeon, S., Y. Yun, H. Kim, and S. Choi (2008) "Phase Diversity for an Antenna-Array System With a Short Interelement Separation," *IEEE Transaction on Vehicular Technology*, vol. 57, no. 1, January
- Johnson, D. H., and D. E. Dudgeon (1993) *Array Signal Processing, Concepts and Techniques*, Prentice-Hall, Englewood Cliffs, New Jersey
- Jong, Y. L. C. (2001) *Measurement and Modeling of Radio wave Propagation in Urban Microcells*, PhD Thesis, Department of Electrical Engineering, University of Technology (EUT), Netherlands
- Jong, Y. L., and M. Herben (1999) "High-resolution Angle of Arrival Measurement of the Mobile Radio Channel," *IEEE Transaction on Antennas Propagations*, vol.47, no.11, pp.1677-1687, November
- Kaplan, E. D. and C. J. Hegarty (2006) *Understanding GPS Principles and Applications*, Artech House, Boston, London, 2nd edition
- Kay, S. M. (1988) *Modern Spectral Estimation: Theory and Application*, Prentice-Hall, Inc
- Kay, S. M. (1993) *Fundamentals of Statistical Signal Processing: Estimation Theory*, Prentice Hall PTR

Kay, S. M. (1998) *Fundamentals of Statistical Signal Processing: Detection Theory*, Prentice-Hall, Inc

Kim, S. (2004) "Acquisition Performance of CDMA Systems with Multiple Antennas," *IEEE Transaction on Vehicular Technology*, vol. 53, no. 5, pp. 1341-1353, September

Klukas, R. W. (1993) *Angle of Arrival Estimation in the Outdoor Radio Environment*, M.Sc. Thesis, University of Calgary, Calgary, Alberta, Canada

Lee, W. Y. (1989) *Mobile Cellular Telecommunications Systems*, McGraw-hill, New York

Li, F., and R. J. Vaccaro (1992) "Sensitivity Analysis of DOA Estimation Algorithms to Sensor Errors," *IEEE Transactions on Aerospace and Electronic Systems*, vol. 28, no.3, July

Liberti, J., and T. S. Rappaport (1999) *Smart Antennas for Wireless Communications: IS-95 and Third Generation CDMA Applications*, Prentice Hall

Litva, J., and T. K. Lo (1996) *Digital Beamforming in Wireless Communications*, Artech House

Lu, D. (2007) *Space-Time Signal Processing-Based Multipath Mitigation for CDMA-Based Location System*, PhD Thesis, Department of Electrical Engineering, The university of Calgary, Canada

Mahfuz, M. U. (2008), *Enhanced Detection of GNSS Signals Based on Spatial Combining*, M.Sc. Thesis, University of Calgary, Calgary, Alberta, Canada

Misra, P., and P. Enge (2001) *Global Positioning System Signals, Measurements, and Performance*, Ganga-Jamuna Press

Mogaddam, A. R. A. (2007) *Enhanced Cellular Network Positioning using Space-Time Diversity*, M.Sc. Thesis, University of Calgary, Calgary, Alberta, Canada

Narayanan, R. M., K. Atanassov, V. Vladimir, and G. R. Kadambi (2004) “Polarization Diversity Measurements and Analysis for Antenna Configurations at 1800 MHz,” *IEEE Transaction on Antennas and Propagation*, vol.52, no. 7, pp.1795-1810, July

Ng, B., C. Meng, and S. See (1996) “Sensor-Array Calibration Using a Maximum-Likelihood Approach” *IEEE Transaction on Antennas and Propagation*, vol. 44, no. 6

Ottersten, B., M. Viberg, and T. Kailath (1991) “Performance Analysis of the Total Least Squares ESPRIT Algorithm,” *IEEE Transactions on Signal Processing*, vol. 39, no. 5, May

Pany, T., M. Paonni, and B. Eissfeller (2008) “Synthetic Phased Array Antenna for Carrier/Code Multipath Mitigation,” *Proceedings of ENC-GNSS 2008*, Toulouse

Papoulis, A., S. U. Pillai (2002) *Probability, Random Variables and Stochastic Processes*, McGraw-Hill, Fourth edition

Parkinson, B. W., and J. J. Spilker (1996) *Global Positioning System: Theory and Applications*, American Institute of Aeronautics and Astronautics, Inc., Washington DC

Parsons, J. D. (2000) *The Mobile Radio Propagation Channel*, John Wiley & Sons LTD, 2nd ed.

Pierre, J., and M. Kaveh (1991) “Experimental Performance of Calibration and

- Direction-Finding Algorithms," *Acoustics, Speech, and Signal Processing ICASSP*
- Pillai, S. U. (1989) *Array Signal Processing*, Springer-Verlag, New York
- Proakis, J. G. (2001) *Digital Communications*, McGraw-Hill, 4th edition
- Rao, B. D., and K. V. S. Hari (1989) "Performance analysis of ESPRIT and TAM in determining the direction of arrival of plane wave in noise," *IEEE Transaction on Acoustic, Speech and Signal Processing*, vol. 37, pp. 1990-1995, December
- Rappaport, T. S. (2002) *Wireless Communications: Principles and Practice*, Prentice Hall PTR, 2nd Edition
- Reddy, V. U., A. Paulraj, and T. Kailath (1987) "Performance Analysis of the Optimum Beamformer in the Presence of Correlated Sources and its Behavior under Spatial Smoothing," *IEEE Transactions on Acoustics, Speech, and Signal Processing*, vol. ASSP-35,no. 7
- Rensburg, C. D. V. (2001) *Novel Spatial Diversity Techniques for Mobile Communications in Correlated Fading Environments*, PhD thesis, Department of Electrical and Computer engineering, University of California, Davis
- Rensburg, C. V., and B. Friedlander (2004a) "The Performance of a Null-Steering Beamforming in Correlated Rayleigh Fading," *IEEE Transaction on Signal Processing*, vol. 52, Bo. 11, pp. 3117-3125, November
- Rensburg, C., and B. Friedlander (2004b) "Transmit Diversity for Arrays in Correlated Rayleigh Fading," *IEEE Transaction on Vehicular Technology*, vol.53, no. 6, pp.1726-1734, November
- Roy, R. (1987) *Estimation of Signal Parameters Via Rotational Invariance Techniques*, PhD Thesis, Department of Electrical Engineering, Stanford

University

Roy, R., and T. Kailath (1989) "ESPRIT- Estimation of Signal Parameters Via Rotational Invariance Techniques," *IEEE Transaction on Acoustics, Speech and Signal Processing*, vol.37, no. 7, pp. 984-995,July

Saleh, A. A. M., and R. A. Valenzula (1987) "A statistical Model for Indoor Multipath Propagation," *IEEE Journal on Selected Areas in Communication*, vol. JSAC-5, pp.128-137, February

Sayed, A. H., A., Tarighat, and N., Khajehnouri (2005) "Network-Based Wireless Location Challenges faced in developing techniques for accurate wireless location information," *IEEE Signal Processing Magazine*, July

Schmidt, R. (1986) "Multiple Emitter Location and Signal Parameter Estimation," *IEEE Transactions on Antennas and Propagation*, vol. AP-34, no.3

Seco, G., and J. A. Fernández-Rubio (1997) "Multipath and Interference Errors Reduction in GPS /GNSS by Joint Pseudorange Measurement and Array Beamforming," *Proceedings of First European Symposium on Global Navigation Satellite Systems*, 21-25 April, Munich, Germany, pp. 605-614

See, C. M. S. (1994) "Sensor Array Calibration in the Presence of Mutual Coupling and Unknown Sensor Gains and Phases," *Electronics Letters, IEE*, vol. 30, no. 5, March

See, C. M. S. (1995) "Method for Array Calibration in High-Resolution Sensor Array Processing," *IEE Proc. Radar, Sonar Navigations*, vol.142, no.3, pp. 90-96, June

Shin, O. and K. B. Lee (2003) "Use of Multiple Antennas for DS/CDMA Code Acquisition," *IEEE Transaction on Wireless Communication*, vol. 2, no. 3, pp.

424-430, May

Soloviev, A., F. V. Graas (2009) "Beam Steering in Global Positioning System Receivers Using Synthetic Phased Arrays," *IEEE Transaction on Aerospace and Electronic Systems*, Accepted for publication

Soon, V. C., and Y. F. Huang (1992) "An analysis of ESPRIT Under Random Sensor Uncertainties," *IEEE Transaction on Signal Processing*, vol. 40, no. 9 , September pp. 2353-2358

Steinberg, B. D. (1976) *Principles of Aperture and Array System Design*, Wiley, New York

Stergiopoulos, S., and H. Urban (1992) "A new passive synthetic aperture technique for towed arrays," *IEEE Journal of Oceanic Eng.*, vol. 17, no. 1, pp. 16-25, January

Swindlehurst, A. L., B. Ottersten, R. Roy, and T. Kailath (1992) "Multiple invariance ESPRIT," *IEEE Transactions on Signal Processing*, vol. 40, no. 4, April

Van Trees, H. L. (2001) *Detection, Estimation, and Modulation Theory, part I*, John Wiley & Sons, Inc., New York

Van Trees, H. L. (2002) *Optimum Array Processing, part IV, Detection, Estimation, and Modulation Theory*, John Wiley & Sons, Inc., New York

Valenzuela-Valdes, J. F., M. A. Garcia-Fernandez, A. M. Martinez-Gonzalez, and D. Sanchez-Hernandez (2006) "The Role of Polarization Diversity for MIMO Systems Under Rayleigh-Fading Environments," *IEEE Antennas and Wireless Propagation Letters*, vol. 5, pp. 534-536

Wang, Y., and J. R. Cruz (2001) "Performance Enhancement of CDMA Cellular Systems with Augmented Antenna Arrays," *IEEE Journal of Selected Areas in*

Communications, vol. 19, pp. 1052–1060, June

Wax, M., and T. Kailath (1985) “Detection of Signals by Information Theoretic Criteria,” *IEEE Transactions on Acoustics, Speech, Signal Processing*, vol. ASSP-33, pp. 387-392

Zoltowski, M., and A. S. Gecan (1995) “Advanced Adaptive Null Steering Concepts for GPS,” *Military Communications Conference*, 5-8 November, San Diego CA, pp. 1214-1218

APPENDIX A: LIMIT OF NIG FOR DIFFERENT VALUES OF V WHEN $T \rightarrow \infty$

Adopting Eq. 4-32 for the case of $M=1$ and considering $\rho(T)$ as the integration output of a moving antenna as

$$\begin{aligned}\rho(T) &= \frac{2\rho_1}{T} \int_0^T (T-u) J_0(2\pi vu) du \\ &= 2\rho_1 \int_0^T J_0(2\pi vu) du - \frac{2\rho_1}{T} \int_0^T u J_0(2\pi vu) du\end{aligned}\quad \text{A-1}$$

and utilizing the identities

$$\begin{aligned}\int_0^\infty x J_0 dx &= x J_1(x) \\ \int_0^\infty J_n(bx) dx &= 1/b\end{aligned}, \quad \text{A-2}$$

the last term in Eq. A-2 can be expressed as

$$\begin{aligned}&\lim_{T \rightarrow \infty} \frac{-2\rho_1}{T} \int_0^T u J_0(2\pi vu) du \\ &= \lim_{T \rightarrow \infty} \frac{-2\rho_1}{(2\pi vu)^2 T} \int_0^T 2\pi vu J_0(2\pi vu) d(2\pi vu) \\ &= \frac{-2\rho_1}{(2\pi vu)^2 T} 2\pi vu J_1(2\pi vu) \Big|_0^{2\pi vT} \\ &= 0\end{aligned}. \quad \text{A-3}$$

Then,

$$\begin{aligned}&\lim_{T \rightarrow \infty} 2\rho_1 \int_0^T J_0(2\pi vu) du \\ &= \frac{1}{\pi v} \rho_1\end{aligned}. \quad \text{A-4}$$

Hence,

$$\lim_{T \rightarrow \infty} NIG = \frac{1}{\pi v} \quad \text{A-5}$$

APPENDIX B: FOR LARGER VALUES OF M $\frac{d\rho_m}{dM} > 0$

This can be shown analytically with the following argument. As noted in the previous section, the PDF of z_i conditioned on H_0 or H_1 is Chi-Squared central with $2M$ DOF. As M becomes larger, these conditional PDFs approach the Gaussian PDF such that⁴

$$\begin{aligned} z|_{H_1} &\sim N\left(\frac{I}{2}\left(1+\frac{\rho_m}{M}\right), \frac{I}{2M}\left(1+\frac{\rho_m}{M}\right)^2\right) \\ z|_{H_0} &\sim N\left(\frac{I}{2}, \frac{I}{2M}\right) \end{aligned} \quad \text{B-1}$$

where $N(\mu, \sigma^2)$ denotes the Gaussian PDF of mean μ and variance σ^2 . P_{FA} is therefore given approximately by

$$P_{FA} \approx \frac{1}{2} \operatorname{erfc}\left(\frac{\gamma - 1}{\sqrt{2/M}}\right) \quad \text{B-2}$$

and P_D by

$$P_D \approx \frac{1}{2} \operatorname{erfc}\left(\frac{\gamma - 1 - \rho_m/M}{\sqrt{2/M}(1 + \rho_m/M)^2}\right) \quad \text{B-3}$$

where $\operatorname{erfc}(v) = 2/\sqrt{\pi} \int_v^\infty e^{-t^2} dt$ is the complementary error function (Kay 1998).

Combining Eq. B-2 and Eq. B-3 gives a useful asymptotic implicit expression for ρ_m in terms of P_{FA} and P_D as

⁴ The PDF of a random variable $z = \sum_{i=1}^M x_i^2$ where $x_i \sim N(0, \sigma^2)$ for large values of M can be approximated by $z \sim N(M\sigma^2, 2M\sigma^4)$ due to central limit theorem (Kay 1998)

$$p_D \approx \frac{1}{2} \operatorname{erfc} \left(\frac{\sqrt{2/M} \operatorname{erfc}^{-1}(2P_{FA}) - \rho_m/M}{\sqrt{2/M} (1 + \rho_m/M)^2} \right). \quad \text{B-4}$$

The variation of ρ_m with respect to M for large M and given (constant) values of P_{FA} and P_D can be determined from

$$\frac{\sqrt{2/M} \operatorname{erfc}^{-1}(2P_{FA}) - \rho_m/M}{\sqrt{2/M} (1 + \rho_m/M)^2} = \text{const.} \quad \text{B-5}$$

Evaluating the total derivative of Eq. B-5 with M and ρ_m as variables results in the observation that $\frac{d\rho_m}{dM} > 0$ for large M , indicating that ρ_m must increase as M increases.

**APPENDIX C: SYNTHETIC ARRAY DETECTION PERFORMANCE
UTILIZING SIGNALS OF MARKET MALL BS**

Figure C-1 shows ROC curves of the Market Mall BS for $T=400 \mu\text{s}$. Table C-1 shows the processing gain of the synthetic array for the Market Mall BS for $T=400 \mu\text{s}$.

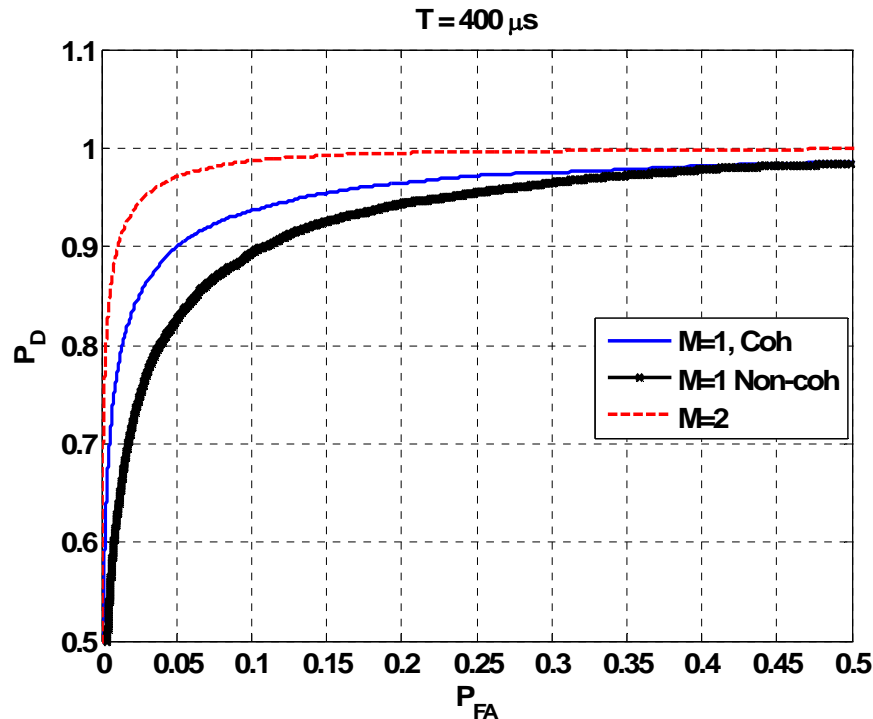


Figure C-1: ROC curves of static coherent integration, static non-coherent process and the synthetic array for $T=400 \mu\text{s}$ receiving from the Market Mall BS

Table C-1: Processing Gain of the moving antenna over the static antenna for different spatial samples, Market Mall BS, $T=400 \mu\text{s}$

	ρ (dB)	P_D		Processing Gain (dB)	
		$P_{FA} = 0.01$	$P_{FA} = 0.1$	$P_{FA} = 0.01$	$P_{FA} = 0.1$
$M = 1$, Coh	13.5	0.77	0.94	0	0
$M=2$, Static Non-coh	13.3	0.62	0.89	-	-
$M=2$, Synthetic	14	0.92	0.98	2	4